Impact of Cooldown Conditions on Trapped Flux in Superconducting Niobium

DISSERTATION
zur Erlangung des Grades eines Doktors
der Naturwissenschaften

vorgelegt von
M.Sc. Felix Kramer

eingereicht bei der Naturwissenschaftlich-Technischen Fakultät
der Universität Siegen
Siegen 2023

Betreuer und erster Gutachter
Prof. Dr. Jens Knobloch
Universität Siegen

Zweiter Gutachter
Prof. Dr. Wolfgang Hillert
Universität Hamburg

Tag der mündlichen Prüfung
23.10.2023

Abstract

Superconducting radio frequency cavities are a key technology in modern accelerators, and, over the past years, their performance improved such that additional losses from trapped magnetic flux are a limiting factor in their performance. This is especially important for accelerators operating in continuous wave mode where high losses in the cavity make operation too energy consuming.

For this reason there are many experiments investigating how trapped flux can be reduced. It is investigated how different materials and their treatments influence trapped flux, and how it is affected by cooldown parameters during the transition from the normal to superconducting state. These experiments are often done using cavities as samples. This makes changing material parameters expensive and time consuming. Additionally, the tests themselves are very time consuming so that the number of obtainable data points are often limited.

Within the scope of this thesis a new experimental setup is designed which uses flat, rectangular samples to investigate trapped flux. Using these samples has the advantage that different materials and treatments can be tested more easily. Additionally, geometric effects during transition are easier to model, and understand. Besides the easier sample preparation the new setup allows for more cooldowns in a shorter period of time so that around 300 thermal cycles can be performed in one day. This is roughly two orders of magnitude more than what is achieved with cavities. With the new setup cooldown parameters like the temperature gradient across the sample, the cooldown rate, and the external magnetic field can be independently controlled so systematic investigations how each parameter influences trapped flux can be performed.

Measurements conducted with different niobium samples confirm effects reported from other experiments. For example a decrease in trapped flux for increasing temperature gradient is observed as well as a linear increase of trapped flux with external magnetic field under certain conditions. But the ability to record more data points and a relative large parameter space also revealed unexpected results: For large grain niobium it is observed that when a sample is cooled down with a temperature gradient across the sample flux gets only trapped when the external field is larger than a certain threshold field which depends on the temperature gradient. Additionally, it is noticed that very fast cooldowns lead to high trapped flux magnitudes almost independent of the temperature gradient.

Besides these newly discovered effects the measured dependence of trapped flux on temperature gradient during cooldown does not agree with an existing model. For this reason a new phenomenological model is developed in cooperation with Prof. T. Kubo.

Zusammenfassung

Eine zentrale Technologie moderner Teilchenbeschleuniger sind supraleitende Hochfrequenzkavitäten, deren Leistungsfähigkeit sich in letzten Jahren so sehr verbessert hat, dass zusätzliche Verluste durch eingefrorenen magnetischen Fluss diese signifikant beeinträchtigt. Dies ist besonders relevant für Beschleuniger, die im Dauerstrichbetrieb arbeiten, da die Verluste in den Kavitäten den Betrieb zu teuer machen würden.

Aus diesem Grund gibt es bereits viele Experimente, die erforschen wie eingefrorener Fluss reduziert werden kann. Es wird untersucht wie unterschiedliche Materialien und deren Behandlung eingefrorenen Fluss beeinflussen und wie die Abkühlbedingungen während des Phasenübergangs von der normal leitenden- zur supraleitenden Phase sich auf diesen auswirken. Diese Experimente nutzen oft Kavitäten als Testobjekte, was es aufwendig und teuer macht unterschiedliche Materialien und Behandlungsmethoden zu untersuchen. Außerdem sind Messungen an Kavitäten sehr Zeitintensiv, sodass oft nur wenige Datenpunkte aufgenommen werden können.

Im Rahmen dieser Arbeit wurde ein neuer experimenteller Aufbau entwickelt, der flache rechteckige Proben verwendet um eingefrorenen Fluss zu untersuchen. Der Gebrauch der einfacheren Proben hat den Vorteil, dass unterschiedliche Materialien und Behandlungen einfacher getestet werden können. Auch vereinfacht die simplere Geometrie die Analyse geometrischer Effekte. Neben der einfacheren Probenvorbereitung ermöglicht es der neue Aufbau etwa 300 thermische Zyklen am Tag durchzuführen, was etwa zwei Größenordnungen mehr entspricht als bei Kavitäten. Der Aufbau ermöglicht es Abkühlparameter wie den Temperaturgradienten über die Probe, die Abkühlgeschwindigkeit und das externe Magnetfeld unabhängig von einander zu variieren. Dies ermöglicht die systematische Untersuchung des Einflusses jedes Parameters auf eingefrorenen Fluss.

Messungen an verschiedenen Niobproben bestätigen Effekte, die auch in anderen Experimenten beobachtet wurden. So wurde zum Beispiel weniger eingefrorener Fluss gemessen je höher der Temperaturgradient über die Probe während des Abkühlens ist und der Betrag des eingefrorenen Flusses steigt, unter gewissen Umständen, linear mit dem Betrag des externen Magnetfeldes. Jedoch haben die Möglichkeit viele Punkte aufzunehmen und der relativ große Parameterraum auch unerwartete Effekte offenbart: Für Niob, bestehend aus nur wenigen Einzelkristallen, das unter einem Temperaturgradienten abgekühlt wird, wird nur magnetischer Fluss eingefroren wenn das externe Feld einen bestimmten Schwellenwert überschreitet, der vom Temperaturgradienten abhängt. Außerdem wurde beobachtet, dass bei sehr schnellen Abkühlvorgängen sehr viel magnetischer Fluss eingefroren wird. Der Betrag ist dann fast unabhängig vom Temperaturgradienten.

Neben dieser neu entdeckten Effekte stimmt die beobachtete Abhängigkeit des eingefrorenen Flusses vom Temperaturgradienten während des Abkühlens nicht mit den Erwartungen eines existierenden Models überein. Daher wurde ein neues phänomenologisches Model in Zusammenarbeit mit Prof. T. Kubo entwickelt.

Contents

List of Figures

List of Tables

List of Abbreviations

AC Alternating Current

ADC Analog Digital Converter

AMR Anisotropic Magnetoresistance

BCS Bardeen Cooper Schrieffer

BCP Buffered Chemical Polishing

CEBAF Continuous Electron Beam Accelerator Facility

CERN Conseil Européen pour la Recherche Nucléaire

CW Continuous Wave

DC Direct Current

EXFEL European X-ray Free Electron Laser

FCC Future Circular Collider

HHC Helmholtz Coil

HOM Higher Order Mode

ILC International Linear Collider

LCLS-II Linac Coherent Light Source-II

LHC Large Hadron Collider

PCB Printed Circuit Board

PID Proportional–Integral–Derivative

RF Radio Frequency

RHIC Relativistic Heavy Ion Collider

RRR Residual Resistivity Ratio

RMSE Root Mean Square Error

SRF Superconducting Radio Frequency

TE Transverse Electric

TM Transverse Magnetic

XRD X-ray diffraction

List of Symbols

$\vec{B}$	Magnetic flux density vector
b	Sensitivity of B^* on temperature gradient
$\vec{B}_\mathrm{e}$	External magnetic flux density vector
B_e	External magnetic flux density magnitude
$\vec{B}_\mathrm{TF}$	Measured trapped magnetic flux vector
B_TF	Trapped magnetic flux density magnitude
B^*	Threshold field above which flux is trapped
c	Speed of light
$\vec{E}$	Electric field vector
E_acc	Accelerating Field
η	flux trapping efficiency
η_0	flux trapping efficiency with no temperature gradient
η_vis	viscous drag coefficient
F	Free energy
F_n	Free energy in normal conducting state
f_p	Pinning force
f_th	Thermal force
G	Geometry factor
g_c	critical gradient
$\vec{H}$	Magnetic field vector
$\hbar$	Reduced Planck constant
$\vec{j}_\mathrm{s}$	superconducting current density
λ_L	London penetration depth
Λ	Order parameter in Ginzburg-Landau theory
m	Mass
μ_0	Vacuum permeability
$\hat{n}$	Surface normal
$n(f_\mathrm{p})$	distribution function of pinning force
n_s	superconducting charge carrier density
ω_0	Resonant angular frequency
P_c	Dissipated power in cavity
Φ_0	Magnetic flux quantum
Ψ	Wave function of cooper pairs
Q_0	Unloaded quality factor
r	ratio of expelled flux
r_trap	ratio of trapped flux
R_BCS	BCS surface resistance
R_res	Residual resistance
R_s	Surface resistance

t	Time
T	Temperature
T_{c}	Critical Temperature
∇T	Temperature gradient
U	Stored energy in Cavity
$\vec{v}$	velocity vector
V_{acc}	Accelerating Voltage
ξ	Coherence length

1. Introduction

Particle Accelerators, the Bigger Picture

Particle Accelerators are a key technology in many fields of research. The best known field is particle physics, specifically research conducted at the Large Hadron Collider (LHC) [1]. But even in the field of particle physics many more particle accelerators (like CEBAF [2] or RHIC [3] in the USA) are used. In these machines two opposed particle beams are collided in detectors to investigate the fundamental structure of matter on a sub-atomic scale. Apart from research in particle physics there are applications for particle accelerators in many fields of science, like chemistry [4], biology [5], engineering [6], metrology [7], material science [6], geology [8], medicine [9], and even more. In these cases accelerated electrons are often not used directly but the synchrotron radiation that they emit when they are deflected in a magnetic field. The advantages of this synchrotron radiation over radiation from for example an x-ray tube are high brilliance, a spectrum that can be calculated analytically, higher achievable photon energies and densities, time resolutions up to fs, and overall better control of the incident light, or x-rays [10]. Examples for such machines are BESSY II in Berlin [11], EXFEL in Hamburg [12], or ALBA in Barcelona [13]. Lastly, there is also an application for smaller accelerators that can be operated by a company or hospital, in contrast to the large accelerators in science that are operated at national or even international (e.g . CERN) science institutes. These smaller accelerators play an important role in medicine where they can be used for irradiation in tumour therapy [14], or for preparation of radioactive isotopes which are used in imaging techniques [15].

The growing number of accelerators all over the world shows the high demand for such machines [16]. Additionally, there is a demand for increasing particle energies for future accelerators (e.g. ILC [17], FCC [18]). This poses a problem because building large accelerators is expensive and the energy consumption during operation is very high. In the context of increasing energy prices it becomes obvious that the energy needed to operate accelerators must be reduced.

Especially for linear accelerators a significant part of the energy consumption of an accelerator stems from operating accelerating cavities. An accelerator cavity is a metal resonator in which a radio frequency electro magnetic field is resonantly excited. The electric field component is used to accelerate the particles in an accelerator. Many years of research have already gone into optimizing their performance with respect to good beam quality and lower energy consumption. One major step was to manufacture cavities from superconducting metals instead of normal conducting metals like copper. How superconductors impact the performance of cavities is discussed next.

Superconductivity

When certain metals are cooled below a specific critical temperature their electric resistance drops to zero as long as the current is not alternating. In the case of accelerating cavities the electro magnetic fields have a frequency in the MHz to GHz range and the induced currents still dissipate power. However, the dissipated power is still 6 orders of magnitude smaller than in copper cavities [19]. This enables linear accelerators to be be operated in continuous wave (CW) mode at high accelerating gradients because the dissipated power in one meter of accelerator is only ≈10 W for superconducting cavities. Copper cavities operating at the same accelerating gradient would dissipate ≈20 MW per meter accelerator. For this reason copper cavities are operated in pulsed mode at high gradients. Building accelerators like LCLS-II which operates in CW with normal conducting cavities would not be possible.

The low losses in SRF cavities also open up new possibilities for the design of a cavity, because it can also be optimized to achieve a good beam quality and must not only be optimized to reduce power consumption. One example on how superconducting cavities can be designed differently concerns higher order modes (HOMs): When a particle beam passes through a cavity the charged particles excite HOMs in the cavity. These HOMs can deflect and deform particle bunches which can lead to beam instabilities, and emittance growths. One way to reduce HOMs is to enlarge the beam tubes but this increases the dissipated power. For normal conducting cavities the beam tubes can not be opened up very far because losses would get to high. Superconducting cavities are, however, not so restricted due to their much smaller losses. In many modern light sources where cavities are operated in CW and a low beam emittance is required superconducting cavities are the only feasible way.

The most significant drawback of superconducting cavities is their operating temperature. Most modern cavities are fabricated from niobium which has a critical temperature of 9.2 K and they are typically operated at temperatures of 1.8 K or 2 K. The efficiency of the cryoplants needed to cool the cavities is limited by the Carnot- and technical efficiency and is very low at these temperatures so that roughly 1 kW of wall plug power is needed cool 1 W of dissipated power in the cavity. But even with this poor efficiency superconducting cavities reduce power consumption by a factor of several hundred compared to normal conducting cavities [19]. Nevertheless, the poor efficiency of cryoplants shows how important it is to reduce the dissipated power in cavities.

Losses in Superconductors

As is already mentioned above, the resistance of superconductors only drops to zero for direct current (DC). In the case of the alternating fields in a cavity power is still dissipated. The losses in a superconductor in an RF field can be characterised by a surface resistance R_s. Part of this resistance (R_BCS) is described by a theory of superconductors, formulated by Bardeen, Cooper, and Schrieffer (BCS) [20]. In addition to this theoretically predicted resistance there is a residual resistance R_res which can stem from various sources. One of which is trapped magnetic flux.

Currently there are three main strategies to reduce power consumption of superconducting radio frequency (SRF) cavities: One is to reduce R_BCS with techniques like

nitrogen infusion [21, 22], and mid-T baking [23, 24]. Another strategy to reduce R_{BCS} and power consumption is to utilise other materials with higher critical temperatures. An important example here is Nb_3Sn with a critical temperature of 18 K [25, 26]. With Nb_3Sn the operating temperature can be increased to 4 K which increases the efficiency of cryoplants or even allows for conduction cooled cavities [27, 28]. The third strategy is to reduce R_{res}. The residual resistance must be considered when other loss mechanism are reduced to such an extend that R_{res} becomes significant. For state of the art cavities this is certainly the case [29, 30] and increased residual resistance due to trapped magnetic flux is the underlying motivation of this thesis.

Trapped Magnetic Flux

In an ideal case, an SRF cavity that is cooled down to its operating temperature expels weak magnetic fields like e.g. the earth's magnetic field. This means that in the superconducting material a magnetisation equal but opposite to the magnetic field is induced so that the magnetic flux density inside the superconductor is zero [31]. This is called Meissner effect. However, in experiments it is observed that not all magnetic flux is expelled and that a certain fraction of the external flux density is trapped in the superconductor [32]. This flux is not expelled from the superconductor even when the external field is reduced. This means for cavities that magnetic flux that is not expelled during the transition from normal to superconducting state is trapped inside the material until it is warmed up above its transition temperature.

It has been shown theoretically [33] as well as experimentally [34] that magnetic flux inside a superconductor exists as quantized flux lines that are held up by superconducting eddy currents. Ideally, these flux lines are pushed out when the material is cooled down. However, in real materials there are always defects which act as pinning centres. If the pinning force of the pinning centre is greater than forces pulling the flux line away from it, the flux line stays at the position of the pinning centre and is trapped. Pinning centres can occur in different forms, like normal conducting precipitates or inclusions, grain boundaries, or defects in the crystal lattice [35].

When flux lines move inside the superconductor it causes normal conducting electrons to flow in the material which creates losses. In case of cavities the RF field causes the pinned flux lines to oscillate back and forth which dissipates energy [36]. This leads to an increased residual resistance. Figure 1.1 shows how the quality factor, which is a measure of the performance of a cavity, decreases by a factor of six when a cavity is cooled down in an external magnetic flux density B_{e} of 10 µT compared to a cooldown where the external flux density is shielded below 1 µT (for comparison: the earth's magnetic field corresponds to a magnetic flux density of $\approx 50\,\mu\mathrm{T}$). This corresponds to an increase of surface resistance from 9 nΩ to 54 nΩ or an increase of dissipated power per meter of accelerator from 13 W to 77 W. This shows how residual resistance due to trapped flux can be a significant contribution to the surface resistance and, therefore, power consumption.

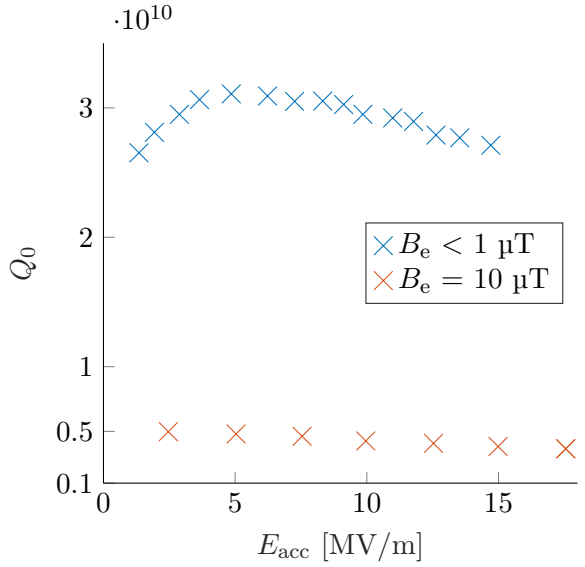

Figure 1.1.: Q_0 versus E_{acc} of a single cell cavity in a shielded cryostat ($B_e < 1\,\mu T$) when no field is applied, and when $10\,\mu T$ are applied in direction of the beam axis. The performance decreases by a factor of 6.

This is why cavities in cryomodules are shielded from external magnetic fields using permalloy shielding. It is, however, impossible to shield off all magnetic field and magnetic field can even be created inside the shield during cooldown [37, 38]. For this reason research is ongoing on how to prevent magnetic flux from being trapped in the cavity material.

Objective of this Thesis

There are experiments investigating trapped flux using cavities [39, 40] or samples [41, 42]. The experiments using samples often use imaging techniques to investigate trapped flux microscopically and how it is affected by material defects. Here, different materials and material treatments are investigated. Up to now these experiments are, however, often limited in the parameters which characterize a cooldown like the temperature gradient over the sample during cooldown, or the cooldown rate. Additionally, the external magnetic flux densities typically need to be in the mT range while trapped flux in cavities is in the µT range. Cavity experiments, on the other hand, show that a larger temperature gradient during cooldown leads to less trapped flux [43, 44]. Systematic investigations using cavities are done [45] but measurements are very time consuming which limits the amount of data points that can be taken. Additionally, the geometry of cavities makes analysis more complex and less clear [46, 47, 48].

The objective of this thesis is to gain a better understanding of how trapped flux is influenced by cooldown conditions. To do so a new experimental setup is developed which is able to measure trapped flux in a sample that can be cycled through its transition temperature many times with different cooldown parameters. Additionally, the cycles should not consume much time so more data points can be taken compared to cavity measurements. With the help of this setup systematic investigations of trapped flux in several samples are performed in order to get a better understanding of how trapped flux is influenced by cooldown- and material parameters. At this point the aim is not to find a perfect method to expel all flux, but rather to understand the flux

trapping phenomenon better. With a better understanding of trapped flux, and the new setup methods to decrease residual resistance can hopefully be developed in the future.

The setup is intended to measure trapped flux as a function of five parameters: Temperature gradient during cooldown, cooldown rate, external magnetic field, material, and material treatment. The first three parameters need to be controlled by the setup directly during measurement. The last two are given by the sample.

Structure of this Thesis

First, a brief theoretical introduction is given in cavities, superconductivity, and trapped flux. This chapter is intended to provide sufficient background information on the theory to allow an interpretation of the presented results.

Then, the newly designed experimental setup is introduced. It is described how the design choices are made to allow easy control of the five parameters mentioned above. Additionally, intrinsic systematic errors of the setup are described and estimated. Lastly, the measurement procedure is described on the basis of a typical cooldown.

It is shown in the course of this thesis that the effect of the parameters are interconnected. For this reason the next chapter first gives a qualitative overview of how the five parameters affect trapped flux one by one. It is shown that the setup can reproduce previous results obtained with cavities, for example that higher temperature gradients lead to less trapped flux and that trapped flux is proportional to the external field at small gradients. However, due to the relatively wide parameter range of the setup, and the ability to record many data points unexpected results are also discovered: It is observed that under certain circumstances flux is only trapped when the external field is above a threshold field. Additionally, a dependence of trapped flux on the cooldown rate is measured which could not be measured in other experiments [44, 49, 50]. During measurements it is not possible to keep all parameters perfectly constant while changing only one parameter. Therefore, after the effects of the parameters on trapped flux are described the effect of these inconsistencies on the measurement data and the implications on the measurement error are described.

In the next chapter the effects of temperature gradient and external field on trapped flux are analysed jointly and a phenomenological model describing trapped flux in dependence of temperature gradient and external field is developed. These studies were done in collaboration with Prof. T. Kubo from the High Energy Accelerator Research Organization (KEK) in Japan.

Finally, a summary of the achieved progress is given together with prospects for future research.

2. Theoretical Background

This chapter gives an introduction of existing theories concerning superconductivity, trapped flux, and how the latter affects superconductors in accelerators.

In this theses trapped magnetic flux is investigated in samples to understand the flux trapping process. But the motivation of the described experiments lies in the application of superconducting radio frequency (SRF) cavities in particle accelerators. Therefore, the concept of radio frequency (RF) cavities for particle acceleration is introduced first. This leads to the advantages of superconducting cavities over normal conducting ones, and theories describing superconductivity. It is then described how trapped magnetic flux reduces the performance of SRF cavities. Finally, an existing theory concerning flux trapping is introduced. Independent from theories concerning superconductivity or flux trapping the anisotropic magneto resistive (AMR) effect is introduced at the end of this chapter because the magnetic field sensors which made the experiment possible rely on it.

2.1. Radio Frequency Cavities

The first particle accelerators relied on electrostatic fields to accelerate charged particles. But electrostatic fields exert a conservative force on the particles which limits the energy that can be achieved by these accelerators because particles can pass it only once. To achieve high energies the accelerators need to be very large and problems like arcing limits the possible achievable energy. Due to these limitations they are used mostly for low energies (MeV range) and pre-accelerators [51].

To circumvent the problem of the conservative force accelerators with time dependent electric fields were invented. This has the advantage that particles can pass the same accelerating structure several times and gain energy on every pass. While there are several types of these accelerators [10] the focus of this thesis lies on RF cavities which are, for example, used in synchrotron accelerators or storage rings.

Cavities are hollow resonators made from conductive material. In these resonators a standing electromagnetic wave is induced, and the electric field is used to accelerate charged particles. Figure 2.1 shows a picture of a TESLA type [52] single cell cavity fabricated from niobium. The resonant frequency for the accelerating mode is 1.3 GHz.

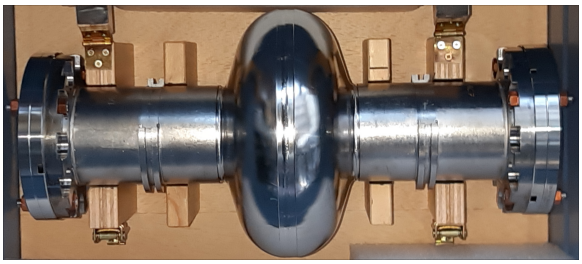

Figure 2.1.: 1.3 GHz TESLA single cell cavity fabricated from Niobium.

The following introduction of cavities and their figures of merit follow the lines of [19]. Since SRF cavities are not directly used in this theses only a brief introduction is given to motivate, and embed the presented research in the accelerator context.

2.1.1. Resonant Modes

Electromagnetic fields within the resonator have to fulfil Maxwell's equations which lead to two boundary conditions for the electric field $\vec{E}$ and the magnetic field $\vec{H}$:

$$\hat{n} \times \vec{E} = 0; \qquad \hat{n} \cdot \vec{H} = 0 \tag{2.1}$$

where $\hat{n}$ is the unit vector normal to the conducting surface of the resonator. It also follows from Maxwell's equations that the fields must obey the wave equation

$$\left(\nabla^2 - \frac{1}{c^2}\frac{\partial^2}{\partial t^2}\right)\begin{pmatrix}\vec{E}\\ \vec{H}\end{pmatrix} = 0 \tag{2.2}$$

with the speed of light c. Equation 2.2 with boundary conditions 2.1 can be solved analytically in case of a simple pill box cavity or numerically in the case of more complex shapes like in Figure 2.1 [19]. The solutions can be classified in two categories: Resonant modes with transverse electric field (TE) or transverse magnetic field (TM). TM modes have a longitudinal (along the beam axis) electrical field and can, therefore, be used to accelerate particles.

An important quantity for accelerators is the accelerating Voltage V_{acc} or the corresponding accelerating field E_{acc} in a cavity. V_{acc} is defined as

$$V_{acc} = \left|\frac{1}{e} \times \text{maximum energy gain possible during transit}\right|. \tag{2.3}$$

Here, e is the charge of an electron. The accelerating field is obtained by dividing V_{acc} by the length of the cavity d

$$E_{acc} = \frac{V_{acc}}{d}. \tag{2.4}$$

2.1.2. Figures of Merit

In order to compare different cavity shapes and performances, as well as the performance of the used material several figures of merit are introduced.

In the context of this thesis the most important quantity is the surface resistance of a material: The electromagnetic fields in the cavity are sustained by electric currents running along the cavity's surface. These alternating currents (AC) create losses and, therefore, power dissipation in the cavity wall. In order to quantify the losses of a given material, depending on the currents, the surface resistance R_s is introduced. The currents are proportional to the square of the magnetic field, so the surface resistance is defined as

$$\frac{\mathrm{d}P_\mathrm{c}}{\mathrm{d}s} = \frac{1}{2} R_s |\vec{H}|^2. \tag{2.5}$$

Here, $\frac{\mathrm{d}P_\mathrm{c}}{\mathrm{d}s}$ is the dissipated energy per surface area and $\vec{H}$ is the RF magnetic field. R_s is, therefore, a property of the material only and does not depend on the shape of the cavity.

Also related to the dissipated power is the unloaded quality factor Q_0 of a cavity. This figure of merit depends on the used material as well as the shape of a cavity. It denotes the ratio of stored energy in a cavity to the energy that is lost to Joule heating in one RF period

$$Q_0 = \frac{\omega_0 U}{P_\mathrm{c}} \tag{2.6}$$

where ω_0 is the resonant angular frequency, U the stored energy in the cavity, and P_c the dissipated power in the cavity's walls.

Q_0 can also be expressed in terms of the geometry factor G. It is defined as

$$G = \frac{\omega_0 \mu_0 \int_\mathrm{V} |\vec{H}|^2 \mathrm{dV}}{\int_\mathrm{S} |\vec{H}|^2 \mathrm{dS}} \tag{2.7}$$

where $\int_\mathrm{V} |\vec{H}|^2 \mathrm{dV}$ is the integral of the RF magnetic field over the volume of the cavity, and $\int_\mathrm{S} |\vec{H}|^2 \mathrm{dS}$ the integral over the surface. G is independent of the material of the cavity and can be used to characterize the design of a cavity. It is related to the quality factor and surface resistance via

$$Q_0 = \frac{G}{R_s}. \tag{2.8}$$

For TESLA 9-cell cavities which are often in used in electron accelerators $G = 270\,\Omega$ [52]. Modern superconducting cavities fabricated from niobium achieve quality factors in the range of $10^{10} - 10^{11}$ [53, 54]. According to equation 2.8 this corresponds to a surface resistance in the order of only a few nΩ. This is a factor 10^6 smaller than copper [19].

This low surface resistance of superconducting materials (typically niobium) is a big advantage over normal conducting materials like copper. It allows the design of the cavities to be optimized for other parameters than just minimizing power dissipation

which increases the beam quality. It also enables higher accelerating gradients in CW mode which makes linear accelerators operating in CW shorter.

These are the main reasons why in many modern accelerators superconducting cavities are used despite the increased complexity due to cryoplants which are needed to cool down the cavities to $\approx 2\,K$ [55].

2.2. Superconductivity

This Phenomenon was first discovered by Kamerling Ones in 1911 who was experimenting with liquid helium. He discovered that the direct current (DC) resistance of mercury dropped to $0\,\Omega$ when it is cooled below 4.2 K [56]. Later in 1933 Meissner and Ochsenfeld discovered that a superconductor expels magnetic flux from its volume when it passes its critical temperature T_c where it becomes superconducting[57]. This effect can not be explained by Maxwell's equations and the assumption of zero resistivity, and is now called Meissner effect. The first phenomenological theory of superconductors was introduced 1935 by F. and H. London who formulated two "London equations" which describe the Meissner effect [58]. The Ginzburg-Landau theory introduced in 1950 was the first quantum mechanical description of superconductivity [59, 60]. By series expansion of the free energy of superconductors close to T_c it is able to predict the temperature dependence of parameters describing the super conductive state, as long as $T - T_c \ll 1$. In 1957 Bardeen, Cooper, and Schrieffer formulated the BCS-theory [20]. It explains superconductivity with cooper pairs which are two electrons with opposite momentum (and in most cases opposite spin) that are coupled by electron-phonon interaction. These quasiparticles behave like bosons which alters the density of states around the fermi energy, creating an energy gap around it. Due to the special interaction with the lattice cooper pairs do not loose energy by dissipation [19].

This thesis presents experiments concerning trapped flux, i.e. magnetic flux that does not get expelled by the Meissner effect but stays within the superconductor. This expulsion of flux happens when the superconductor passes its transition temperature which makes the Ginzburg-Landau theory applicable. For this reason the Meissner effect and the Ginzburg-Landau theory are presented next. The following three subsections again follow the line of [19].

2.2.1. Meissner Effect

Before the Meissner effect is introduced the behaviour of a perfect conductor in a magnetic field is investigated to illustrate the difference to superconductors.

In a perfect conductor with zero resistivity electrons are accelerated freely in an electric field $\vec{E}$:

$$m\frac{\partial \vec{v}}{\partial t} = -e\vec{E} \tag{2.9}$$

where m is the mass of the electron, and e its charge. $\vec{v}$ is the velocity. This can be expressed in terms of the superconducting current density $\vec{j}_\mathrm{s} = -n_\mathrm{s} e\vec{v}$ with the

superconducting charge carrier density n_s:

$$\frac{\partial \vec{j}_\mathrm{s}}{\partial t} = \frac{n_\mathrm{s} e^2}{m} \vec{E} \tag{2.10}$$

This equation is the first London equation. Using $\nabla \times \vec{E} = -\frac{\partial \vec{B}}{\partial t}$ it is equivalent to

$$\frac{\partial}{\partial t} \left(\nabla \times \vec{j}_\mathrm{s} + \frac{n_\mathrm{s} e^2}{m} \vec{B} \right) = 0 \tag{2.11}$$

Further application of Maxwell's equations leads to

$$\nabla^2 \left(\frac{\partial \vec{B}}{\partial t} \right) = \frac{1}{\lambda_\mathrm{L}^2} \frac{\partial \vec{B}}{\partial t}, \quad \lambda_\mathrm{L}^2 = \frac{m}{n_\mathrm{s} e^2 \mu_0} \tag{2.12}$$

Applying this equation to a semi infinite perfect conductor in the half space $x > 0$ and a magnetic flux density B_0 in y-direction shows the implications of above equation. It becomes:

$$\frac{\partial \vec{B}(x)}{\partial t} = \frac{\partial B_0}{\partial t} \exp\left(-\frac{x}{\lambda_\mathrm{L}} \right) \tag{2.13}$$

Here, $\vec{B}(x)$ is the magnetic flux density inside the superconductor. Equation 2.13 implies that in the bulk of the material where $x \gg \lambda_\mathrm{L}$, $\frac{\partial \vec{B}(x)}{\partial t}$ goes to zero. This means that a perfect conductor will not expel magnetic flux, instead it conserves it. A perfect conductor that is cooled below its transition temperature in an external magnetic field would, therefore, trap all magnetic flux. This is contrast to the observed Meissner effect where (in the ideal case) all magnetic flux is expelled. To achieve this the term in equation 2.11 must not only be time independent but zero, so that

$$\nabla \times \vec{j}_\mathrm{s} + \frac{n_\mathrm{s} e^2}{m} \vec{B} = 0. \tag{2.14}$$

This is the second London equation. They describe the magnetic flux density within a superconductor as

$$\nabla^2 \vec{B} = \frac{1}{\lambda_\mathrm{L}} \vec{B}. \tag{2.15}$$

In the same scenario as above with a semi infinite superconductor in $x > 0$ and a magnetic field in y-direction the y-component of the magnetic flux density in the superconductor becomes

$$B_y(x) = B_0 \exp\left(-\frac{x}{\lambda_\mathrm{L}} \right). \tag{2.16}$$

Equation 2.16 describes an exponential decay of the magnetic flux density with a decay constant λ_L inside the superconductor. This represents the observed behaviour of superconductors which expel magnetic flux when they become superconducting and also do not let in magnetic flux once they are superconducting. λ_L is called the London penetration depth and is an important quantity to characterize a superconductor (see also section 2.2.4).

2.2.2. Critical Magnetic Field

In the context of the Meissner effect the critical magnetic field must also be mentioned. It is stated above that superconductors expel magnetic flux during transition and repel it once they are superconducting. This is only true if the external magnetic flux density is below the temperature dependent critical flux density B_c of the superconductor. If the external flux density is larger than B_c the energy needed to expel the magnetic flux is larger than the energy gained from being in the superconducting state. Therefore, superconductivity breaks down at that point.

Here, two types of superconductors can be distinguished: Type I superconductors expel all magnetic flux (Meissner state) until the external field reaches the critical field. Then superconductivity breaks down completely. Type II superconductors also expel all magnetic flux for low external field magnitudes. When the external flux density reaches a critical flux density B_{c1} superconductivity does not break down completely, but quantized flux lines enter the superconductor. The core of these flux lines is normal conducting (see section 2.3) but the rest of the superconductor stays superconducting. This state is called Shubnikov phase. When the external flux density is increased further, more flux lines enter up to a second critical magnetic flux density B_{c2}. At this flux density superconductivity breaks down. The difference between the two types can be characterized by the Ginzburg-Landau theory (section 2.2.4).

An empirical formula for the temperature dependence of both critical magnetic flux densities is given by [61]

$$B_c(T) = B_c(0)\left(1 - \left(\frac{T}{T_c}\right)^2\right). \tag{2.17}$$

This also implies that in an external field the temperature at which a certain phase manifests itself changes depending on the field magnitude.

2.2.3. Demagnetization Factor

In the experiments presented in this thesis the transition region where the samples become superconducting plays in important role. And an effect that might influence this transition region is caused by the demagnetization factor[31].

To demonstrate this effect assume a sphere of a type I superconductor in the Meissner state in an external field $\vec{H}_0$. Inside the sphere is a homogeneous field $\vec{H}$. The magnetic flux density vector is parallel to it so that one can write

$$n\vec{B} + (1-n)\mu_0\vec{H} = \mu_0\vec{H}_0 \tag{2.18}$$

where n is the demagnetization factor with $0 < n < 1$ ($n = 1/3$ for a sphere). Since the sphere is in the Meissner state $\vec{B} = 0$, so that

$$\vec{H} = \frac{\vec{H}_0}{1-n} \tag{2.19}$$

Due to the expelled flux from the sphere the magnetic field increases around it (with the maximum a the equator). When the external field reaches a value $\vec{H}_0 = (1-n)\vec{H}_c$

the Meissner state breaks down. If the Meissner state would brake down completely the field enhancement outside the sphere would also break down which would reduce the external field magnitude H_0 below H_c and the Meissner state could be established again. Further analysis shows that this unstable state cannot not be solved with a normal conducting belt around the equator (which would reduce n) [31].

Instead, the sphere is divided into thin parallel alternating layers of normal- and superconducting regions [31]. This is called intermediate state.

2.2.4. Ginzburg-Landau Theory

The introduction of the Ginzburg-Landau theory is along the lines of [31]. It describes the properties of a superconductor close to its transition temperature T_c. Since the investigated phenomenon of flux trapping happens in the transition region of normal- to superconducting phase the temperature is close to T_c and the theory is valid. It is, therefore, a useful tool to describe the state of the superconductor when it traps flux. The Ginzburg Landau theory is included in the microscopic theory of superconductors (BCS-theory), and can be derived from it. However, for the considerations in this thesis the Ginzburg-Landau theory is sufficient and the BCS-theory is not introduced here.

The idea of the theory is to expand the free energy of the superconductor in terms of an order parameter Λ which describes the difference in symmetry between the normal- and superconducting state. Λ is zero when the material is normal conducting and non-zero when it's superconducting. Since the phase transition from normal- to superconducting is of second order it is assumed that Λ changes slowly close to the transition temperature. The order parameter is the complex wave function of the superconducting electron pairs.

Instead of expressing the free energy F directly as a function of Λ, $\Psi = (4m/\hbar^2 d)^{1/2}\Lambda$ is introduced where $|\Psi|^2$ is the density of superconducting pairs divided by two. Here, m is the electron mass, $\hbar$ the reduced planck constant, and d a constant. With this the free energy is expressed as

$$F = F_\mathrm{n} + \int \left(\frac{\hbar^2}{4m} |\nabla \Psi|^2 + a|\psi|^2 + \frac{b}{2}|\psi|^4 + ... \right) \mathrm{d}V \tag{2.20}$$

where a, b are phenomenological constants, V the volume of the superconductor, and F_n the free energy of the superconductor in the normal conducting state.

The gradient in equation 2.20 means that there is a characteristic length $\xi(T)$ in which Ψ changes. ξ is called coherence length and its temperature dependence is found to be

$$\xi(T) = \xi_0 \left(1 - \frac{T}{T_\mathrm{c}} \right)^{-1/2}. \tag{2.21}$$

Here, ξ_0 is the coherence length at $T = 0\,\mathrm{K}$. Introducing an external magnetic field alters the free energy and for small external flux densities B_e ($B_\mathrm{e} \ll B_\mathrm{c}$) the second London equation is obtained. In this context a penetration depth λ is also defined. It has the same temperature dependence as ξ so that

$$\lambda(T) = \lambda_\mathrm{L} \left(1 - \frac{T}{T_\mathrm{c}} \right)^{-1/2}. \tag{2.22}$$

The Ginzburg-Landau parameter $\kappa = \frac{\lambda}{\xi}$ is temperature independent. It depends on the properties of the superconducting material and can be used to distinguish between superconductors of type I and II.

With its help it is possible to calculate the surface energy at the boundary between normal- and superconducting phase. Superconductors with a small value of κ have a positive surface energy. This means that energy is needed to increase the boundary area between normal- and superconducting volumes. This is the case for a Type I superconductor. For large values of κ the surface energy in negative and for a field higher than H_{c1} the superconductor is split into normal- and superconducting regions until the microscopic limit ξ is reached. When the field is increases further superconductivity breaks down. This is the case for type II superconductors.

The crossover from type I to type II was found numerically to be at $\kappa = 1/\sqrt{2}$. Niobium has a London penetration depth of 32 nm and a coherence length of 39 nm [62]. The Ginzburg-Landau parameter of niobium is, therefore, just above $1/\sqrt{2}$ making it a type II superconductor.

2.3. Flux Lines in Superconductors

Before it is described how magnetic flux lines create losses in cavities and how they might get pinned the structure of flux lines is described with help of the Ginzburg-Landau theory. The derivation follows the argument in [61].

2.3.1. Quantization of Flux

To derive the quantization of flux in a superconductor a superconductor in a sufficiently weak magnetic field is assumed. It is further assumed that the flux is localized at a certain region inside the superconductor.

The complex order parameter Ψ can be written as

$$\Psi = |\Psi| \exp(i\phi) \tag{2.23}$$

with the phase ϕ. Then, one of the Ginzburg-Landau equations becomes

$$\vec{j} = -\frac{2\hbar e}{m^*}|\Psi|^2 \nabla\phi - \frac{4e^2}{m^*}|\Psi|^2 \vec{A} \tag{2.24}$$

where $\vec{A}$ is the vector potential of the magnetic field, and m^* the mass of the cooper pair. Then a closed path C is chosen around the region with magnetic field. It is chosen large enough so the current density drops to zero. Hence,

$$\vec{A} = -\frac{\hbar}{2e}\nabla\phi. \tag{2.25}$$

This is integrated over C which results in:

$$\oint_C \vec{A} \mathrm{d}\vec{s} = \int \vec{B} \mathrm{d}\vec{S} = \Phi \tag{2.26}$$

Here, Φ is the magnetic flux going through C. Plugging equation 2.25 in above equation 2.26 yields:

$$\Phi = -\frac{\hbar}{2e}\oint_C \nabla\phi \mathrm{d}s = \frac{\hbar}{2e}\Delta\phi \tag{2.27}$$

$\Delta\phi$ is the variation of ϕ over one circulation on C. Since Φ must be a single valued function $\Delta\phi$ must be a multiple of 2π, so that

$$\Phi = n\frac{2\pi\hbar}{2e} = n\phi_0. \tag{2.28}$$

Here, n is an integer and ϕ_0 is the magnetic flux quantum $\phi_0 \approx 2.00678 \cdot 10^{-15}\,\mathrm{Tm}^2$

2.3.2. Structure of Flux Lines

Next, the structure of a single flux line is described. In order to describe it using the Ginzburg-Landau theory a type II superconductor with large κ is assumed. While this is not case for niobium it still gives a good approximation of the nature of flux lines.

To investigate the structure of a flux line a type II superconductor in a magnetic field just above H_{c1} is assumed. This way flux lines are spaced far apart and do not influence each other. One flux line is assumed to be at $x = 0$, $y = 0$ and to be pointing in z-direction. Trying to describe the magnetic flux density in the vicinity of the flux line with the first London equation yields a contradiction. Because integration over a closed loop that is far away from the flux lines shows that the London equation predicts $B = 0$ within in the loop. This cannot be correct, since the flux line is within the loop. Therefore, the London equation is modified to

$$\vec{B} + \lambda^2 \nabla \times \nabla \times \vec{B} = \hat{i}_z \phi_0 \delta(\vec{r}) \tag{2.29}$$

where $\hat{i_z}$ is the unit vector in z-direction, ϕ_0 the flux quantum, and $\delta(\vec{r})$ the two dimensional delta function. $\vec{r}$ is a vector in the x-y plane, and r denotes the magnitude of $\vec{r}$. The solution is found to be

$$B_z(r) = \frac{\phi_0}{2\pi\lambda^2} K_0\left(\frac{r}{\lambda}\right). \tag{2.30}$$

Here, K_0 is the modified Bessel function of zeroth order. It diverges for $r \to 0$ so the modified London equation still does not describe the magnetic flux density close the centre of the flux line but it gives an approximation for $r > \xi$. The magnetic flux density near the core can be estimated using the GL equations. For this it assumed that $|\Psi|$ is symmetrical around the centre, and is only a function of the distance r. So it can be expressed as

$$\frac{\Psi}{|\Psi|_\infty} = f(r)\exp(-i\phi). \tag{2.31}$$

Ψ_∞ is the equilibrium value of Ψ far away from the flux lines. $f(r)$ characterizes the deviation of Ψ to Ψ_∞ and approaches 1 for large r. The derivation of $f(r)$ can be found in [61]. It results in

$$f(r) \approx cr\left[1 - \frac{r^2}{8\xi^2}\left(1 + \frac{B(0)}{\mu_0 H_{c2}}\right)\right] \tag{2.32}$$

where c is a constant. For small fields it can be approximated by

$$f(r) \approx \tanh\left(\frac{r}{r_\mathrm{n}}\right) \tag{2.33}$$

with $c \approx 1/r_\mathrm{n}$. With the help of numerical calculations a formula can also be found for r_n [61]. B and Ψ of a flux line are schematically depicted in

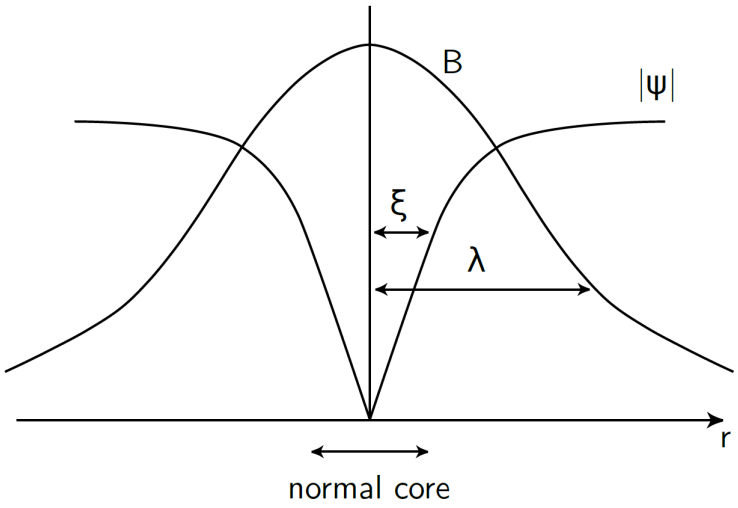

Figure 2.2.: Schematic depiction of B and Ψ as a function of r in the vicinity of a flux line. The figure is taken from [61].

When the external field is increased the density of flux lines increases and they start to influence each other. Then a triangular lattice is formed by the flux lines [61].

2.3.3. RF Losses due to Trapped Flux

Before a theoretical description of losses due to trapped flux in cavity walls is given, measurement data from a test with a TESLA shaped single cell cavity is shown. It shows the negative effect of trapped flux for cavity performance very clearly. Figure 2.3 shows measurement data of the unloaded quality factor versus accelerating field in a shielded cryostat. The remaining flux density in the cryostat is below 1 µT. When an external magnetic flux density $B_\mathrm{e} = 10\,\mu\mathrm{T}$ is applied with Helmholtz coils the quality factor drops by a factor of 6.

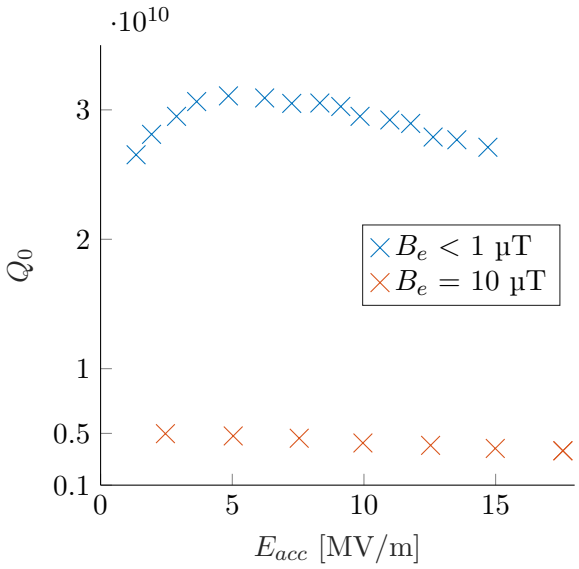

Figure 2.3.: Q_0 versus E_{acc} of a single cell cavity in a shielded cryostat ($B_{\mathrm{e}} < 1\,\mu\mathrm{T}$) when no field is applied, and when $10\,\mu\mathrm{T}$ are applied in direction of the beam axis.

The geometry factor of this cavity is $270\,\Omega$ [52]. So at $5\,\frac{\mathrm{MV}}{\mathrm{m}}$ the surface resistance increased from $9\,\mathrm{n}\Omega$ to $54\,\mathrm{n}\Omega$.

The reason for the increased losses are oscillations of the flux lines in the RF field. The mechanism is explained by A. Gurevich and G. Ciovati in [36]. Here, magnetic flux lines are regarded as elastic strings that oscillate in a RF magnetic field parallel to the superconductor's surface. It is assumed that the pinning centre is a distance $l > \lambda$ away from the RF surface so that the flux line "behind" the pinning centre is not affected by the RF field. Additionally, the pinning centres are assumed to be "hard" pinning centres so the flux line cannot move at the position of the pinning centre. With these boundaries there are three different configurations of magnetic flux lines that are influenced by an RF field. They are depicted in Figure 2.4.

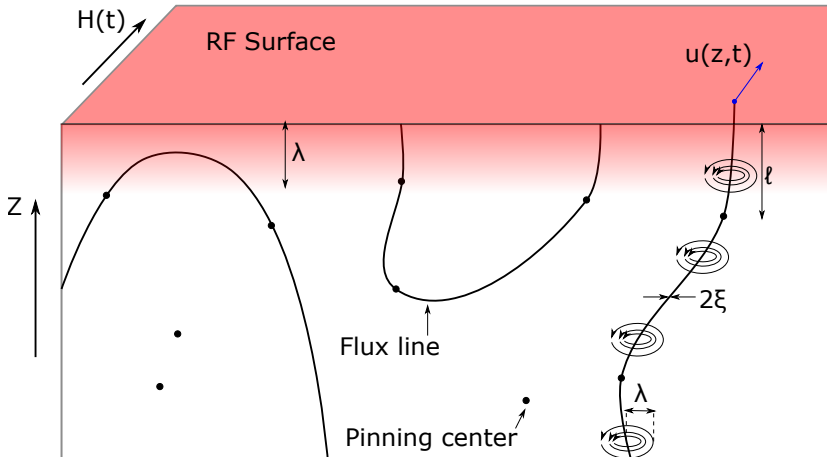

Figure 2.4.: Possible configurations for pinned flux line, where either a segment, both ends or one end of the flux line is in region of the RF penetration depth. The displacement of the flux line from its equilibrium parallel to the surface is described with $u(z,t)$. The flux lines are held up by circular currents. Figure is adapted from [36, 63] .

In one case only a segment of the flux line crosses the region where the RF field penetrates the superconductor (left). In another configuration the flux line forms a semi-loop which starts and ends at the RF surface (middle). Or the flux line passes the superconductor and only one end is influenced by the RF field (right).

The dissipated power due to flux lines is calculated for the last two cases where the flux line penetrates the RF surface and is pinned a distance l below it. A RF field parallel to the surface of magnitude H_p, and angular frequency ω takes the form $H(z,t) = H_\mathrm{p}\exp(-z/\lambda + i\omega t)$ inside the superconductor. Here, z is the coordinate perpendicular to the surface (see Figure 2.4). The displacement $u(z,t)$ of a flux line is described by

$$\eta\frac{\mathrm{d}u}{\mathrm{d}t} = \hat{\epsilon}\frac{\mathrm{d}^2u}{\mathrm{d}z^2} + F\exp(-z/\lambda + i\omega t). \tag{2.34}$$

$\eta = \phi_0\frac{B_{c2}}{\rho_\mathrm{n}}$ is the viscous drag coefficient (see chapter 2.4.5) with the normal state resistivity ρ_n, and $\hat{\epsilon}$ is a tensor describing the dispersive line tension of a flux line. $F = \phi_0\frac{H_\mathrm{p}}{\lambda}$ is the magnitude of the force created by the RF field acting on the flux line.

There are two boundary conditions imposed on the flux line: Firstly, it does not move at the pinning centre, and secondly, it is perpendicular to the surface of the superconductor. This can be summarized as

$$u(l) = 0, \qquad \left.\frac{\mathrm{d}u}{\mathrm{d}z}\right|_{z=0} = 0. \tag{2.35}$$

The solution of equation 2.34 with boundaries 2.35 is

$$u(z,t) = \sum_{n=0}^{\infty} A_\mathrm{n}\cos(k_\mathrm{n}z)e^{i\omega t}, \quad k_\mathrm{n} = \frac{\pi}{l}\left(n+\frac{1}{2}\right). \tag{2.36}$$

The coefficients A_n and their derivation can be found in [36]. The motion of the flux lines is always greatest at the surface and decays towards the bulk material. But, depending on the frequency of the RF field more or less of the flux line is moving. For low frequencies $\omega < \omega_\mathrm{l}$ the whole vortex segment up to the pinning centre oscillates. For $\omega_\mathrm{l} < \omega < \omega_\lambda$ the oscillations are localized in the surface layer of thickness $1/q_\omega$ smaller than l but larger than λ. At high RF frequencies $\omega > \omega_\lambda$ the flux line oscillates only in a thin layer in the order of λ. The values of ω_l, ω_λ, and q_ω can be found in [36]. In the case of a 1.3 GHz cavity made out of niobium the frequency range of $\omega_\mathrm{l} < \omega < \omega_\lambda$ is applicable.

According to the different motions of flux lines the dissipated power is also calculated for each frequency range individually. The explicit results are not stated here, but can be found in [36].

With the calculated dissipated power P, the surface resistance due to trapped flux which is defined as $R_\mathrm{i} = \frac{2P}{H_\mathrm{P}^2}$ can also be calculated. Here, the result is only stated for the frequency range $\omega_\mathrm{l} < \omega < \omega_\lambda$ which is

$$R_\mathrm{i} = \frac{B_0}{B_\mathrm{c}} \left(\frac{\mu_0 \rho_\mathrm{n} \omega}{2g} \right)^{1/2} . \tag{2.37}$$

Here, B_0 is the trapped flux density, and g is a function of the anisotropy of a material which is 0.5 for isotropic niobium [36].

In a 1.3 GHz niobium cavity this results in an increase of 16 nΩ for 1 µT trapped flux. This is significant compared to the 9 nΩ measured above. The increase is more than what is observed in Figure 2.3 but in the experiment not all of the applied field got trapped and the flux is not distributed evenly across the cavity walls.

2.4. Flux Pinning in Superconductors

Flux pinning mechanisms are investigated typically for type II superconductors that are used for high DC applications like superconducting magnets. In these cases the superconductor is operated in the Shubnikov phase and magnetic flux lines penetrate the superconductor. The high current exerts a Lorentz force on the flux lines which causes them to move through the superconductor. This dissipates energy an the performance of the superconductor degrades. For the DC applications pinning centres are introduced on purpose to stop flux lines from moving through the superconductor.

This is in contrast to cavity applications. Here, the superconductor is operated in the Meissner state because due to the RF field losses in the Shubnikov phase would be so high that the cavity would quench (become normal conducting) immediately. As is shown above even pinned flux lines create losses is RF fields, which is why in cavities pinning centres should be avoided so all magnetic flux is expelled from the material.

While the loss mechanism in both cases are different, the observations made for pinning centres in the DC case are still applicable for cavities.

2.4.1. Pinning Centres

The following explanation is adapted from [61]. Pinning centres differ from the rest of the material in their material properties like T_c, H_c, ξ, and λ. These changes might

be caused by normal conducting precipitates, or inclusions, lattice defects, or grain boundaries. The locally changing parameters lead to a locally changing free energy.

For the case of a normal conducting pinning centre a descriptive explanation can be given: To establish flux lines in the superconductor energy is needed to break up cooper pairs since the core of the flux line is normal conducting. However, at the pinning centre the material is already normal conducting and no energy is needed no break up copper pairs. Therefore, less energy is needed to keep the flux line at this position which results in a local minimum of energy. In the complete Meissner state the total energy would be even smaller but to achieve this the flux line must overcome the pinning force of the pinning centre.

A schematic depiction of the pinning potential and the resulting pinning force is depicted in Figure 2.5. Where U is the flux line's energy and the pinning force f_p is given by

$$f_\mathrm{p} = -\frac{\partial U}{\partial x}. \tag{2.38}$$

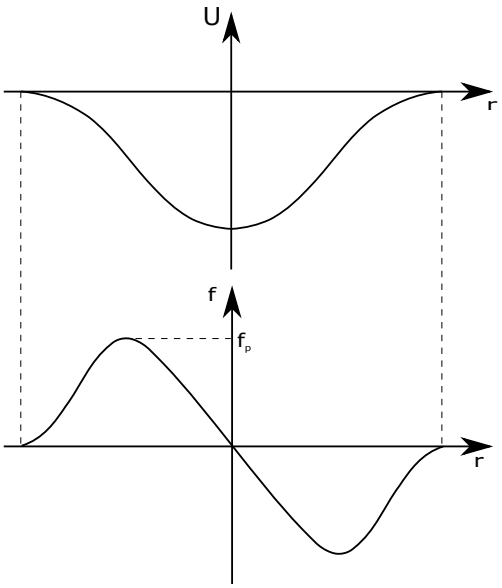

Figure 2.5.: Pinning potential and the resulting force. It shows, how the flux line is pulled back towards the pinning centre at $r = 0$. The maximal force f_p is the pinning force. Figure is adopted from [61].

The example above of a normal conducting pinning centre is only one of several pinning mechanisms. In [61] they are distinguished by the underlying mechanisms in several categories: Condensation energy interaction with normal precipitates and grain boundaries, elastic interaction, magnetic interaction, and kinetic interaction. More detail on the different mechanism can be found in [61].

2.4.2. Flux Pinning during Transition

For DC applications the pinning force is often measured by critical current density measurements in dependence of an external magnetic field [34]. In this case magnetic

flux lines are pushed through the superconductor by a Lorentz force and get pinned at pinning centres. When the Lorentz force becomes larger than the pinning force the flux lines gets de-pinned.

For the case of cavities where superconductors are operated in the Meissner state flux lines can not be de-pinned when the cavity is at its operating temperature around 2 K. The only way to expel magnetic flux from the superconductor is during transition where flux lines can be pushed into normal conducting regions. Here, the forces acting on flux lines stem from the change of free energy in the superconductor, a thermal force (see section 2.4.3), and a force by the external magnetic field (see section 2.4.4). If the pinning force is greater than the sum of these forces the flux lines gets pinned and is not expelled from the superconductor. Whether a flux line gets pinned or not is, therefore, determined in the transition region between the normal- and superconducting phase.

A theory of how flux lines interacted with pinning centres in this region is presented by T. Kubo in [64].

The developed theory bases on the Ginzburg-Landau theory. A rectangular type-II superconductor in a weak external magnetic field is assumed that is cooled from right to left (Figure 2.6) with a temperature gradient $T' = \mathrm{d}T/\mathrm{d}x < 0$, and $\mathrm{d}T/\mathrm{d}y = \mathrm{d}T/\mathrm{d}z = 0$. Since the critical flux densities of superconductors are temperature dependent the superconductor is in three states at the same time. The warm end is still normal conducting ($B_\mathrm{e} > B_\mathrm{c2}$) and the cold end is in the Meissner state ($B_\mathrm{e} < B_\mathrm{c1}$). Between the two regions is a region where $B_\mathrm{c1} < B_\mathrm{e} < B_\mathrm{c2}$ so the sample is in the Shubnikov phase. The coordinate system is chosen such that $x = 0$ at the point where $T = T_\mathrm{c}$.

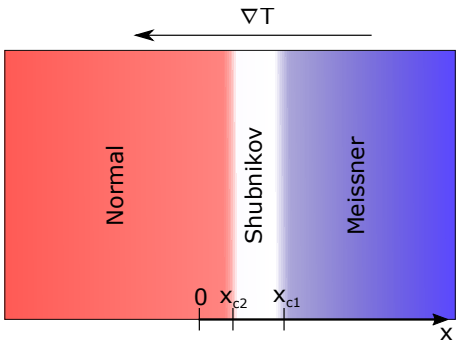

Figure 2.6.: Schematic depiction of the superconductor during transition. It is simultaneously in three different states. The coordinate system moves with the phase front, so that at $x = 0$, $T = T_\mathrm{c}$. Figure is adapted from [64]

In this coordinate system the temperature can be expressed as a function of position

$$T(x) = T_\mathrm{c} + T'(0)x = T_\mathrm{c}[1 - |\widetilde{T}'(0)|x] \tag{2.39}$$

where $\widetilde{T} = \frac{T}{T_\mathrm{c}}$, and $\widetilde{T}' = \mathrm{d}\widetilde{T}/\mathrm{d}x$. With the help of the Ginzburg-Landau theory the

critical flux densities can also be expressed as a function of position

$$B_{c2}(T(x)) = \frac{\phi_0}{2\pi\xi_0^2}|\widetilde{T}'|x, \tag{2.40}$$

$$B_{c1}(T(x)) = \frac{\phi_0(\ln\kappa + a)}{4\pi\kappa^2\xi_0^2}|\widetilde{T}'|x. \tag{2.41}$$

Here, a is a numerically determined parameter. With help of the position dependent critical flux densities the transition points x_{c1} and x_{c2} can be determined (Figure 2.6). The transition from Meissner to Shubnikov phase is at point x_{c1} and the transition from Shubnikov phase to normal conducting is at x_{c2} where x_{c1}, and x_{c2} are given by

$$x_{c2} = 2\pi\xi_0^2\frac{B_e}{\phi_0}|\widetilde{T}'|^{-1} \tag{2.42}$$

$$x_{c1} = \frac{4\pi\kappa^2\xi_0^2}{\ln\kappa + a}\frac{B_e}{\phi_0}|\widetilde{T}'|^{-1}. \tag{2.43}$$

Here, B_e is the external magnetic flux density magnitude. With x_{c1}, and x_{c2} the thickness of the region in the Shubnikov phase δx can be calculated

$$\delta x = x_{c1} - x_{c2} = 4\pi\xi_0^2 f_-(\kappa)\frac{B_e}{\phi_0}|\widetilde{T}'|^{-1}. \tag{2.44}$$

Where $f_-(\kappa) = \kappa^2/(\ln\kappa + a) - 1/2$. The order of magnitude of δx is around 100 µT for temperature gradients around 0.1 $\frac{\mathrm{K}}{\mathrm{cm}}$ which is also achieved in the experiments presented in this thesis.

In the Shubnikov phase flux lines penetrate the superconductor and their normal conducting core size is in the order of ξ. ξ depends on the temperature at the position of the flux line. To estimate ξ in the Shubnikov phase an average of both extremes at x_{c1}, and x_{c2} is calculated:

$$\bar{\xi} = \frac{1}{\sqrt{2\pi f_+(\kappa)}}\sqrt{\frac{\phi_0}{B_e}} \tag{2.45}$$

where $f_+(\kappa) = \frac{\kappa^2}{\ln\kappa + a} + \frac{1}{2}$.

When the sample is cooled down flux lines in the Shubnikov phase are transported through the sample with the moving phase fronts (boundary between phases) and can be trapped by pinning centres in the material. To estimate the number of pinned flux lines N_{trap} an analogy with a beam-target collision event is used. Additionally, it is assumed that the ambient field is parallel to the surface of the sample. Using the beam-target analogy

$$N_{trap} \propto N_{pin}N_\phi\sigma \tag{2.46}$$

is obtained. Here, N_{pin} is the number of relevant pinning centres, N_ϕ is the number of flux lines contained in the Shubnikov phase domain, and σ is a reaction cross-section. The number of relevant pinning centres is not equal the total number of pinning centres because a thermal force (see section 2.4.3) acts on the flux lines which pulls them away

from pinning centres. If the pinning force of a pinning centre is weaker than the thermal force, it is not included in N_{pin}. The number of flux lines in the Shubnikov phase domain is proportional to the ambient magnetic flux density and the thickness δx:

$$N_\phi \propto B_\mathrm{e}\delta x \propto B_\mathrm{e}^2|\widetilde{T}'|^{-1} \tag{2.47}$$

It is assumed that the number of flux lines stays constant and does not decrease due to trapped flux lines or increase due to the demagnetization factor. Finally, the cross section σ is estimated to be

$$\sigma \propto \bar{\xi}^2 \propto B_\mathrm{e}^{-1} \tag{2.48}$$

With these estimations N_{trap} is found to be

$$N_{\mathrm{trap}} = A_M B_\mathrm{e}|\widetilde{T}'|^{-1}. \tag{2.49}$$

A_M is a material dependent parameter which is proportional to N_{pin} and a function of κ and ξ_0. A descriptive explanation of the factor $|\widetilde{T}'|^{-1}$ is that with increasing $|\widetilde{T}'|$ the width of the Shubnikov phase domain decreases which decreases the number of flux lines in this domain. This in turn reduces the reaction probability.

When $|\widetilde{T}'|$ is so large that the Shubnikov phase domain is smaller than ξ the model ceases to be valid but there might still be a contribution to N_{trap}, so that in general

$$N_{\mathrm{trap}} = A_M B_\mathrm{e}\left(|\widetilde{T}'|^{-1} + D_M\right). \tag{2.50}$$

The constant D_M stems from the contribution mentioned above and generally depends on material properties.

In the paper implications for the residual resistance and comparison with measurements are also presented. But this is not relevant for this thesis and can be found in [64].

2.4.3. Thermal Force

Assuming a type-II superconductor in a temperature gradient which is fully in the Shubnikov phase, [65] describes a force which pushes flux lines from the warmer region to the colder region. The force arises due to a thermal diffusion process of particles (in this case flux lines). It is driven by a difference in entropy of the normal conducting flux lines compared to the superconducting material surrounding it. In [65] this force is called thermal force and it is given per unit length of flux line by

$$f_{\mathrm{th}} = -S^*\nabla T \tag{2.51}$$

Here, S^* is the transport entropy per unit length of flux line. Noting that $S^* > 0$ equation 2.51 shows that flux lines are pushed towards the colder region. Measurements with various materials, including niobium have confirmed this force [66]. The theoretical calculation of S^* for general cases is still an open question. But for the high field limit an expression is given in [67]. For low temperatures the expression

$$S^*(T) = -\Phi_0\frac{\mathrm{d}H_{\mathrm{c1}}(T)}{\mathrm{d}T} \tag{2.52}$$

is often used [47, 64]. In [68] measurements of S^* are presented.

2.4.4. Force by an External Field

When flux lines get trapped during transition there must be an external field present which is inevitably in the same orientation as the flux lines inside the superconductor. The external flux density pushes flux lines inside the superconductor further inside it because flux lines repel each other. In [69] Bean and Livingston describe this force as part of their description of a surface barrier that magnetic flux needs to overcome to enter a superconductor. They describe the change in energy E due to the external field as

$$E(z) = \frac{\phi_0 H_\mathrm{e}}{4\pi} \exp\left(-\frac{z}{\lambda}\right) \tag{2.53}$$

where z is the distance from the surface of the superconductor, and H_e the external field magnitude. In [47] the corresponding force is calculated as

$$f_\mathrm{B}(z) = \frac{\phi_0 H_\mathrm{e}}{\lambda} \exp\left(-\frac{z}{\lambda}\right) \tag{2.54}$$

2.4.5. Viscous Force

In chapter 4.3 it is reported that the cooldown rate changes the magnitude of trapped flux which hints at slow moving flux lines. This might be explained by a viscous force acting on the flux lines which it introduced here.

It can be shown that when flux lines move through a superconductor normal electrons flow inside and outside the normal conducting core of a flux line [61]. This dissipates energy and, therefore, creates a viscous force which counteracts the driving force which moves the flux lines.

The dissipated power due to the normal conducting electrons can be calculated and expressed in terms of an effective resistivity, or "flow resistivity" ρ_f

$$\rho_\mathrm{f} = \frac{B}{\mu_0 H_\mathrm{c2}} \left(1 + \frac{B}{2\mu_0 H_\mathrm{c2}}\right)^{-1} \rho_\mathrm{n}. \tag{2.55}$$

Here, B is the magnetic flux density inside the superconductor and ρ_n the normal state conductivity. In the case $B \ll H_\mathrm{c2}$, or when the flux lines are far apart and do not react with each other, it reduces to

$$\rho_\mathrm{f} = \frac{B}{\mu_0 H_\mathrm{c2}} \rho_\mathrm{n}. \tag{2.56}$$

ρ_f can also be expressed in terms of a viscous coefficient η_vis:

$$\rho_\mathrm{f} = \frac{\phi_0 B}{\eta_\mathrm{vis}} \tag{2.57}$$

$$\Leftrightarrow \eta_\mathrm{vis} = \frac{\phi_0 B}{\rho_\mathrm{f}} \tag{2.58}$$

$$\Rightarrow \eta_\mathrm{vis} = \frac{\phi_0 \mu_0 H_\mathrm{c2}}{\rho_\mathrm{n}} \tag{2.59}$$

The last equation holds only if B is small, so flux lines do not interact. Finally the viscous force can be expressed as

$$F_{\mathrm{v}} = \eta_{\mathrm{vis}} v, \tag{2.60}$$

where v is the flux lines velocity.

2.5. AMR Effect

Finally, a short introduction to the anisotropic magneto resistive (AMR) effect and magnetic field sensors based on this effect is given because the measurement setup relies on these sensors.

A more in depth description can be found in [70, 71]. Here, only a phenomenological explanation is given to understand the working principle of the sensors.

The phenomenon that the electrical resistivity of a ferro magnetic material depends on the angle between the current and the magnetization of the material is described by the AMR effect. On a microscopic scale the preferred spin orientation of the electrons in the conduction band is influenced by the magnetisation of the material. And a change in this spin orientation leads to a different scattering amplitude of the conduction electrons via the spin orbit coupling [70]. This again leads to a different resistivity on a macroscopic scale. The resistance ρ can be calculated in terms of the angle θ between the current density $\vec{j}$ and magnetization $\vec{M}$ [72]

$$\rho = \rho_{\perp} + \left(\rho_{\parallel} - \rho_{\perp}\right) \cos^2(\theta), \tag{2.61}$$

where $\rho_{\perp}$, and $\rho_{\parallel}$ are the resistances when $\vec{j}$ and $\vec{M}$ are perpendicular or parallel to each other. The function is depicted in Figure 2.8.

2.5.1. AMR Sensors

The AMR effect can be exploited to measure magnetic fields: A magnetization is set in a ferromagnetic material and a voltage is applied on the ends of the material which causes a current to flow. When a magnetic field is applied perpendicular to the magnetization the magnetization is rotated which changes the resistance of the material. This can easily be measured and the magnetic field strength can be extracted from the resistance by calibrating the sensor with known fields.

In the experimental setup in this thesis commercially available sensors AFF755B from Sensitec [73] are used. A schematic drawing of the sensor is shown in Figure 2.7.

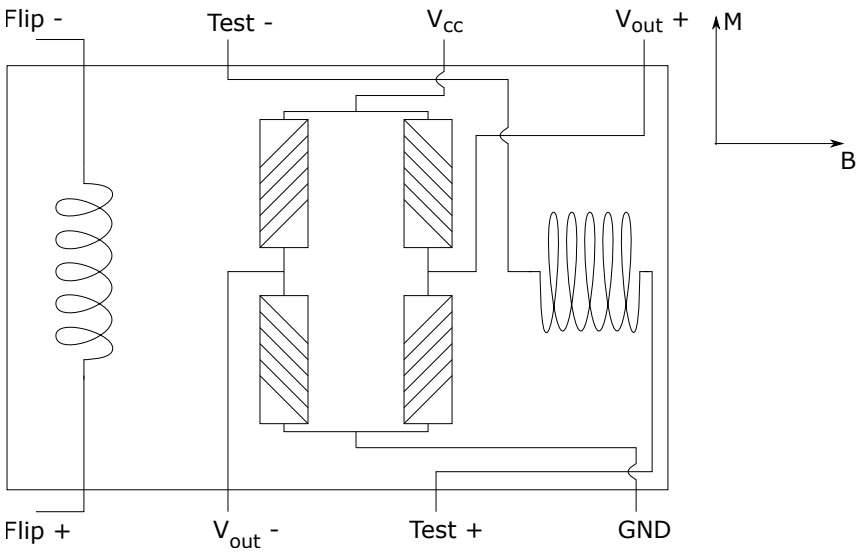

Figure 2.7.: Sketch of an Sensitec AFF755B AMR sensor. It consists of a Wheatstone bridge assembly of four AMR elements, a flip coil (left) to reset the magnetisation and a test coil (right) to calibrate the sensitivity of the sensor. On the right the easy axis for the magnetisation and the sensitive axis are indicated. Figure is adapted from [73].

The sensitive part consists of a Wheatstone bridge arrangement of four AMR elements. They are arranged in a Wheatstone bridge in order to increase the sensitivity by a factor four [72]. The elements are made of a nickel-iron thin film deposited on a silicone waver which have a barber pole structure of shorting bars sputtered on top. In these shorting bars the resistivity is much smaller than in the ferromagnetic iron-nickel alloy. The current, therefore, flows in the shortest possible way from shorting bar to shorting bar, so that the current flows in a 45° angle with respect to the long dimension of the AMR element and, therefore, the magnetization. This effectively changes the operating point of the AMR sensor from $\theta = 0°$ to $\theta = 45°$ (see Figure 2.8).

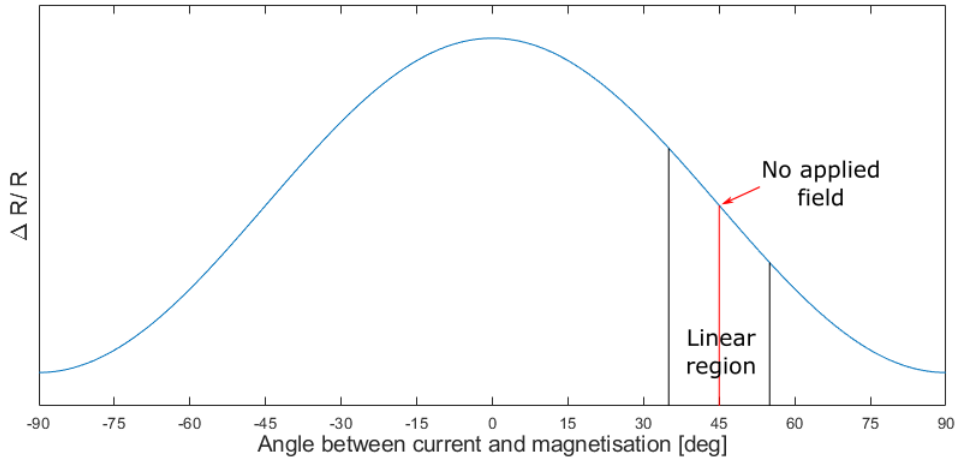

Figure 2.8.: Change in resistance versus angle between current and magnetisation. Due to the barber pole structure the angle is at 45° for no applied field. The maximal change is only 2-3%.

The advantage of this operating point at $\theta = 45°$ is twofold: Firstly, it makes the response of the Sensor asymmetric for changes in θ. This allows the sensor to distinguish the polarity of the applied field. Secondly, it makes the response linear, which makes calibration easier and gives a better sensitivity.

The elements are build such that there is an easy axis for the magnetization (see Figure 2.7) so it returns to $\theta = 45°$ if the external field is turned off. If the magnetization is destroyed by to high fields or vibrations, etc. it can be restored by the flip coil (left in Figure 2.7). It can also be used to ”flip” the magnetization, i.e. rotating it 180°. Typically this is used to perform an offset correction of the sensors. However, the magnetization can not be flipped consistently at cryogenic temperatures which makes this method of offset correction not applicable for measurements described in this thesis. For a more detailed investigation of this problem see [74]. In the setup presented here the sensors are calibrated in each measurement run to Fluxgate sensors which are used as reference. The method is described in section 3.2.3.

Lastly, the test coil (right in Figure 2.7) applies a field in the sensitive direction of the sensor which can be used to calibrate its sensitivity. However, for the measurements conducted in this thesis it is not used.

3. Experimental Setup

A new setup has been designed to measure trapped flux in samples. The measurement is done indirectly, by measuring the magnetic field in the immediate vicinity of the sample and deducing the actual trapped flux from the obtained values. The goal of the experimental setup is to measure trapped flux depending on the parameters already mentioned in chapter 1: Temperature gradient, cooldown speed, external magnetic field as well as the material and its treatment.

By moving away from cavity measurements to sample measurements these parameters are easier to control, change, and understand. An additional benefit of the sample measurements is the significantly larger experimental throughput compared to measurements with cavities. With cavities only a few cooldowns per day can be achieved. With the new setup the sample can be cycled through its transition temperature around 300 times per day. The biggest drawback of the measurement with samples compared to cavity measurements is the inability to measure the surface resistance of the samples. It's only possible to measure the trapped flux, but not its effect on surface resistance.

This section presents the setup in detail and shows how the parameters are controlled. First, the experimental infrastructure is introduced. This includes everything that is not the core setup and might be used for other experiments as well, namely the cryostat and coils to control the magnetic field. Then, the experiment to measure trapped flux is described and the measurement procedure is illuminated.

3.1. Experimental Infrastructure

3.1.1. Cryostat

All known superconductivity applications require operation at cryogenic temperatures. In this thesis the flux trapping behaviour of niobium - the most commonly used material for SRF cavities - is investigated which makes the superconducting transition at T_c =9.2 K. The medium of choice for such temperatures is liquid helium which provides a temperature reservoir of 4.1 K. The sample is placed above the liquid helium level and cooled by the evaporating helium gas. This setup allows the sample to be heated up above T_c and than cooled down again below it (cycling).

The experiments were conducted in a glass cryostat. A technical drawing is depicted in Figure 3.1. Figure 3.2 shows two pictures of the cryostat. It consists of an inner dewar which is filled with liquid helium and an outer dewar which is filled with liquid nitrogen. The nitrogen acts as a radiation shield for the inner helium dewar, decreasing the static losses in the helium to only 0.35 W. Surrounding the two dewars is a protective housing made from aluminium. A 1.5 cm wide slit in the aluminium and the mirror covers of the dewars allows to look inside the cryostat, and check the helium level by eye.

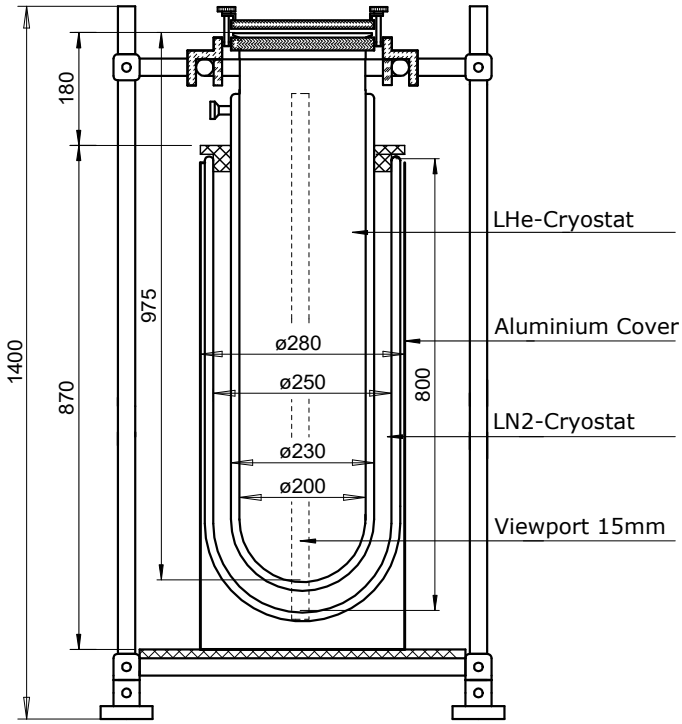

Figure 3.1.: Drawing of the cryostat. The final lid with feedthroughs is not depicted. All dimensions are in mm.

3.1.2. Magnetic Field Control

Since the cryostat has no permalloy shielding to reduce the ambient magnetic field caused by the earth, and other sources, an active field compensation is necessary to be able to expose the sample to a controlled and well defined external field. As the surrounding field can have arbitrary orientation, three coils are necessary to compensate the external field. At the same time, with three coils it is possible to apply an external field in any direction. The parameter of external magnetic field mentioned above can, therefore, be precisely controlled. Since the coils are build to compensate the earth's magnetic field which corresponds to a magnetic flux density of roughly 50 µT, the flux densities achieved with the coils are of the same order of magnitude (see Table 3.1).

For the two coils which contribute to the field in the horizontal plane a rectangular Helmholtz-coil (HHC) design is chosen. This design achieves a high field flatness at the sample position and can be better integrated in the infrastructure of the cryostat, compared to a round Helmholtz-coil design. For the coil which applies field in the vertical direction, a solenoid design is chosen. Due to the fact that is realised by winding a insulated copper wire around the aluminium shielding of the cryostat it occupies nearly no space around the cryostat while still achieving high field flatness. Figure 3.2 shows pictures of the three coils. The design parameters of the different coils are discussed in more detail in the following.

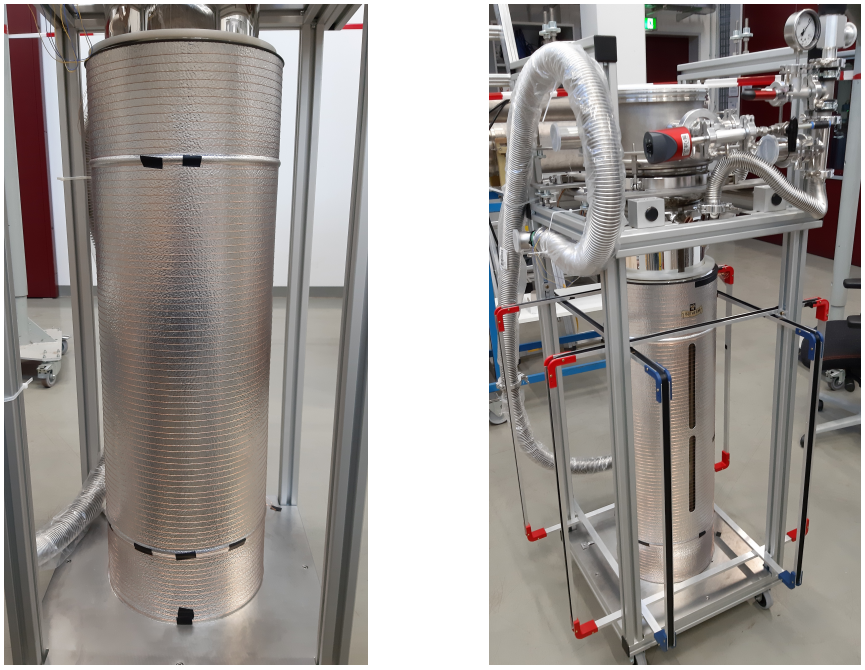

(a) (b)

Figure 3.2.: Cryostat with only the solenoid wound around the aluminium cover (a) and with additionally mounted Helmholtz-coils (b)

Solenoid Coil

The diameter and maximum length of the solenoid is given by the diameter and length of the cryostat. This leaves only the pitch (distance between two windings) of the coil to be determined: This is done with COMSOL Multiphysics® simulations [75]. By simulating the coil not only an appropriate pitch can be determined, but also the field flatness can be estimated.

Instead of modelling the wire itself, the solenoid is modelled as tube with a wall thickness of 0.1 cm. COMSOL offers the possibility to set the number of wire turns in this tube. While this might not be an exact representation, it is sufficient to lay out the coil. The dimensions of the solenoid predetermined by the cryostat are the radius $r = 14.5\,\text{cm}$ and length $l = 88\,\text{cm}$. A pitch of 1 cm is chosen, resulting in 88 turns over the whole length. The used copper wire has a diameter of 0.4 mm, making a driving current of 1 A reasonable, without damaging the wire. A representation of the obtained results of the simulation with the above parameters is shown in Figure 3.3.

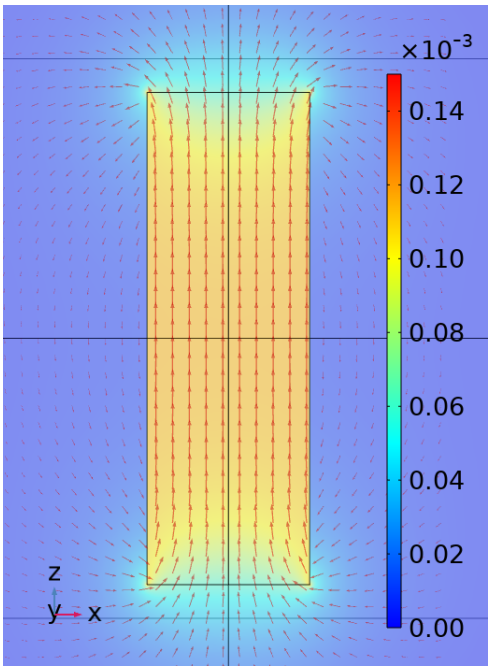

Figure 3.3.: Simulated field created by the Solenoid coil with 1 A driving current. The heat map shows the magnetic flux density magnitude in T. The arrows show the strength and direction of the generated field.

The experiment uses a sample of dimensions $(10 \times 6 \times 0.3)$ cm. Since all other parts of the setup have a μ_r close to one, a homogeneous field is only critical in the volume the sample typically occupies. In the final setup, the sample is placed in the x-z plane, i.e. the short dimension of 0.3 cm is along the y-axis. The coordinate system is depicted in the lower left corner of Figure 3.3. The centre of the sample is not in the middle of the solenoid but shifted 5 cm up. This allows for more helium to be filled below the setup which results in a lower number of necessary refills, and thus lower helium consumption.

In order to address field flatness the z-component of the magnetic flux density is plotted along three lines going vertically through the solenoid in Figure 3.4 (z-Axis). One goes through the centre of the solenoid (and, therefore, a hypothetical sample). The other two are offset by ± 3 cm in x-direction and go though the outer edges of a hypothetical sample. The solenoid is centred around $z = 0$ cm but since the centre of the sample is shifted 5 cm up, the region of interest is not symmetrical around $z = 0$ cm but between $z = 0$ and $z = 10$ cm. A close-up of this area is depicted in Figure 3.4 (b). Figure 3.5 shows the z-component of the magnetic flux density along five lines going horizontally through the sample. The five lines are 2.5 cm apart with the lowest at the bottom edge of the sample and the highest at the top edge of the sample. The solenoid is centred around $z = 0$ cm. Horizontally the sample is located in the centre of the solenoid and since it is 6 cm wide the region of interest is now from $x = -3$ to $x = 3$ cm. This region is again shown in more detail in Figure 3.5 (b).

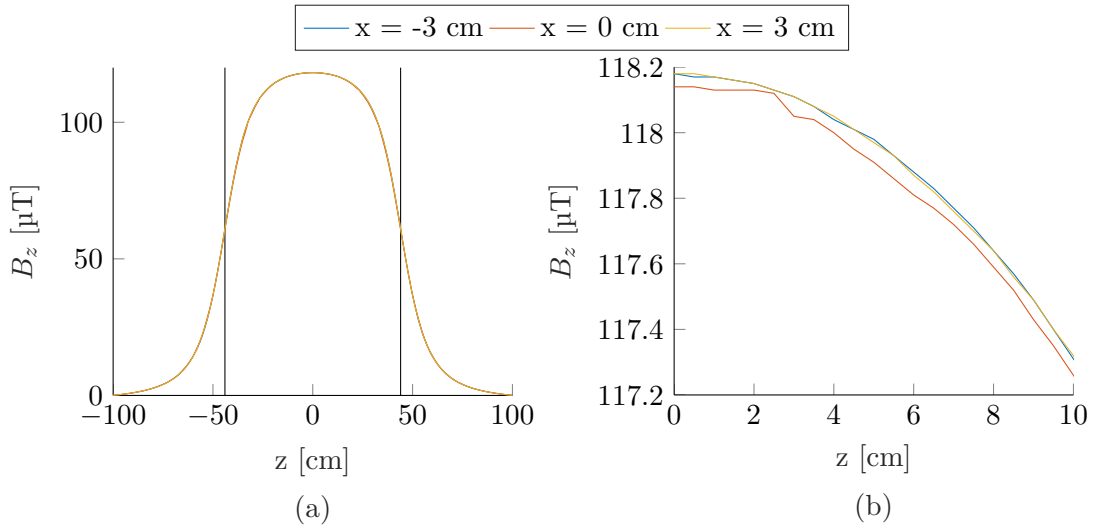

Figure 3.4.: z-component of magnetic flux density along three vertical lines at $x = -3, 0, 3\,\text{cm}$. The solenoid is centred around $z = 0\,\text{cm}$. The two lines at $z = \pm 44\,\text{cm}$ indicate the ends of the solenoid. The legend is identical for both plots, however, in (a) no difference is visible between the three lines. (b) shows a close up of the same data at the sample position from $z = 0$ to $z = 10\,\text{cm}$. The maximal flux density deviation in the sample volume is less than $1\,\mu\text{T}$.

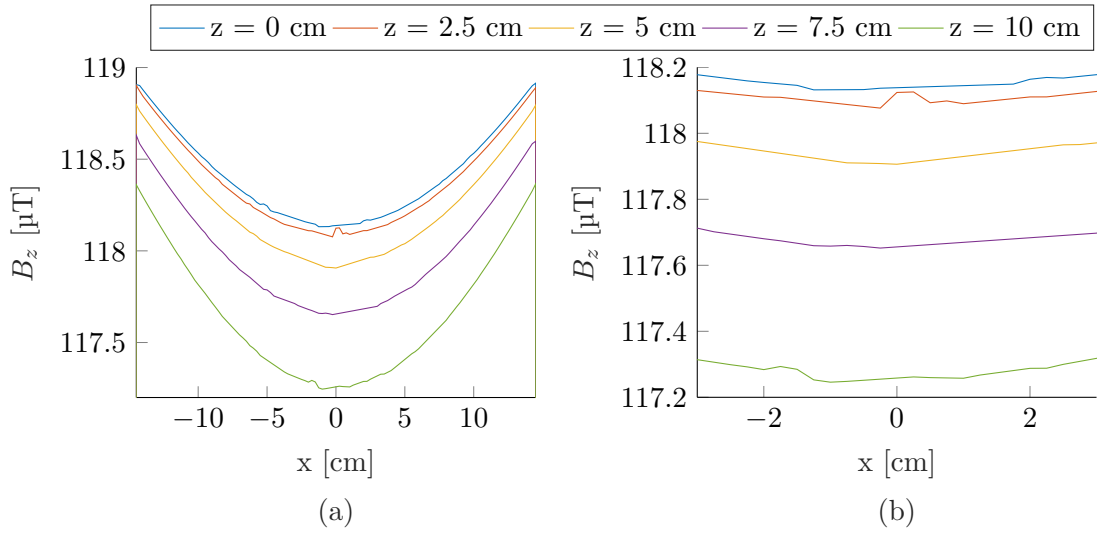

Figure 3.5.: z-component of flux density along five horizontal lines at z= 0, 2.5, 5, 7.5, 10 cm. The solenoid is centred around $x = 0\,\text{cm}$. (b) shows a close up of the same data at the sample position from $x = -3$ to $x = 3\,\text{cm}$.The maximal flux density deviation in the sample volume is less than $1\,\mu\text{T}$.

Regarding the vertical field flatness, Figure 3.4 (b) shows that the sample is not in the

region with the lowest gradient $\frac{\partial B}{\partial z}$ because it is shifted 5 cm up. However, the difference between top and bottom of the sample is below 1 µT. Regarding the horizontal field flatness, Figure 3.5 shows that the maximum field is not in the centre of the coil, but at the edges. Figure 3.5 (b) indicates that the horizontal deviation is below 0.1 µT across the sample. According to the simulation the maximum difference in the volume of the sample is 0.93 µT. This equates to a relative error of only 0.8%. By shifting the sample additional 2 cm up, the relative error increases to 1.1%. Therefore, a relative error of 1% is realistic for real experiments.

The solenoid does not create a field perfectly aligned to the z-axis. Therefore, the maximum flux density in x- or y-direction in the sample volume must also be investigated. The simulation shows a maximal x-component at the top edge of the sample of 0.3 µT and in y-direction the field is less than 0.1 µT. This difference between x- and y-component is caused by the asymmetric sample and not the solenoid itself.

To check the difference between simulation and experiment the excitation current of the solenoid is ramped from -1.5 A to 1.5 A in 0.1 A steps. In Figure 3.6 the flux density generated by the solenoid is plotted against the excitation current. The magnetic field is recorded with three single axis Fluxgate sensors which are described in more detail in section 3.2.3.

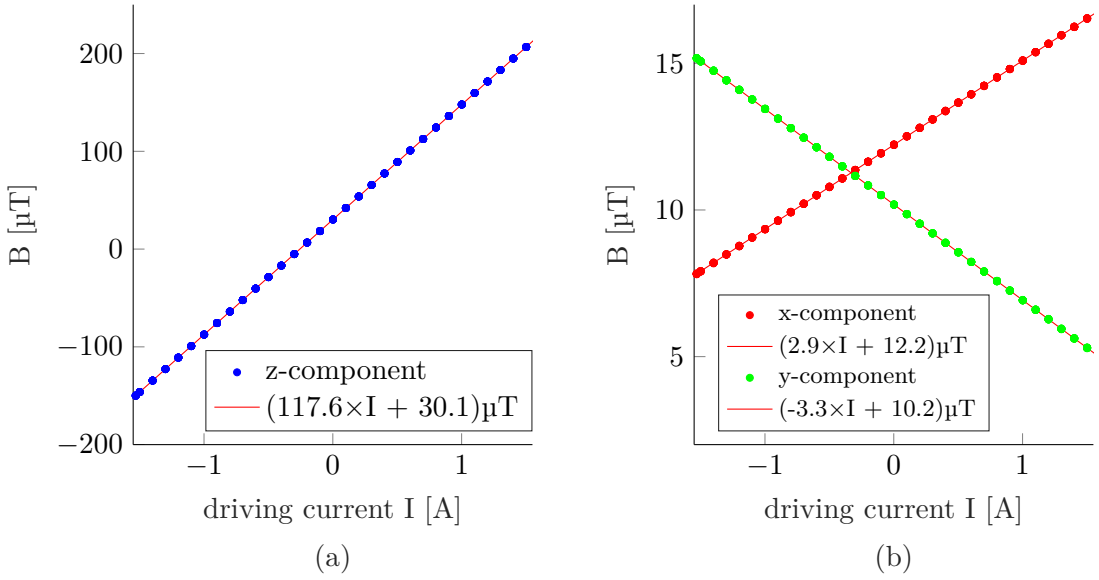

Figure 3.6.: Generated flux density versus the driving current. (a) shows the z-component, and (b) the x- and y-components. Additionally, linear regressions are performed for each data set. The slope of the fit in (a) agrees well with simulations. Due to a misalignment of ≈ 1.5° of sensors and coil the slopes in (b) are not zero.

The recorded data shows good agreement with the simulation. At the sensor position the simulation predicts the z-component of the magnetic flux density to be 117.9 µT with 1 A driving current. The slope of the fitted line is 117.6 $\frac{\mu T}{A}$ and, therefore, only

0.3% smaller than expected. This can easily be explained with imperfections in the winding, misalignment or shifting of the sensor. The slope of the x- and y-direction predicted by the simulation are $0.07\,\frac{\mu T}{A}$. The measured data shows an inclination of $2.9\,\frac{\mu T}{A}$ and -3.2 $\frac{\mu T}{A}$ respectively. The most likely cause for this error is misalignment of the sensors by $\approx 1.5°$ which cannot be ruled out.

The Offset at zero current is the earth's magnetic field at the position of the sensors.

Helmholtz-coils pairs

To reduce the size of the Helmholtz-coils a square design is chosen over a round design. This alters the Helmholtz-condition which is the ratio between distance of the two coils and their size to achieve the best field flatness. In square Helmholtz-coils the optimal ratio of distance between the two coils and side length of the squares is given by

$$\frac{h}{2} = 0.5445 \times a \tag{3.1}$$

[76], where h is the distance between the two coils and a is half the side length of the coils.

One pair is mounted to the inside of the aluminium frame of the cryostat (see Figure 3.2). This fixes the distance h and, therefore, side lengths of one of the Helmholtz-coil pairs. The other coils have to be either larger or smaller to allow them to be placed around or in the first pair. To keep the design more compact the seconds pair is smaller.

The coils are build with aluminium U-profile with a width of 2 cm, height of 1 cm and wall thickness of 0.2 cm. The profiles are connected via 3D-printed connectors (red and blue corners in Figure 3.2). They are designed to increase the bending radius in the corners to 1 cm. This way the copper wire is bend not as sharply which reduces stresses and increases the lifetime of the coils. The dimensions of the large Helmholtz-coil pair are: Side length $2 \times a = 73.4$ cm; distance between the middle of the coils $h = 40$ cm.

The coils are again simulated in COMSOL to determine the number of necessary windings and estimate the field flatness in the sample volume. The channels created by the profiles are used as the coil geometry in the simulation. In the simulation discussed in the following plots, the excitation current is set to 1 A and the number of winding is 75. This equals the number of windings in the built coil. It is mounted such that it creates field in x-direction. Figure 3.7 depicts a heat map of the magnetic flux density created by the large Helmholtz-coil. The arrows show direction and magnitude of the magnetic flux density. To compress the range, they are scaled logarithmically.

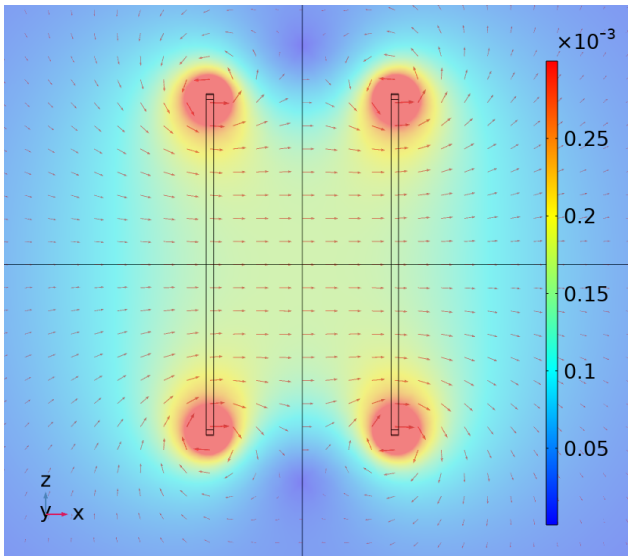

Figure 3.7.: Simulated field created by the large Helmholtz-coil with 1 A driving current. The heat map shows the magnetic flux density magnitude in T. The arrows show the strength and direction of the generated field. They are scaled logarithmically.

Figure 3.8 and 3.9 show the x-component of the magnetic flux density along the same lines as for the solenoid. Figure 3.8 shows it along three vertical lines at $x = -3, 0, 3\,\mathrm{cm}$ and Figure 3.9 along five horizontal lines in x-direction at $z = -5, -2.5, 0, 2.5, 5\,\mathrm{cm}$. Since the Helmholtz-coils are positioned such that the centre of the coil is at the centre of the sample the sample volume is now symmetrical around $z = 0\,\mathrm{cm}$. The field profile along the y-direction is not depicted, since the coil is symmetrical in z- and y-direction.

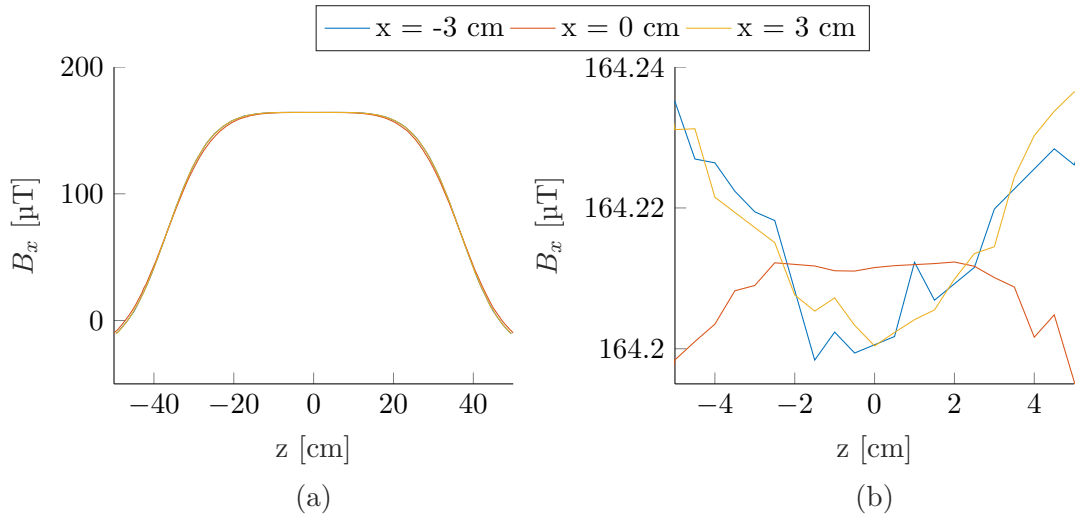

Figure 3.8.: x-component of flux density created by the large Helmholtz-coil pair along three vertical lines at $x = -3, 0, 3\,\mathrm{cm}$. The coils are centred around $x = 0\,\mathrm{cm}$. (b) shows a close up of the same data at the sample position from $z = -5\,\mathrm{cm}$ to $z = 5\,\mathrm{cm}$. The legend is identical for both plots. The field is nearly constant within the sample volume.

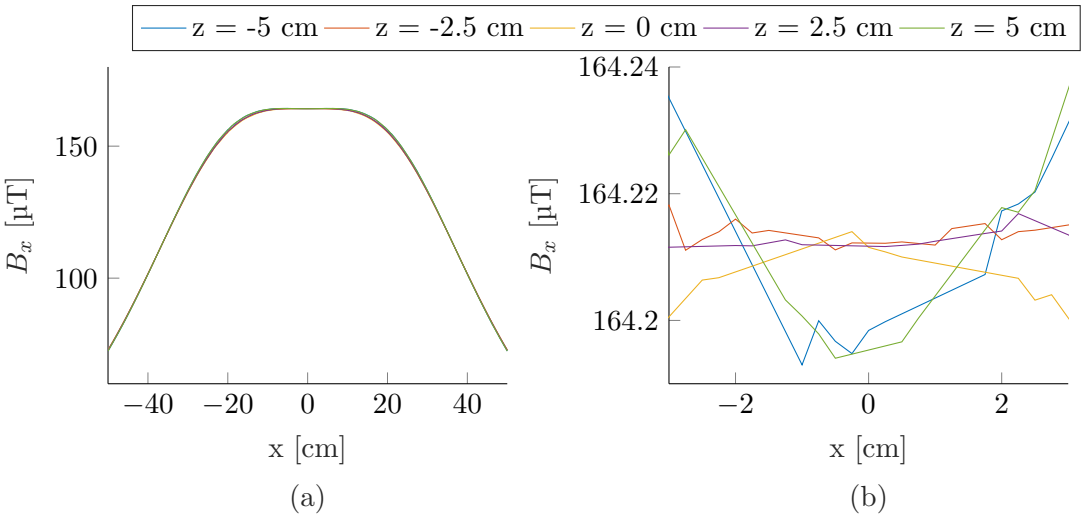

Figure 3.9.: x-component of flux density created by the large Helmholtz-coil pair along five horizontal lines at $z = -5, -2.5, 0, 2.5, 5\,\mathrm{cm}$. The coils are centred around $x = 0\,\mathrm{cm}$. (b) shows a close up of the same data at the sample position from $x = -3\,\mathrm{cm}$ to $x = 3\,\mathrm{cm}$. The legend is identical for both plots. The field is nearly constant within the sample volume.

The largest deviation of $0.04\,\mu\mathrm{T}$ is visible in Figure 3.8 (b). This corresponds to a relative error smaller than 0.1%. If the sample is shifted an additional $2\,\mathrm{cm}$ up in the real experiment, the maximum deviation does not change significantly. Therefore, a

relative error of 1% in real experiments is again reasonable. The maximum generated magnetic flux density in y- and z-direction are both 0.1 µT and, therefore, negligible.

For a comparison between simulation and experiment, the coil current is ramped from -1.1 A to 1.1 A in 0.1 A steps. The span is smaller then for the solenoid, because the resistance of the Helmholtz-coils is higher and the employed power supply is limited to 70 V.

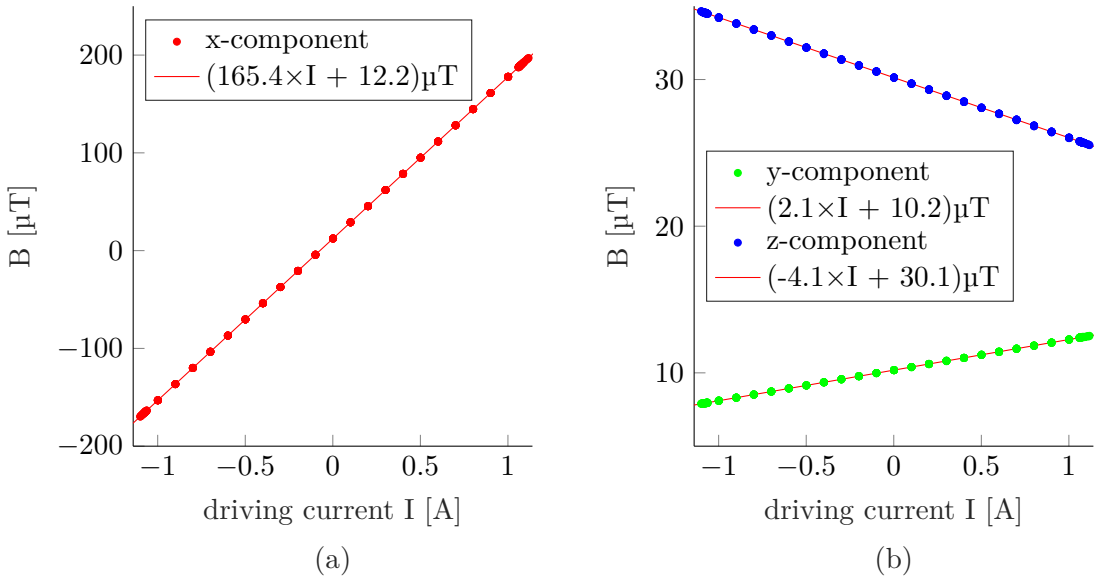

Figure 3.10.: (a) Measured x-component generated by the large Helmholtz-coil pair versus the excitation current with linear fit. (b) y- and z-component generated by the large Helmholtz-coil with linear fits. Due to a misalignment of ≈ 1° of sensors and coils the slopes in (b) are not zero.

The linear fit in Figure 3.10 (a) shows a coil constant of 165.4 $\frac{\mu T}{A}$ while the simulation predicts 164.2 $\frac{\mu T}{A}$. The discrepancy between simulation and experiment is 0.7% and, therefore, the simulation agrees well with the real experiment.

The fits for y- and z-direction yield a non-zero slope. This is most likely caused by a misalignment of coils and sensors. A rotation of ≈ 1° of the sensors compared to the coil is sufficient to result in the fitted slopes.

The offsets of the fits equal the earth's magnetic field and are the same as in Figure 3.6.

The smaller Helmholtz-coil pair is not discussed in detail. The side-length was chosen 2 cm shorter, this way it fits just inside the larger pair. The dimensions are: side-length $2 \times a = 71.4$ cm, distance between coils $h = 38.9$ cm. It is mounted perpendicular to the large Helmholtz-coil so it creates magnetic field in y-direction. A more detailed description of the small Helmholtz-coil can be found in appendix A.1. Parameters of all three coils are summarised in Table 3.1. In Appendix A.1 the field flatness and stray fields are also computed in cubes of 10 cm and 20 cm side length.

Table 3.1.: Technical data for the self-made coils integrated into the small bath cryostat. Field flatness and field in non-dominant direction are calculated in the sample volume. The maximum flux density stated here is reached with a power supply limited at 70 V and 1.5 A.

	Solenoid Z-direction	HHC large radial direction	HHC small radial direction
Diameter / side-length [cm]	29	73.4	71.4
Length / coil distance [cm]	88	40	38.9
Number of windings	88	75	75
Coil constant (simulated) $[\frac{\mu T}{A}]$	117.9	164.2	169.0
Coil constant (experiment) $[\frac{\mu T}{A}]$	117.6	165.4	169.9
Max. flux density [µT]	180	190	180
Field flatness [%]	0.8	<0.1	<0.1
Max. stray field [%]	0.3	<0.1	<0.1

Active Compensation

As is shown in Figure 3.6 and 3.10 the coils are not aligned perfectly with the sensors and also not with respect to each other which results in stray fields in the non-dominant directions. To achieve a good field compensation, an iterative compensation procedure was developed: In a first step the magnetic field is measured and the current needed to compensate the field is calculated using the parameters in Table 3.1. Then the currents are applied and after the field is settled, the resulting magnetic field is measured again. Since the coils create magnetic field in the non-dominant direction the compensation is not perfect. In the next step the coil currents are adjusted to compensate the new field which reduces the field further. This is repeated until a certain field level is reached. In experiments this level is typically set to 25 nT. The same method is used to set an arbitrary field.

As is discussed above, the field generated by the coils is very homogeneous at the position of the sample. The external field, however, might be inhomogeneous. As a result the compensated magnetic field is only known precisely at the position of the sensors. Any inhomogeneities that exist in the surrounding magnetic field are translated in the compensated field. These inhomogeneities can differ greatly depending on where the cryostat is set up, since the surrounding field is influenced by many factors as for example steel in walls and ground, 19" racks, and also movable items like gas bottles, or dewars.

To estimate the inhomogeneities in the surrounding field, the cryostat is moved 10 cm in ±x- and ±y-direction. Additionally the lid is lifted 10 cm up. The field is measured at each position with the Fluxgate sensors. Interpolating linearly between the field measured at the different points gives an estimation of the field inhomogeneities. The results are summarized in Table 3.2.

Table 3.2.: Estimation of field inhomogeneities in the surrounding magnetic field. "Direction (i)" denotes the direction the cryostat is moved in, and $\frac{\partial B_n}{\partial x_i}$ the gradient of the n-component of B in i-direction. $\frac{\partial |\vec{B}|}{\partial x_i}$ is the gradient of the magnetic flux density magnitude along i-direction.

Direction (i)	$\frac{\partial B_x}{\partial x_i}$ $[\frac{\mu T}{cm}]$	$\frac{\partial B_y}{\partial x_i}$ $[\frac{\mu T}{cm}]$	$\frac{\partial B_z}{\partial x_i}$ $[\frac{\mu T}{cm}]$	$\frac{\partial \lvert\vec{B}\rvert}{\partial x_i}$ $[\frac{\mu T}{cm}]$
x	0.05	0.01	0.14	0.11
y	0.06	0.20	0.01	0.04
z	0.15	0.02	0.23	0.26

Table 3.2 shows inhomogeneities in x- and z-direction along the x- and z-axis. Residual field in these directions are, however, not critical: Measurements show that a field which is applied perpendicular to the sample's surface and gets trapped is not detectable with the existing sensor arrangement. Since the sample is positioned such that the normal of the large surface points in y-direction, trapped flux from the inhomogeneities in x- and z-direction is not detected. The y-component differs mostly in y-direction. Since the sample is 0.3 cm thick the deviation is only 0.06 µT in the sample. In x-direction it is also 0.06 µT and in z-direction 0.2 µT. The largest deviation overall is in the z-component in z-direction of 2.3 µT.

The method of active field compensation is well suited for trapped flux measurements in samples, because in contrast to cavities the inhomogeneities seen above are not as crucial. This has two reasons: First, the sample is smaller and, therefore, the inhomogeneities are smaller as well. Second, cavity measurement concerning trapped flux are typically done at smaller field levels [45, 77] than the these sample measurements where fields up to 200 µT are used. The benefits of active field compensation are lower costs compared to a permalloy shield and the ability to apply field in an arbitrary direction. If a permalloy shield is installed, the coils would have to be inside the shield. This would limit their size and reduce field flatness.

3.2. Setup to Measure Flux Trapping in Flat Samples

A dedicated experiment was designed which holds the sample in the cryostat. The setup is designed with two main goals: The first is to control the parameters mentioned at the beginning of the section as precisely as possible, and the other is to measure trapped flux as accurately as possible.

The parameter of external magnetic field is already addressed with the active field compensation. The parameters of geometry and material and its treatment are mostly influenced with the sample shape which is discussed next.

3.2.1. The sample

In [74] it is reported that the shape of the cavity influences how magnetic flux is trapped. The shape of the cavity and the distance of the sensors to the surface made interpretation of the results difficult. To isolate geometric effects from other effects, sensors should be very close to the sample and the geometry of the superconductor should be as simple as possible. To achieve this goal the sample shape is chosen to be a flat, rectangular sheet. The rectangular shape was chosen so that when the sample is cooled down the phase front which marks the transition between normal- and superconducting phase is a straight line. This reduces the impact of geometry compared to a round sample. The thickness of the sheet is chosen to be 0.3 cm which is the typical wall thickness of cavities. The other two dimensions should be large enough to be able to place several AMR sensors above the sample, and also not be dominated by effects on the sample's edges: Having several magnetic field sensors across the sample enables the investigation of flux trapping dynamics during the cooldown. Some of these sensors should be far enough away from the sample's edges because flux trapping behaviour might be influenced by sharp corners. To determine the final dimensions COMSOL simulations are carried out to investigate how different edge magnetizations affect the field at the sensor positions.

The final dimension of the sample are $(10 \times 6 \times 0.3)$ cm. This allows an sensor array of 3 by 5 sensors to be placed over the sample. To have a sensor placed in the middle of the sample, the number of rows and columns are chosen to be uneven. Figure 3.11 shows the magnetic flux density that would be measured at the sensor positions if 100 µT were trapped in the sample in y-direction. To simulate trapped flux a remanent flux density of 100 µT is fixed inside the sample and the resulting field is simulated with COMSOL. To investigate the influence of edge effects, the remanent flux density in a rim of 0.1 cm around the sample is changed. In Figure 3.11 (a) the remanent flux density in the edge of the sample is 0 µT, in (b) it is 300 µT.

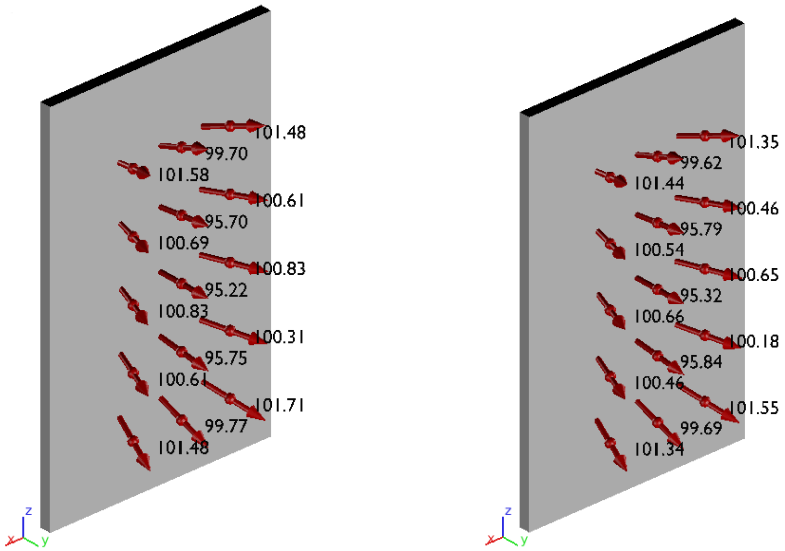

(a) (b)

Figure 3.11.: Simulated magnetic flux density at the sensor positions resulting from 100 µT trapped flux pointing in y direction in the sample. In the 3D representation in (a) the edge has no trapped flux, in the representation (b) 300 µT are trapped in the edge. The numbers next to the arrows show the flux density at the sensor position in µT. The magnetization of the edge has almost no effect on the measured flux density.

A comparison between the two representations in Figure 3.11 shows nearly no difference. The largest deviation is 0.2 µT which is negligible compared to other sources of errors like the inhomogeneities in the surrounding field. The measurement setup is, therefore, not sensitive to edge-effects.

To conclude there are two reasons to use a relatively large sample like this ($(10 \times 6 \times 0.3)$ cm). First, it allows for more sensors to be placed next to it which makes the analysis of flux trapping dynamics possible. In section 4 measurements are shown which would not be possible with a small sample. Second, it is not sensitive to edge effects.

Using a flat rectangular sheet makes analysis of geometric effects easier and the samples are easy to manufacture. This reduces costs, so more materials can be tested to investigate the influence of the material on trapped flux. Possible treatments like heat-treatments, chemical-polishing, coatings, etc. are easier to apply to the samples compared to cavities because it is smaller and has no curved surfaces.

3.2.2. Mounting and Temperature Control

So far the parameters of external magnetic field, geometry, and material / treatment are addressed. This leaves temperature gradient and cooldown speed.

To measure trapped flux the sample must be cooled down below its transition temperature T_c. To measure it again with different cooldown parameters the sample must

first be warmed up above T_c and then cooled down again (thermal cycling). With a critical temperature of 9.2 K the niobium sample cannot be placed in the liquid helium, as it would make it impossible to warm up above T_c. For that reason the sample is suspended above a liquid helium reservoir and is only cooled by helium gas. Alternatively, the sample could have been enclosed in a vacuum chamber, but simulations suggest that this would complicate the temperature control. Figure 3.12 shows a schematic view of the setup, and a picture of it partially assembled.

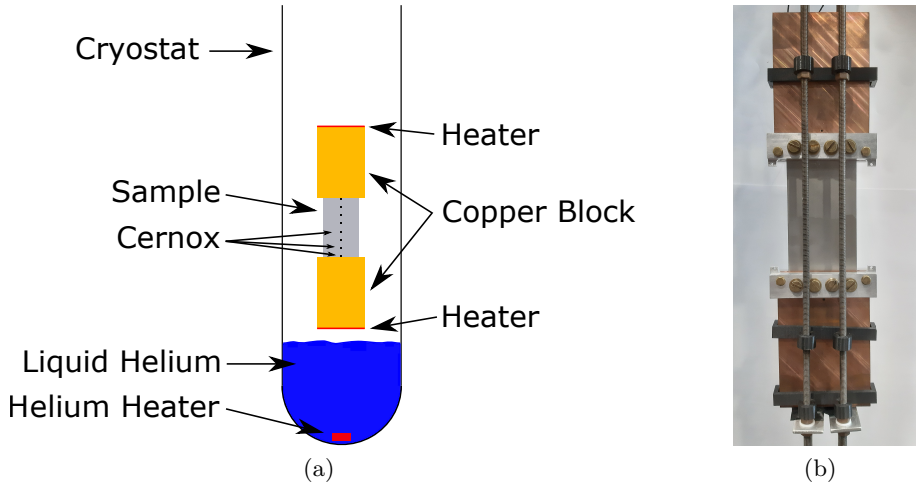

Figure 3.12.: (a) schematic view of the setup in the cryostat. (b) picture of the partially assembled setup.

To control the temperature gradient the temperatures at the top and the bottom edges must be controlled independently. The temperature is controlled with electrical heaters because they react quickly and the power can easily be adjusted. They have the drawback that they create a magnetic field induced by the current flowing through them. To reduce the field of the heaters at the sample position, two copper block are used to transfer the heat from the heaters to the sample. The heaters are glued to the ends of the blocks. By moving the heaters away from the sample the field is reduced enough to not be detectable by the magnetic field sensors.

In order to achieve a good thermal contact between copper and niobium the sample is clamped in each copper block. The blocks have slits of 0.31 cm width and 2 cm depth at their end to host the sample. A technical drawing can be found in appendix A.3. The sample is inserted in the top 0.2 cm of the slit, which is then compressed with nuts and bolts. To spread the pressure more evenly, two 1 cm thick aluminium blocks are used as "washers" on each copper block. To clamp the sample like this has the advantage that no holes must be drilled in the sample to tighten it to the copper. As holes might influence the flux trapping behaviour this method is chosen.

The heater powers are controlled individually via two PID controllers in LabView [78]. For control input the temperature of the temperature sensor on the sample closest to the respective sample edge (see section 3.2.3) is used. The power is set in a range of

0-25 W. The PID controllers adjust the power every 100 ms which allows quick changes in temperature.

The entire setup is mounted to titanium threaded rods hanging from the cryostat's lid. All materials in the vicinity of setup are non-ferromagnetic.

In addition to the heaters on the copper blocks, a separate heater is submerged in the liquid helium. It is used to evaporate helium in a controlled manner. Due to the well insulated cryostat not enough helium evaporates on its own and the gas above the reservoir heats up above 9.2 K. The heater power usually ranges between 5-10 W and is adjusted according to the parameters that need to be reached. To reach high gradients or fast cooldowns the heater power must be increased. This not only increases helium consumption but also increases the cooling power in the middle of the sample. This becomes especially problematic for cooldowns with a low temperature gradient: The sample is cooled so much by the gas that the temperature in the middle of the sample is actually lower then the temperature at the ends and the temperature gradient is not constant along the sample (see section 4.8.1). The heater power must, therefore, be adjusted depending on the desired cooldown parameters. To reduce the cooling in the middle of the sample cotton wool is packed around the sample.

With these different control parameters the temperature gradient across the sample and the cooldown speed can be influenced and their effect on trapped flux can be investigated in detail.

3.2.3. Sensors and Readout

With the experiment described to far it is possible to control all the parameters which are suspected to have an influence on trapped flux. During measurement temperature gradient, cooldown speed, external field, and trapped flux must be measured and recorded. For this purpose temperature sensors, and magnetic field sensor are necessary which are discussed below.

Temperature Sensors

For temperature sensors eight Cernox sensors type CX-SD 10-50 [79] are used. They have a temperature dependent resistance which is measured with a four wire measurement and compared it to a calibration curve provided by the manufacturer. With the calibration curve their resistance is translated to a temperature. The sensors are glued directly to the sample with silver conductive paint. This ensures a good thermal contact between sensor and sample. Since the sensors are glued they can be placed arbitrarily on the sample. Typically they are glued equidistantly in a straight line from top to bottom of the sample. To investigate the horizontal temperature distribution across the sample they are glued in a cross shape on the sample: four equidistantly vertically along the sample and the remaining four at the height of the second sensor equidistantly horizontally across the sample. Figure 3.13 shows both configurations. Additionally to the eight Cernox sensors on the sample three Cernox sensors type CU are used [79]. One is mounted on each of the copper blocks and an additional one measures the gas temperature close to the sample.

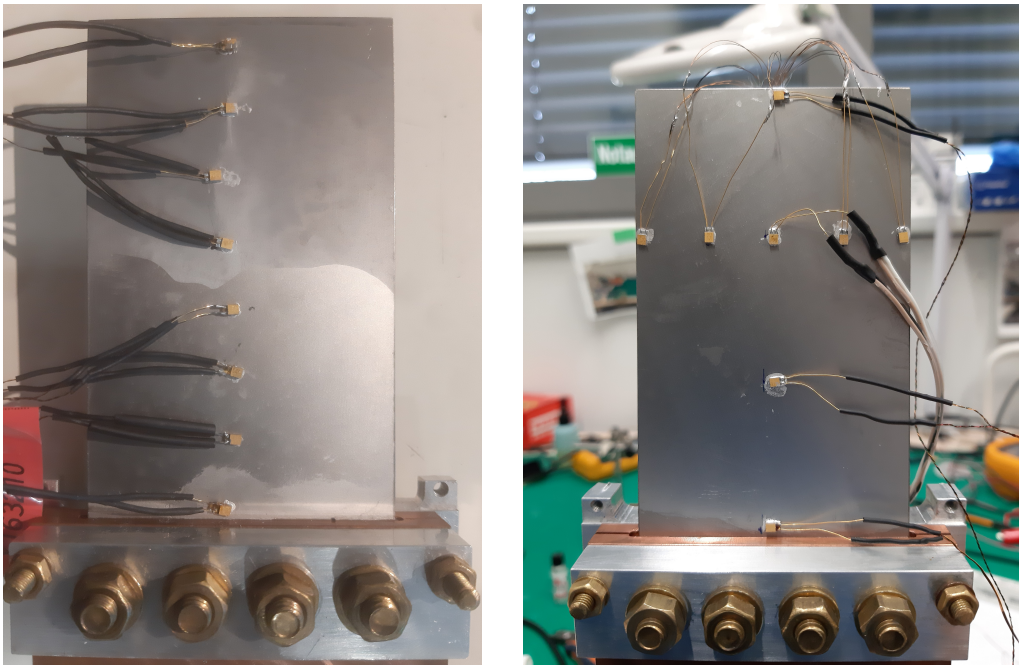

(a) (b)

Figure 3.13.: Pictures of Cernox sensors glued to the sample. (a) typical configuration. (b) configuration to measure horizontal temperature distribution.

The temperatures are read out with a temperature monitor 218 by Lakeshore [80]. It provides a 10 µA driving current and measures the voltage drop across the sensors. The calibration curves are stored on the device and the temperature data is transmitted digitally to a control computer. The devices have a resolution of 100 mΩ, which corresponds to roughly 0.5 mK at 9 K, depending on the sensor. Their drawback is a maximum read out rate of 2 Hz, which is too slow to record fast cooldowns. To bypass this problem the temperature monitor is used only as the constant current source and the voltage of the eight sensors on the sample is measured with a multichannel analogue-digital converter (ADC).

The ADC is a SPARTAN device by imc [81]. It has 128 channels with 16 bit resolution and every channel is independently amplified. The measurement ranges are adjustable between ±50 mV and ±60 V. In the smallest range of ±50 mV a 16 bit resolution equates to a resolution in voltage of 3.05 µV. With the driving current of 10 µA from the temperature monitor this results in a resolution in resistance of 300 mΩ, or roughly 1.5 mK temperature resolution around 9K. The advantage of the imc device is the fast read-out speed of up to 500 Hz. However, a read-out speed higher than 100 Hz results in high noise for the Cernox sensors.

Due to an impedance difference the temperature monitor and the imc device cannot be connected in parallel, as the imc influences the read-out of the temperature monitor. The wires for the voltage measurement are, therefore, routed through a relay-box which switches the connection between imc and temperature monitor. This insures separation

of the two devices. The resistance measured by the imc device does not equal the resistance measured by the temperature monitor exactly. The calibration curves provided by Lakeshore can, therefore, not be used for conversion of the resistance data obtained with the imc device to temperature values. To calibrate the imc data an additional calibration curve must be generated relating the resistance measured by the imc device to the temperature measured by the temperature monitor. To achieve this, the temperate measured by the temperature controller is saved in an array. Afterwards the read-out is switched to the imc device and the corresponding voltage is recorded as well. This is done while the sample is slowly warming up and the points are taken every 0.1 K. Once this table is recorded it is used to translate the voltages measured by the imc to temperatures. As the points are only 0.1 K apart from each other a linear interpolation is sufficient to calculate the temperature from the recorded voltage.

Magnetic field Sensors

The magnetic field is measured with a combination of two sensors types: Fluxgate [82] and AMR sensors. The Fluxgate sensors are used as reference for the AMR sensors, and active field compensation. The AMR sensors are located closely to the sample and are used to measure the trapped flux.

To measure the magnetic field in 3D, three single axis Fluxgate probes Mag-F are used in combination with the Mag-01H readout by Bartington [83]. This combination results in an offset error of 5 nT and resolution of 1 nT in the range of 0-20 µT and 10 nT in the range of 20-290 µT. The read-outs only have an analogue output which is recorded with the imc ADC. This limits the resolution to 6 nT.

The sensors are mounted with a 3D-printed part to the threaded rods hanging from the cryostat's lid. The fixture aligns the sensors orthogonally to each other and in directions of the coils. As is discussed in section 3.1.2 the misalignment of sensors and coils is in the order of 1°. Due to the inhomogeneities in the surrounding field it is important that the Fluxgate sensors are as close to the sample and the AMR sensors as possible. A picture of the Fluxgate sensors and their position in relation to the sample and AMR sensors is shown in Figure 3.14.

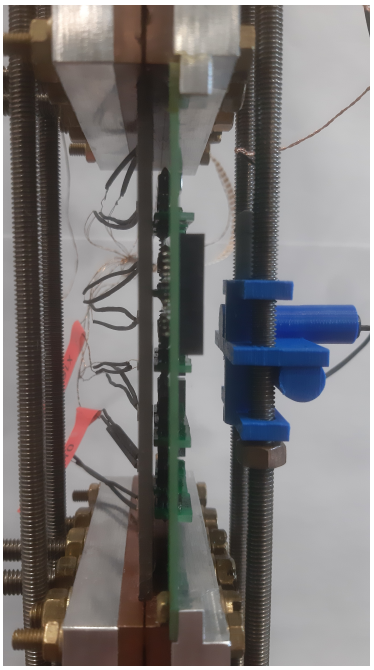

Figure 3.14.: Picture of mounted Fluxgates in 3D-printed fixture (blue). The AMR sensors are mounted between Fluxgate sensors and sample on the green PCB. Cernox sensors are glued to the left side of the sample.

To measure trapped flux in the sample AMR sensors are used. They are much cheaper ($\sim$1 € instead of $\sim$1000 €) and smaller ($\sim 10mm^2$ wafer instead of 20 mm long cylinder) than the Fluxgates which allows the sensors to be placed closer to the sample. A custom printed circuit board (PCB) is designed which connects the sensors to the necessary power supplies and read-out electronics. It also serves as mounting fixture for the sensors. It is mounted to two of the aluminium blocks (see Figure 3.14).

To measure magnetic field in 3D, three AMR sensors are combined in one sensor group: The sensor measuring in x-direction is soldered to the back of the board, the sensor in z-direction directly opposite to the front. To measure in y-direction the sensor must be rotated out of the PCB plane. To achieve this, adapter PCBs are printed to which sensors are soldered. The adapters are inserted perpendicular to the main board in routed slits in the latter. A picture of the PCB is shown in Figure 3.15.

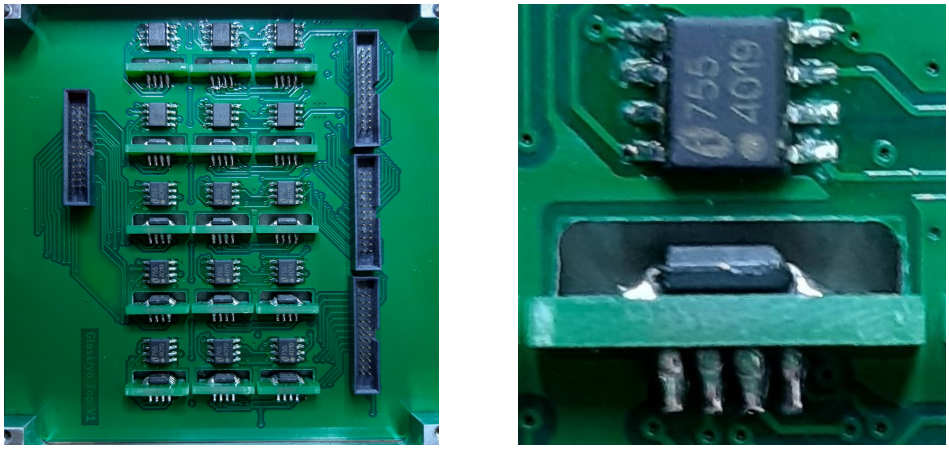

Figure 3.15.: Picture of PCB which holds AMR sensors. The right picture shows a close up of one sensor group. Sensors measuring in x-direction are on the backside.

The sensor groups are spaced 1.3 cm apart in x-direction (horizontal) and 1.6 cm in z-direction (vertical). The Sensors closest to the sample's surface are the sensors measuring in x-direction (horizontal, parallel to surface), they are 0.25 cm away from the surface. The sensors measuring in y-direction (perpendicular to surface) are 0.38 cm away from the surface and the sensors in z-direction (vertical) 0.51 cm. The vertical distance between y-sensor and the other two is 0.5 cm. Figure 3.16 shows the sensor group distribution across the sample. The sensor groups are labelled 1-15.

Figure 3.16.: Distribution of AMR sensor groups across the sample. The red dots mark the centre of the sensor groups. The sensor groups are labelled 1-15.

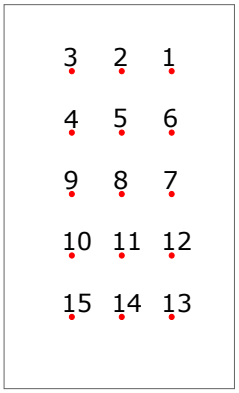

As is mentioned in section 2.5 the AMR sensors cannot be operated in the intended way, and must be recalibrated at cryogenic temperatures. During soldering the sensors are not aligned perfectly. Therefore, the coordinate system of each sensor group is not only misaligned compared to the coordinate system of the Fluxgate sensors, but also the measurement axes within one sensor group are not perfectly perpendicular to each other. A simple calibration where the sensors of each direction are calibrated separately leads to errors in the final result, because a sensor that is supposed to measure in x-direction

might give a signal when field is applied in z-direction. It is impossible to know, whether this signal actually stems from a small field in x-direction or the sensor is misaligned and measures a small component of the field in z-direction. During calibration the information of how the sensors are aligned must be gained and stored.

At this point three coordinate systems play a role which are all slightly misaligned: The coordinate system of the coils, of the Fluxgate sensors, and of the AMR sensors. Because the Fluxgate sensors are needed for calibration and their fixture is 3D-printed and, therefore, accurate the coordinate system of the Fluxgate sensors is used as the reference frame. All other coordinate systems are adjusted to fit to this. This means that the current in the coils is adjusted, until the Fluxgate sensors show the desired value and all misalignments in the AMR sensors are calibrated to fit to the coordinate system of the Fluxgate sensors.

The output voltages of the AMR sensors of one group in dependence of the magnetic field components can be expressed as:

$$\begin{aligned} V_x &= \alpha_x B_x + \beta_x B_y + \gamma_x B_z + \delta_x \\ V_y &= \alpha_y B_x + \beta_y B_y + \gamma_y B_z + \delta_y \\ V_z &= \alpha_z B_x + \beta_z B_y + \gamma_z B_z + \delta_z, \end{aligned} \tag{3.2}$$

where V_i is the output voltage of the sensor with dominant measurement direction in i-direction, and B_i are the flux density components. $\alpha_i, \beta_i, \gamma_i, \delta_i$ are fit parameters. δ_i is the offset voltage of a sensor, and $\alpha_i, \beta_i, \gamma_i$ equal the sensitivities of every sensor in each direction. Equation 3.2 can also be written as

$$\vec{V} = \boldsymbol{S}\vec{B} + \vec{V_0} \tag{3.3}$$

with $\boldsymbol{S}$ the sensitivity matrix in $\vec{V_0}$ the offset voltages. If the sensors were aligned perfectly, $\boldsymbol{S}$ would only have entries on the diagonal.

To determine the sensitivities and offset values 15 randomly chosen magnetic fields are applied with the coils. After each field is set, the output voltages of the sensors V_i and the magnetic flux density measured by the Fluxgates $\vec{B}$ are stored. Then a 4-dimensional linear fit is performed for each sensor according to the corresponding equation in equation 3.2, to determine the fit parameters.

To measure magnetic flux density with one sensor group, the output voltages $\vec{V}$ are measured. Since $\boldsymbol{S}$ and $\vec{V_0}$ are known from the fit, the system of linear equations in equation 3.3 can be solved numerically for $\vec{B}$.

The 4-dimensional fitting is done in LabView and the results are stored in a file. During measurement the system of linear equations to calculate the flux density is solved with LabView as well. For raw data which is used for analysis after the measurement is completed the system of linear equations is solved with Matlab [84], utilizing the fit parameters generated by LabView. Both programs yield the same result for the numerically solved system.

Since the offset voltages of the AMRs change for each cooldown from room temperature (see [74]), and the alignment of PCB to Fluxgate sensors can change after a new sample is installed, the calibration must be performed for every new experiment.

The offset error of this calibration is typically in the range of 0.2 µT and the relative error is less than 1%. Figure 3.17 shows the measured field when the external field is compensated to zero, 100 µT are applied in y-direction, and without compensation. For the last case, the Fluxgate sensors measure $|\vec{B}_e| = 32.5\,\mu T$.

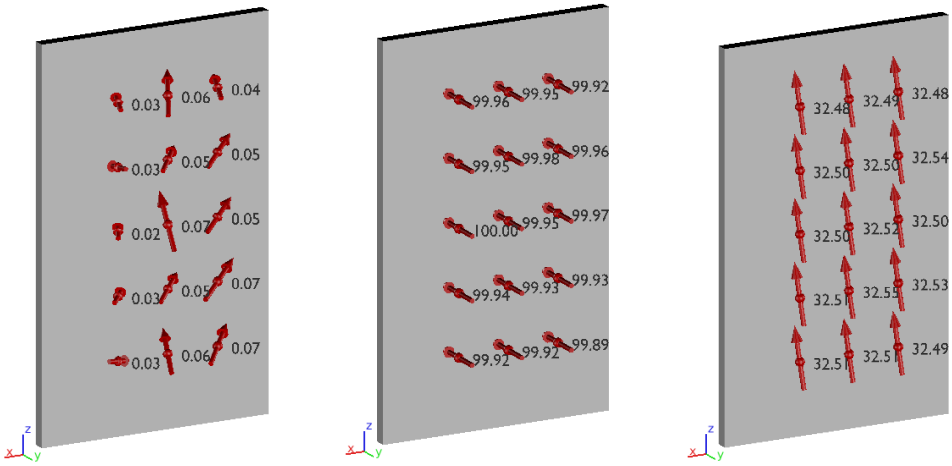

(a) (b) (c)

Figure 3.17.: Field measured by AMR sensors. (a) zero field, (b) $\vec{B}_e = (0, -100, 0)\,\mu T$, (c) surrounding field, no compensation. The arrows are always scaled to the maximum of the momentarily measured flux density. For comparison of the flux density magnitude between different 3D representations the numbers next to the arrows which give the flux density magnitude in µT at this sensor position must be considered. In all cases the sensor groups measure the expected values.

As can be seen in Figure 3.17, the calibration works very well and shows the desired values. It has, however, one drawback: Since all AMR sensors are calibrated to the Fluxgate sensors, any inhomogeneities in the magnetic field are set to zero in the calibration and cannot be measured by the AMR sensors. The absolute values are, therefore, only reliable within the margins of the inhomogeneities of the surrounding magnetic field. In section 3.1.2 the inhomogeneities are estimated to be 2.3 µT in the worst case. This is considered in the systematic error of AMR data, which is estimated to 2 µT.

3.2.4. Measurement Procedure

For the initial cooldown the cryostat is first filled with liquid nitrogen which is allowed to evaporate and thus pre-cools the setup to around 80 K. This procedure reduces the heat-load for the subsequent cooling step. Once the nitrogen is depleted, liquid helium is pushed from a dewar into the cryostat via a helium transfer line. The cryostat is filled until the liquid helium level reaches just below the setup. The helium that evaporated during filling already cools the sample below its transition temperature of 9.2 K. The

following measurement procedure is described using a specific cooldown as example. In this cooldown a magnetic flux density of -100 µT in y-direction, a temperature gradient of 0.06 $\frac{\mathrm{K}}{\mathrm{cm}}$, and a cooldown rate of 0.07 $\frac{\mathrm{K}}{\mathrm{s}}$ are chosen.

The two heaters on the copper blocks are used to heat the sample above 9.2 K. At the same time the heater in the helium bath is turned on with a constant power of 5 W to ensure a constant helium flow. Once the sample is normal conducting the active field compensation can be used. First, the external field is reduced to zero (zero-field) and the necessary coil currents are saved. Then, the desired flux density is set (in this case $B_y = -100\,\mu\mathrm{T}$). When the field is reached, the coil currents are saved and kept constant.

To achieve a temperature gradient of 0.06 $\frac{\mathrm{K}}{\mathrm{cm}}$ the set points of the PID-controllers controlling the heaters on the copper blocks are set to 9.5 K at the bottom and 10.1 K at the top. With the sample length of 10 cm, this yields the desired gradient. Next, the set temperatures are simultaneously lowered with a rate of 0.07 $\frac{\mathrm{K}}{\mathrm{s}}$. This ensures a constant temperature gradient during cooldown while the sample becomes superconducting from the bottom to the top. After the sample is fully superconducting the coil currents are restored to the zero-field values which were saved earlier. This way the coils compensate the external magnetic field and thus the field measured by the AMR sensors only stems from trapped flux in the sample. When trapped flux is analysed in the following chapters it corresponds to the field measured at this point. After the magnetic field is recorded, the PID set points are increased again above 9.2 K and a new cooldown with different parameters can be performed.

Figure 3.18 shows the temperature of the Cernox sensors for the exemplary cooldown from above. They were glued in a cross shape like in Figure 3.13 (b). Figure 3.19 shows the magnetic field for different stages of the cooldown.

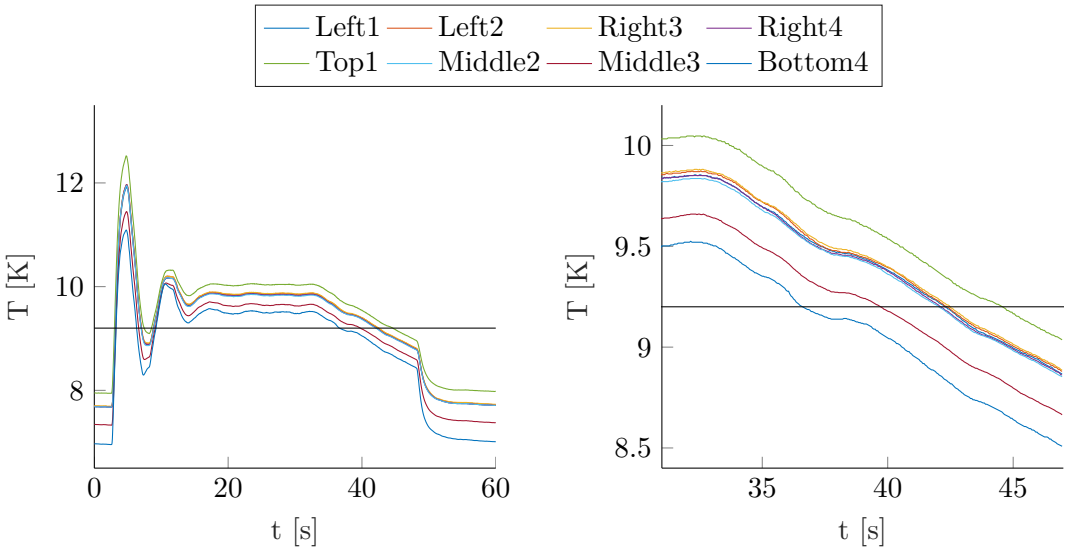

Figure 3.18.: Typical temperature profile during a cooldown versus time. The Sensors glued in a cross shape and are labelled 1-4 from top to bottom and 1-4 from left to right. The right plot shows the same data, but only the cooldown itself. The black horizontal line is inserted at 9.2 K.

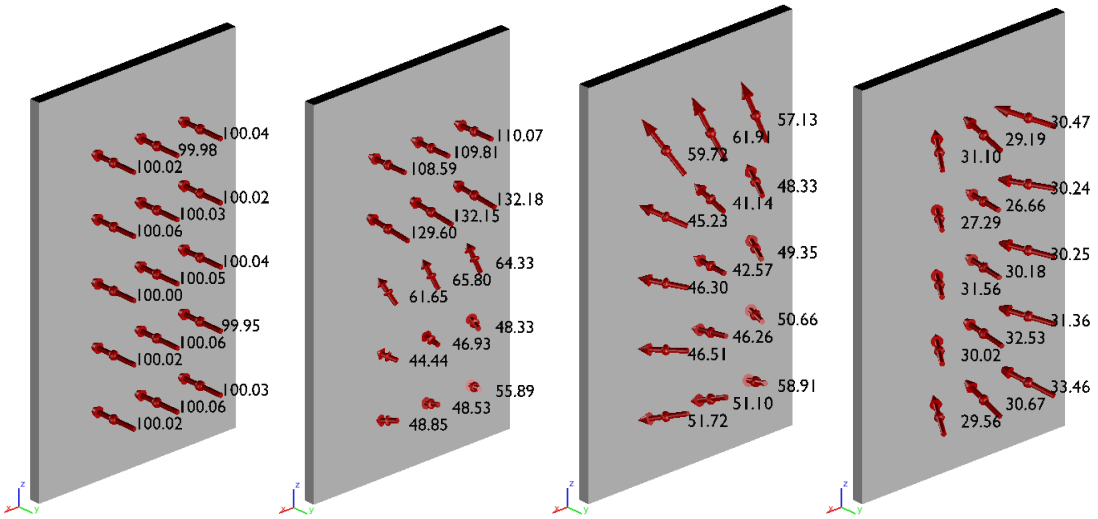

(a) (b) (c) (d)

Figure 3.19.: Measured magnetic field for different stages during the cooldown: (a) sample is normal conducting and $\vec{B_e} = (0, -100, 0)\,\mu\text{T}$. (b) sample is partially superconducting. (c) sample is fully superconducting, $\vec{B}_\text{e}$ is still applied. (d) sample stays fully superconducting, $\vec{B}_\text{e} = (0, 0, 0)\,\mu\text{T}$, the measured field stems from trapped flux. The numbers next to the arrows show the flux density magnitude at the sensor position in µT.

During the filling procedure helium is evaporating and the cold helium gas cools the sample below its transition temperature of 9.2 K. During this cooldown a large natural temperature gradient is established across the sample, which makes these cooldown interesting for investigating the dependence of trapped flux on temperature gradient.

4. Results: Survey of Parameters

This section describes the data measured with the above introduced setup. The impact of the parameters: temperature gradient, cooldown rate, external magnetic field, geometry, material, and material treatment are presented one by one. As is shown in chapter 5 the effects of the parameters are interconnected, therefore, this section only describes the measured effects to give an overview. With a concept on how different parameters affect trapped flux an error estimation is done at the end of this chapter. The detailed analysis is done in chapter 5.

For the following description of the measured effects only sensor group 8 of the AMR sensors is used most of the time. As can be seen in Figure 3.11 the flux density measured by each sensor is different, even when the flux is distributed homogeneously throughout the sample. Therefore, the measurements taken by the individual sensor groups cannot be averaged. Since sensor group 8 is in the centre of the sample it is chosen to illustrate the effects different parameters have on trapped flux. The differences between sensor positions are described in section 4.4 and chapter 5.

4.1. Temperature Gradient

Many studies have investigated the effect of temperature gradient on trapped flux [43, 45, 85]. It is consensus that a large temperature gradient across a superconductor while it makes the superconducting transition leads to less trapped flux. With the new setup and the ability to perform more cooldowns in a shorter time it is now possible to map out the dependence in much more detail.

To measure the effect of the temperature gradient across the sample on flux trapping the gradient is varied while all other parameters are kept constant. The external magnetic field is set to $\vec{B}_\mathrm{e} = (0, -100, 0)\,\mu\mathrm{T}$ (perpendicular to the large sample surface), and the cooldown rate to $0.07\,\frac{\mathrm{K}}{\mathrm{s}}$. The data shown here is recorded with an untreated large grain sample: It consists of only 2 grains with a grain boundary running horizontally though the middle of the sample. It was cut with water-jet from a large sheet sawn off a billet. The sample is tested in this condition without any further treatment. This means the crystal structure close to the surface ($100\,\mu\mathrm{m}$) is most likely damaged [86]. This might have an effect on the flux trapping behaviour. A picture of the sample is shown in Figure 4.1 where the grain boundary is clearly visible.

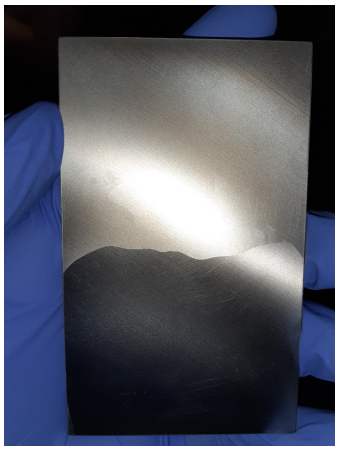

Figure 4.1.: Picture of large grain sample with grain boundary running horizontally through the middle.

Figure 4.2 shows trapped magnetic flux $|\vec{B}_{\mathrm{TF}}|$ measured by central sensor group 8 versus the local temperature gradient during cooldown at the AMR sensor position. To calculate the local temperature gradient, the temperature difference between one Cernox sensor and the sensor above it is calculated when the sensor passes the transition temperature of 9.2 K. The temperature difference is then divided by the distance between the two sensors. For sensor 1 at the top edge the difference is calculated to the sensor below it. The flux density is measured when zero field is applied, as described in section 3.2.4.

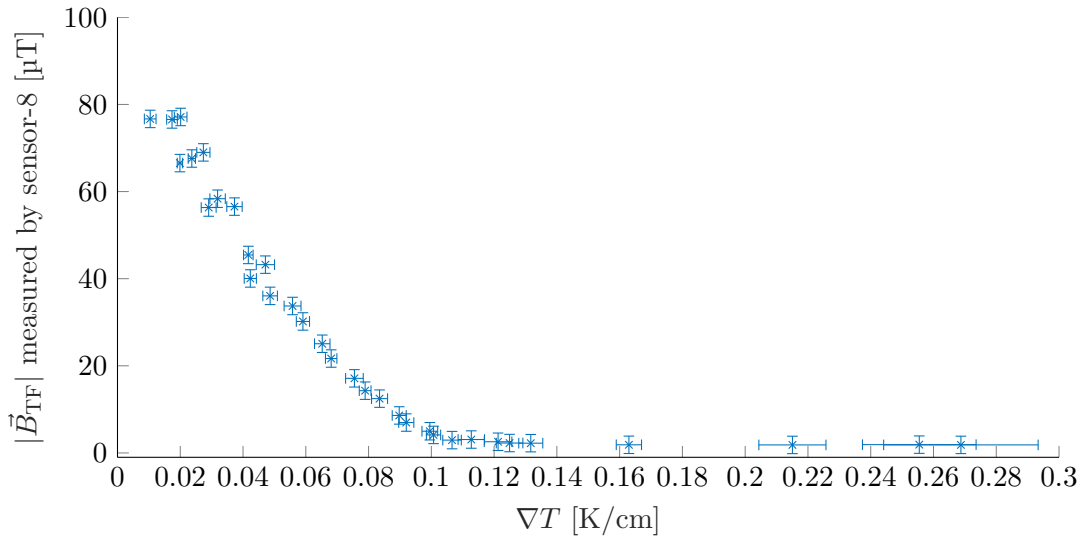

Figure 4.2.: Trapped flux measured by the central sensor group 8 versus local temperature gradient during cooldown. Trapped flux decreases with increasing temperature gradient and above $\nabla T \approx 0.1 \frac{\mathrm{K}}{\mathrm{cm}}$ near full expulsion is achieved.

A clear trend is visible that larger temperature gradients lead to less trapped flux. This is in line with the expectations. A rough extrapolation to $\nabla T = 0 \frac{\mathrm{K}}{\mathrm{cm}}$ suggests that nearly all available flux of 100 µT gets trapped. In this case of the large grain

material the achieved temperature gradients are large enough to expel all magnetic flux ($\nabla T > 0.11\,\frac{\mathrm{K}}{\mathrm{cm}}$). For different materials this does not necessarily have to be the case (see section 4.5).

4.2. External magnetic field strength

In section 4.1 the external magnetic flux density $\vec{B}_e$ was kept constant at 100 µT perpendicular to the surface. Now it is investigated how the flux density influences trapped flux. To do so, the temperature gradient during cooldowns is kept constant for a series of measurements and the magnitude $|\vec{B}_e|$ is altered between cooldowns. The orientation of $\vec{B}_e$ is always kept constant, pointing perpendicular at the sample's surface ($\vec{B}_e = (0, B_y, 0)$). Once several measurement points are taken at a fixed temperature gradient, the gradient is altered and a new series is recorded. Figure 4.3 shows trapped magnetic flux measured by the central sensor group 8 versus B_y. The different colours indicate different measurement series with constant temperature gradients, respectively. The data is recorded with the same large grain sample described in section 4.1.

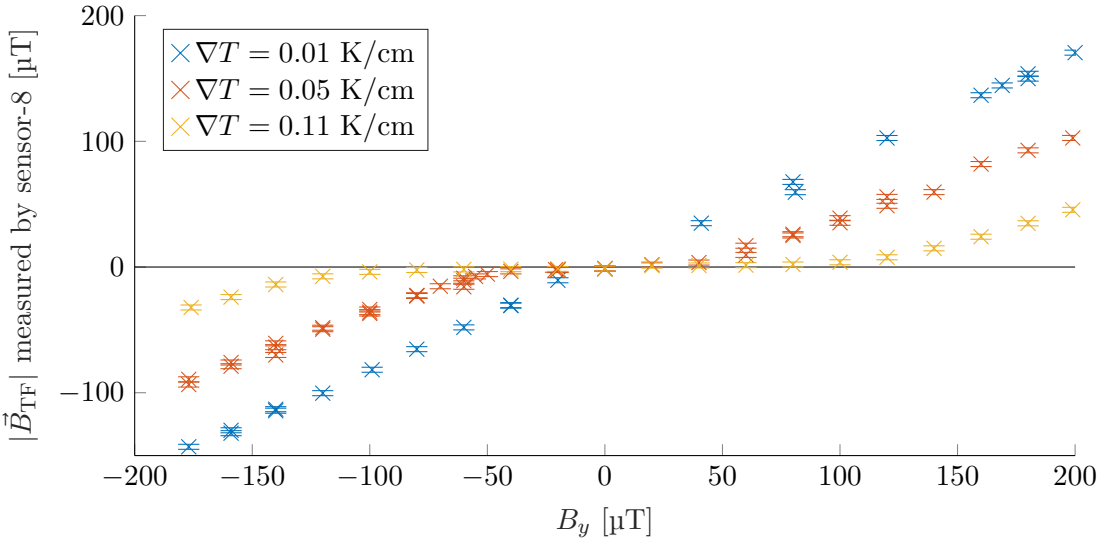

Figure 4.3.: Trapped flux measured by the central sensor group 8 versus the component of the external flux density perpendicular to the surface, B_y. Three measurement series with different temperature gradients are depicted. At higher temperature gradients flux is only trapped when $|B_y|$ is larger than a threshold field.

This plot shows several features: For the smallest temperature gradient of $0.01\,\frac{\mathrm{K}}{\mathrm{cm}}$, the trapped flux increases linearly with increasing applied field. This is in agreement with measurements done in [87]. However, for larger temperature gradients this is not the case anymore: Flux is only trapped once a certain threshold field level B^* is reached. As can be seen from the comparison of $\nabla T = 0.05\,\frac{\mathrm{K}}{\mathrm{cm}}$ and $\nabla T = 0.11\,\frac{\mathrm{K}}{\mathrm{cm}}$, B^* depends on the temperature gradient. Once the threshold field is reached trapped flux seems

to increase linearly with external field magnitude. A second effect that can be seen in the plot is a decrease of the slope of this linear dependence for increasing temperature gradient. Both effects have the same consequence for the flux-trapping behaviour: They lead to less trapped flux for larger temperature gradients. This also confirms what is expected from section 4.1.

4.3. Cooldown rate

In this section the effect of the cooldown rate on trapped flux is investigated. For this purpose an external field of 100 µT is applied perpendicular to the sample ($\vec{B}_\mathrm{e} = (0, 100, 0)\,\mu\mathrm{T}$) and kept constant for all cooldowns. Within one measurement series the temperature gradient is kept constant as well and only the cooldown rate $\left[\frac{\mathrm{K}}{\mathrm{s}}\right]$ is altered. After several points are taken, the temperature gradient is changed for the next series. Figure 4.4 (a) shows trapped flux measured by sensor group 8 versus cooldown rate. Figure 4.4 (b) shows the same data points, but plotted against "transition time". The "transition time" is the time it takes the sample to become fully superconducting, once it starts to transition at the bottom. Because of different temperature gradients for the different series this is not only the inverse of the cooldown rate: For a fixed cooldown rate the transition time is longer for a cooldown with a large temperature gradient than for a cooldown with a small temperature gradient, because in the first case the top edge starts at a much higher temperature and, therefore, takes longer to fall below T_c at a given rate. The data in Figure 4.4 is again measured with the same large grain sample. Plots regarding the cooldown rate or transition time do not show error bars because the error mainly stems from inconsistent cooldown dynamics and, as can be seen in the plots, is much larger than 2 µT. Chapter 4.8.3 investigates this issue further.

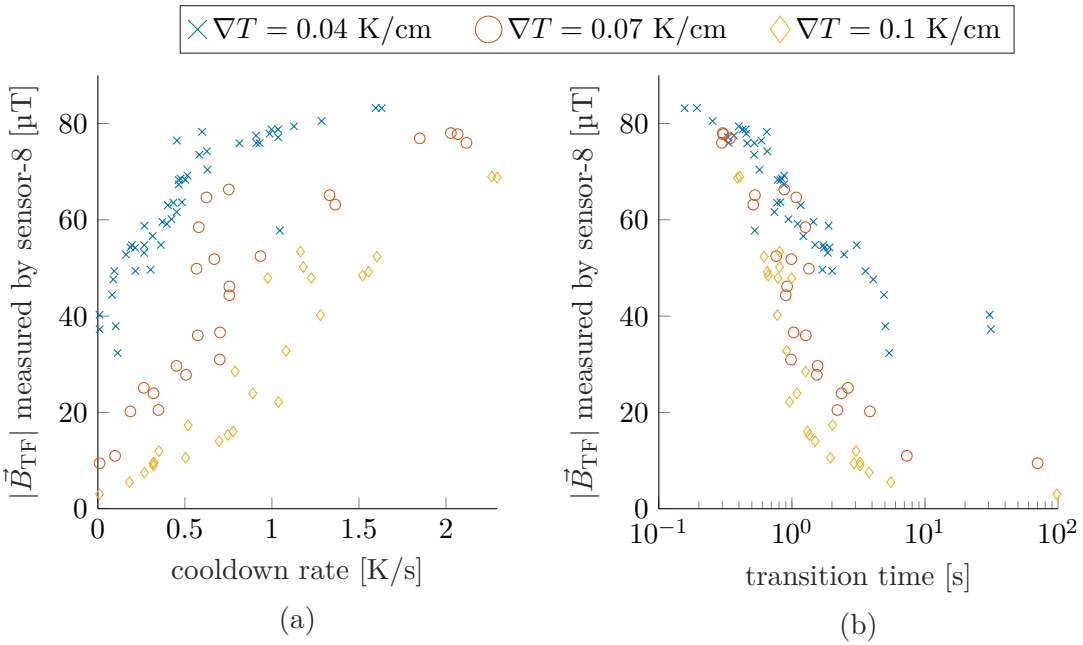

Figure 4.4.: Trapped flux measured by the central sensor group 8 versus cooldown rate (a), and transition time (b). Both plots depict the same measurement points but illuminate different aspects of the trapped flux behaviour. The legend is identical for both plots. Note the logarithmic x-axis in (b). For transition times below 1 s a sharp increase of trapped flux is evident.

Figure 4.4 (a) shows increasing trapped flux for higher cooldown rates. This is equivalently shown in Figure 4.4 (b) where trapped flux increases towards shorter transition times. Figure 4.4 (a) shows again how larger temperature gradients lead to less trapped flux, however, Figure 4.4 (b) shows that for very short transition times trapped flux becomes almost independent of temperature gradient. Only for transition times in the range of 1-2 s the temperature gradient starts to affect the amount of trapped flux. After which trapped flux decreases depending on the temperature gradient and levels out at transition times of around 6-7 s. Even longer transition times do not seem to change the amount of trapped flux. The final level then only depends on the temperature gradient. This strong dependence of trapped flux on the transition time has not yet been measured with cavity measurements which shows the importance of these sample measurements in order to get a better understanding of trapped flux.

In addition to the measurement of trapped flux in the final state, it can also be analysed how much flux is expelled during the cooldown: As can be seen in Figure 3.19 (b), magnetic flux is expelled from the sample which leads to an increase in flux density above the phase front. During a cooldown the Meissner transition expels magnetic field from the sample such that it piles up with the already existing field in regions that are still normal conducting. The resulting field changes can be described like a wave of magnetic flux driven by the migrating phase front between superconducting and normal conducting regions. The magnitude of this wave depends on the cooldown

rate. To illustrate what a cooldown looks like in the raw data of the AMR sensors and how the magnitude of the wave is extracted, Figure 4.5 shows the raw data of a slow cooldown (transition time = 15 s) with $\nabla T = 0.01 \frac{\mathrm{K}}{\mathrm{cm}}$. In the AMR data the five sensor rows are clearly distinguishable by the five peaks. Each peak consists of three lines from the three AMR sensor groups in one row. Since no additional information is gained from the exact sensor number the legend is omitted.

The increasing peak heights in Figure 4.5 (c), and (d) show how the wave builds up above of the phase front. The wave magnitude that is discussed in the following plots is the peak height of the highest peak compared to the start value. In this case the wave magnitude is 39.4 µT in y-direction, and 81.1 µT in z-direction. For the x-direction the wave magnitude is the maximum deviation from the start value. However, this data does not show the magnitude of the wave but how much flux is expelled and pushed out to the sides.

Figure 4.6 shows the wave magnitude in all three directions. Figure 4.6 (a) shows the expulsion of flux to the sides of the sample. The behaviour of the flux expulsion reflects the amount of trapped flux depicted in Figure 4.4: At very small transition times below one second the flux expulsion seems to be almost independent of the temperature gradient and above 6-7 s there seems to be no further significant change in expelled flux. In y-direction the wave magnitude increases in the range from 0-1 s and decreases for longer transition times. In z-direction the wave magnitude increases again in the range of 0-1 s and stays constant in the case of the large temperature gradient of $0.1 \frac{\mathrm{K}}{\mathrm{cm}}$. For the smaller temperature gradients it still increases but less steep then in the region of 0-1 s. Together with the trapped flux data this hints at slow moving flux lines inside the superconductor and a time constant of ≈ 1 s.

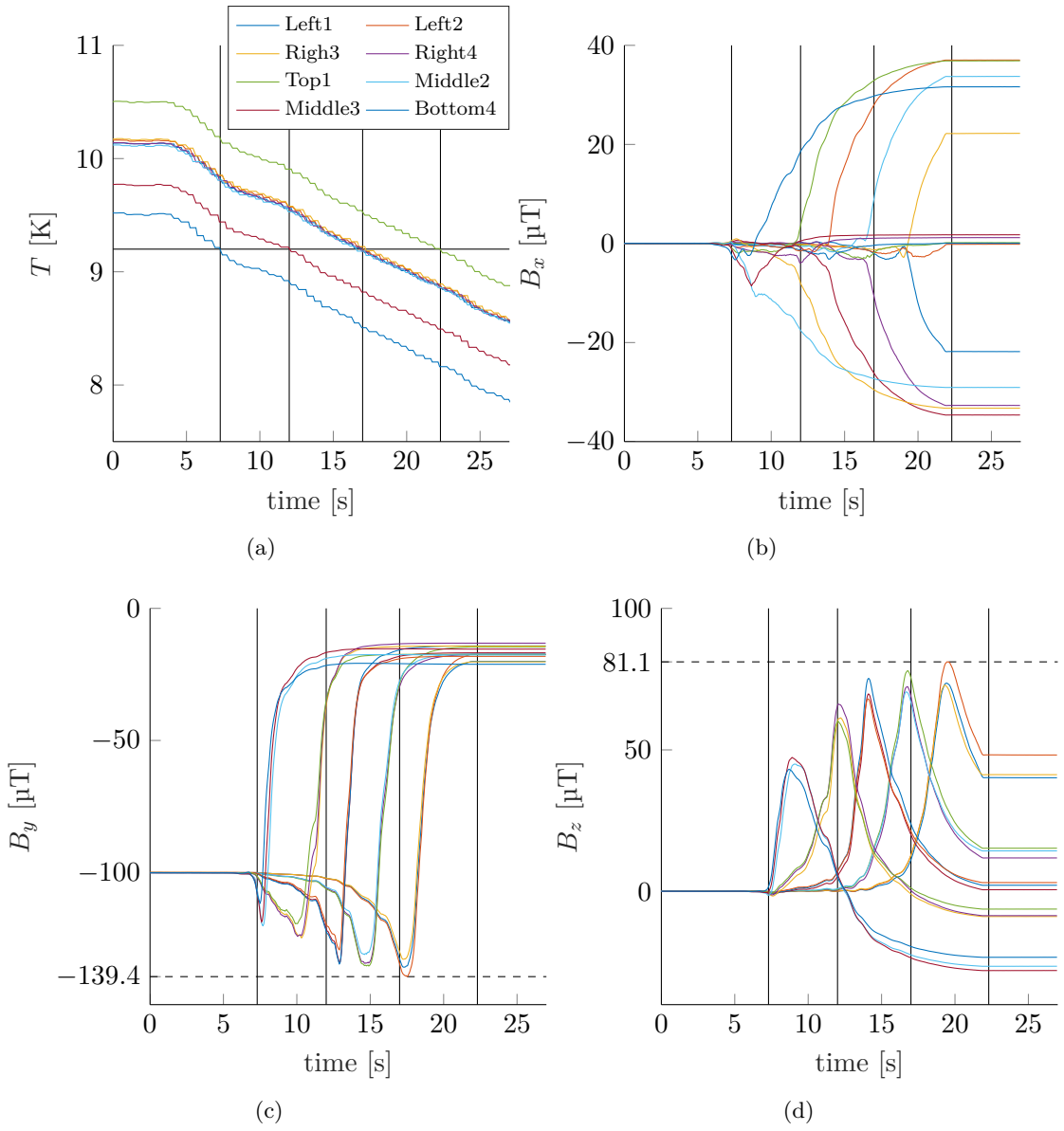

Figure 4.5.: Raw data of temperature (a) and AMR (b)-(d) sensors during a cooldown. The temperature sensors are glued in a cross shape. The sensors are distributed in the expected way, where the top sensor (green) is warmest and the temperature decreases with lower sensor positions with the bottom sensors (blue) the coolest. At the second position five sensors lay on top of each other since they are glued in a horizontal line on the sample. The black horizontal line indicates the transition temperature of niobium (9.2 K). The vertical black lines indicate the times when a sensor crosses the transition temperature. The position of the vertical lines are identical in all four plots. (b)-(d) show the raw data recorded with the AMR sensors in x-direction (b), y-direction (c), and z-direction (d). For better readability the legend for the 15 AMR sensors per plot are omitted. However, the five sensor rows are clearly visible in the peaks: The lowest peaking first and the top one last. The dashed line indicates the wave magnitude.

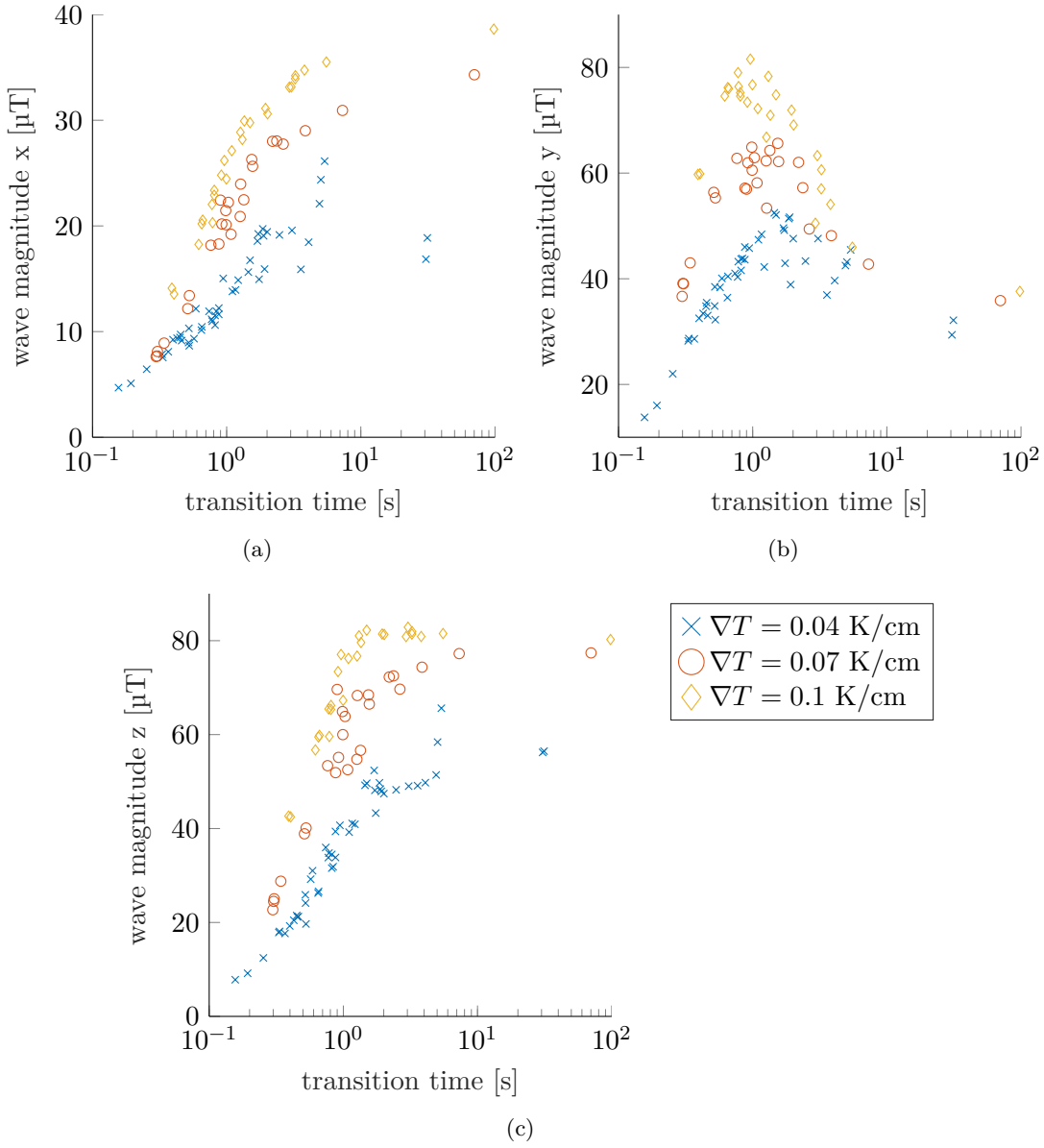

Figure 4.6.: Wave magnitude in each direction versus transition time for different temperature gradients. The legend is identical for all plots. In y- and z-direction a time constant of $\approx 1 - 2\,\mathrm{s}$ is evident.

4.4. Geometry

Even though the sample shape is chosen to make the geometry as simple as possible the geometry still affects the distribution of trapped flux. In the previous section 4.3 it is shown how the expelled flux builds up before the phase front. Therefore, the external field at the sample position is enhanced when the phase front reaches the top of the sample. As can be seen in section 4.2 this leads to increased trapped flux. Figure 4.7 shows two cases of trapped flux in the large grain sample.

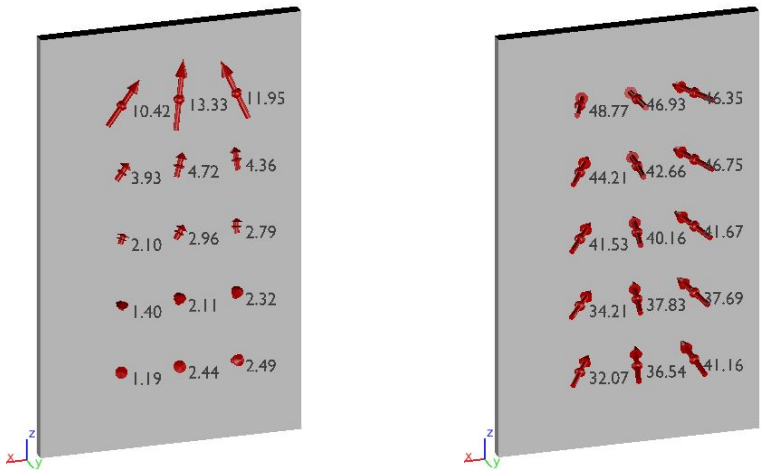

(a) (b)

Figure 4.7.: Two different cases of trapped flux in the large grain sample. In case (a) the transition time is 100 s and in case (b) 0.8 s. The arrow size is scaled for each representation separately. To compare the results, the magnitude in µT depicted next to the arrows must be considered. Due to the short transition time in (b) magnetic flux is increased towards the top which is reflected in the trapped flux.

In case (a) in Figure 4.7 the magnetic flux has sufficient time to exit the superconductor and it is pushed out of all the sample except the top edge where still increased trapped flux is measured. In case (b) with a short transition time, a wave of 79 µT in y-direction builds up ahead of the phase front, and a continuous increase of trapped flux is detected towards the top.

Figure 4.7 (b) also shows how the finite shape of the sample still has an impact on the distribution of trapped flux because the wave can build up in the sample. In a smaller sample this would not be the case. Another way to illustrate the effect of the finite geometry is to plot the averaged trapped flux magnitude in one row versus the row number. As an example, data from the measurement with the large grain sample is depicted in Figure 4.8. For these cooldowns the external magnetic flux density is always set to $\vec{B}_e = (0, -100, 0)\,\mu\mathrm{T}$ and the temperature gradient was varied in a range from $\nabla T = 0.01\,\frac{\mathrm{K}}{\mathrm{cm}}$ to $\nabla T = 0.12\,\frac{\mathrm{K}}{\mathrm{cm}}$.

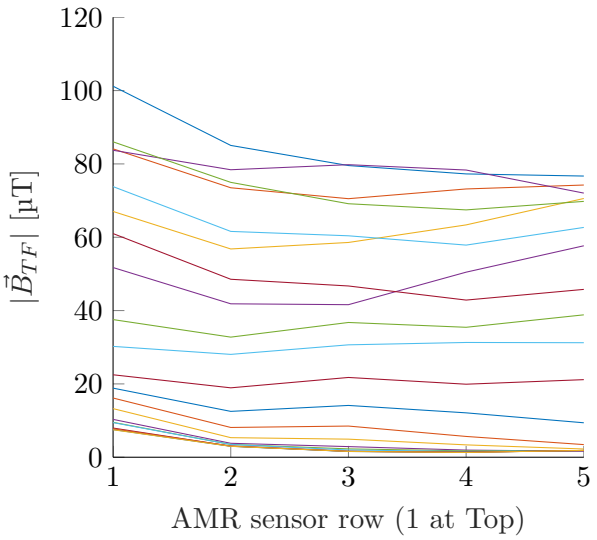

Figure 4.8.: Averaged trapped flux magnitude in AMR sensor rows 1 to 5 for cooldowns with different temperature gradients. Sensor row 1 is at the top, and row 5 at the bottom. For almost all cooldown more flux is trapped at the top of the sample.

In Figure 4.8 the cooldown with the highest temperature gradient is at the bottom, with the least amount of trapped flux. The cooldown with the lowest temperature gradient and, therefore, most trapped flux is at the top. Independent of the temperature gradient, the cooldowns show a higher magnitude of trapped flux towards the top of the sample in most cases. For the cooldown with the lowest temperature gradient, the magnitude even rises above the applied 100 µT in row 1. The expelled flux from below the phase front increases the external field above it, which results in more trapped flux in the higher sensor rows.

In addition a large increase in the top row in Figure 4.7 (a) is evident which can also be seen in Figure 4.8. This might be an artefact of the setup itself rather then the sample. As this chapter is only intended to give a brief overview of the observed results, this phenomenon will be further examined in section 4.8.4.

4.5. Materials

So far, the effects of different cooldown parameters are investigated for only one sample (large grain). Now the different samples are introduced in more detail and how the material affects the amount of trapped flux in dependence of the parameters discussed so far is described.

4.5.1. Single Grain

The first investigated sample consists of only one single grain. Figure 4.9 shows the sheet the sample is cut from with a water jet.

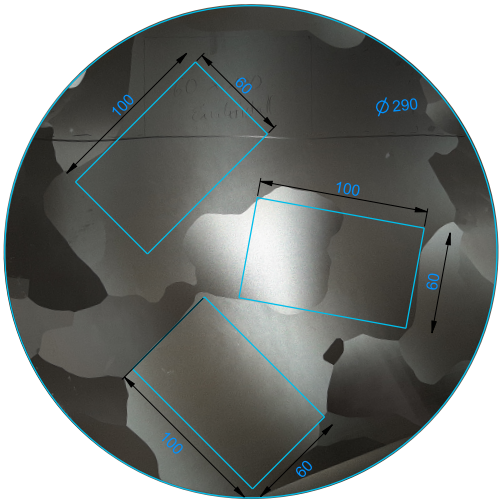

Figure 4.9.: Full sheet of large grain material with three samples marked to be cut out. The grain boundaries are easily distinguishable due to the different reflectivity of the grains.

The sheet depicted in Figure 4.9 is a large grain sheet of cavity grade material. The grain boundaries are easily distinguishable due to the different reflectivity of the grains. The purity is typically measured by the residual-resistivity-ratio (RRR) [19]. For cavity production a RRR of 300 is commonly used which is the nominal RRR of this sheet, as communicated by the manufacturer, Heraeus. The sheet was sawn off a large multiply recrystallized ingot and not treated afterwards. The top crystal layers are, therefore, most likely damaged and not in a perfect crystalline orientation [86]. As was already mentioned in the beginning of this chapter this might have an effect on the flux trapping behaviour, however, the sample is first tested in this completely untreated state as a baseline measurement, so effects of different treatments can be investigated systematically. Figure 4.9 shows the outline of three samples that are cut out from the sheet. Two of them consist of only one crystal (top and bottom) and one consists of two crystals with the grain boundary running through the middle of the sample (right). The data of the latter is already discussed in the previous sections 4.1 to 4.4. Now, the flux trapping behaviour of the top single grain sample is discussed first, and then a short comparison with the bottom sample is presented. As the samples are orientated in a 90° angle the crystal orientation within the sample should differ between the samples. Due to the damaged layer this could not be confirmed experimentally.

Temperature Gradient

Figure 4.10 shows how much trapped flux is measured by sensor group 8 using the single grain sample. As reference the data of the large grain sample is also depicted.

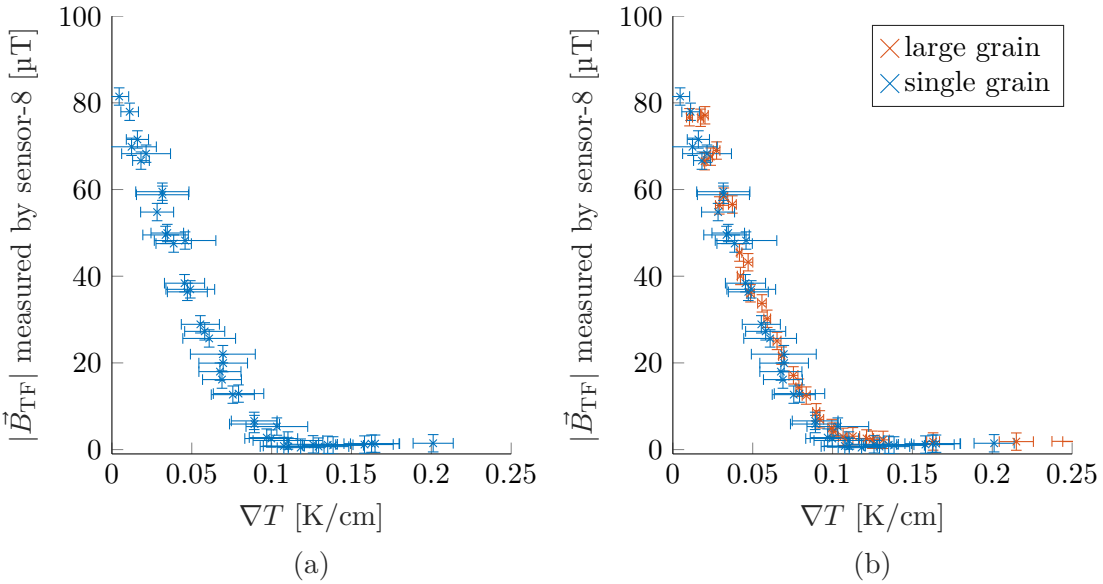

Figure 4.10.: Trapped flux measured by the central sensor group 8 versus local temperature gradient during cooldown. (a) data of only the single grain sample. (b) data of single grain sample, and additionally data of large grain sample for comparison. No significant difference between large- and single grain sample is measurable.

The single grain sample shows a very similar behaviour compared to the large grain sample. The maximal trapped flux measured is around 80 µT. And the amount of trapped flux decrease to ≈0 µT at a temperature gradient of 0.1 $\frac{\mathrm{K}}{\mathrm{cm}}$. Figure 4.10 (b) where the data of both samples are plotted, emphasises the similarity between the two samples.

External Magnetic Field Strength

Figure 4.11 shows the trapped flux magnitude versus the y-component of the external magnetic flux density. The fields direction is again perpendicular to the largest sample surface, like in section 4.2.

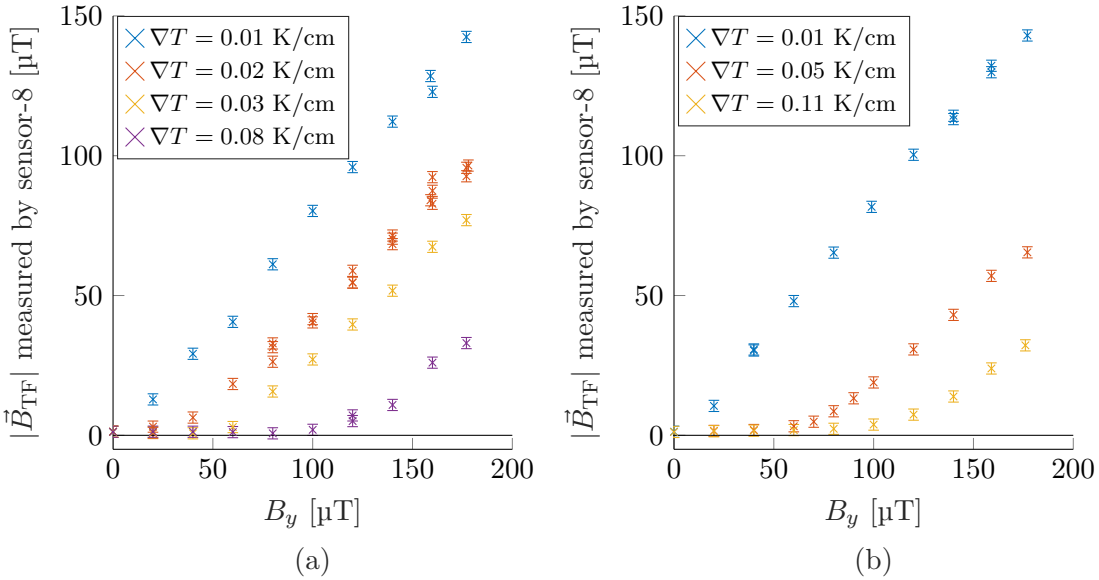

Figure 4.11.: Trapped flux measured by the central sensor group 8 versus the component of the external flux density perpendicular to the surface, B_y. (a) data of the single grain sample. (b) data of large grain sample for comparison. A similar behaviour is measured in both samples.

As is the case for the temperature gradient dependent data, the sample shows very similar behaviour to the large grain sample. This is especially evident for the case of $\nabla T = 0.01\,\frac{\mathrm{K}}{\mathrm{cm}}$: An increase from $|\vec{B}_e| \approx 0\,\mu\mathrm{T}$ is detected and a maximal trapped flux magnitude of 142 µT for the single grain is detected in comparison to 143 µT for the large grain sample. For $\nabla T = 0.08\,\frac{\mathrm{K}}{\mathrm{cm}}$ (single grain) or $\nabla T = 0.1\,\frac{\mathrm{K}}{\mathrm{cm}}$ (large grain) an increase of trapped flux is detected at 100 µT and a maximal trapped flux magnitude of 33 µT for the single grain sample and 32 µT for the large grain sample is measured. The data agrees well, however, the series were recorded at different temperature gradients. The reason for this discrepancy is most likely causes by in inhomogeneous temperature gradient across the sample. This issue is discussed in further detail in section 4.8.2. The data of $\nabla T = 0.02\,\frac{\mathrm{K}}{\mathrm{cm}}$ and $\nabla T = 0.03\,\frac{\mathrm{K}}{\mathrm{cm}}$, seem to fit in with the recorded data with $\nabla T = 0.05\,\frac{\mathrm{K}}{\mathrm{cm}}$ of the large grain sample.

Cooldown Rate

Lastly the effect of cooldown rate on the single grain sample is investigated: Figure 4.12 shows the magnitude of trapped flux measured by sensor group 8 versus the cooldown rate for different temperature gradients during cooldown. For comparison the data gathered from the large grain sample is also depicted.

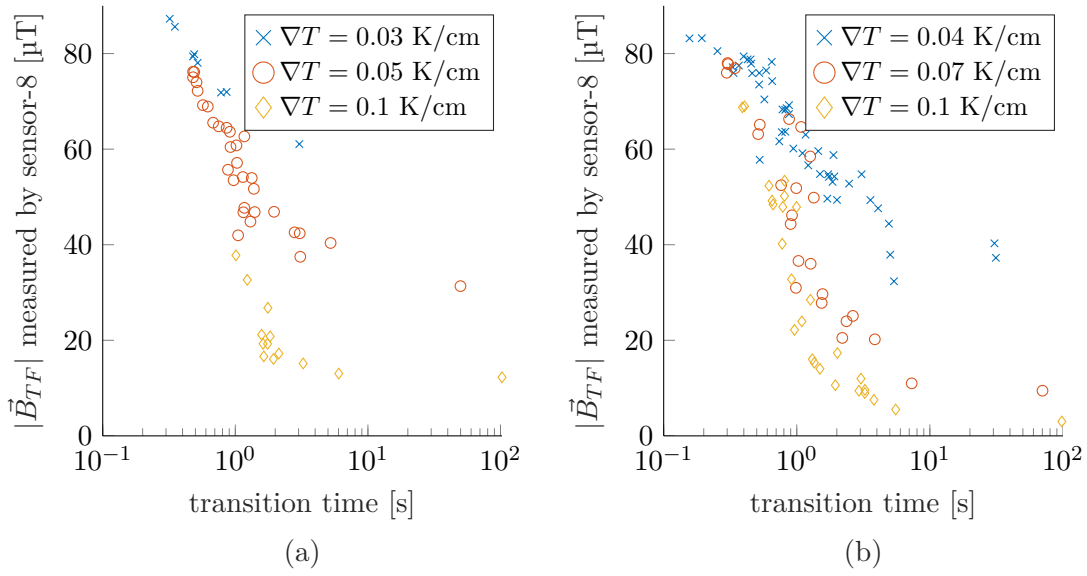

Figure 4.12.: Trapped flux measured by the central sensor group 8 versus transition time. (a) data of the single grain sample. (b) data of large grain sample for comparison. Note the logarithmic x-scale in both plots. The time constant of ≈1 s is evident in both plots.

As for the large grain sample a sharp increase of trapped flux is evident for transition times shorter than 1-2 s. The minimal trapped flux that is reached is only 13 µT instead of only 3 µT in case of the large grain sample. This probably stems again from an inconsistent temperature gradient between the two measurement runs because Figure 4.11 predicts smaller values of trapped flux at this temperature gradient. Section 4.8 illuminates this problem.

Crystal Orientation

To investigate whether the crystal orientation within the sample has an effect on flux trapping, two samples were cut out of the large sheet depicted in Figure 4.9 (a). As can be seen, the two samples are cut our from the same grain but are rotated 90° to each other. This should ensure a different crystal orientation within the sample, however, due to the damaged layer or non-perfect crystallisation this could not be verified by X-ray diffraction (XRD).

Figure 4.13 shows the magnitude of trapped flux versus temperature gradient for both single grain samples.

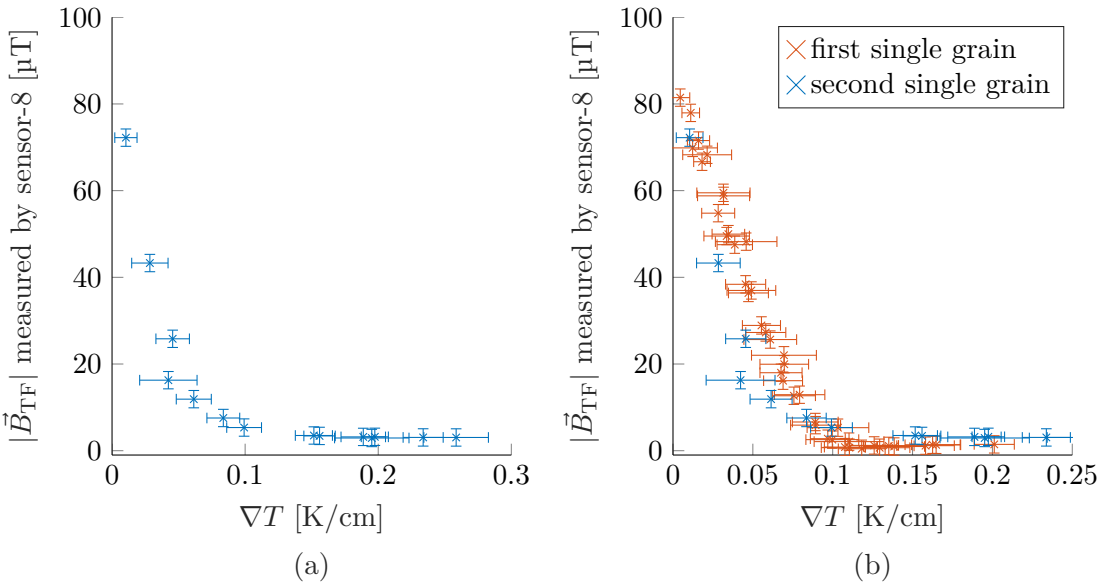

Figure 4.13.: Trapped flux measured by the central sensor group 8 versus local temperature gradient during cooldown. (a) data of only the second single grain sample. (b) data of first and second single grain for comparison. No significant difference due to the crystal orientation is measured.

The experiment conducted with this sample was one of the first with the new setup which is why the number of points are lower than for later experiments. However, as can be seen in Figure 4.13 (b), there is no significant difference between the two samples.

4.5.2. Fine Grain

Apart from the large grain sheet another niobium sheet that was rejected for cavity fabrication is cut into samples and the flux trapping behaviour is investigated. This sheet consists of fine grain material with a grain size in the order of (100) µm. The small grain size makes the material more homogeneous and easier to machine and manipulate than the large grain material [88]. Therefore, cavities are in most cases manufactured from fine grain material. But the small grain size also means that there are more grain boundaries in the material and also possibly more imperfections [89, 90]. This might have in influence on the flux trapping behaviour. The material has a RRR of 300 like the large grain sheet. It was rejected for cavity fabrication because of a defect that was detected with eddy current measurements [91]. The defect was marked, so that the samples can be cut in a way to either omit the defect or include it in a sample to investigate whether it has an effect on trapped flux. Figure 4.14 (a) shows the fine grain sheet with the defect marked in red and the outlines of the samples that are cut from the sheet. As can be seen in Figure 4.14 (a), one sample includes the defect. Similar to the large grain material this sheet is also untreated and the samples are cut out with a water jet. Therefore, a damage layer is present as well.

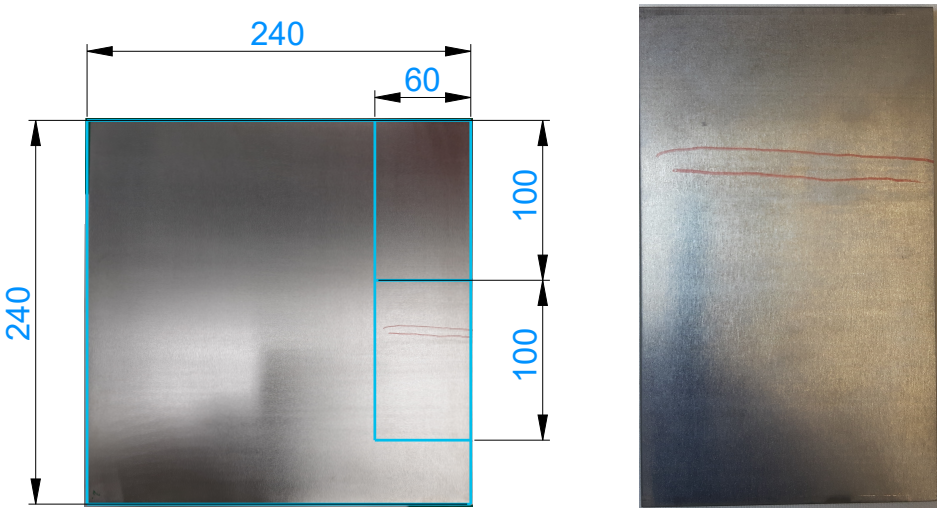

(a) (b)

Figure 4.14.: (a) full sheet of fine grain material with two samples marked to be cut out. The bottom one includes a defect marked in red. (b) resulting fine grain sample including the defect.

First, results from the sample without defect are presented and then compared to results from the sample with defect. Similar to the single crystal sample the different parameters are presented one by one.

Temperature Gradient

Figure 4.15 depicts the magnitude of trapped flux measured with the fine grain sample without defect.

Figure 4.15 (a) shows that the fine grain sample traps most of the applied flux at low temperature gradients and expels increasingly more with higher temperature gradients just like the samples before. However, the minimal trapped flux magnitude reached, is 52 µT, and a decrease in trapped flux is clearly discernible up to a temperature gradient of 0.27 $\frac{\mathrm{K}}{\mathrm{cm}}$. It is already mentioned in section 3.2.4 that in addition to the temperature gradients that can be achieved by heating up the copper blocks with heaters and reducing their temperature simultaneously, the filling procedure creates cooldowns with large temperature gradients. The data point with $\nabla T = 0.51\,\frac{\mathrm{K}}{\mathrm{cm}}$ is an example of such a cooldown. It is, therefore, systematically different than the cooldowns created with the heaters. However, due to temperature monitoring with Cernox sensors the temperature gradient can be extracted and it is reasonable to add the data point in the graph. The error bar of this point is larger than of the others, indicating a non homogeneous temperature gradient during cooldown which must also be taken into account when analysing the data. But the data point shows a higher magnitude of trapped then would be expected by extrapolating the first data points.

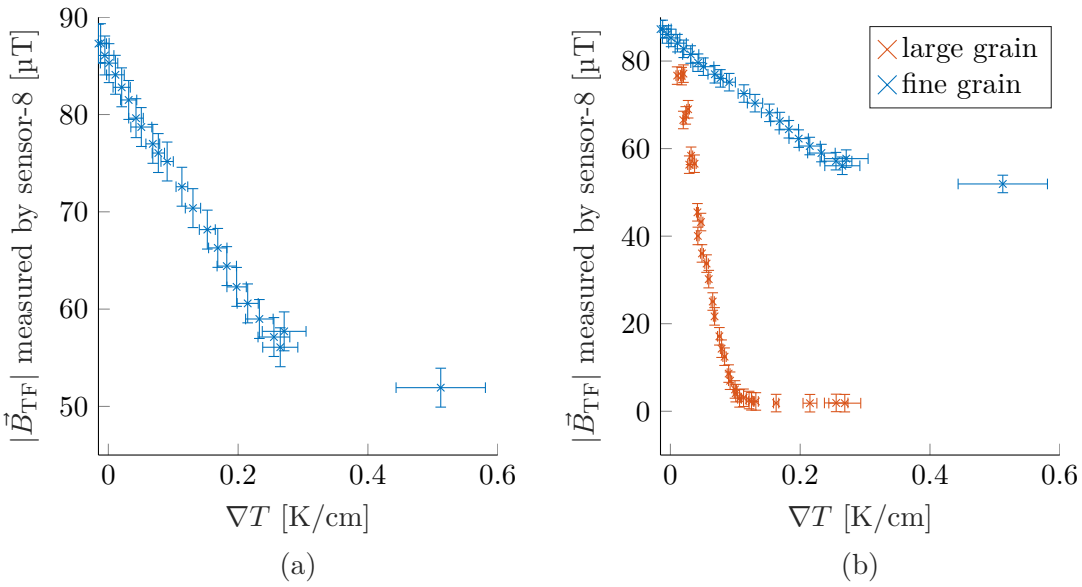

Figure 4.15.: Trapped flux measured by the central sensor group 8 versus local temperature gradient during cooldown. (a) data of only the fine grain sample. (b) data of fine grain sample as well as the large grain sample for comparison. The fine grain sample shows higher values of trapped flux. Full expulsion is not achieved.

Comparing the fine grain data with the data gathered from the large grain sample (Figure 4.15 (b)) yields that at temperature gradients close to zero, the fine grain sample traps more flux than the large grain. At $\nabla T = 0.02\,\frac{\mathrm{K}}{\mathrm{cm}}$ sensor group 8 measures $(83 \pm 2)\,\mu\mathrm{T}$ for the fine grain and only $(76 \pm 2)\,\mu\mathrm{T}$ for the large grain. It is also noticeable that the decrease in trapped flux per temperature gradient is smaller for the fine grain compared to the large grain material and no complete flux expulsion can be achieved.

External Magnetic Field Strength

Next, the flux trapping behaviour of the fine grain sample as a function of applied field magnitude is investigated. Figure 4.16 shows trapped flux measured by sensor group 8 in dependence of B_y (component of the external flux density perpendicular to the surface). Since the field is applied perpendicular to the sample surface $|B_y| = |\vec{B}_{\mathrm{e}}|$. Three different temperature gradients are chosen to display the effect of temperature gradient on the $\vec{B}_{\mathrm{TF}}$ vs. B_y curve.

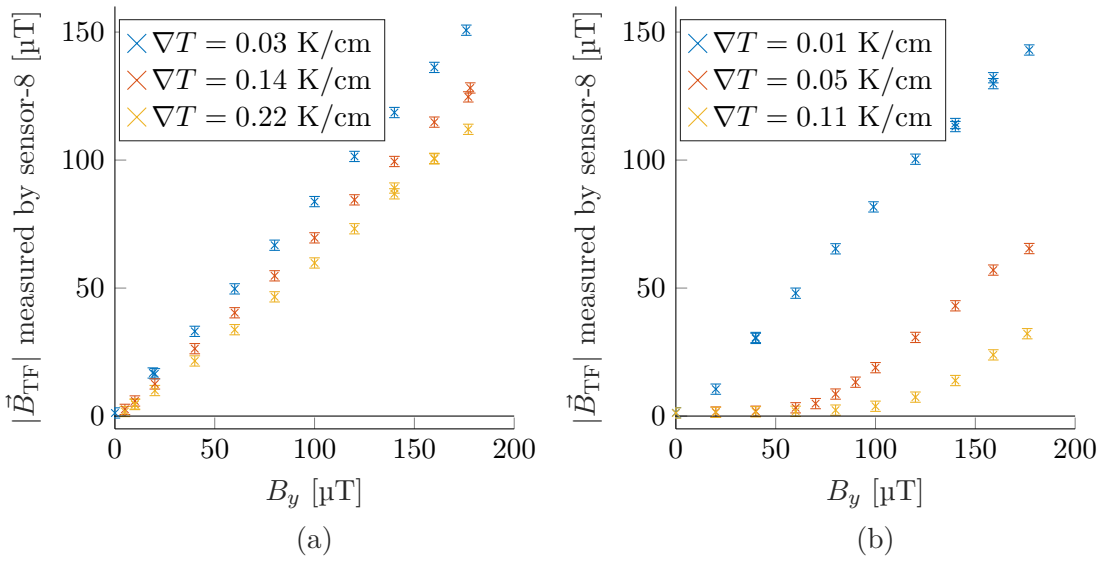

Figure 4.16.: Trapped flux measured by the central sensor group 8 versus the component of the external flux density perpendicular to the surface, B_y. (a) data of the fine grain sample. (b) data of large grain sample for comparison. No threshold field is measured for the fine grain sample.

For small temperature gradients the fine grain sample (Figure 4.16 (a)) behaves very similar to the large grain sample (Figure 4.16 (b)): A linear increase in trapped flux is measured with a x-axis crossing at 0 µT. The fine grain sample does trap slightly more of the applied field, so that at $B_y = 177$ µT sensor group 8 measures 151 µT for the fine grain and 143 µT for the large grain, while the temperature gradient is actually higher for the fine grain ($\nabla T = 0.03 \frac{\mathrm{K}}{\mathrm{cm}}$) than for the large grain ($\nabla T = 0.01 \frac{\mathrm{K}}{\mathrm{cm}}$). This is in line with the observations that stem from the temperature gradient dependent analysis above.

Most noticeable is, however, the discrepancy between the two samples at higher temperature gradients. While there is a linear dependency between trapped flux and external magnetic flux density, the slopes and most importantly offsets of the lines differ from lines of the large grain sample. With $\nabla T = 0.22 \frac{\mathrm{K}}{\mathrm{cm}}$, the magnitude of measured trapped flux at $B_y = 177$ µT is a factor 3.5 higher than what is measured for the large grain sample with $\nabla T = 0.11 \frac{\mathrm{K}}{\mathrm{cm}}$. And there is no threshold field detectable in the data of Figure 4.16 (a). This means that there is always a fraction of the applied field that gets trapped. This fraction decreases with increasing temperature gradient, as can be seen at the decreasing slopes in Figure 4.16 (a), but it never vanishes (at least in the regime that can be explored with this setup).

Cooldown Rate

To investigate how flux trapping is affected by cooldown rate, the same procedure as before is performed where the external magnetic field is kept constant at $\vec{B}_e = (0, -100, 0)$ µT and the cooldown rate is varied in several series of different temperature

gradients. Figure 4.17 shows the results for the fine grain sample as well as the large grain sample for comparison.

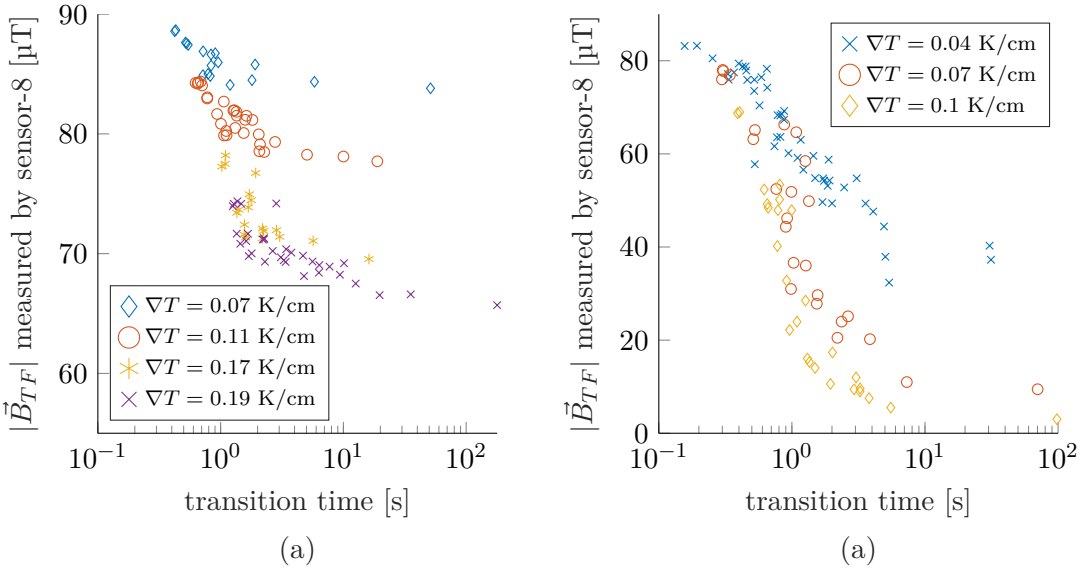

Figure 4.17.: Trapped flux measured by the central sensor group 8 versus transition time. (a) data of the fine grain sample. (b) data of large grain sample for comparison. Note the logarithmic x-axis and the differently scaled y-axes. The time constant of ≈1 s is evident in both plots.

As can be expected from the results so far, the fine grain material (Figure 4.17 (a)) trapped more flux even at higher temperature gradients than the large grain material (Figure 4.17 (b)). Nevertheless, similarities between the two samples are evident: At very short transition times the trapped flux magnitude is the largest with a sharp decrease up to 1-2 s. Longer transition times then lead to a less steep decline in trapped flux up to ≈ 10 s. Even longer transition times do not seem to change the amount of trapped flux.

The measurements above where partly conducted with high temperature gradients because they lead to more flux expulsion and larger measurable effects. The downside of these large temperature gradients is that with the finite cooldown rate achievable with the setup very short transition times cannot be reached. So the sharp increase of trapped flux below ≈ 2 s cannot be measured at the high temperature gradients.

Defect

Lastly, it is examined whether the defect in the second sample described at the beginning of this chapter has an effect on flux trapping. In order to do so, the three kinds of measurements conducted so far for every sample are repeated for the second fine grain sample containing the defect (see Figure 4.14 (b)). Since no new information is gained from the measurements of trapped flux versus external magnetic field strength and cooldown rate, the data is not shown here but can be found in appendix A.2.1.

Figure 4.18 shows trapped flux magnitude in the fine grain sample with defect. Due to a bad thermal contact of one Cernox sensor, the local temperature gradient at the position of sensor group 8 cannot be determined. Instead, the mean temperature gradient across the sample during cooldown is used. The data is, therefore, systematically different from the data shown for the other samples. However, it can still serve as comparison between the sample with and without defect.

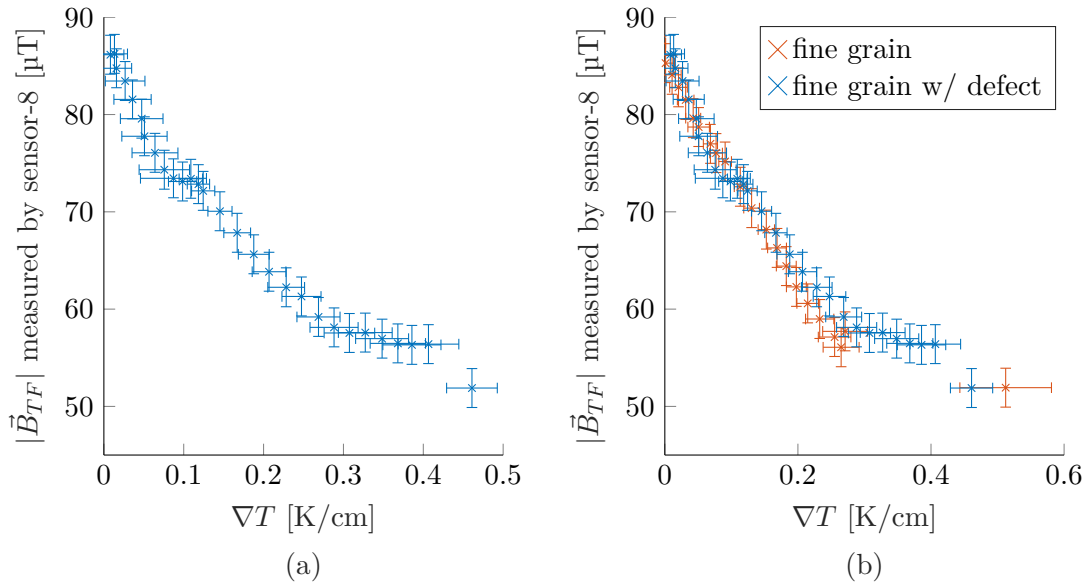

Figure 4.18.: Trapped flux measured by the central sensor group 8 versus mean temperature gradient during cooldown. (a) data of only the fine grain sample with defect. (b) data of fine grain sample with defect as well as the fine grain sample without defect for comparison. No significant effect of the defect is measured.

Two features are evident in Figure 4.18 (a): First, a plateau around $\nabla T = 0.1\,\frac{\mathrm{K}}{\mathrm{cm}}$ is evident. Second, a jump at $\nabla T = 0.4\,\frac{\mathrm{K}}{\mathrm{cm}}$ is visible. This stems most likely from the different cooldown conditions of the last point which is recorded during a helium refill. Since only the average temperature gradient can be evaluated the local temperature gradient might actually differ from the value estimated here.

A comparison between the two fine grain samples (with and without defect) shows no significant difference between the two, as shows Figure 4.18 (b).

4.5.3. Niobium coated on Copper

In addition to the bulk niobium samples investigated so far, a coated sample is tested to study how a niobium film traps magnetic flux. The substrate of the investigated sample is copper. A 4 µm thick niobium film is sputtered on the substrate by the group "Oberflächentechnik" from Universität Siegen. Pictures of the coated sample are depicted in Figure 4.19.

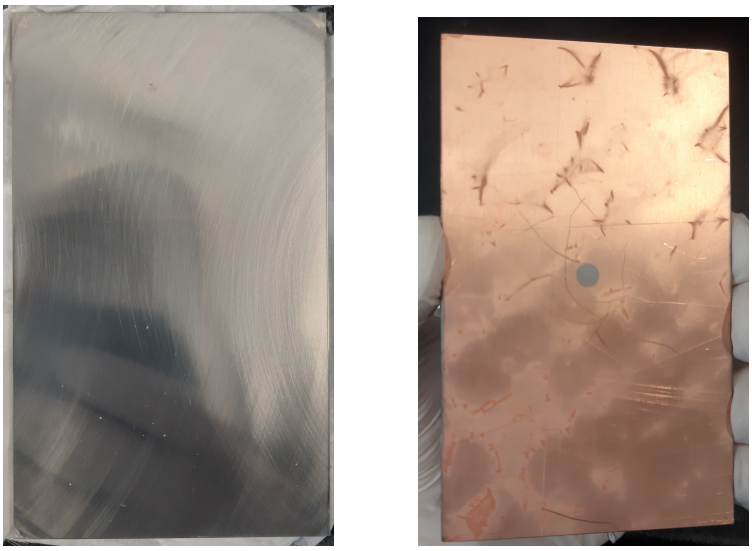

(a) (b)

Figure 4.19.: Pictures of coated niobium on copper substrate.(a) front (b) back.

The substrate preparation consisted of the following steps:

- Degrease 20 min. Ultrasonic bath: EC70 10% (pH13)
- Activation 20 min. Ultrasonic bath: EC75 10% (Ammonia)
- Grinding: 80/250/800/4000
- Cleaning 10+8 min. Ultrasonic bath: EC75 10% (Ammonia)
- Rinsing in Aqua Dest.
- Dry Blow (N2)

The coating itself consisted of

- Coating: Recipe 20220901, ID: 2131
- Cool down until <50°C
- Venting, dismantle sample, waiting for cool down (table)

Ideally the copper is chemically polished before coating [92]. But the sample did not fit in existing treatment baths, and due to time constraints no new treatment equipment could be manufactured. Therefore, the substrate's surface is still rough from polishing with 4000 grid sandpaper. The grooves can still be seen though the niobium in Figure 4.19 (a).

Figure 4.20 shows the magnitude of trapped flux in the coated sample versus the temperature gradient.

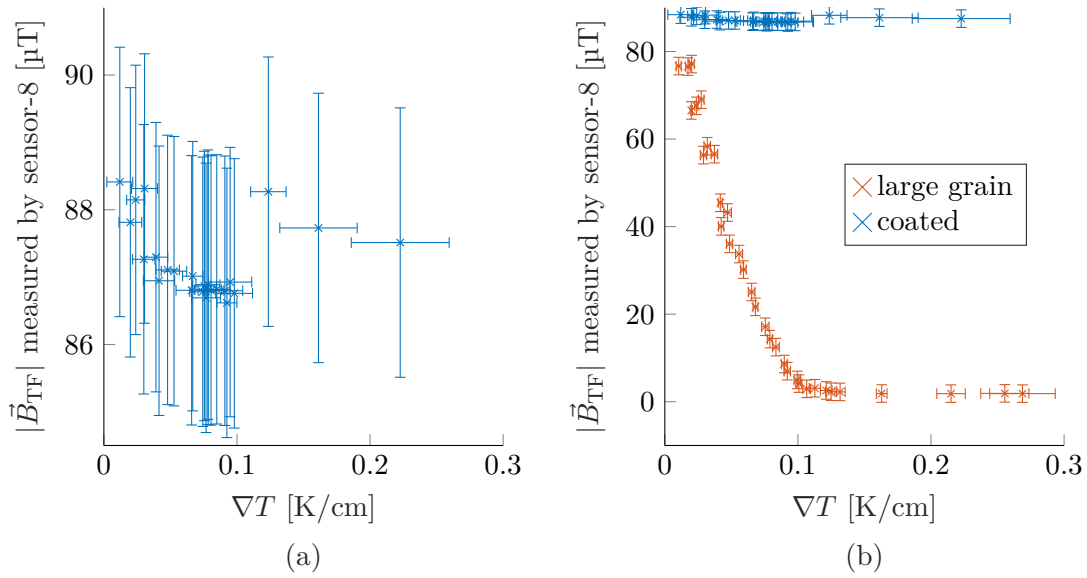

Figure 4.20.: Trapped flux measured by the central sensor group 8 versus temperature gradient during cooldown. (a) data of only the coated sample. (b) data of the coated sample as well as the large grain sample for comparison. The trapped flux in the coated sample is independent of the temperature gradient.

Figure 4.20 (a) shows that the magnitude of trapped flux is independent of the achieved temperature gradients, and that almost all flux gets trapped. As the thermal conductivity of copper is much higher than the thermal conductivity of niobium, the maximal achieved temperature gradient is smaller than the ones achieved for niobium samples. Figure 4.20 (b) illustrates the difference in trapping behaviour of the coated sample compared to the large grain sample. The poor flux expulsion efficiency is in contrast to measurements with niobium coated copper cavities that are used in the LHC. There, a low sensitivity of R_{res} on the external magnetic field is reported and the cryomodules are even designed without magnetic shielding [93, 94].

Since the sample traps all magnetic flux at the highest achievable temperature gradient, the data investigating different external magnetic flux densities and cooldowns speeds are not shown here, since no significant deviation is measurable.

4.6. Treatments

The bulk samples investigated so far are tested in an untreated state. These measurements give insight into different trapping behaviours and serve as a baseline. Cavities are, however, chemically etched and heat treated before they are installed in an accelerator. To measure how these treatments affect the trapping behaviour the treatments must be performed consecutively with measurements in-between every treatment step. In a first step, the effect of chemical etching of the fine grain sample is investigated but due to technical difficulties a heat treatment furnace could not be commissioned and no heat treatments could be performed. Other experiments investigate the effects of heat

treatment and a decrease in flux trapping at high bake out temperatures is reported in [87, 90].

4.6.1. Buffered Chemical Polishing

It is mentioned above that the samples have an outer damaged layer which might affect flux trapping. In a buffered chemical polishing (BCP) this outer layer is removed with hydrofluoric acid. For this test 91 µm are etched from either side of the fine grain sample without defect. Then the flux trapping is again measured. Figure 4.21 shows trapped flux versus temperature gradient for the etched sample.

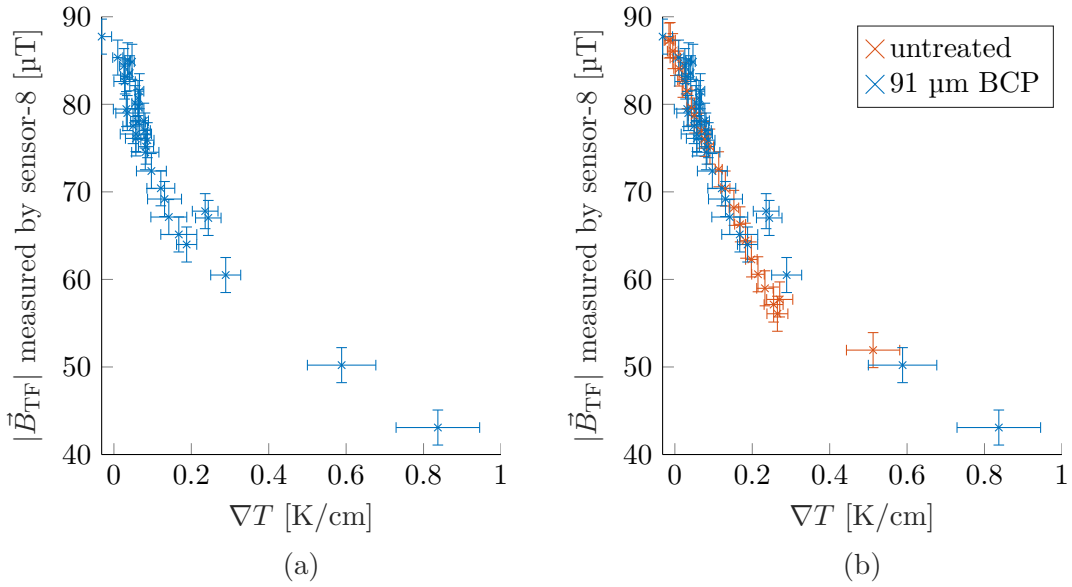

Figure 4.21.: Trapped flux measured by the central sensor group 8 versus temperature gradient during cooldown. (a) data of only the etched sample. (b) data of the sample in an etched and untreated state for comparison. No significant change after the BCP is measured.

Figure 4.21 (b) shows no significant difference between the etched and untreated state. Two points lay above the other points at $\nabla T \approx 0.24\,\frac{\mathrm{K}}{\mathrm{cm}}$ and $|\vec{B}_{\mathrm{TF}}| \approx 67\,\mu\mathrm{T}$. These were recorded with no active temperature control, but only with evaporating helium from the reservoir. These cooldowns occur when helium is evaporated to cool down the setup after a Cernox calibration where the gas temperature rises above 12 K. The cooldown dynamics are, therefore, different compared to a normal cooldown where the setup is surrounded by cold gas and only heated above T_c with electrical heaters.

Since there is no significant difference evident after the etching, measurements where the external magnetic field strength and cooldown rate are varied are not presented here, but can be found in appendix A.2.2.

4.7. Summary

At this point a short summary of the observed effects is given to recapitulate what is presented so far. Figure 4.22 shows trapped flux versus temperature gradient for all three investigated materials.

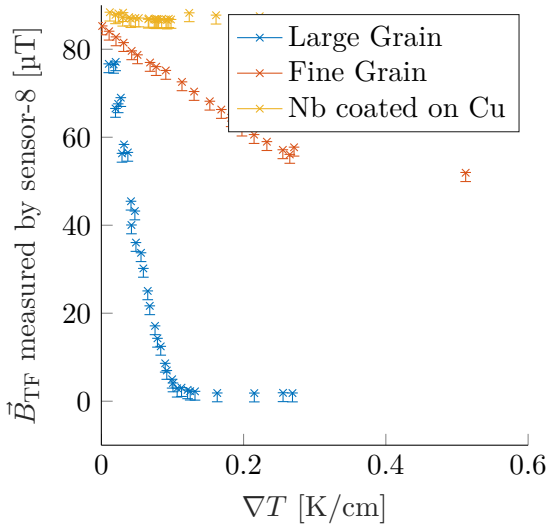

Figure 4.22.: Trapped flux versus temperature gradient of all three investigated materials. A clear difference between the samples is evident.

The measurements show that with increasing temperature gradient trapped flux is reduced and depending on the material the decrease of trapped flux with ∇T is more or less steep. For large- and single grain samples the decrease is steeper than for fine grain samples, and nearly full expulsion is achieved. For fine grain material full expulsion could not be achieved with the reachable temperature gradients. In case of the coated sample nearly full trapping is observed independent of the temperature gradient.

Furthermore, it is observed that at small temperature gradients trapped flux is proportional to the external magnetic flux density magnitude. For large- and single grain material at higher temperature gradients trapped flux is only measured when the external field is larger than a certain threshold field. This threshold field increases with increasing temperature gradient. Additionally, the increase of trapped flux with external flux density magnitude is less steep at higher temperature gradients. For fine grain material no threshold field can be directly measured but the increase of trapped flux with external flux density magnitude is less steep at higher temperature gradients, like for the large grain material.

Measurements with varying cooldown rates revealed that for very short transition times trapped flux becomes nearly independent of the temperature gradient and very high trapped flux magnitudes are measured. A sharp decrease of trapped flux is observed with increasing transition times up to $\approx 1 - 2\,\mathrm{s}$ which is then followed by a slower decrease until a steady state is reached at $\approx 10\,\mathrm{s}$. This behaviour is observed for large- and fine grain material, even though for fine grain samples the effect could not be

measured in such detail because due to necessary high gradients very short transition times can not be reached.

Geometry effects are also observed because flux expulsion in the already superconducting part of the sample leads to increased flux density above the phase front.

Effects due to crystal orientation in the single grain samples, as well as effects of the grain boundary in the large grain sample are not detected. Since there is only a single grain boundary in the large grain sample, effects might just not be measurable with the current setup. The same is true for the defect in the fine grain material.

An effect of the BCP on trapped flux is also not observed.

4.8. Error sources

This chapter so far describes how the different parameters influence trapped flux. Ideally the parameters are constant during a cooldown for the complete sample and only one parameter is changed in a measurement series. However, analysing the data in more detail reveals that for example the temperature gradient is not perfectly constant across the sample during a cooldown and is also hard to reproduce for cooldowns with different cooldown rates. To asses the quality of the gathered data errors stemming from such inconsistencies are analysed now.

In order to keep an overview over the parameters, the data displayed above is repeated in the same order, only now sources of errors are investigated for the featured results. This detailed analysis is done for the parameters of temperature gradient, external magnetic field strength, cooldown rate and geometry. Since the error sources are comparable for all investigated materials this analysis is not shown for all measured samples.

4.8.1. Temperature gradient

If possible, the local temperature gradient at the sensor position has been used for data analysis in chapter 4. To illustrate the difference between local and global temperature gradient the local gradient is plotted for two measurement series. The chosen example stems from the measurements of trapped flux versus temperature gradient with the large grain sample because the measurement series was repeated during the same measurement run. This makes it possible to compare the effect of utilizing the local temperature gradient. Figure 4.23 shows the local temperature gradient from the two measurement series. To calculate the local temperature gradient, the temperature difference between one Cernox sensor and the sensor above it is calculated when the sensor passes the transition temperature of 9.2 K. The temperature difference is then divided by the distance between the two sensors. For sensor 1 at the top edge the difference is calculated to the sensor below it. As was already mentioned, in this test only four Cernox sensors were glued in vertical direction to the sample.

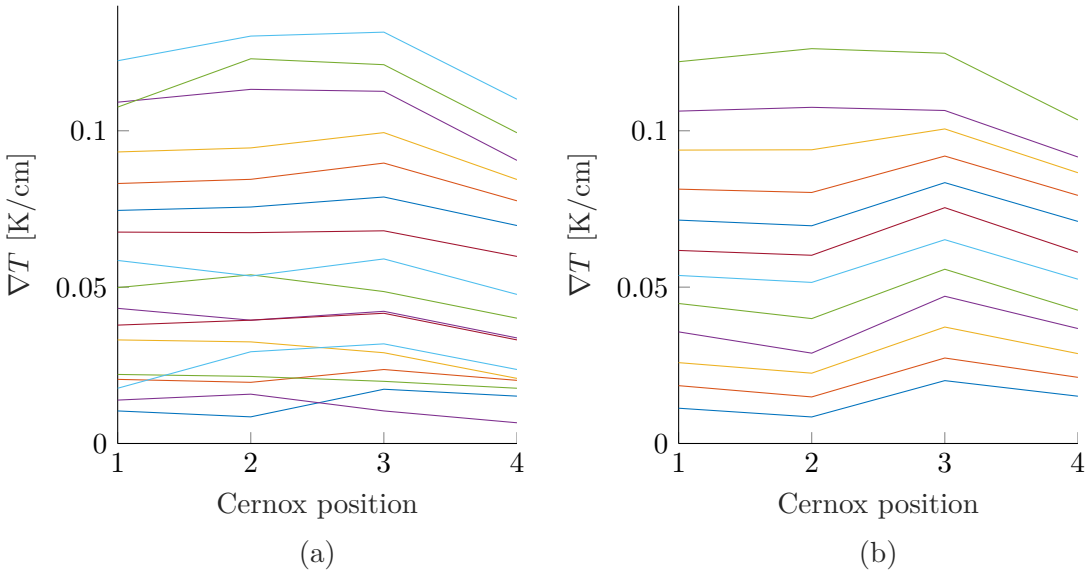

Figure 4.23.: Local temperature gradient at Cernox positions. Cernox 1 is at the top of the sample, 4 at the bottom. The temperature gradient is calculated with respect to the Cernox sensor above. Except for Cernox 1 for which it is calculated with respect to the one below. (a) shows data gathered from the first measurement series, (b) from the second. Each line represents a different cooldown. The plots show a systemic difference between the two series.

Between the two measurement series in Figure 4.23 (a) and (b) is a systematic difference of the temperature distribution. Figure 4.23 (b) shows a clear pattern for all cooldowns which is shifted depending on the desired temperature gradient. The only exception are the top two cooldowns. This pattern is not so prominent in the first measurement series, where the temperature distribution in general seems to be more even.

The different temperature distributions between the two series most likely stem from varying ambient parameters like gas flow and temperature: During measurements it was observed that a too high helium flow rate cools down the middle of the sample to much, so that the middle is colder than the heated ends of the sample, which is why the sample is now packed in cotton wool in order to reduce cooling of the sample itself. A varying gas flow also makes temperature control more difficult and the PID controllers of the heaters react differently which might influence the temperature distribution and, therefore, the local gradient.

The variations in Figure 4.23 show that it is vital to have more than just two temperature sensors on the sample to measure the temperature gradient, and that the local temperature gradient should be used to analyse the data.

Figure 4.24 shows results of the two measurement series. For plot (a) the local temperature gradient is used, in (b) the global temperature gradient is used. The global temperature gradient is calculated by averaging all local gradients.

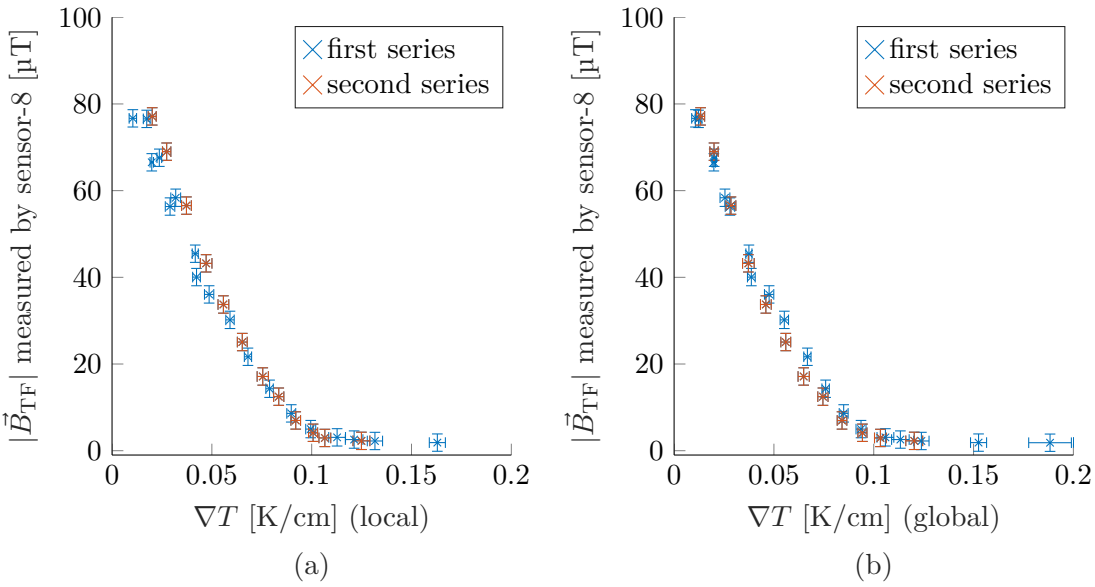

Figure 4.24.: Trapped flux magnitude measured by sensor group 8 versus local- (a) and global- (b) temperature gradient. The difference between the plots is small.

In the range of $\nabla T \approx 0.04{-}0.1\,\frac{\mathrm{K}}{\mathrm{cm}}$ both series agree better when the local temperature gradient is used. In the range of $\nabla T < 0.04\,\frac{\mathrm{K}}{\mathrm{cm}}$ the data points agree better when the global temperature gradient is used. Over all, the difference between the two plots in Figure 4.24 is not large. The mean difference in temperature gradient of all points between (a) and (b) is $0.008\,\frac{\mathrm{K}}{\mathrm{cm}}$. This shows that the local temperature gradient should be used if possible but if a sensor is badly connected and the local temperature gradient cannot be used, the global temperature gradient can be used as surrogate.

The issue of badly connected sensors brings up the next source of error: It is impossible to know the exact temperature of the sample. This is because the sensor only give information about their own temperature, and while the sensors are glued to the sample with their thermally conductive plate the sensors are still cooled from the other sides with cold helium gas. Depending on the thermal contact of the sensor to the sample this cooling becomes more or less dominant. An example of a bad thermal contact is depicted in Figure 4.25.

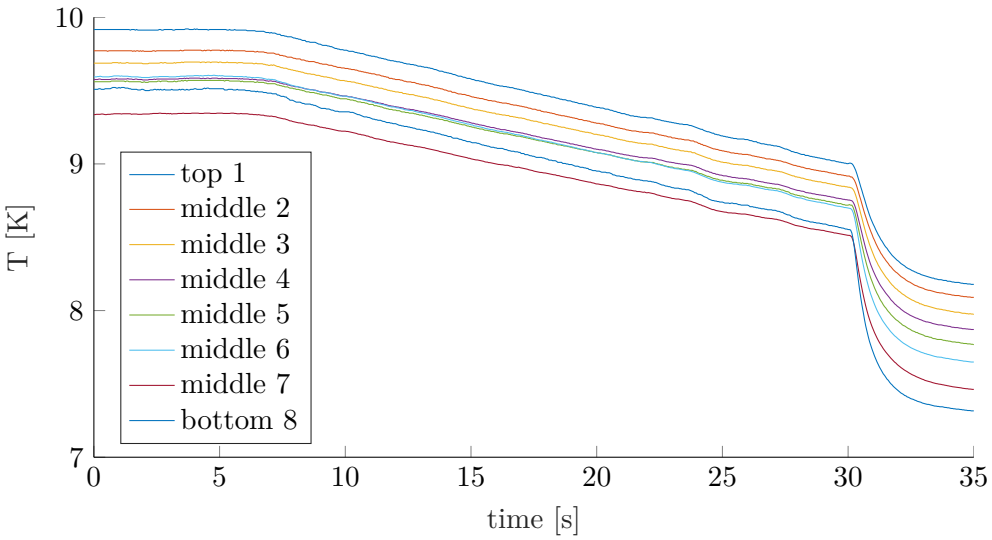

Figure 4.25.: Measured temperature during a cooldown. Sensor 7 has a bad thermal contact.

As can be seen in Figure 4.25 sensor 7 is colder than sensor 8 below it while the sample is still being heated with the heaters. Once the heaters are turned off at $t = 30\,\mathrm{s}$ the temperature rises above the temperature measured by sensor 8. This behaviour is an indication for a bad contact because the sensor shows the expected temperature only when the sample is not heated and adjusts its temperature to the ambience. At this point the cooling from the outside gas is not significant any more as the sample is nearly at the same temperature.

That sensor 7 measures a too low temperature can also be deduced from magnetic field data because the expulsion of flux at 9.2 K is visible for field sensors. Since no change in magnetic field is detected up to the point when sensor 8 passes 9.2 K, sensor 7 does not show the real temperature, but one too low.

Figure 4.25 also shows that the temperature of sensor 6 seems to high because it shows temperatures nearly as warm as sensor 5. All other sensors are equidistant but as was already mentioned above, it is only possible to measure the sensor temperature and not the sample temperature directly. The temperature measurements are, therefore, always subject to errors. The absolute temperature of the sample is, however, not critical as only the temperature gradient is used for analysis. To estimate the error of the temperature gradient, the local gradient is calculated for every sensor. From these values the mean temperature gradient and error of a single measurement are calculated. These resulting errors are depicted in all plots concerning temperature gradient.

In the case of a bad connection like in Figure 4.25, the sensor is excluded from the analysis.

Apart from the measurement of temperature gradient, magnetic field measurements are done for the analysis of the dependence of trapped flux on temperature gradient. The different sources of errors in the magnetic field data are already described in section 3.2.3 and stem mostly from inhomogeneities in the ambient magnetic field and

errors in the AMR calibration. In section 3.2.3 a systematic error of 2 µT is established, and used in the corresponding plots.

4.8.2. External magnetic field strength

The most obvious source of error would be the external magnetic flux density magnitude. It is, however, adjusted to a precision of 25 nT using the Fluxgate sensors and is, therefore, negligible. The inhomogeneities in the ambient field lead to locally increased field but this is already included in the 2 µT error of the AMR data.

A much larger error stems again from the temperature gradient: For one measurement series the same temperature gradient must be used for all cooldowns. But this is not possible due to changing ambient conditions and the PID controllers which always react slightly different. It is, therefore, necessary to set a boundary which deviation in gradient from the desired gradient is acceptable. This boundary has to be chosen tight enough that the results are not to heavily influenced by the variations in temperature gradient but also wide enough to not exclude nearly all data points.

To illustrate this problem Figure 4.26, and 4.27 show data points of the measurement series of trapped flux versus flux density magnitude with the large grain sample with different boundaries. In Figure 4.26 the boundary for acceptable points is set at $\nabla T = 0.0032 \frac{\mathrm{K}}{\mathrm{cm}}$. To determine if a point is accepted, the global temperature gradient of a cooldown is compared to the desired temperature gradient of a measurement series. If the global temperature gradient is within $\nabla T = 0.0032 \frac{\mathrm{K}}{\mathrm{cm}}$ of the desired value, the point is accepted. The exact threshold arises because the algorithm testing the points is actually checking for deviations in temperature differences. There, a threshold of $\Delta T = 0.03\,\mathrm{K}$ is set. Since the top and bottom Cernox sensors are 9.5 cm apart the 0.03 K correspond to $\nabla T = \frac{0.03\,\mathrm{K}}{9.5\,\mathrm{cm}} = 0.0032 \frac{\mathrm{K}}{\mathrm{cm}}$.

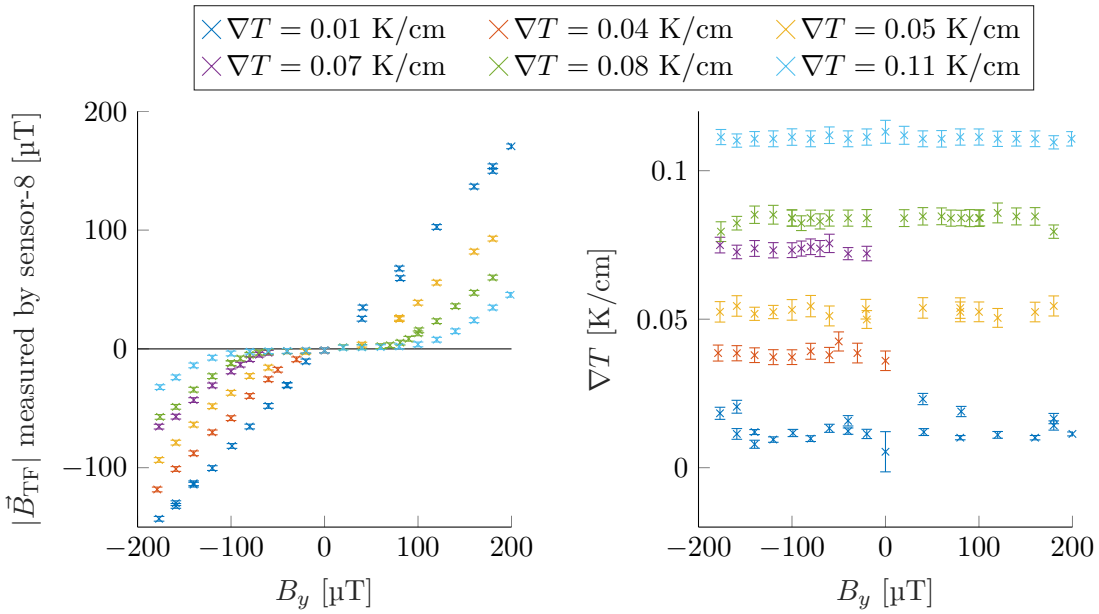

Figure 4.26.: (a): $|\vec{B}_{\mathrm{TF}}|$ versus the component of the external flux density perpendicular to the surface, B_y. (b) corresponding temperature gradients of the same cooldowns. The allowed deviation in temperature gradient is set to $\nabla T = 0.0032\,\frac{\mathrm{K}}{\mathrm{cm}}$. The legend is valid for both plots. The scatter in (a), and (b) is fairly small.

Figure 4.26 (a) shows the dependence of trapped flux on external field magnitude for different temperature gradients. Figure 4.26 (b) depicts the local temperature gradient of the same cooldowns. For the measurement series with $\nabla T = 0.01\frac{\mathrm{K}}{\mathrm{cm}}$ the variations are slightly higher because the local temperature gradient can differ more from the global temperature gradient which is used for selecting the points.

For comparison, Figure 4.27 shows the same data only now the boundary is set to $\nabla T = \frac{0.05\,\mathrm{K}}{9.5\,\mathrm{cm}} = 0.0053\,\frac{\mathrm{K}}{\mathrm{cm}}$.

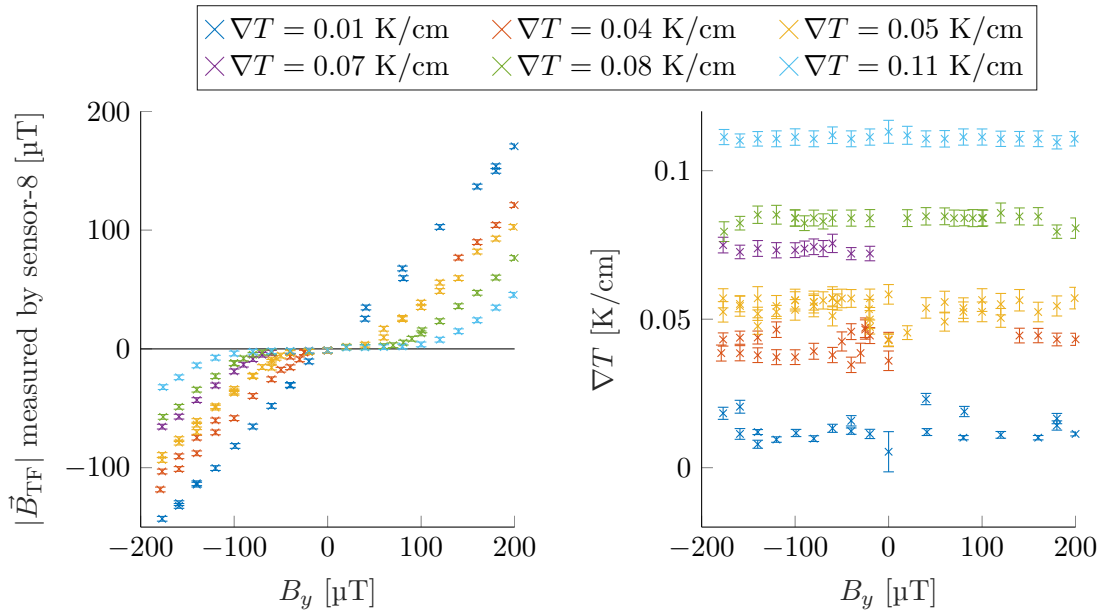

Figure 4.27.: (a): $|\vec{B}_{\mathrm{TF}}|$ versus the component of the external flux density perpendicular to the surface, B_y. (b) corresponding temperature gradients of the same cooldowns. The allowed deviation in temperature gradient is set to $\nabla T = 0.0053\,\frac{\mathrm{K}}{\mathrm{cm}}$. The legend is valid for both plots. The scatter in (b) is larger than in Figure 4.26. This translates to a larger scatter in (a).

There are more data points in Figure 4.27 compared to Figure 4.26. However, the variation within one series is also larger in Figure 4.26. This is clearly visible for the measurement series $\nabla T = 0.04\frac{\mathrm{K}}{\mathrm{cm}}$ at high field magnitudes. In Figure 4.27 (a) the measurement points split up at $B_y = -120\,\mu\mathrm{T}$, however, as Figure 4.27 (b) shows, this is only due to a too high temperature gradient of some of the cooldowns.

At this point it is not possible to predict how much an error in temperature gradient translates to an error in trapped flux. For this a model has to be developed first, so a proper error propagation can be performed. But it is important to keep in mind that all cooldowns of one series have slightly different temperature gradients during cooldown which limits the precision of the data.

4.8.3. Cooldown Rate

For these measurements there are two main error sources, both connected to temperature control and measurement: The consistency and determination of transition time, and the temperature gradient.

Transition time is measured by taking the time difference from the point where the lowest and highest Cernox sensor pass the transition temperature. If one of the sensors is connected worse than the other the measured temperature does not correspond to the real temperature which would skew the calculated transition time in one direction. Additionally, it is a complex task to keep the cooldown rate constant during a sin-

gle cooldown. A local cooldown rate might, therefore, be different from the average cooldown rate. This is because the PID controllers have to be set in a way which allows fast temperature changes (i.e. transition times). This makes the temperature control less stable and makes overshooting the temperature more frequent. During a cooldown the heater power might be lowered too fast at the beginning and is then lowered slower in the end. Figure 4.28 illustrates this case with data from the large grain sample. Figure 4.28 (a) shows the temperature history, and Figure 4.28 (b) the corresponding flux density measurements in y-direction. Since no information is gained from the exact sensor number the legend in Figure 4.28 (b) is omitted but the 5 peaks of the 5 sensor rows are again clearly visible.

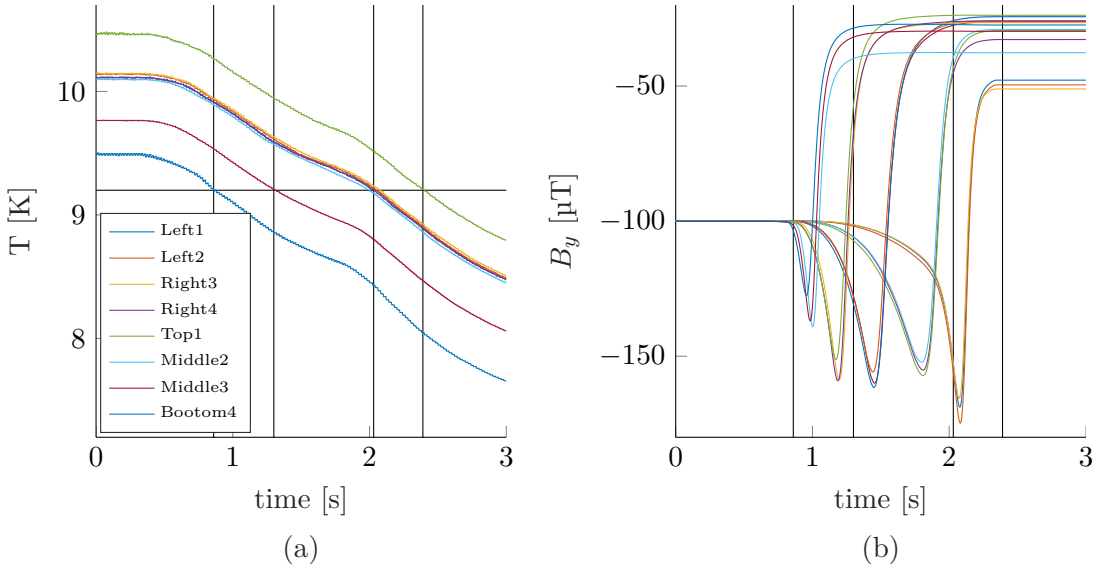

Figure 4.28.: Example of an inconsistent cooldown rate during cooldown. (a) depicts the temperature, and (b) the flux density measured in y-direction at the same time by the 15 AMR sensor groups. The horizontal line in (a) is at 9.2 K and the vertical lines represent the time at which a Cernox sensor passes 9.2 K. The vertical lines are at the same times in both plots. The wave magnitude decreases when the cooldown rate decreases momentarily.

The momentarily lower cooldown rate at $t \approx 1-2\,\mathrm{s}$ in Figure 4.28 (a) results in lower cooldown rate on average. The slower cooldown rate is perceptible due to the larger time difference between the 2. and 3. vertical line. Figure 4.28 (b) shows how this lower cooldown rate affects the wave that is being pushed in front of the phase front: The peak height of the wave that is measured by the AMR sensors rows actually decreases due to the momentarily slower cooldown rate, instead of the usual increase from row to row. These inconsistencies can therefore affect the measured wave magnitude and also trapped flux magnitude.

The other error source is the reproducibility of the temperature gradient within one

measurement series. This problem is already described for the measurement series for external magnetic field strength in section 4.8.2 above. This problem is even more pronounced for measurement series with varying cooldown rates: Especially for fast cooldowns the heater power must be changed in large increments by the PID controller to achieve the desired temperature quickly. The large step size and no time for corrections can lead to deviations from the desired temperature at one or both ends of the sample which alters the temperature gradient. Figure 4.29 (a) shows trapped flux magnitude vs transition time data of the large grain sample already depicted in section 4.3. Now, the corresponding temperature gradients of the cooldowns are plotted in Figure 4.29 (b) to illustrate the Problem.

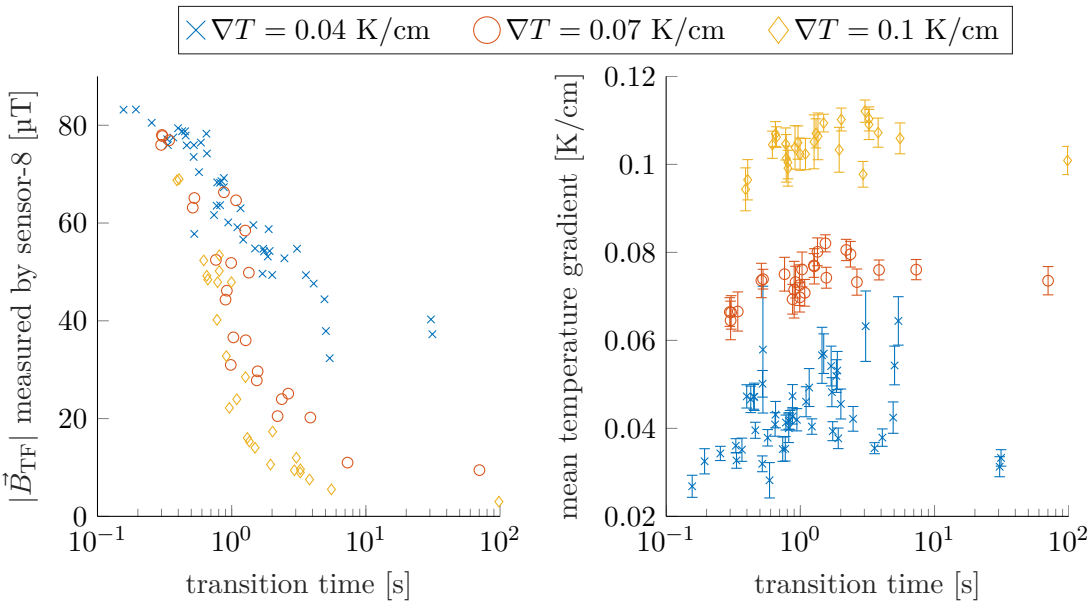

Figure 4.29.: (a) trapped flux magnitude versus transition time, measured with large grain sample. (b) corresponding temperature gradients during cooldown. The legend is valid for both plots. The large scatter in temperature gradient translates to a large scatter in the trapped flux data.

Compared to other measurement series investigating temperature gradient or external magnetic field strength, the scatter of data points in Figure 4.29 (a) is large. As can be seen in Figure 4.29 (b) an inconsistent temperature gradient between cooldowns is a major part of this dispersion. For example, there are three blue marks above each other at a transition time of $\approx 5\,\mathrm{s}$ in Figure 4.29 (b). This large dispersion in temperature gradient is translated to a large dispersion in trapped flux visible in Figure 4.29 (a) for the same cooldowns at a transition time of $\approx 5\,\mathrm{s}$.

The effect of inconsistent temperature gradients between cooldowns and inconsistent cooldown rates during a single cooldown makes the data less precise and the error is hard to estimate. For this reason no error bars are displayed in the data concerning the cooldown rate. But due to a relative large number of points, observations can still be made like in section 4.3.

4.8.4. Geometry

The effect of geometry on trapped flux can only be measured by measuring the distribution of trapped flux across the sample. However, the distribution is also influenced by the local temperature gradient and cooldown speed. In the areas where the sample is clamped in the copper blocks is no temperature gradient established because the copper has a good thermal conductivity and brings the sample area to the same temperature. This means that in these areas flux can get trapped easily which might affect the flux density measured by the AMR sensors. To investigate the effect of the clamped area, three measurement runs were performed with different clamping areas. In the first the sample was clamped 5 mm at either end of the sample. In the second only 2 mm were clamped at either end, and in the third the sample was clamped 2 mm at the bottom edge but was not clamped at all at the top edge. Instead of clamping a copper block to the sample a block was just standing on top of the sample. In all experiments a single grain sample was used which was also rotated between the measurements. The flux distribution of all three cases are depicted in Figure 4.30. For all cooldowns the temperature gradient is $\nabla T = 0.2\,\frac{\mathrm{K}}{\mathrm{cm}}$ and the transition time 28 s.

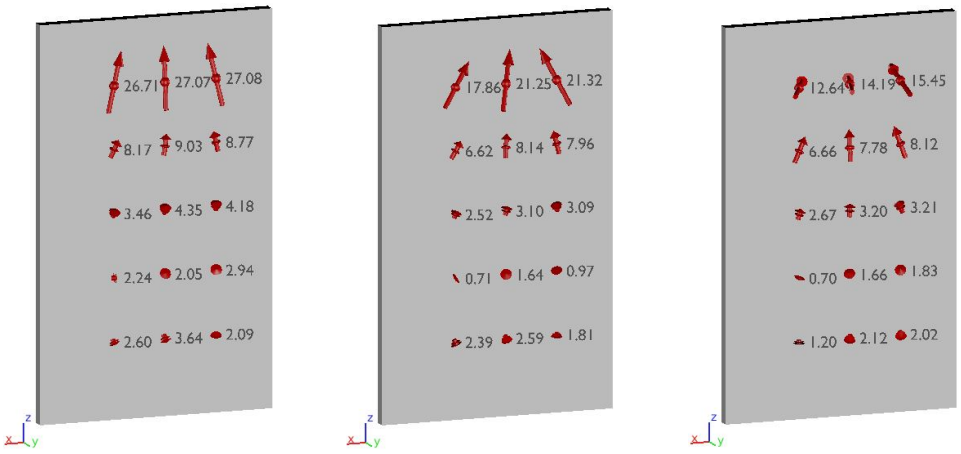

(a) (b) (c)

Figure 4.30.: Flux density distribution for three different clamping areas. (a) 5 mm, (b) 2 mm, (c) 0 mm. The arrow size is scaled for each representation separately. To compare the results, the magnitude in µT depicted next to the arrows must be considered. Less trapped flux is measured with smaller clamping areas.

Figure 4.30 shows how the trapped flux magnitude in the top row decreases with decreasing clamping area. But even when the top block is just set on top of the sample (c) the field is still enhanced. Moreover, this effect is not observed for the bottom row where is sample is also clamped. Therefore, the clamping area contributes to the flux measured by the top AMR row but is not the only cause for the detected field enhancement at the top.

Since the thermal contact between sample and top copper block is worse if it only stands on top of the sample, a consistent temperature control is harder to achieve, and the accessible parameter space is smaller. For that reason, this layout was not repeated, and for all other measurements the top and bottom 2 mm were clamped in the blocks. This offers a compromise between temperature control and edge effects.

Another reason for the high field levels in the top row might be the increased field level when the phase front reaches the top edge: Since the phase front pushes magnetic flux lines ahead of it, the local flux density just above the phase front is higher then the original applied field.

To estimate the increase of flux density just above the phase front COMSOL simulations are carried out. In these simulations an external flux density $\vec{B}_e = (0, -100, 0)\,\mu\mathrm{T}$ is set. The lower 90 mm of the sample are simulated as a perfect superconductor with $\mu_r = 1 \times 10^{-9}$ and the top 10 mm are simulated as a normal conductor with $\mu_r = 1$. To estimate the field enhancement the flux density is evaluated in the centre of the sample (x = 0 mm; y = 0 mm) at the height of the boundary (z = 90 mm), and 1 mm above it (z = 91 mm). The simulation results show an increased flux density at the boundary of 330 µT, and 1 mm above the boundary, the field level is still increased to 270 µT.

In the simulation the boundary is assumed to be a perfect plane in the sample. In a real experiment the phase front is more likely slightly deformed and has rounded edges. This influences the distribution of flux and, therefore, the real enhancement cannot be simulated exactly. However, a field of 300 µT is a reasonable assumption for the field just above the phase front when all field is expelled.

With this assumption more simulations can be performed to estimate how the clamping area influences trapped flux and the corresponding flux densities measured by the AMR sensors. In these simulations the sample is assumed to be in a perfect Meissner state with $\mu_r = 1 \times 10^{-9}$ and zero trapped flux, except at the top and bottom edge. In these regions 100% flux trapping is assumed due to the clamping. At the bottom edge a trapped flux magnitude of 100 µT is assumed and at the top edge 300 µT are assumed. The size of the area which traps flux is varied in different simulations and the resulting field distribution is extracted at the real sensor positions. This data is then compared to real measurements.

Figure 4.31 shows the simulation results for three different area sizes. Figure 4.31 (a) shows the simulated flux densities that would have been measured by the AMR sensors if the top 2 mm of the sample would have trapped 300 µT and the bottom 2 mm would have trapped 100 µT. Figure 4.31 (b) shows the same data, if the top and bottom 5 mm would have trapped flux, and (c) the top and bottom 6 mm. The arrows are scaled to the maximum flux magnitude within one simulation result. To compare the results of the three simulations, the magnetic flux density magnitude which is depicted next to the arrows must also be considered.

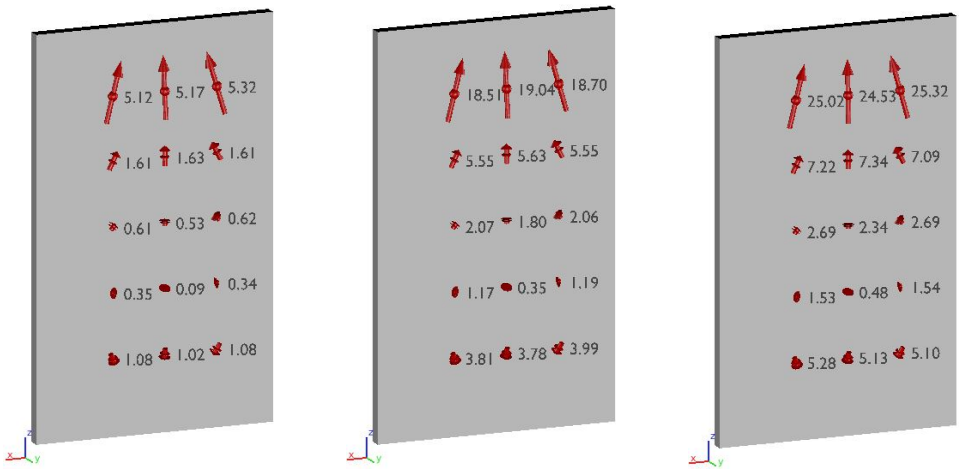

(a) (b) (c)

Figure 4.31.: Simulated flux density distribution for three different areas of high trapped flux. (a) 2 mm, (b) 5mm, (c) 6mm. The arrow size is scaled for each representation separately. To compare the results, the magnitude in µT depicted next to the arrows must be considered. (b) and (c) show magnitudes close to the measured ones in Figure 4.30.

Figure 4.31 (a) shows the case if only the top and bottom 2 mm of the sample would trap flux. This corresponds to the case where no temperature gradient is established in the area that is in contact with copper and all flux is consequently trapped. The comparison to Figure 4.30 (b) shows that this scenario does not lead to the field levels measured in the experiment. Figure 4.31 (b) and (c), on the other hand, depict field levels that are close to the flux densities measured in Figure 4.30 (b). This implies that not only the area that is in contact with the copper experiences a low temperature gradient during cooldown but also the area just next to the copper blocks. The simulations suggest an area of additional 3-4 mm length beyond the copper blocks. The temperature gradient over such small distances cannot be measured with Cernox sensors and is, therefore, not yet experimentally observed.

In real experiments the trapping efficiency is not 100% as in the simulation and there is no hard cut between 100% trapping and 0% trapping, but the simulations give a plausible explanation of the increases trapped flux magnitude measured by the top sensor row.

The simulation results in Figure 4.31 point to another geometry related problem. This issue is not caused by the sample's geometry but by the AMR PCB: The finite dimension of the AMR sensors force the points where the individual magnetic field components are measured within one sensor group apart. This causes an asymmetry in the sensor groups where the x- and z-direction are measured 5 mm above the y-direction. This is the reason why the magnetic flux density "measured" by the top sensor row in Figure 4.31 is roughly a factor 5 larger than the magnitude measured by the bottom row. If the sensor groups were point like, the top row would measure flux densities only

a factor 3 larger than the bottom row due to the assumed flux density enhancement to 300 µT.

At this point it must be mentioned that the geometry effects discussed above affect all other measurements. At the beginning of this section it is already mentioned that the results are discussed only with sensor group 8 as an example. This is necessary because even with homogeneously distributed flux in the sample the sensor groups do not show the same value, as is shown in Figure 3.11. Due to flux expulsion the external field that is present in the sample when the phase front reaches a certain height is dependent on the position in the sample: At higher points in the sample, $|\vec{B}_\mathrm{e}|$ is larger than at lower points. This makes the expected difference between sensor groups even larger which makes averaging less meaningful.

In order to estimate the change of external magnetic field depending on the height in the sample, multiple COMSOL simulations are carried out. The flux density magnitude just above the phase front, of course, depends on the expulsion efficiency of the sample at a given temperature gradient: If no magnetic flux is expelled, the flux density above the phase front does not change, and with full expulsion it changes the most. In the simulation the worse case scenario of full expulsion is assumed.

The simulations are done similarly to the simulation described above where a constant external magnetic flux density $\vec{B}_e = (0, -100, 0)$ µT is set, and one part of the sample is in the perfect Meissner state with $\mu_r = 1 \times 10^{-9}$, and the other part is normal conducting with $\mu_r = 1$. In these simulations, however, the phase front moves through the sample from bottom to top in 5 mm steps. The magnetic flux density is then extracted from each individual simulation at the position of the phase front and 1 mm above it. The results are depicted in Figure 4.32.

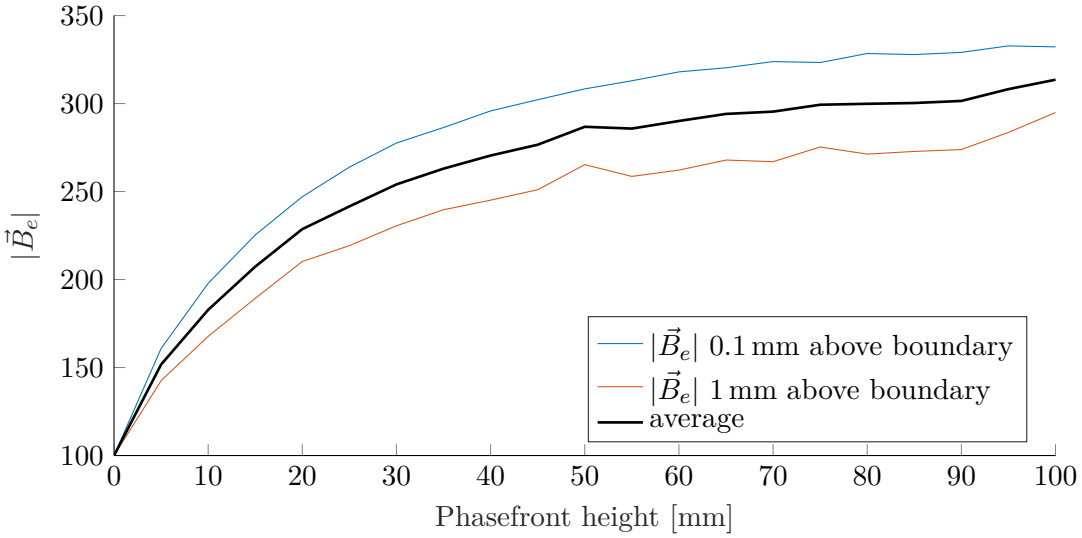

Figure 4.32.: Simulated field enhancement above the phase front caused by flux expulsion.

Figure 4.32 shows a steep increase in external flux density above the phase front when the sample starts to become superconducting at the bottom. When the phase front is at a height of only 15 mm, the external magnetic flux density has already doubled. When the phase front moves up the sample the increase becomes less steep. This is due to the sample's shape: Since it is longer than wide flux is being pushed out more to the side instead of to the top. This plot also shows the 300 µT at a phase front height of 90 mm that were estimated above. The simulation shows that the actual field levels in the sample are, depending on cooldown conditions, a factor 2 or 3 higher then the applied external field.

This field enhancement is strictly speaking not an error source, since this will always happen in a superconductor. But it must be considered in the data analysis.

As is already described above, the simulations depict an idealized scenario, and the values in real experiments might differ from simulated values. However, they can give an estimation of the actual field level inside the sample during transition. Since the field level cannot be measured using conventional sensors, simulations are the best tool to estimate it with the current setup. To measure field levels inside the sample methods like neutron tomography [95] or myon spin rotation [96] must be used.

The only way to judge the feasibility of the simulation is to extract the field levels at the sensor positions and compare it to data measured in experiments. Simulation results of magnetic flux density at the sensor positions are shown in Figure 4.33 in black. Since the simulations are done in a stationary model and the phase front position is raised in discrete steps of 1 mm the simulation emulates the case of a very long transition time where magnetic flux has sufficient time to exit the sample.

For comparison Figure 4.33 also shows measurement data of a cooldown of the large grain sample with $\nabla T = 0.2 \frac{\mathrm{K}}{\mathrm{cm}}$ and a transition time of 32 s. These cooldown condition lead to a trapped flux magnitude measured by sensor group 8 of 1.8 µT, suggesting near full expulsion. The condition are, therefore, similar to the ones in the simulation. The measured data is depicted in red. The x-axis of the measurement data is scaled such that the first deviation in magnetic field is at $t = 0\,\mathrm{s}$, and ends when no change in magnetic flux density is visible any more at $t = 32\,\mathrm{s}$.

Since the simulated flux densities are plotted against the phase front height [cm], and the measured data against time [s], both data sets must be plotted with their own x-axis. The x-axis of the measured data is depicted below the plots, and the x-axis for the simulated data is depicted above the plots. The axes are also coloured like the corresponding data. The y-axis is identical for both data sets in order to make a comparison easier.

In general the simulation results agree very well with the measured data, since all prominent features that can be seen in the measurement data are also present in the simulation results: In x-direction the central sensor stays at zero field, and the outer sensors increase in flux density in their corresponding direction (pointing outward). The sharp peak is caused by the simulation mesh. In y- and z-direction 5 prominent peaks are present in both data sets and the field evolution before and after the peaks also match. This is translated in the flux density magnitude, where a small bump is depicted on the falling slope in both data sets. The bump is caused by the peaks in z-direction, which are slightly later in time than the peaks in y-direction.

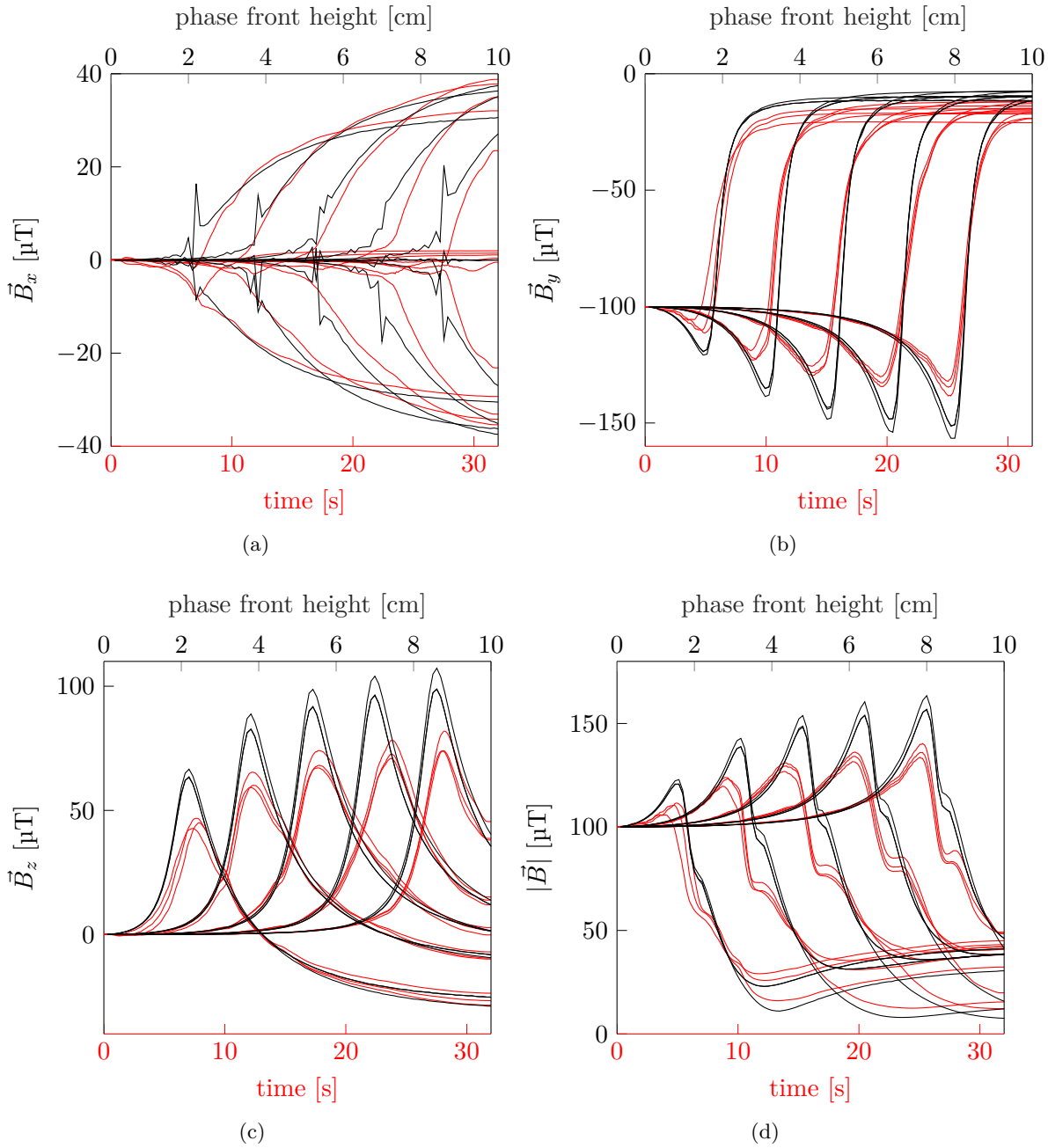

Figure 4.33.: Simulated flux density at the sensor positions for a moving phase front (black). Measured flux density of a cooldown of the large grain sample with $\nabla T = 0.2\,\frac{\mathrm{K}}{\mathrm{cm}}$ and a transition time of 32 s (red). (a) shows the x-component of the magnetic flux density. (b) shows the y-component, (c) the z-component, and (d) the magnitude. Due to different units of the x-axes of both data sets the x-axis of the simulated data is depicted on top of the plots. The y-axis is identical for both data sets. The simulation agrees well with the measurement.

In x-direction the magnitude of the signals agree with each other. In y- and z-direction, however, the simulation predicts a higher signal than what is measured in the experiment. To quantify how much larger the peak height in the simulation is, the ratio of two corresponding peaks is calculated, as well as the absolute difference between them. This is done for the y- and z-direction. For the ratio in y-direction 100 µT are added to all data points because the initial flux density in y-direction is -100 µT. The results are summarised in table 4.1.

Table 4.1.: Ratio and difference of peak heights of simulation and measurements. Row 5 indicates the AMR sensor row at the bottom, row 1 at the top.

	row 5	row 4	row 3	row 2	row 1
Ratio y	1.73	1.77	1.60	1.59	1.47
Ratio z	1.42	1.35	1.32	1.33	1.30
Difference y [µT]	8	17	18	20	18
Difference z [µT]	20	23	24	26	25

In y-direction the peaks of the simulation are on average a factor 1.63 larger than the peaks of the measured data. In z-direction the factor is on average 1.35. There is also a trend noticeable that the ratio gets smaller towards higher sensor rows. By means of the calculated difference of the peaks it becomes evident that the ratio gets only smaller because the absolute values increase and the difference stays more or less constant.

There might be several reasons for the discrepancy between simulations and experiment: The first is that in real experiments 100% flux expulsion might not be possible. Secondly, it is already discussed above that the ends where the sample is clamped in the blocks trap more flux. These regions affect the overall expulsion. Thirdly, the phase front in the real experiment is not a perfect plane moving through the sample. Lastly, the phase front might not be perfectly horizontally in the sample. In fact, A. Cierpka devised a setup to measure the temperature distribution on the sample in a grid of 3×5 sensors and measured that the phase front was tilted in the observed cooldowns [97].

The average of the ratios in y- and z-direction is $1.49 \approx 1.5$. The field enhancement just above the phase front was simulated above to be maximal 330 µT. Dividing the increase from 100 µT to 330 µT (230 µT) by 1.5 yields an increase of 150 µT, or a flux density of 250 µT above the phase front. The estimated enhancement of a factor 2-3, therefore, still holds.

By limiting the x-axis of the measurement data like described above the two data sets fit on top of each other very well. These plots can, therefore, even be used to estimate the phase front height at a given time. Figure 4.34 shows the same data as Figure 4.33 (b) and (c). Only now, the height of the AMR sensor rows are marked in the simulation data using vertical lines.

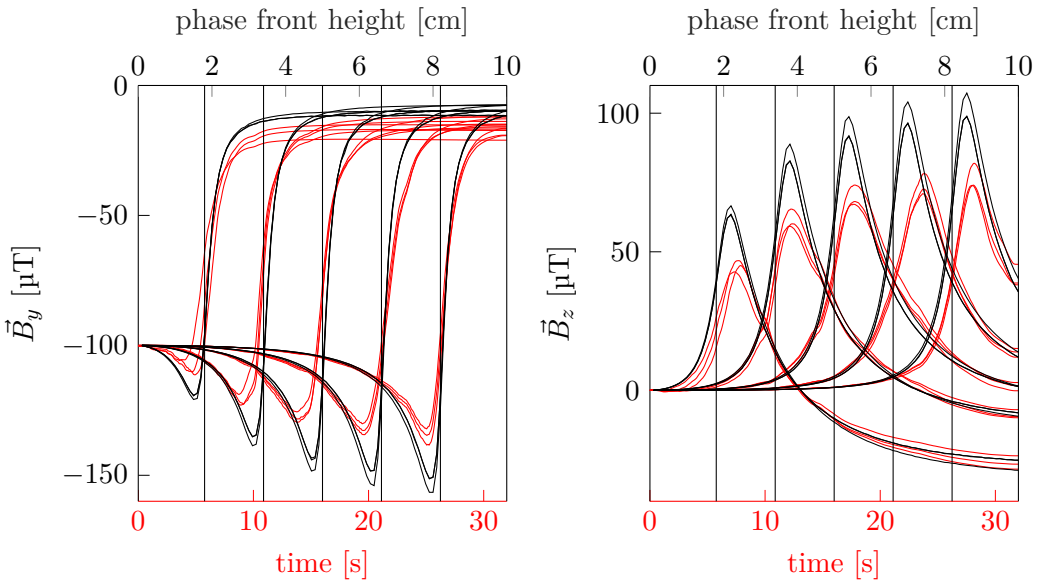

Figure 4.34.: Simulated flux density at the sensor positions for a moving phase front (black). Measured flux density of a cooldown of the large grain sample with $\nabla T = 0.2\,\frac{\mathrm{K}}{\mathrm{cm}}$ and a transition time of 32 s (red). (a) shows the y-component of the simulated magnetic flux density at the sensor positions. (b) shows the z-component. In addition, the height of the AMR sensor rows are indicated with vertical lines on the x-axis of the simulation data. With help of these lines the position of the phase front relative to the measured peaks can be extracted.

Figure 4.34 shows that the maximum in y-direction is detected when the phase front is 3 mm below the sensor group position. Since the sensor measuring in y-direction is 2.5 mm below the centre of the group. The maximal flux density in y-direction is measured when the phase front is at the height of the sensor. In z-direction the peak is measured when the phase front is 4 mm above the group's centre. The z-sensor is again 2.5 mm above the centre. The peak in z-direction is, therefore, measured when the phase front is 1-2 mm above the sensor. The x-direction is not depicted, but here the sharp increase in flux density start when the phase front just passes the sensor.

5. Modelling Trapped Flux

In this chapter data described in chapter 4 is analysed in more detail and a phenomenological model describing trapped flux behaviour is introduced. First, an existing model developed by T. Kubo [64] is applied to the data. Doing so shows that the model does not agree with the data. Then, a simple model is developed to illustrate the underlying idea of the new model. In a next step this model is refined using the gathered data. Finally, an estimation of the flux line velocity is given at the end of this chapter.

In the following analysis $|\vec{B}_{\mathrm{TF}}|$ is abbreviated as B_{TF}, and $|\vec{B}_{\mathrm{e}}|$ as B_{e}.

5.1. Applying the existing Model

The model described in [64] is introduced in more detail in chapter 2.4.2. It predicts that B_{TF} is proportional to $(\nabla T)^{-1}$. Therefore, a function $a/\nabla T + b$ is fitted to the data of the large grain sample. Figure 5.1 shows the results. The obtained parameters are: $a = (1.27 \pm 0.12)\,\frac{\mu\mathrm{T\,cm}}{\mathrm{K}}$, $b = (2 \pm 4)\,\mu\mathrm{T}$.

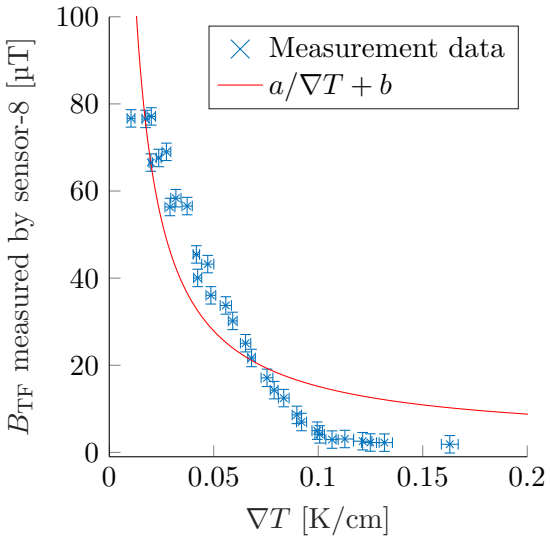

Figure 5.1.: B_{TF} versus ∇T measurement data of the large grain sample. The red line shows the fit results according to $a/\nabla T + b$. The model does not agree well with the data.

Figure 5.1 shows no good agreement between fit and measurement results. For data gathered from the fine grain sample the used fit algorithm could not find a fit at all and the results are not depicted here.

The reason why the model cannot be applied to this data is twofold[1]: Firstly, the model is developed for superconductors with sparse pinning centres. In this case of untreated samples there seem to be many pinning centres which makes an interaction of a flux line with pinning centres much more likely. Secondly, it is assumed that the external field is parallel to the superconductor's surface which reduces the interaction region. However, the data shown in Fig. 5.1 was taken with external magnetic field perpendicular to the sample surface.

Figure 5.1, and the paragraph above show that the existing model cannot be used to describe trapped flux for the investigated samples. Therefore, a new model is developed in the further course of this chapter which models the dependence of trapped flux on temperature gradient. It does so with help of a distribution function of the pinning strength of pinning centres instead of an interaction cross section.

5.2. The Base Model

This model was developed by Prof. T. Kubo on the basis of the data presented in this thesis. He also suggested the parametrisation that is used in section 5.3. The model is supposed to predict trapped flux magnitude depending on the temperature gradient. The idea of the model is to describe the amount of trapped flux lines with a density distribution of the pinning forces of the pinning centres. If or if not a flux line gets pinned by a pinning centre depends on whether the pinning force is larger or smaller than the thermal force pulling the flux lines away from the pinning centre.

The model adapts ideas from the model by T. Kubo which is introduced in chapter 2.4.2: Due to the external magnetic field the sample is in three phases simultaneously when the phase front moves through the sample. Above the phase front where the sample is warmer than T_c it is normal conducting. Due to the external field the sample is actually still normal conducting when the temperature reaches T_c. Below the point where $T = T_c$ there is a region of thickness δx where the sample is in the Shubnikov phase. Even further below, the sample is cold enough so that $B_e < B_{c1}$ and the sample is in the Meissner state. Figure 5.2 depicts this state. The size of the Shubnikov state is not to scale.

[1] Private communication with Prof. T. Kubo.

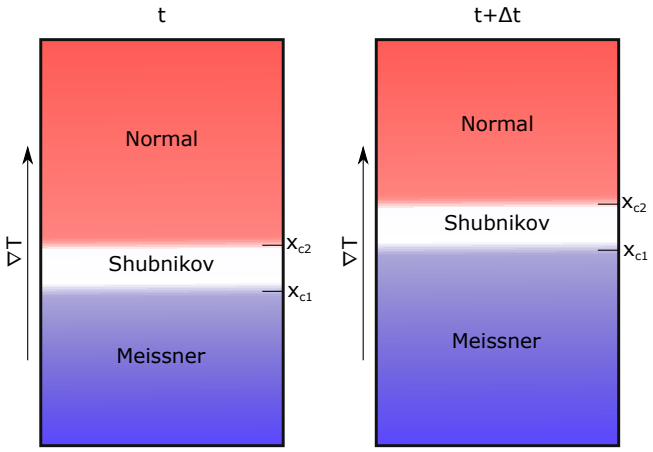

Figure 5.2.: Schematic depiction of phase front in the sample. x_{c2} denotes the position where the sample transitions to the Shubnikov state, x_{c1} where it transitions to the Meissner state. Figure is adapted from [64].

Figure 5.2 shows that the phase front is actually not a one dimensional line, but rather a transition area that moves up the sample with time. At x_{c2} where the sample transitions into the Shubnikov phase, new quantized flux lines are formed, and while they are in the region of the Shubnikov phase they can move. The introduction of the thermal force in chapter 2.4.3 shows that flux lines in a superconductor which is in the Shubnikov phase move from the warmer region to the colder region. This means that in Figure 5.2 flux lines below x_{c2} are actually pushed towards the region which is in the Meissner state at x_{c1}. But at x_{c1} flux lines must be pushed up again. Otherwise, the observed data where a "wave" builds up ahead of the phase front could not be explained.

At this stage the mechanism which pushes flux lines out of the Meissner state is not yet understood. It might be explained using microscopic theories of superconductivity like the BCS theory, but this is not part of this thesis.

The flux line dynamics at the phase front are not fully understood on a microscopic level but for this model the following assumption is made: If a flux line is pinned by a pinning centre and is, therefore, at the position of the pinning centre when the Meissner state at x_{c1} reaches it, it is not expelled but is trapped in the superconductor. If, however, the flux line is in the "clean" superconductor without pinning centre when the Meissner state reaches it, it is expelled. The second case can be achieved if the thermal force is larger than the pinning force and the flux line is pulled away from the pinning centre.

In section 2.4.3 the thermal force is introduced and described as

$$f_{\mathrm{th}} = a\nabla T. \tag{5.1}$$

Where for now a is just a constant. The pinning force is denoted as f_{p}. A flux line gets pinned if $f_{\mathrm{p}} > f_{\mathrm{th}}$. The pinning force of each pinning centre is not known, hence a distribution function $n(f_{\mathrm{p}})$ is introduced which describes the probability of a flux line

to interact with a pinning centre with pinning force f_p. The distribution function is normalized to satisfy

$$\int_0^\infty n(f_\mathrm{p})\mathrm{d}f_\mathrm{p} = 1. \tag{5.2}$$

At this point the distribution function is not known and depends on the material and its treatment. Figure 5.3 shows a hypothetical example of how it might look. The function is discontinuous because different pinning mechanisms might lead to pinning forces not achievable for other mechanisms. f_0 to f_4 denote the most extreme forces reachable for a certain pinning mechanism.

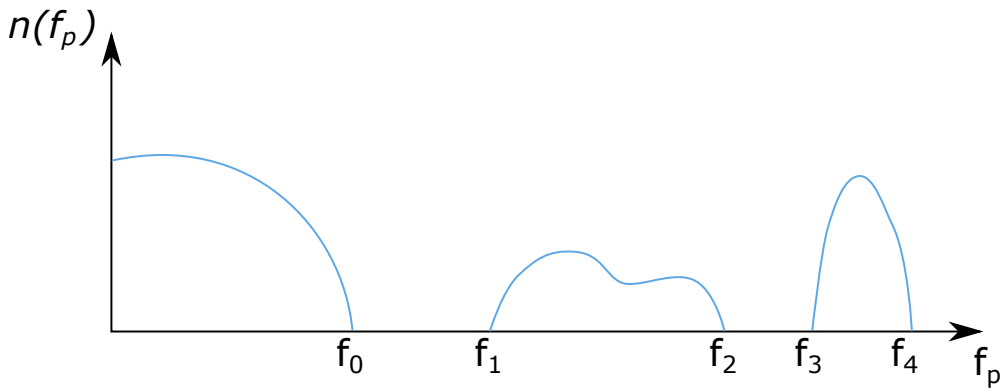

Figure 5.3.: Hypothetical distribution function of pinning force f_p.

The ratio of flux lines that get trapped depends on how strong the thermal force is compared to the pinning strength distribution. It can be written as $r_\mathrm{trap}(\nabla T) = 1 - r(\nabla T)$, with

$$r(\nabla T) = \int_{f_\mathrm{p}<f_\mathrm{th}} n(f_\mathrm{p})\mathrm{d}f_\mathrm{p}. \tag{5.3}$$

r is the ratio of flux lines that are expelled. Equation 5.3 states that flux lines only get pinned at pinning centres with pinning strengths larger than the thermal force.

In order to make predictions from this model two assumptions are made which, for now, are chosen as simple as possible:

1. The maximal achievable thermal force is larger than f_0 but smaller than f_1: $f_0 < a|\nabla T|_\mathrm{max} < f_1$
2. $n(f_\mathrm{p})$ is constant for f_p smaller than f_0: $n(f_\mathrm{p} < f_0) = n_0 = const.$

The physical interpretation of the first assumption is that the achievable temperature gradient and, therefore, thermal force, is large enough to push flux lines over "weak" pinning centres but not large enough to prevent flux lines to be pinned at "strong" pinning centres. The second assumption must be made because the distribution function is not known and a constant value is a good starting point.

With these assumptions the ratio of expelled flux as a function of temperature gradient $r(\nabla T)$ can be calculated. This is then used to calculate the ratio of trapped flux $r_{\mathrm{trap}}(\nabla T)$:

$$r(\nabla T) = \int_{f_\mathrm{p}<f_\mathrm{th}} n(f_\mathrm{p})\mathrm{d}f_\mathrm{p} \tag{5.4}$$

$$= \int_0^{a|\nabla T|} n(f_\mathrm{p})\mathrm{d}f_\mathrm{p} \begin{cases} = n_0 a|\nabla T| & \text{for } |\nabla T| < \dfrac{f_0}{a} \\ = n_0 f_0 & \text{for } |\nabla T| \geq \dfrac{f_0}{a} \end{cases} \tag{5.5}$$

$$= n_0 a|\nabla T| \left[1 - \theta\left(|\nabla T| - \frac{f_0}{a}\right)\right] + n_0 f_0 \theta\left(|\nabla T| - \frac{f_0}{a}\right) \tag{5.6}$$

$$= k|\nabla T| \left[1 - \theta\left(|\nabla T| - \frac{R_w}{k}\right)\right] + R_w \theta\left(|\nabla T| - \frac{R_w}{k}\right). \tag{5.7}$$

Here, θ is the heaviside step function, and k is defined as $k = n_0 a$ with n_0 the constant introduced in assumption 2. R_w is the ratio of weak pinning centres: $R_w = \int_{f_\mathrm{p}<f_0} n(f_\mathrm{p})\mathrm{d}f_\mathrm{p} = n_0 f_0$.

The ratio of trapped vortices is given by $r_{\mathrm{trap}} = 1 - r$. Since r_{trap} is the ratio of flux lines that get trapped, r_{trap} must be multiplied with the external flux density B_e in order to calculate B_{TF}. This results in:

$$B_{\mathrm{TF}} = (1 - r(\nabla T))B_\mathrm{e} \tag{5.8}$$

$$= B_\mathrm{e} - B_\mathrm{e}\left[k|\nabla T| \left[1 - \theta\left(|\nabla T| - \frac{R_w}{k}\right)\right] + R_w \theta\left(|\nabla T| - \frac{R_w}{k}\right)\right]. \tag{5.9}$$

Equation 5.9 contains two fitting parameters k and R_w which must be determined experimentally for each material.

This model predicts a linear decrease in trapped flux with increasing temperature gradient with slope $(-B_\mathrm{e}k)$ up to a gradient $\frac{R_w}{k}$. For higher temperature gradients a constant value of $B_\mathrm{e}(1 - R_w)$ is predicted.

Figure 5.4 shows data from trapped flux versus temperature gradient measurements from the large grain sample, as well as from the fine grain sample (without defect). For these plots sensor group 8 is chosen again as the exemplary sensor group. The other sensor groups will be analysed further below. Additionally, the red lines show the results from fitting equation 5.9 to the data. In the fit B_e is set to 95 µT because the simulations in section 3.2.1 show that with full trapping only 95 µT are measured by sensor group 8. The obtained fit parameters are: $k = (11.7 \pm 0.6)\,\frac{\mathrm{cm}}{K}$, $R_w = 0.96 \pm 0.03$ for the large grain, and $k = (2.0 \pm 0.5)\,\frac{\mathrm{cm}}{K}$, $R_w = 0.41 \pm 0.08$ for the fine grain. To estimate the goodness of the fit the root mean square error (RMSE) is determined. For the large grain it is RMSE = 3.87, and for the fine grain RMSE = 5.94.

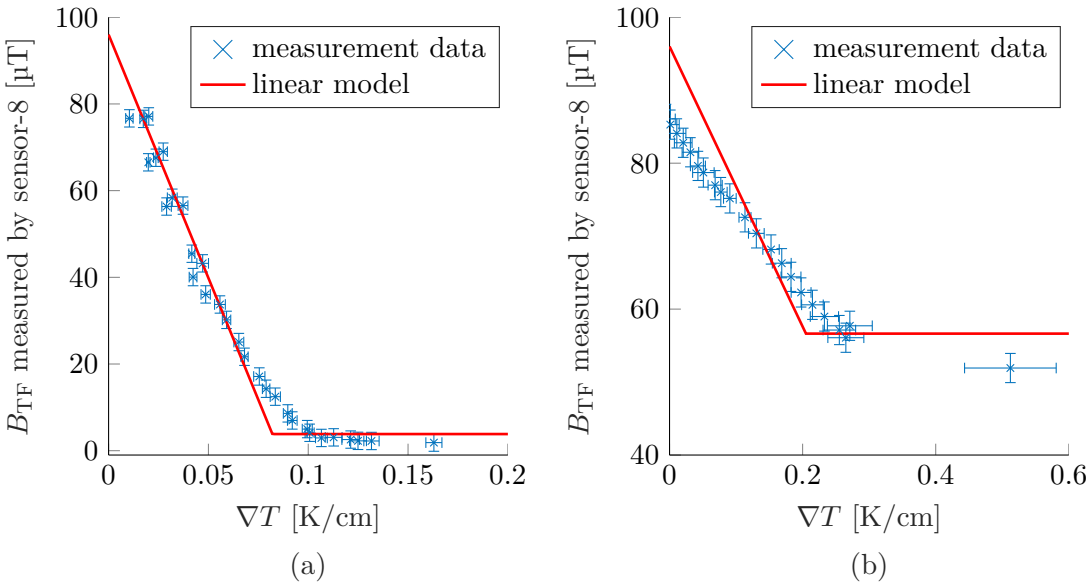

Figure 5.4.: (a) B_{TF} versus ∇T measurement data of the large grain sample. (b) shows the same data set for the fine grain sample (without defect). The red lines show the fit results according to equation 5.9. The model shows better agreement with the data than the existing model but must be refined further.

The fit agrees well with the large grain data in Figure 5.4 (a) but does agree not well with the fine grain data in (b). This is mainly caused by the fact that in the model 100% flux trapping is assumed at $\nabla T = 0\,\frac{\mathrm{K}}{\mathrm{cm}}$. The worse agreement of the fine grain data is also reflected in the RMSE values cited above. However, the fit parameter R_w which denotes the ratio of weak pinning centres does fit with the expectation: For the large grain where almost full expulsion is achievable the ratio of weak pinning is almost 1 and for the fine grain it is only 0.41. This implies that almost 60% of the pinning centres in the fine grain samples are strong pinning centres where flux cannot be pushed over by the thermal force.

5.3. Refining the Model

Figure 5.4 shows that the model has the potential to describe the measured data but must be refined further. To do so, the second assumption that $n(f_\mathrm{p})$ is constant for f_p smaller than f_0 is dismissed. In order to predict how the distribution function for weak pinning centres might look like the data B_{TF} versus B_e is analysed in more detail. In section 4.2 it is mentioned that the magnitude of trapped flux increases linearly with increasing external flux density once a threshold field is passed. This behaviour is now investigated further.

Figure 5.5 shows data from measurements with the large grain sample. Here, data points that are recorded at the same temperature gradient are fitted with linear regression. The boundary at which points are accepted to belong to the same temperature

gradient is set at $\nabla T = \pm 0.0021 \frac{\mathrm{K}}{\mathrm{cm}} \hat{=} \Delta T = \pm 0.02\,K$. It is already mentioned in section 4.2 that flux only gets trapped above a threshold field B^*. In order to avoid that points below B^* skew the linear regression, all points with $B_{\mathrm{TF}} \leq 5\,\mu\mathrm{T}$ are excluded from the fit. The threshold is set at $5\,\mu\mathrm{T}$ so that a transition region that might exist when fields just starts to get trapped is also excluded. Above this transition region the relation between B_{TF} and B_{e} is assumed to be linear.

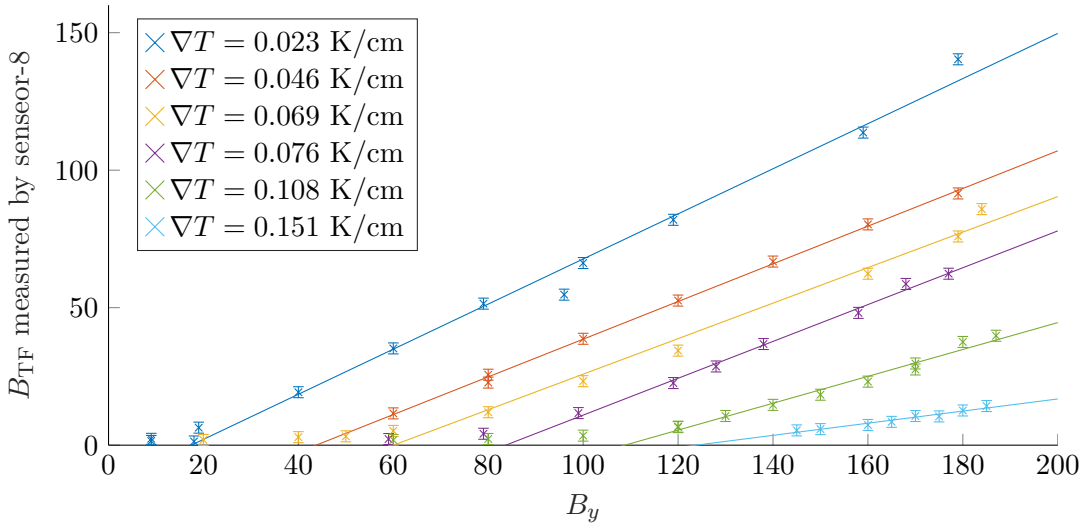

Figure 5.5.: Trapped flux magnitude versus applied flux density in y-direction (perpendicular to the surface). Data points that have the same temperature gradient and where $B_{\mathrm{TF}} > 5\,\mu\mathrm{T}$ are fitted with linear regression. The results from the linear regression are plotted in the same colour as the data points. The linear regressions agree well with the data and shows the threshold field.

The linear regressions in Figure 5.5 fit well to the data and a linear increase of trapped flux with external magnetic flux density seems reasonable.

Since the B_{TF} versus B_{e} curves are recorded for different temperature gradients, Figure 5.5 contains two kinds of information: 1. How is trapped flux influenced by external magnetic flux density, and 2. how does the temperature gradient influence trapped flux at a given field level.
The information of the temperature gradient can now be used to plot the slope η of the fits in Figure 5.5 versus the temperature gradients that were applied for the various series.

Figure 5.6 shows the slopes versus the average temperature gradient of the measurement points that are used for the individual fit. Figure 5.6 shows more slopes than there are fits in Figure 5.5 because for better readability not all recorded measurement series are depicted in Figure 5.5. Figure 5.6, however, shows fit results from all available series.

The fitted slope η seems to decrease linearly with increasing temperature gradient. This trend is emphasized using a weighted linear regression. The dependence of the

slope η on the temperature gradient is parametrised as

$$\eta(|\nabla T|) = \eta_0 \left(1 - \frac{|\nabla T|}{g_c}\right). \tag{5.10}$$

The parametrisation is chosen like this, so the physical interpretation of the parameters becomes clearer: The slope or "trapping efficiency" η equals a trapping efficiency η_0 at $|\nabla T| = 0\,\frac{\mathrm{K}}{\mathrm{cm}}$, and decreases linearly with $|\nabla T|$ up to a critical temperature gradient g_c. At this gradient the trapping efficiency vanishes.

The best parameters are found to be $\eta_0 = 0.90 \pm 0.017$, and $g_c = (0.21 \pm 0.02)\,\frac{\mathrm{K}}{\mathrm{cm}}$. The error bars given here correspond to the 68.3% confidence interval (or 1-σ). This is also true for error bars depicted in Figure 5.6, and the following plots. Uncertainties obtained from fit results given below always correspond to the 68.3% confidence interval.

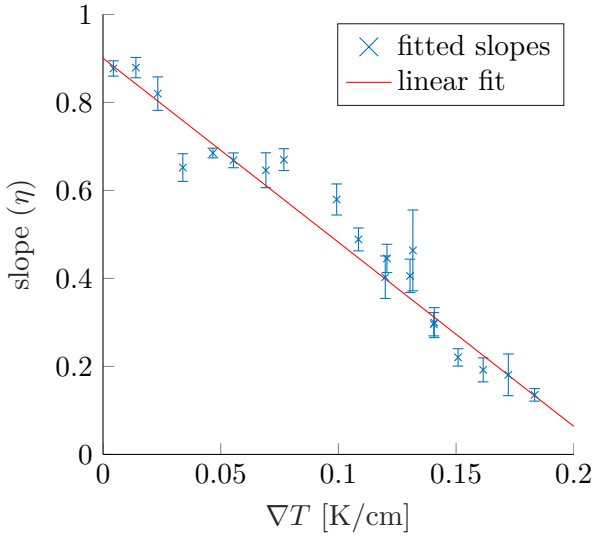

Figure 5.6.: Slope of linear fits like in Figure 5.5 versus average temperature gradient of the points used for the fit. Additionally, a linear fit ($\eta = \eta_0 \left(1 - \frac{|\nabla T|}{g_c}\right)$) of the slopes versus temperature gradient is depicted. $\eta_0 = 0.90 \pm 0.017$, and $g_c = (0.21 \pm 0.02)\,\frac{\mathrm{K}}{\mathrm{cm}}$.

Figure 5.6 clearly shows how the slopes of the linear fits decrease with increasing temperature gradient. Additionally, an assumption is made that the decrease is linear.

Similar to what is depicted in Figure 5.6 the x-axis crossings of the fits in Figure 5.5 can be plotted against the average temperature gradient of the individual series. Like in Figure 5.6, a linear correlation between x-axis crossing and temperature gradient is assumed and a linear regression is performed. The physical interpretation of the x-axis crossing is the threshold field B^* at which flux starts to get trapped. The parametrization is again chosen such that the physical interpretation becomes clearer:

$$B^*(|\nabla T|) = b\frac{|\nabla T|}{g_c} \tag{5.11}$$

Here, the threshold field B^* increases linearly with normalized temperature gradient $\frac{|\nabla T|}{g_c}$ with the threshold field's sensitivity to the temperature gradient b. g_c is taken from above. Figure 5.7 shows B^* values extracted from the fits in Figure 5.5 as well as a fit according to equation 5.11.

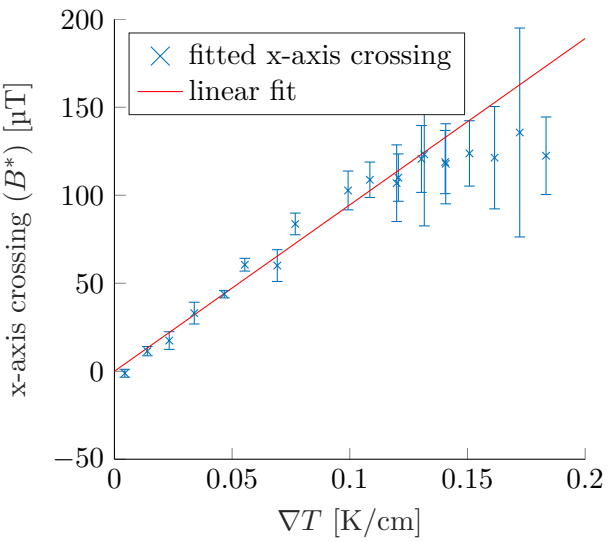

Figure 5.7.: x-axis crossing of linear fits like in Figure 5.5 versus average temperature gradient of the points used for the fit. Additionally, a linear fit ($B^*(|\nabla T|) = b\frac{|\nabla T|}{g_c}$) of the x-axis crossings versus temperature gradient is depicted. $b = (204 \pm 6)\,\mu\mathrm{T}$; $g_c = (0.21 \pm 0.02)\,\frac{\mathrm{K}}{\mathrm{cm}}$.

Figure 5.7 shows a linear correlation between B^*, and temperature gradient ∇T. At temperature gradients above $0.15\,\frac{\mathrm{K}}{\mathrm{cm}}$, the x-axis crossing seems to stay constant but the uncertainties are also very large, so no definitive statement can be made, whether the correlation continues linearly or the x-axis crossing stays constant. For now, it is assumed that the correlation stays linear.

The large error bars stem from the limitation in B_e of the setup: At large temperature gradients very high fields must be applied in order to trap any flux. But since the maximum achievable flux density is 185 µT, the recorded points are close together (see Figure 5.5). Additionally, the 2 µT error on the magnetic field data becomes more significant when less flux is trapped. These two effects lead to larger uncertainties in the fit at high temperature gradients.

In order to extract the density function $n(f_p)$ from this data, three assumptions are made:

1. The dependence of trapped flux on applied field magnitude is linear once flux starts to get trapped above B^* (Figure 5.5).

2. The slope of the linear fits in 1. decreases linearly with increasing temperature gradient (Figure 5.6).

3. The x-axis crossing, or B^*, increases linearly with increasing temperature gradient (Figure 5.7).

From condition 1 it follows that B_{TF} can be expressed as

$$B_{TF}(B_e) = mB_e + n, \tag{5.12}$$

as long as $B_e > B^*$. Here, m and n are constants as long as the temperature gradient is fixed. Using Figures 5.6 and 5.7 the slope m and the threshold field B^* can be

extracted. With this information the offset n is calculated:

$$B_{\mathrm{TF}}(B^*) = 0 \tag{5.13}$$
$$\Leftrightarrow mB^* + n = 0 \tag{5.14}$$
$$\Leftrightarrow n = -mB^* \tag{5.15}$$

Using assumptions 2 and 3 it follows with equation 5.15 that the offset n must be quadratic in ∇T:

$$\left.\begin{array}{l} 2. : m(\nabla T) \propto \nabla T + c_1 \\ 3. : B^*(\nabla T) \propto \nabla T + c_2 \end{array}\right\} \Rightarrow n \propto (\nabla T)^2 + \nabla T + c \tag{5.16}$$

To verify whether n is quadratic in $|\nabla T|$ the y-axis crossings extracted from the fits in Figure 5.5 are plotted against temperature gradient. Additionally a polynomial of second order is fitted to the data. The expected y-axis crossing can also be calculated from the linear fits in Figure 5.6, and 5.7 (equation 5.15). Figure 5.8 shows all of the above.

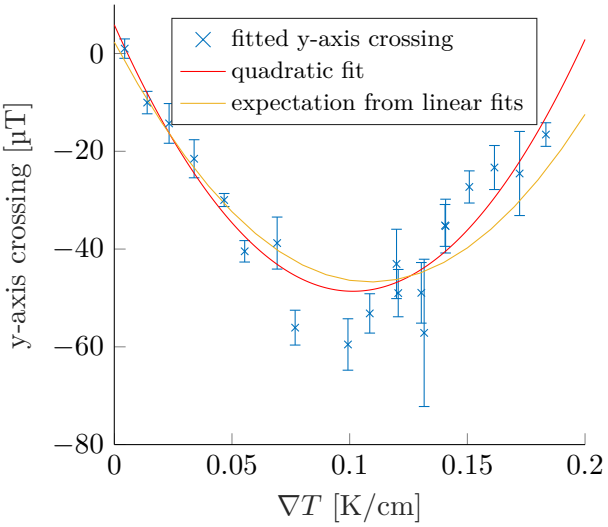

Figure 5.8.: y-axis crossing of linear fits like in Figure 5.5 versus average temperature gradient of the points used for the fit. Additionally, a second order polynomial fit is depicted, as well as the expected values extracted from the previous two fits. A quadratic dependence is clearly visible.

Figure 5.8 shows the quadratic dependence of the y-axis crossing on temperature gradient, and that the quadratic fit (red) is close to the expected value which is calculated from fits in Figures 5.6 and 5.7 (yellow).

Plugging m and n back in equation 5.12 yields an equation for trapped flux as a function of external field and temperature gradient

$$B_{\mathrm{TF}}(B_{\mathrm{e}}, \nabla T) = B_{\mathrm{e}} m(\nabla T) + n(\nabla T). \tag{5.17}$$

Equation 5.16 and Figure 5.8 show that n is proportional to $|\nabla T|^2$. Therefore, B_{TF} also has a term that is proportional to $|\nabla T|^2$. This is in contrast to the linear behaviour that is predicted by the basic model in section 5.2.

The above derivation of n in combination with data in Figure 5.8 support the quadratic $|\nabla T|$ term in B_{TF}. The quadratic term can, however, also be calculated by expressing B_{TF} in terms η and B^* that are described above:

$$B_{\mathrm{TF}}(B_{\mathrm{e}}, \nabla T) = \eta(\nabla T)(B_{\mathrm{e}} - B^*(\nabla T)) \tag{5.18}$$

Plugging equation 5.10 and 5.11 in equation 5.18 yields

$$B_{\mathrm{TF}} = \eta_0 \left(1 - \frac{|\nabla T|}{g_{\mathrm{c}}}\right) \left[B_{\mathrm{e}} - b\frac{|\nabla T|}{g_{\mathrm{c}}}\right] \tag{5.19}$$

$$= \eta_0 \left(B_{\mathrm{e}} - b\frac{|\nabla T|}{g_{\mathrm{c}}} - B_{\mathrm{e}}\frac{|\nabla T|}{g_{\mathrm{c}}} + b\left(\frac{|\nabla T|}{g_{\mathrm{c}}}\right)^2\right) \tag{5.20}$$

$$= \eta_0 B_{\mathrm{e}} - \eta_0(B_{\mathrm{e}} + b)\frac{|\nabla T|}{g_{\mathrm{c}}} + \eta_0 b\left(\frac{|\nabla T|}{g_{\mathrm{c}}}\right)^2 \tag{5.21}$$

Equation 5.21 is only valid if $B_{\mathrm{e}} > B^*$. To extend the range of validity, equation 5.21 is used to derive a distribution function $n(f_{\mathrm{p}})$ which is then used to derive $B_{\mathrm{TF}}(B_{\mathrm{e}}, |\nabla T|)$ like in chapter 5.2. The resulting formula for B_{TF} is valid independently of the combination of B_{e}, and $|\nabla T|$.

First, B_{TF} is expressed in terms of the ratio of expelled flux r that was used above:

$$B_{\mathrm{TF}}(B_{\mathrm{e}}, \nabla T) = (1 - r)B_{\mathrm{e}} \tag{5.22}$$

$$\Leftrightarrow r = -\frac{B_{\mathrm{TF}}}{B_{\mathrm{e}}} + 1 \tag{5.23}$$

$$= -\eta_0 \frac{b}{B_{\mathrm{e}} g_{\mathrm{c}}^2}|\nabla T|^2 + \frac{\eta_0}{g_{\mathrm{c}}}\left(1 + \frac{b}{B_{\mathrm{e}}}\right)|\nabla T| - \eta_0 + 1 \tag{5.24}$$

$$= -\eta_0 \frac{b}{B_{\mathrm{e}} g_{\mathrm{c}}^2 a^2}(a|\nabla T|)^2 + \frac{\eta_0}{g_{\mathrm{c}} a}\left(1 + \frac{b}{B_{\mathrm{e}}}\right)(a|\nabla T|) - \eta_0 + 1 \tag{5.25}$$

In the last step $|\nabla T|$ is replaced by $(a|\nabla T|)$ which makes the following derivation equivalent to the one in chapter 5.2.

At this point the equation for r is known for $B_{\mathrm{e}} > B^*$ (equation 5.25), and $n(fp)$ must be chosen to result in this equation of r. Therefore, equation 5.25 is differentiated with respect to $(a|\nabla T|)$ to find $n(fp)$. This way the desired equation is obtained after integration

$$\frac{\partial r}{\partial(a|\nabla T|)} = -2\eta_0 \frac{b}{B_{\mathrm{e}} g_{\mathrm{c}}^2 a^2}(a|\nabla T|) + \frac{\eta_0}{g_{\mathrm{c}} a}\left(1 + \frac{b}{B_{\mathrm{e}}}\right) \tag{5.26}$$

From this it is deduced that

$$n(f_{\mathrm{p}}) = -2\eta_0 \frac{b}{B_{\mathrm{e}} g_{\mathrm{c}}^2 a^2} f_{\mathrm{p}} + \frac{\eta_0}{g_{\mathrm{c}} a}\left(1 + \frac{b}{B_{\mathrm{e}}}\right) \tag{5.27}$$

Equation 5.27 shows that the distribution function of the weak pinning centres is not constant any more, like it is assumed in section 5.2, but it decreases linearly with

pinning force. It also shows a dependence on external field. The distribution function, therefore, not only describes the pinning force but also how the pinning force is affected by the external magnetic flux density.

Now, the same derivation as in chapter 5.2 is performed with the refined distribution function

$$r(\nabla T) = \int_{f_\mathrm{p}<f_\mathrm{th}} n(f_\mathrm{p})\mathrm{d}f_\mathrm{p} \tag{5.28}$$

$$= \int_0^{a|\nabla T|} n(f_\mathrm{p})\mathrm{d}f_\mathrm{p} \tag{5.29}$$

$$= \begin{cases} -\eta_0 \dfrac{b}{B_\mathrm{e} g_\mathrm{c}^2 a^2}(a|\nabla T|)^2 + \dfrac{\eta_0}{g_\mathrm{c} a}\left(1+\dfrac{b}{B_\mathrm{e}}\right)(a|\nabla T|) & \text{for } |\nabla T| < \dfrac{f_0}{a} \\ -\eta_0 \dfrac{b}{B_\mathrm{e} g_\mathrm{c}^2 a^2} f_0^2 + \dfrac{\eta_0}{g_\mathrm{c} a}\left(1+\dfrac{b}{B_\mathrm{e}}\right) f_0 & \text{for } |\nabla T| > \dfrac{f_0}{a} \end{cases} \tag{5.30}$$

$$= \left[-\frac{\eta_0 b}{B_\mathrm{e} g_\mathrm{c}^2}|\nabla T|^2 + \frac{\eta_0}{g_\mathrm{c}}\left(1+\frac{b}{B_\mathrm{e}}\right)\nabla T\right]\left[1-\theta\left(|\nabla T| - \frac{f_0}{a}\right)\right] + \left[-\frac{\eta_0 b}{B_\mathrm{e} g_\mathrm{c}^2}\left(\frac{f_0}{a}\right)^2 + \frac{\eta_0}{g_\mathrm{c}}\left(1+\frac{b}{B_\mathrm{e}}\right)\left(\frac{f_0}{a}\right)\right]\theta\left(|\nabla T| - \frac{f_0}{a}\right) \tag{5.31}$$

$$= \left[-\frac{\eta_0 b}{B_\mathrm{e}}\left(\frac{|\nabla T|}{g_\mathrm{c}}\right)^2 + \eta_0\left(1+\frac{b}{B_\mathrm{e}}\right)\frac{|\nabla T|}{g_\mathrm{c}}\right]\left[1-\theta\left(|\nabla T| - \kappa\right)\right] + \left[-\frac{\eta_0 b}{B_\mathrm{e} g_\mathrm{c}^2}\kappa^2 + \frac{\eta_0}{g_\mathrm{c}}\left(1+\frac{b}{B_\mathrm{e}}\right)\kappa\right]\theta\left(|\nabla T| - \kappa\right) \tag{5.32}$$

In the last step $\kappa = \frac{f_0}{a}$ is defined. At this point the model predicts flux expulsion only if $\nabla T > 0\,\frac{\mathrm{K}}{\mathrm{cm}}$. However, this does not to be the case. In fact, an ideal superconductor is expected to expel all flux independent of the temperature gradient. Therefore, B_TF is not expressed as $B_\mathrm{TF} = (1-r)B_\mathrm{e}$ but as $B_\mathrm{TF} = (\eta_0 - r)B_\mathrm{e}$. This ensures that flux can still be expelled at $\nabla T = 0\,\frac{\mathrm{K}}{\mathrm{cm}}$.

Now, B_TF can be expressed as a function of B_e, and ∇T in the complete parameter space:

$$B_\mathrm{TF}(B_\mathrm{e}, \nabla T) = (\eta_0 - r)B_\mathrm{e} \tag{5.33}$$

$$= \eta_0 B_\mathrm{e} - \left\{\left[-\eta_0 b\left(\frac{|\nabla T|}{g_\mathrm{c}}\right)^2 + \eta_0(B_\mathrm{e}+b)\frac{|\nabla T|}{g_\mathrm{c}}\right]\left[1-\theta(|\nabla T| - \kappa)\right] + \left[-\frac{\eta_0 b}{g_\mathrm{c}^2}\kappa^2 + \frac{\eta_0}{g_\mathrm{c}}(B_\mathrm{e}+b)\kappa\right]\left[\theta(|\nabla T| - \kappa)\right]\right\} \tag{5.34}$$

At $\nabla T = 0\,\frac{\mathrm{K}}{\mathrm{cm}}$ a fraction η_0 of the applied flux density gets trapped. With increasing temperature gradient up to κ trapped flux decreases not strictly linearly, but linearly with a quadratic correction term. For temperature gradients higher than κ the trapped flux magnitude stays constant. $\kappa = \frac{f_0}{a}$ is the temperature gradient which corresponds to the highest pinning force exerted by "weak" pinning centres (see f_0 in Figure 5.3).

Equation 5.34 can now be fitted to B_{TF} versus ∇T data. First it is fitted to data recorded with the large grain sample, that is already known from Figure 4.2 and 5.4. Figure 5.9 shows the resulting fit. The fit parameters are quoted in Table 5.1. For comparison Figure 5.9 also displays the linear fit according to the base model.

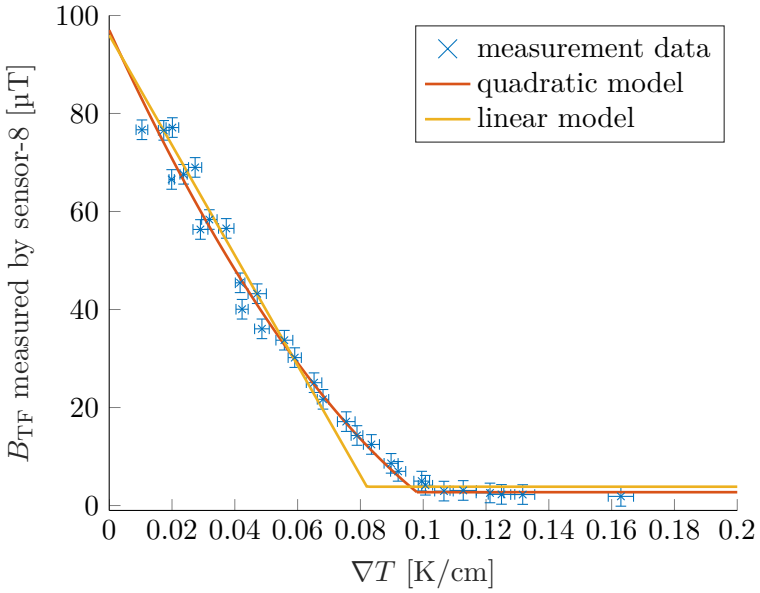

Figure 5.9.: Trapped flux magnitude versus temperature gradient of large grain sample. A fit according to equation 5.34 is depicted and labelled "quadratic model". Table 5.1 states the fit parameters. For comparison the "linear model" according to equation 5.9 is also depicted. The quadratic model agrees very well with the data.

Figure 5.9 shows good agreement of measurement and fit. The difference between the two models is not too large, however, the quadratic model does represent the slight curve in the data better, which is especially evident at temperature gradients around $0.1\,\frac{\mathrm{K}}{\mathrm{cm}}$. The RMSE improved from RMSE = 3.87 for the linear model to RMSE = 2.85 for the quadratic model. Figure 5.9 also shows that the quadratic term in equation 5.34 is not dominant in this regime. It is rather a correction term to the linear decrease. For other materials with larger b or smaller g_{c} the term becomes more dominant.

Figure 5.9 also shows that there is a "kink" in the function at $\nabla T = \kappa$ where the derivation is discontinuous. This is because the distribution function is assumed to have a hard edge (i.e. it is discontinuous) at f_0. For realistic distributions this not very likely but at this stage it is sufficiently accurate.

The obtained fit parameters are quoted in Table 5.1. Table 5.1 also shows fit parameters obtained with the same fit, but for each sensor individually. The sensor positions and labels are depicted in Figure 3.16. In the fit algorithm b is limited to 300 µT. If a parameter runs into a limit it is considered fixed and no confidence interval is stated.

Table 5.1.: Fit parameters obtained from fitting equation 5.34 to data from all sensors individually. b is limited to 300 µT in the fit algorithm. The errors are extracted from square roots of the diagonal elements of the covariance matrix. If a parameter runs in a limit no confidence interval is stated.

Sensor	b [µT]	η_0	g_c [$\frac{K}{cm}$]	κ [$\frac{K}{cm}$]
1	$100 \pm 3e5$	1.168 ± 0.03	0.12 ± 180	0.089 ± 0.006
2	$100 \pm 1e7$	1.21 ± 0.03	0.12 ± 8000	0.083 ± 0.005
3	$100 \pm 3e5$	1.19 ± 0.028	0.12 ± 200	0.088 ± 0.006
4	150 ± 50	1.06 ± 0.02	0.15 ± 0.04	0.090 ± 0.005
5	$100 \pm 2e5$	0.98 ± 0.02	0.11 ± 140	0.090 ± 0.007
6	120 ± 80	1.03 ± 0.02	0.12 ± 0.05	0.091 ± 0.007
7	170 ± 60	1.05 ± 0.03	0.18 ± 0.05	0.098 ± 0.006
8	200 ± 80	0.96 ± 0.03	0.22 ± 0.07	0.098 ± 0.005
9	180 ± 50	1.02 ± 0.03	0.19 ± 0.04	0.102 ± 0.006
10	$300 \pm -$	1.01 ± 0.03	0.28 ± 0.09	0.089 ± 0.003
11	$300 \pm -$	0.97 ± 0.03	0.29 ± 0.09	0.093 ± 0.003
12	250 ± 70	0.99 ± 0.03	0.23 ± 0.06	0.093 ± 0.003
13	$300 \pm -$	0.97 ± 0.03	0.25 ± 0.10	0.079 ± 0.003
14	$300 \pm -$	0.95 ± 0.04	0.23 ± 0.13	0.075 ± 0.004
15	$300 \pm -$	0.96 ± 0.04	0.23 ± 0.14	0.075 ± 0.004

Noticeably, the uncertainties of b are very large. This is especially true for sensors 1 to 3. For these sensors the uncertainties of g_c are also very large. This is because the fit parameters are not independent of each other, so that in general fit results are fairly insensitive to changes in a single parameter, since a change in one parameter can be compensated by other parameters. Therefore, the large uncertainties are not necessarily of physical nature but stem from the fit algorithm. This limits the applicability of the model in some ways, but Table 5.2 shows that the parameters can be obtained using a more robust fit. The fact that the parameters are not independent of each other is also why b is limited to 300 µT because for sensors 13-15 b is predicted to be 650 µT which is then compensated by g_c of 0.5 $\frac{K}{cm}$. It should be noted that sensors 1-3 are in the top row of the AMR PCB where trapped flux is heavily influenced by the sample's top edge (see section 4.8.4). This also influences the fit parameters.

It is also evident that b and g_c become larger with increasing sensor number (or lower sensor position on the sample). For η_0 the opposite is true as it decreases with increasing sensor number. This is to be expected, since at the top of the sample more flux is being pushed ahead of the phase front, so more then the 100 µT of applied field can actually be trapped. This is reflected in $\eta_0 > 1$. In the case of b, and g_c the large uncertainties make the increase insignificant.

Parameters b, η_0, and g_c can also be extracted from fits according to equation 5.10 and 5.11. The fits are done equivalent to what is shown in Figure 5.6 and 5.7 but now for all sensor groups. Table 5.2 shows the obtained results.

Table 5.2.: Fit parameters obtained from fitting equation 5.10 and 5.11 to data from all sensors individually. The errors correspond to the 68.3% confidence interval, or 1-σ.

Sensor	$b\,[\mu\mathrm{T}]$	η_0	$g_\mathrm{c}\,[\frac{\mathrm{K}}{\mathrm{cm}}]$	$\kappa\,[\frac{\mathrm{K}}{\mathrm{cm}}]$
1	110 ± 9	0.92 ± 0.04	0.197 ± 0.006	–
2	94 ± 11	0.90 ± 0.05	0.195 ± 0.006	–
3	103 ± 11	0.92 ± 0.04	0.203 ± 0.008	–
4	187 ± 8	0.93 ± 0.02	0.212 ± 0.006	–
5	184 ± 8	0.88 ± 0.03	0.221 ± 0.008	–
6	190 ± 8	0.95 ± 0.03	0.225 ± 0.008	–
7	207 ± 6	0.922 ± 0.014	0.210 ± 0.004	–
8	204 ± 6	0.901 ± 0.016	0.215 ± 0.005	–
9	205 ± 6	0.935 ± 0.018	0.208 ± 0.004	–
10	243 ± 8	0.909 ± 0.019	0.194 ± 0.005	–
11	234 ± 7	0.890 ± 0.016	0.201 ± 0.004	–
12	229 ± 7	0.952 ± 0.017	0.198 ± 0.004	–
13	260 ± 7	0.88 ± 0.02	0.178 ± 0.005	–
14	251 ± 9	0.92 ± 0.02	0.194 ± 0.007	–
15	216 ± 2	0.938 ± 0.019	0.203 ± 0.003	–

It is evident that the uncertainties of the obtained results are much smaller than the uncertainties in Table 5.1. This has two reasons: First, for this method only linear fits are necessary, which makes fitting easier and more robust. Second, for this method 219 measurement points are used in total to extract the three parameters. For the fits of B_TF versus ∇T, that is performed above, only 30 measurement points are used. The drawback of doing the fits like in Table 5.2 is that a fit must be performed with fit results from a previous fit.

In Table 5.2 there is again a trend observable that b increases for higher sensor numbers. However, g_c stays constant. The result that the sensitivity of the threshold field to the applied temperature gradient b increases is expected because at a given external field, flux might not be trapped at the sample's bottom but at its top it does, hence, leading to larger B^* at the bottom than at the top. g_c is expected to decrease the lower the sensor is on the sample because the gradient that expels all flux is expected to be lower at the bottom of the sample then at the top. The increase in Table 5.1, therefore, might not be real, and the uncertainties actually make the increase insignificant. In Table 5.2 η_0 stays constant, which is not expected, since an increase like in Table 5.1 is expected due to geometry effects.

In general the parameters stated in Table 5.1 and 5.2 agree, and similar trends are observable in the two. Taking the centre sensor group 8 as an example, the two fit methods yield almost exactly the same result. This not only supports the developed model, but also shows that the setup yields reproducible data, since the data sets for the two fit methods are recorded in different measurement runs, nine months apart.

Using the fit results for sensor 8 in Table 5.1 that are obtained at $B_\mathrm{e} = 100\,\mu\mathrm{T}$,

the model can be used to predict trapped flux at different external flux densities. To verify the predictions the data points in Figure 5.5 are not grouped in series of constant temperature gradient but constant external flux density. This is depicted in Figure 5.10 where points with the same B_e are grouped in series and colour coded. In the same colour the predictions according to equation 5.34 are plotted. The fit parameters are taken from Table 5.1 and B_e in equation 5.34 is plugged in accordingly to the B_e from the respective series.

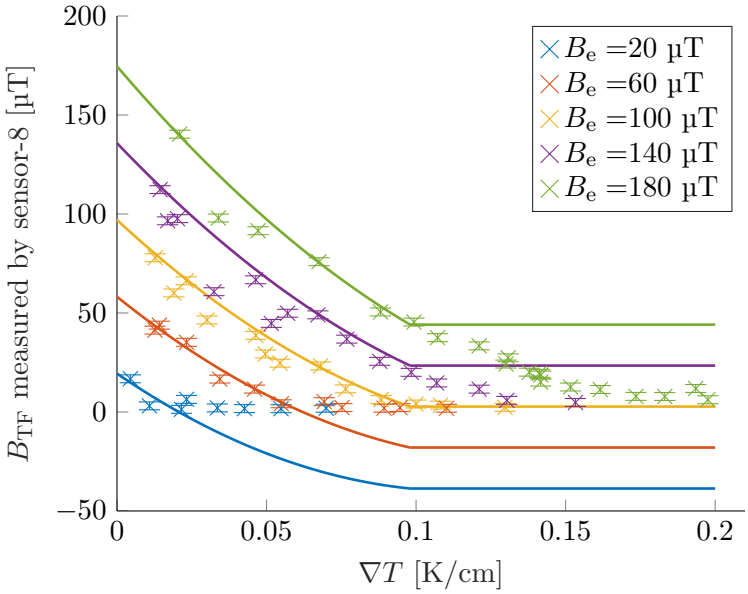

Figure 5.10.: Trapped flux magnitude versus temperature gradient. Data points with the same B_e are grouped in series and lines according to equation 5.34 are depicted in the same colour. The fit parameters are taken from Table 5.1. The predictions are wrong because κ needs to be rescaled.

As can be seen in Figure 5.10 the predictions agree well with the measured data in a certain interval, but disagree in others. For $B_\mathrm{e} < 100\,\mu\mathrm{T}$ the model predicts unphysical negative trapped flux magnitudes. This stems from a wrong parameter κ. In fact, κ is only correct for $B_\mathrm{e} = 100\,\mu\mathrm{T}$ for which it is fitted.

To understand why κ changes depending on the external magnetic flux density the forces acting on magnetic flux lines must be investigated further. But since the flux line dynamics on a microscopic level are not understood yet, the mechanism how the external field influences trapped flux, and how B^* arises is not understood either at this point.

The force exerted by the external field is already considered in the shape of equation 5.34 because it is derived from Figure 5.5. This is also the reason why $n(f_\mathrm{p})$ depends on B_e. However, the force exerted by B_e also has an effect on the boundary f_0 up to which $n(f_\mathrm{p})$ is integrated. This is not yet considered in equation 5.34. There are still open questions how B_e influences trapped flux and a simple model with a constant force due to the external field cannot explain the different behaviour of large- and fine

grain material to changes in B_e. For this reason no physical derivation on how to scale κ can be given. Therefore, κ is scaled at this point with the help of Figure 5.10.

Figure 5.10 shows that at small fields ($B_e = 20\,\mu T$) a temperature gradient of $0.02\,\frac{K}{cm}$ is sufficient to expel all flux and this ratio scales up linearly (e.g. $\kappa = 0.098\,\frac{K}{cm}$ at $B_e = 100\,\mu T$.) Therefore, an assumption is made that κ scales linearly with B_e.

Figure 5.11 shows the results when equation 5.34 is plotted for different external magnetic flux densities with parameters from Table 5.1. κ is now scaled linearly with external magnetic flux density: $\kappa(B_e) = \kappa(B_e = 100\mu T)\frac{B_e}{100\mu T} = 0.098\frac{B_e}{100\mu T}\frac{K}{cm}$. Figure 5.11 (a) shows the measured trapped flux magnitude in µT, and (b) shows the trapped flux magnitude as a fraction of the applied field. Since the simulation for full trapping in Figure 3.11 shows that sensor group 8 measures only 95% of the flux density that is trapped in the sample the fraction is calculated as $\frac{B_{TF}}{0.95B_e}$. The estimated systematic error for trapped flux measurements is 2 µT. The error bars in Figure 5.11 (b) scale accordingly, so that for $B_e = 20\,\mu T$ the error is 10%. Plotting these large error bars would make Figure 5.11 (b) very hard to read which is why they are omitted.

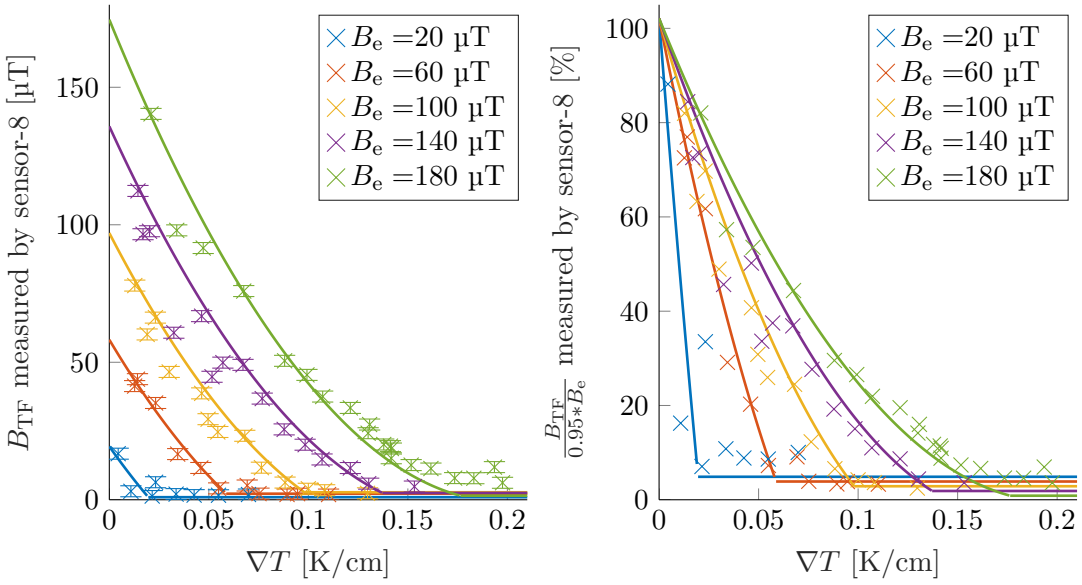

Figure 5.11.: (a) Trapped flux magnitude versus temperature gradient. Data points with the same B_e are grouped in series and predictions according to equation 5.34 are depicted in the same color. The fit parameters are taken from Table 5.1. κ is scaled with B_e. (b) shows the same data points as (a), but B_{TF} is presented as a fraction of $0.95B_e$. The factor of 0.95 is inserted because simulations show that only 95% of trapped flux density is measured by sensor group 8. In (b) error bars are omitted for better readability. With rescaled κ the model predicts trapped flux correctly.

With the adjusted κ the model agrees very well for all B_e. It also predicts the slower

decrease for high external flux densities at high gradients. This also shows well in Figure 5.11 (b) where a much sharper decrease in trapped flux is predicted for small external flux densities than for high external flux densities. For higher flux densities the quadratic term is much more evident.

Figure 5.11 shows that the model can be used to predict trapped flux for different magnitudes of the external flux density based on measurements at one specific external flux density magnitude.

5.4. Applying the Model

5.4.1. Fine Grain Sample

The model is now applied to measurement data from the fine grain sample. First, B_{TF} versus B_{e} data is analysed and fits according to equation 5.10 and 5.11 are performed in order to determine b, η_0, and g_{c}. Then B_{TF} versus ∇T data is used to perform the fit according to equation 5.34. For this sample B_{TF} versus ∇T curves are recorded for $B_{\mathrm{e}} = 20, 40, 100, 160\,\mu\mathrm{T}$. The predictions from the fit with $B_{\mathrm{e}} = 100\,\mu\mathrm{T}$ can, therefore, be validated with three datasets that are specifically recorded as B_{TF} versus ∇T curves. The plots shown here take sensor group 8 as an exemplary sensor group. The fit parameters of the other sensors are again summarized in Tables 5.3, and 5.4 at the end.

Figure 5.12 shows B_{TF} versus B_{e} data from the fine grain sample. Data points that have the same temperature gradient and where $|\vec{B}_{TF}| > 5\,\mu\mathrm{T}$ are fitted with linear regression. The threshold for data points to be accepted to a certain temperature gradient is set at $\nabla T = \pm 0.01\,\frac{\mathrm{K}}{\mathrm{cm}}$.

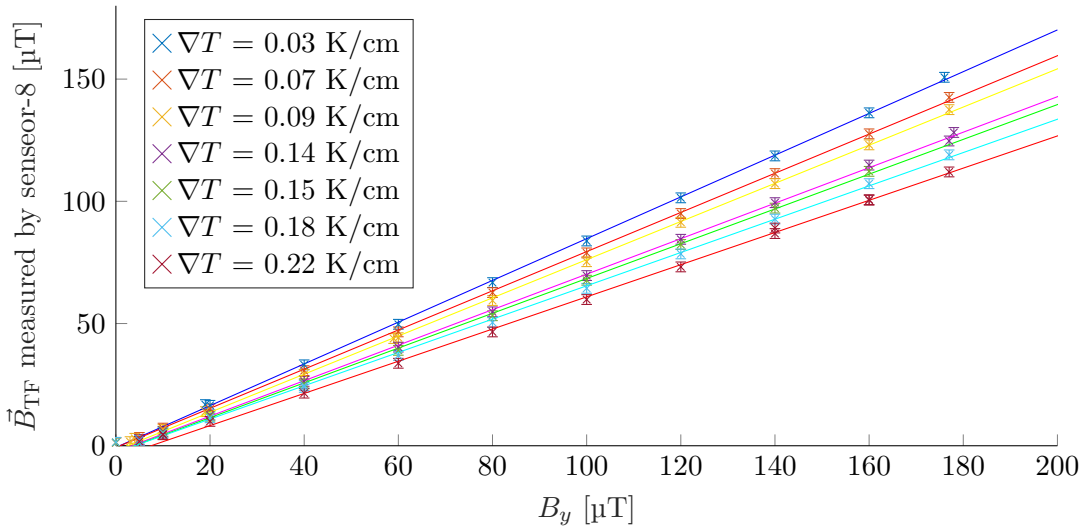

Figure 5.12.: Trapped flux magnitude versus external flux density. Data points that have the same temperature gradient and where $B_{\mathrm{TF}} > 5\,\mu\mathrm{T}$ are fitted with linear regression. The fit results are depicted in the same colour as the data points. The linear regressions agree well with the data. No clear threshold field is evident.

Figure 5.13 shows the slope and x-axis crossing of the linear fits in Figure 5.12 versus corresponding temperature gradient. Additionally the fitted lines according to equation 5.10 and 5.11 are depicted in red.

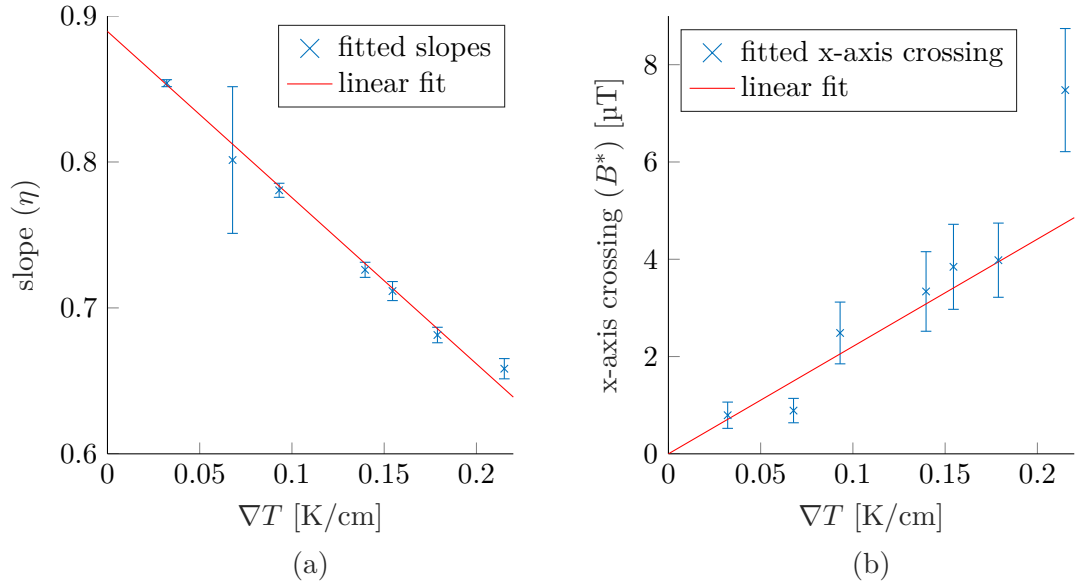

Figure 5.13.: Fitted slopes (a) and x-axis crossings (b) from fits in Figure 5.12. Additionally fit results according to equation 5.10 are shown in (a), and to equation 5.11 in (b). The obtained parameters from (a) are $\eta_0 = 0.882 \pm 0.004$, and $g_c = (0.78 \pm 0.03)\,\frac{\mathrm{K}}{\mathrm{cm}}$. (b) yields $b = (17 \pm 2)\,\mu\mathrm{T}$. The slopes of the linear fits (red) are much shallower than for the large grain sample.

Figure 5.13 (a) shows a linear decrease of the fitted slopes with increasing temperature gradient. In comparison to the data from the large grain sample the decrease is less steep. This is reflected in a higher critical gradient $g_c = (0.78 \pm 0.03)\,\frac{\mathrm{K}}{\mathrm{cm}}$ (Large grain: $g_c = (0.215 \pm 0.005)\,\frac{\mathrm{K}}{\mathrm{cm}}$). The trapping efficiency at zero gradient $\eta_0 = 0.882 \pm 0.004$ is, however, close to the large grain sample ($\eta_0 = 0.901 \pm 0.016$). Figure 5.13 (b) shows a linear increase of the threshold field B^*. But the sensitivity of the threshold field to the temperature gradient $b = (17 \pm 2)\,\mu\mathrm{T}$ is much smaller compared to the large grain sample with $b = (204 \pm 6)\,\mu\mathrm{T}$. This is expected because the lines in Figure 5.12 cross the x-axis close to zero.

According to the small value of b that is obtained above, equation 5.34 predicts an almost linear decrease of trapped flux magnitude with increasing temperature gradient. This can easily be seen because the quadratic term in equation 5.34 is proportional to b.

Figure 5.14 shows B_{TF} versus ∇T data of the fine grain sample that is recorded at $B_e = 100\,\mu\mathrm{T}$. Additionally, two fits according to equation 5.9 and 5.34 are depicted. Figure 5.14 shows the almost strictly linear decrease with a very small quadratic correction term that is expected.

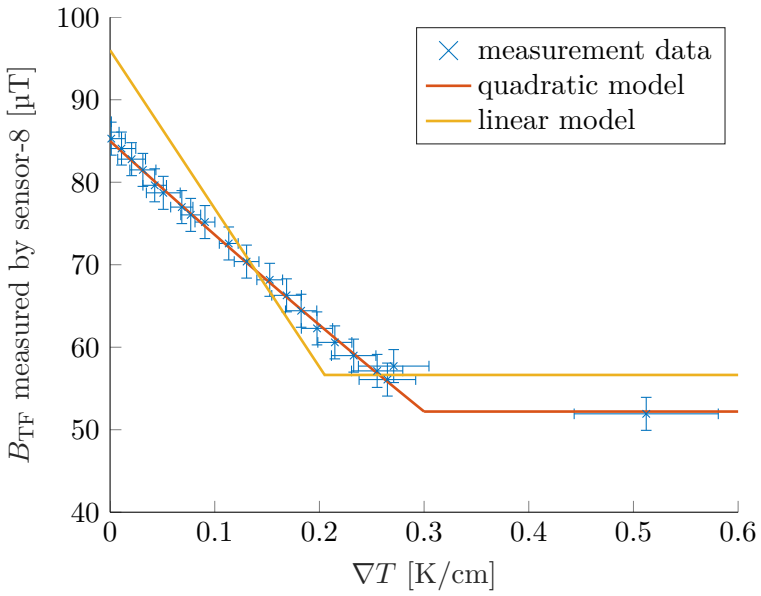

Figure 5.14.: Trapped flux magnitude versus temperature gradient of fine grain sample. A fit according to equation 5.34 is depicted and labelled "quadratic model". Table 5.3 states the fit parameters. For comparison the "linear model" according to equation 5.9 is also depicted. The quadratic model agrees well with the data.

Figure 5.14 shows good agreement between measurement data and fit. The RMSE reduces from RMSE = 5.94 from the linear fit to RMSE = 0.61 for the quadratic fit. This is mostly caused by the fact that trapped flux at $\nabla T = 0 \frac{\mathrm{K}}{\mathrm{cm}}$ is not predicted to be 100% like in the linear model. The fit algorithm yields the following results: $b = 20\,\mu\mathrm{T}$, $\eta_0 = 0.85 \pm 0.002$, $g_\mathrm{c} = (0.88 \pm 0.15)\,\frac{\mathrm{K}}{\mathrm{cm}}$, and $\kappa = (0.302 \pm 0.009)\,\frac{\mathrm{K}}{\mathrm{cm}}$. To achieve these results b must be limited to 20 µT (This is also why no confidence interval is stated for b). Leaving it unlimited leads to fit results of $b = (100 \pm 5e6)\,\mu\mathrm{T}$, $\eta_0 = 0.85 \pm 0.002$, $g_\mathrm{c} = (1.4 \pm 3e4)\,\frac{\mathrm{K}}{\mathrm{cm}}$, and $\kappa = (0.307 \pm 0.009)\,\frac{\mathrm{K}}{\mathrm{cm}}$. This shows again that the fit is not very stable and that deviations in one parameter can be compensated by others. Since the uncertainties are so much larger for the second set of parameters a limitation of b to the interval [0,20] is reasonable.

Similarly to the large grain sample both fit methods are applied to each sensor group. Table 5.3 shows the results when the parameters are obtained from the fit according to equation 5.34, and Table 5.4 states the obtained results from fits with equation 5.10 and 5.11.

Table 5.3.: Fit parameters obtained from fitting equation 5.34 to data from fine grain sample for all sensor groups individually. b is limited to 20 µT in the fit algorithm. If a parameter runs in a limit no confidence interval is stated. The errors are extracted from square roots of the diagonal elements of the covariance matrix.

Sensor	b [µT]	η_0	g_c [$\frac{K}{cm}$]	κ [$\frac{K}{cm}$]
1	$20 \pm -$	0.984 ± 0.019	0.8 ± 0.5	0.285 ± 0.013
2	$20 \pm -$	0.985 ± 0.019	0.9 ± 0.5	0.285 ± 0.013
3	$20 \pm -$	0.97 ± 0.02	0.8 ± 0.4	0.282 ± 0.014
4	$20 \pm -$	0.944 ± 0.010	0.9 ± 0.4	0.312 ± 0.013
5	$20 \pm -$	0.903 ± 0.009	0.9 ± 0.3	0.311 ± 0.012
6	$20 \pm -$	0.926 ± 0.009	0.9 ± 0.3	0.309 ± 0.012
7	$20 \pm -$	0.903 ± 0.003	0.87 ± 0.17	0.302 ± 0.010
8	$20 \pm -$	0.851 ± 0.002	0.88 ± 0.15	0.302 ± 0.008
9	$20 \pm -$	0.900 ± 0.003	0.87 ± 0.14	0.304 ± 0.009
10	$20 \pm -$	0.930 ± 0.005	0.87 ± 0.16	0.358 ± 0.012
11	$20 \pm -$	0.881 ± 0.004	0.88 ± 0.15	0.358 ± 0.011
12	$20 \pm -$	0.912 ± 0.004	0.89 ± 0.14	0.357 ± 0.011
13	$20 \pm -$	0.898 ± 0.006	0.75 ± 0.15	0.363 ± 0.018
14	$20 \pm -$	0.871 ± 0.005	0.74 ± 0.12	0.361 ± 0.016
15	$20 \pm -$	0.870 ± 0.004	0.76 ± 0.11	0.361 ± 0.013

Like in Table 5.1 the estimated uncertainties in g_c are very large, and b is artificially limited for all sensors to 20 µT. η_0 decreases the further down the sensors are located on the sample, which is expected as was already mentioned above for the large grain data: Because flux is pushed ahead of the phase front the external field is enhanced when the phase front reaches the upper sensor positions. Additionally, the top sensor row (sensors 1-3) measure higher fields due to the clamping area (see chapter 4.8.4). It is also stated above for the large grain data that g_c is expected to decrease for lower sensor groups. That is the case in Table 5.3, however, the uncertainties make the decrease insignificant. There is also an increase in κ noticeable in Table 5.3. This is mainly caused by the single data point at high gradients ($\nabla T = 0.51 \frac{K}{cm}$). This data point was recorded during a refill of the cryostat with liquid helium and the cooldown parameters are not consistent over the sample: For sensor groups higher on the sample the local temperature gradient is smaller and more trapped flux is measured. For lower sensor groups less trapped flux is measured. On average 61 µT is measured in the top row and only 41 µT in the bottom row. This very large difference leads to higher κ values for sensor groups located at lower position on the sample. However, this is only one data point that was measured during a refill. The value of κ has thus a larger uncertainty than what is obtained from the fit algorithm.

For comparison Table 5.4 states the parameters b, η_0, and g_c that are obtained when equation 5.10 and 5.11 are fitted to the data like in Figure 5.13.

Table 5.4.: Fit parameters obtained from fitting equation 5.10 and 5.11 to data from all sensors individually. The errors correspond to the 68.3% confidence interval, or 1-σ.

Sensor	$b\,[\mu T]$	η_0	$g_c\,[\frac{K}{cm}]$	$\kappa\,[\frac{K}{cm}]$
1	0 ± 3	0.980 ± 0.006	0.86 ± 0.05	–
2	0 ± 0.11	0.988 ± 0.006	0.83 ± 0.05	–
3	0.8 ± 0.8	0.983 ± 0.007	0.79 ± 0.05	–
4	5.7 ± 0.7	0.968 ± 0.005	0.82 ± 0.02	–
5	9 ± 2	0.928 ± 0.006	0.82 ± 0.04	–
6	9 ± 2	0.957 ± 0.006	0.80 ± 0.04	–
7	10.1 ± 0.7	0.934 ± 0.002	0.755 ± 0.014	–
8	17 ± 2	0.882 ± 0.004	0.78 ± 0.03	–
9	16 ± 2	0.923 ± 0.003	0.762 ± 0.017	–
10	10.1 ± 0.2	0.932 ± 0.004	0.88 ± 0.04	–
11	12.7 ± 1.6	0.882 ± 0.006	0.91 ± 0.05	–
12	11.1 ± 1.2	0.917 ± 0.005	0.88 ± 0.04	–
13	12.0 ± 0.4	0.911 ± 0.007	0.74 ± 0.05	–
14	16.4 ± 1.7	0.884 ± 0.008	0.74 ± 0.05	–
15	18 ± 3	0.885 ± 0.008	0.74 ± 0.05	–

Like in the case of the large grain sample the parameters obtained with this method are more precise than the ones obtained when fitting B_{TF} versus ∇T data. The parameters obtained from both methods are close to each other but not all lay within a 3-σ interval. The uncertainties stated here are, however, only statistical errors obtained from fit algorithms and no systematic errors are included.

Again, an increase in b is observed for lower sensor positions like for the large grain sample. There is also a decrease in η_0 for lower sensor positions which is also expected. g_c also decreases as it is expected with the exception of the fourth sensor row (sensors $10-12$) where g_c rises again. The cause might be an incorrectly measured temperature gradient.

The parameters from Table 5.3 can now be used to predict trapped flux in dependence of temperature gradient for different external field magnitudes. Since dedicated measurement series are recorded for the fine grain sample these series are shown in Figure 5.15. Additionally, equation 5.34 is plotted for the corresponding external magnetic flux magnitude and parameters taken from Table 5.3. Figure 5.15 shows the data for sensor group 8.

Before trapped flux is predicted with equation 5.34, κ must be scaled like it was done for the large grain sample. As can be seen in Figure 5.15 (a) even with $B_e = 20\,\mu T$ there is still trapped flux at high temperature gradients. Therefore, the effect of the external field on κ is smaller than for the large grain sample. The parameter b gives the sensitivity of B^* to ∇T and, therefore, a relation between B_{TF}, B_e and ∇T. Since b is a factor of 10 smaller for the fine grain sample than for the large grain sample the effect of B_e on κ is also assumed to be a factor of 10 smaller. So that κ for the fine

grain sample is estimated as

$$\kappa(B_\mathrm{e}) = \kappa(B_\mathrm{e} = 100\mu\mathrm{T}) + \frac{B_\mathrm{e} - 100\mu\mathrm{T}}{100\mu\mathrm{T}} \cdot 0.01 \frac{\mathrm{K}}{\mathrm{cm}} \tag{5.35}$$

The constant of 0.01 is the κ value of the large grain (≈ 0.1) divided by 10. The physical interpretation why the fine grain sample reacts so differently on the external magnetic field is not yet understood which is why the scaling has to be done like this for now. It still leaves open questions but can serve as a tool to predict trapped flux. Figure 5.15 shows the results.

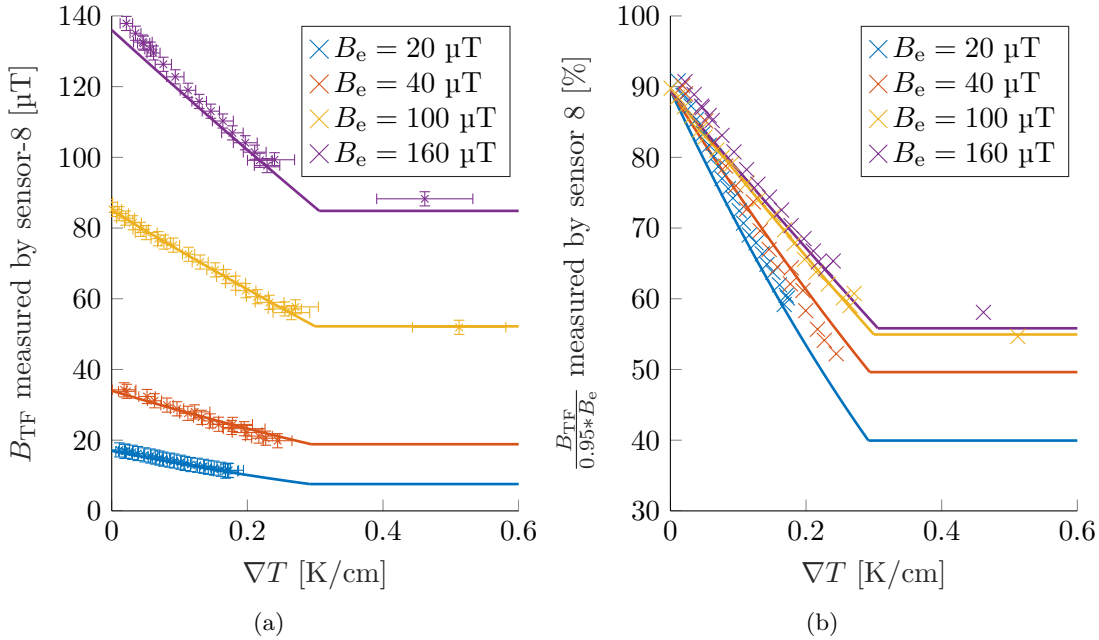

(a) (b)

Figure 5.15.: (a) Trapped flux magnitude versus temperature gradient of fine grain sample for different external magnetic flux densities. Equation 5.34 is plotted with parameters from Table 5.3. κ is scaled according to equation 5.35. (b) Shows the same data points as in (a), but B_TF is presented as a fraction of $0.95 B_\mathrm{e}$. The factor of 0.95 is inserted because simulations show that only 95% of trapped flux density is measured by sensor group 8. In (b) error bars are omitted for better readability. The model predicts trapped flux correctly.

The predictions agree well with the data. The largest source of error is κ. But since κ is determined on the basis of only one data point ($\nabla T = 0.51 \frac{\mathrm{K}}{\mathrm{cm}}$) it is not possible to predict κ precisely.

5.4.2. Fine Grain Sample with Defect

Next, the model is applied to data from the fine grain sample with the defect, and the single grain sample. For theses samples no detailed B_TF versus B_e measurement data

is available. Therefore, only the fit of B_{TF} versus ∇T according to equation 5.34 is performed. Here, only sensor group 8 is shown as the exemplary sensor group.

Figure 5.16 shows the results for the fine grain sample with defect. For this sample dedicated B_{TF} versus ∇T measurement series are recorded. The fit according to equation 5.34 is done for the series with $B_{\mathrm{e}} = 100\,\mu\mathrm{T}$ the resulting line is plotted in red. The RMSE equals 1.29, and the obtained parameters are: $b = 20\,\mu\mathrm{T}$, $n_0 = 0.847 \pm 0.006$, $g_{\mathrm{c}} = (0.99 \pm 0.04)\,\frac{\mathrm{K}}{\mathrm{cm}}$, and $\kappa = (0.29 \pm 0.01)\,\frac{\mathrm{K}}{\mathrm{cm}}$. The lines for the other measurement series are predictions with the parameters from the first fit and a scaled κ according to equation 5.35.

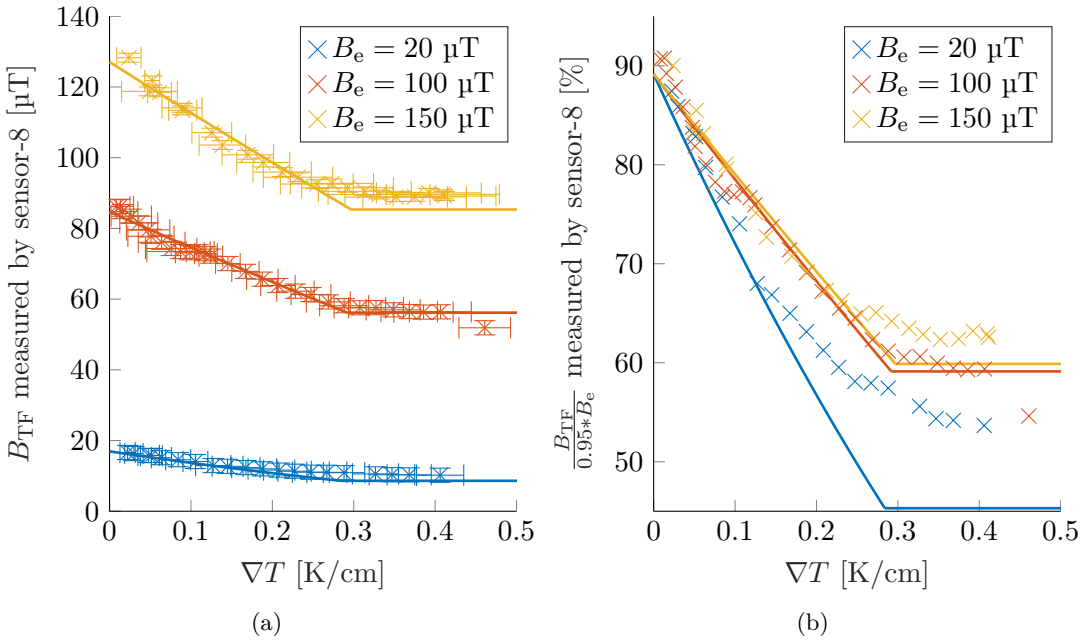

(a) (b)

Figure 5.16.: (a) Trapped flux magnitude versus temperature gradient of fine grain sample with defect for different external magnetic flux densities. Equation 5.34 is plotted with parameters gained from a fit to the measurement series at $B_e = 100\,\mu\mathrm{T}$ and stated in the paragraph above. κ is scaled according to equation 5.35. (b) Shows the same data points as in (a), but B_{TF} is presented as a fraction of $0.95 B_{\mathrm{e}}$. The factor of 0.95 is inserted because simulations show that only 95% of trapped flux density is measured by sensor group 8. In (b) error bars are omitted for better readability. The model predicts trapped flux correctly, including the plateau at $\nabla T > 0.3\,\frac{\mathrm{K}}{\mathrm{cm}}$.

As is already mentioned in section 4.5.2 the local temperature gradient at sensor position 8 cannot be extracted due to a bad thermal contact. This makes the temperature gradient data less accurate and is the most likely cause for the bump at $\nabla T \approx 0.1\,\frac{\mathrm{K}}{\mathrm{cm}}$ in the $B_{\mathrm{e}} = 100\,\mu\mathrm{T}$ series. Uncertainties in ∇T have, of course, an influence on the fit. But the predictions fit very well with the data. The discrepancy between measurement and prediction in Figure 5.16 (b) for $B_{\mathrm{e}} = 20\,\mu\mathrm{T}$ seem very large, but Figure 5.16 (a) shows

that the predictions are within the error bars. For $B_e = 150\,\mu T$ and high gradients the predictions underestimate trapped flux but are is still within a 3-σ interval.

One point that stands out is at $\nabla T = 0.46\,\frac{K}{cm}$ in the $B_e = 100\,\mu T$ series. This point is recorded during a helium refill where a large natural temperature gradient is established across the sample. The temperature gradient during these cooldowns are, however, not as consistent as for heater controlled cooldowns. This makes the error on the extracted temperature gradient larger. It also affects the overall dynamics because geometry effects are changing during the cooldown due to the changing temperature gradient. Nevertheless, the point is included in the fit. Excluding this point decreases κ to $(0.278 \pm 0.009)\,\frac{K}{cm}$ which yields even better agreement between prediction and measurement.

Besides that, in the model it is assumed that there is a large gap in the distribution function of the pinning force between f_0 and f_1 (Figure 5.3) so that trapped flux is independent of the temperature gradient once f_0 is reached. This, however, does not have to be the case and contributions from different types of pinning centres might actually overlap. This would mean that B_{TF} does not necessarily stay constant above κ, but decreases with a different slope.

5.4.3. Single Grain Sample

Finally the model is applied to the single grain sample. The measurement with this sample was the first where a threshold field B^* as described in chapter 4.2 was observed. Since this insight was only gained while post-processing the data, no detailed measurement series of B_{TF} versus B_e were conducted, and B_{TF} versus ∇T was only measured at $B_e = 100\,\mu T$.

Figure 5.17 (a) shows the fit of equation 5.34 to the measurement series. The obtained parameters are: $b = (361 \pm 130)\,\mu T$, $\eta_0 = 0.887 \pm 0.019$, $g_c = (0.34 \pm 0.12)\,\frac{K}{cm}$, $\kappa = (0.095 \pm 0.003)\,\frac{K}{cm}$. As with the fits before the large errors on b and g_c stand out. b and g_c are also larger than for the large grain sample, even though in chapter 4.5.1 no significant difference between the two samples is observed. And due to the large uncertainties of b and g_c the parameters of single and large grain sample actually agree with each other.

Nevertheless, the difference seems large, so as a test b is limited to $230\,\mu T$. This results in: $b = 230\,\mu T$, $\eta_0 = 0.904 \pm 0.013$, $g_c = (0.232 \pm 0.004)\,\frac{K}{cm}$, and $\kappa = (0.098 \pm 0.002)\,\frac{K}{cm}$. Figure 5.17 (b) shows the fit.

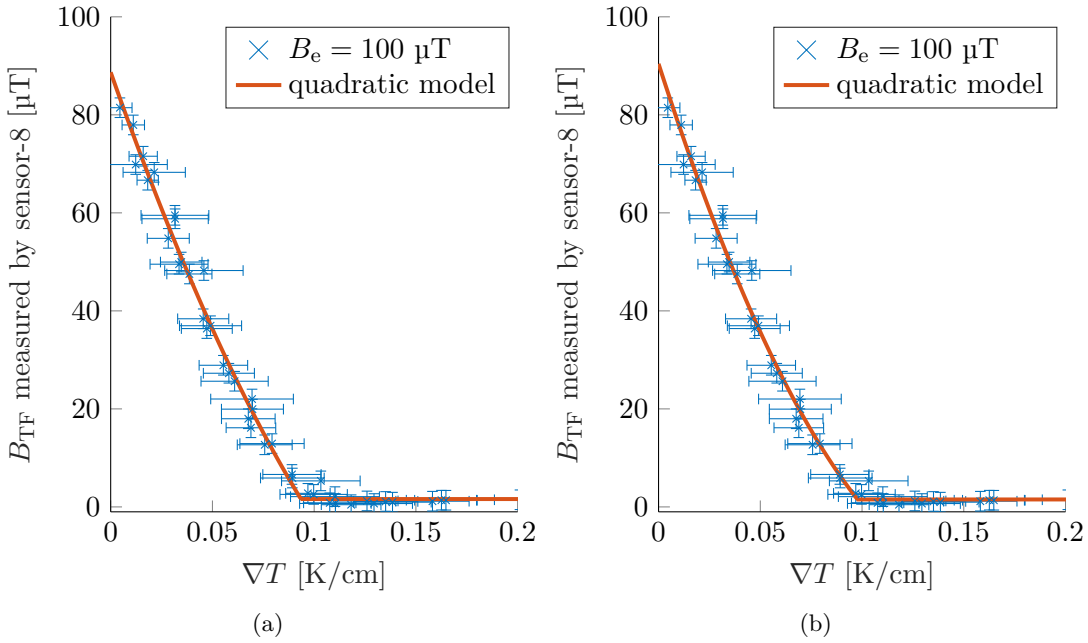

Figure 5.17.: Trapped flux magnitude versus temperature gradient of single grain sample. A fit according to equation 5.34 is depicted and labelled "quadratic model". The fit parameters are stated in the two paragraphs above. (a) shows the fit without limits, in (b) b is limited to 230 µT. No difference between the two plots is discernible.

Both fits in Figure 5.17 (a) and (b) fit well with the data. The root mean square error (RMSE) of the unlimited fit is 2.624 and for the limited it is 2.652. This is a difference of 1.06%. By limiting b, $g_{\mathrm{c}} = (0.232 \pm 0.004)\,\frac{\mathrm{K}}{\mathrm{cm}}$ is also much closer to the value of the large grain ($g_{\mathrm{c}} = 0.22 \pm 0.07$) $\frac{\mathrm{K}}{\mathrm{cm}}$.

This example shows that fits according to equation 5.34 are fairly insensitive to changes in b because they can be compensated by adjusting g_{c} accordingly. This is a problem for the fit which is also reflected in the large uncertainties of b and g_{c}. To determine the parameters in the model more accurately fits according to equation 5.10, and 5.11 are more reliable. These fits, however, require much more data points, since several measurement series of B_{TF} versus B_{e} must be recorded.

5.4.4. Implications for Large and Fine Grain

Analyses of the large and fine grain samples with the aid of the developed model reveal distinct differences between the two. Firstly, it indicates that there are different kinds of pinning centres in the fine grain material with a pinning force greater than f_0 (Figure 5.3). This is evident in Figure 5.16 where trapped flux stays constant for $\nabla T > \kappa$. Grain boundaries might be the cause of these pinning centres, but in [90] no pinning at boundaries is observed. However, in [87, 90] fine grain niobium also showed more trapped flux than large grain material. Impurities that might be introduced in the rolling process are a possible explanation [64, 90]. Secondly, it revealed that the

maximal pinning force of "weak" pinning centres f_0 is smaller in the large grain material than the fine grain material because κ of the large grain material is much smaller than κ of the fine grain material.

Besides differences in flux pinning centres the response to an external magnetic field is also very different between the two materials. This is evident in the large difference in b as well as in Figure 5.5 and 5.12. The reason why the two materials behave so differently is not yet understood and is subject for further investigation.

5.5. Flux Line Velocity

Lastly, the velocity of flux lines inside the superconductor is estimated and compared to measurement data. This estimation of the flux line velocity is again proposed by Prof. T. Kubo. Since flux expulsion or trapping happens close to T_c the derivation is done with the Ginzburg-Landau approximation. In chapter 4.3 it is observed that the trapped flux magnitude depends on the transition time (or cooldown rate). For the case of full expulsion ($B_e < B^*$) the flux motion is given by the equilibrium of thermal force and a viscous force f_{vis}:

$$f_{vis} = f_{th} \tag{5.36}$$

$$\eta_{vis} v = S^* \nabla T \tag{5.37}$$

Here, η_{vis} is the viscosity, and v the flux line velocity. The viscosity is given by $\eta_{vis} = \frac{\Phi_0 B_{c2}}{\rho_n}$ with B_{c2} the second critical flux density, and ρ_n the normal conducting conductivity. The transport entropy can also be expressed as $S^* \approx \frac{\partial}{\partial T} \frac{\Phi_0^2}{4\pi\mu_0\lambda(T)^2}$. In the Ginzburg-Landau regime it holds that $\lambda(T)^{-2} = \lambda_0^{-2}\left(1 - \frac{T}{T_c}\right)$. Plugging this in equation 5.37 and using the GL approximation from chapter 2.2.4 yields

$$v = \frac{\rho_n}{2\mu_0\kappa^2} \frac{\nabla T}{T_c} \left(1 - \frac{T}{T_c}\right)^{-1} \tag{5.38}$$

The normal conductivity is estimated to be $\rho_n = \frac{\rho_n(300\mathrm{K})}{RRR} = \frac{1.45 \cdot 10^{-7}\Omega\mathrm{m}}{300} \approx 0.5 \cdot 10^{-9}\Omega\mathrm{m}$. ∇T is set to $0.1\,\frac{\mathrm{K}}{\mathrm{cm}}$, $T/T_c = 0.999$ (see [64]), and $\kappa = 0.82$ [62]. The value for T/T_c is obtained by calculating (using the Ginzburg-Landau theory) the temperature at which $B_{c1} = 100\,\mu\mathrm{T}$. Plugging this in the equation above yields

$$v \approx 30\,\frac{\mathrm{cm}}{\mathrm{s}}. \tag{5.39}$$

To validate this velocity the trapped flux magnitude as well as the wave magnitude in y-direction from the large grain measurements are again plotted in Figure 5.18 like in chapter 4.3.

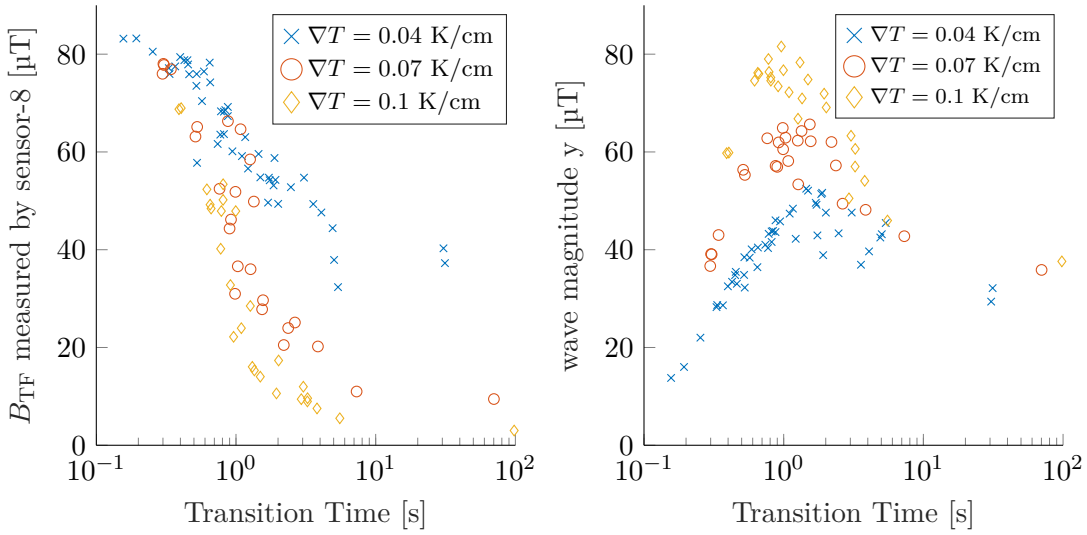

Figure 5.18.: (a) B_{TF} versus transition time for different temperature gradients. (b) Wave magnitude in y-direction of the same cooldowns versus transition time. The legend is identical for both plots. Both plots show a time constant of 1 s.

In Figure 5.18 (b) there is a peak at 1 s for $\nabla T = 0.1 \frac{K}{cm}$. A descriptive explanation for this could be that for transition times smaller than one second the phase front moves too fast for flux lines to be de-pinned and be pushed ahead of it. And for transition times longer than one second the flux lines have enough time to be pushed out to the sides. In Figure 5.18 (a) a sharp decrease in B_{TF} is evident up to a transition time of 1 s, which again shows a time constant of 1 s.

Since the sample is 10 cm long, in the first order approximation this would correspond to a velocity of 10 $\frac{cm}{s}$. This is a factor of three smaller then the expected velocity. It is, however, in the correct order of magnitude. If $\frac{T}{T_c}$ would be set to 0.997 it results in $v = 10 \frac{cm}{s}$. So maybe flux lines are still moving at lower temperatures within the sample, or the movement is more complex.

It is also evident in the plot that the peak moves to longer transition times for smaller temperature gradients. For $\nabla T = 0.04 \frac{K}{cm}$ the peak is around at 1.6 s. According to equation 5.38 the peak would be expected at 0.78 s for $\frac{T}{T_c} = 0.999$ and at 2.3 s for $\frac{T}{T_c} = 0.997$. This implies that a simple adjustment of the temperature at which flux lines can still move to $\frac{T}{T_c} = 0.997$ is not sufficient as an explanation for the discrepancy between prediction and measurements. The more likely explanation is a more complex flux line movement which is not fully covered in the model. However, the tendency to where the peak shifts is correctly predicted. But due to the large scatter in the data points, these plots can anyway only give an estimation of the effect of the temperature gradient. Data from the fine grain samples is not shown again at that point but can be found in chapter 4.5.2. It agrees with the data from the large grain sample.

Simulations with flux lines in a viscous medium might also help to understand the

relationship between flux line velocity and the peak position. Due to time constraints these investigations could not be done in the scope of this thesis and must be subject for further research. A better understanding of the microscopic dynamics of the flux lines would also give more insight in the relation of cooldown rate and trapped flux.

6. Summary and Outlook

The goal of this thesis is to improve the understanding of flux trapping mechanisms so that with these insights new material treatments or cooldown schemes to reduce trapped flux in SRF cavities might be developed in the future. For this purpose a new experimental setup was designed which allows parameters that influence trapped flux to be altered independently. In contrast to the elaborate cavity measurements the new setup relies on measurements conducted with samples. The presented results give new insights in the dynamics of flux trapping and a phenomenological model is developed based on these results. With the obtained results and developed model this thesis can be used as foundation for further research on the influence of materials and their treatments on trapped flux.

6.1. Conclusion

6.1.1. Experimental Setup

An important, and large part of the presented work was the design, building, and commissioning of the setup. The presented results show that the setup fulfils its purpose. Namely, to alter the cooldown parameters independently, and to perform more cooldown cycles in a shorter time compared to cavity measurements which gives much better statistics. Additionally, the preparation procedure for a test is much less elaborate compared to cavity measurements because the sample does not need to be particle free. Another benefit is the reduces helium consumption.

The newly implemented active field compensation proved to be very effective and is able to reduce the magnetic flux density at the position of the reference sensors below 25 nT. The simulations of the coils show good agreement to the measurements and suggest a deviation of the magnetic field at the sample position of less than 1%. So that together with the field inhomogeneities of the surrounding field the measurement error in the magnetic flux density data is estimated to be only 2 µT. In the context of the external magnetic field a new method to calibrate the AMR sensors is discussed and Figure 3.17 shows that it yields the expected results. The drawback of this method is, however, that any inhomogeneities in the surrounding field are included in the calibration so they cannot be measured.

The relatively large sample size ($10 \times 6 \times 0.3$ cm) makes the setup less susceptible to any edge effects that might occur during flux expulsion. It also provides sufficient space to place a sensor array of 5×3 sensors over the sample which makes the investigation of dynamic and geometric effects possible. The simple geometry also makes interpreting the recorded data easier and, therefore, more unambiguous than for a cavity geometry.

Controlling the temperature and temperature gradient with two independently PID controlled electric heaters proved to be a fast and relatively accurate way to perform the

cooling cycles. They allow the temperature gradient and cooldown rate to be controlled independently within certain limits. And by moving the heaters away from the sample with copper blocks no magnetic field created by the heaters can be detected. The large number of thermal sensors makes it possible to measure the local temperature gradient on the sample and not only the mean gradient.

On the other hand inconsistencies in the cooldown gradient and cooldown rate are the largest source of error in the current setup: Firstly, the middle of the sample is cooled by the helium gas surrounding the sample, so that the temperature gradient is not constant across the sample. Wrapping the sample in cotton wool reduces the problem but does not resolve it completely. Secondly, the thermal contact of the glued temperature sensors is not always consistent so the local temperature gradient cannot be extracted when a sensor does not have a proper contact. Thirdly, the temperature is not always lowered at a constant rate for fast cooldowns, for which the temperature gradients are also reproducible less exact than for slower cooldowns.

But as can be seen in chapter 4 the data recorded with this setup is self-consistent, and reproducible across different samples (see Figure 4.10, and 4.18), as well as for the same sample, as is shown for the remeasured large grain sample (chapter 5.3). The setup is also able to reproduce expected results (see chapter 6.1.2). But due to the large number of cooldowns and relatively large parameter space in ambient field, temperature gradient, and cooldown rate, the curves could be recorded in more detail compared to cavity measurements. This also showed unexpected behaviours (see section 6.1.2).

6.1.2. Measurement Results

The measurements show that with increasing temperature gradient the magnitude of trapped flux decreases. This is in agreement with other measurements [43, 45, 85]. Depending on the material the expulsion is more or less effective: In case of the samples cut from the large grain material near 100% flux expulsion is reached with sufficiently large gradients. Whereas, the measured fine grain samples always trap flux and the decrease with temperature gradient is less steep. The most extreme case is observed with the coated sample where no decrease in trapped flux magnitude was measurable with the achieved gradients.

Investigation of the trapped flux magnitude in dependence of the external magnetic flux density magnitude revealed expected as well as unexpected results: For small temperature gradients a linear correlation between trapped flux and external flux magnitude is observed. This confirms the results reported in [87]. However, for larger temperature gradients it is observed that magnetic flux only gets trapped when the external flux density magnitude is larger than a temperature gradient dependent threshold field. This threshold field increases for increasing temperature gradient. This phenomenon could be measured directly for the large grain sample (Figure 4.3) but for the fine grain sample the effect is so small that it can only be detected by fitting a line through data points with the same temperature gradient (Figure 5.13).

A parameter that is generally believed to have no effect on flux trapping is the cooldown rate [44, 49]. The measurement results presented in chapter 4.3, however, show a clear correlation of trapped flux on the cooldown rate: For very fast cooldowns with transition times below one second a steep increase of trapped flux is measured

with decreasing transition time for all temperature gradients and only for transition times above $\mathcal{O}(10\text{s})$ trapped flux does not depend on it. This is also reflected in the wave magnitude that is pushed in front of the phase front. The most likely explanation for this behaviour is the viscous force which slows down flux lines (chapter 5.5).

Lastly, it is found that even the simple geometry of the sample has an influence on the distribution of trapped flux. Due to expulsion of flux in the already superconducting part the flux density at the position of the phase front is enhanced. With help of simulations an enhancement by a factor of roughly 2 is estimated in the case of full expulsion. This effect might also be important for cavity operation where, depending on the configuration of a cryomodule, flux could be pushed towards regions of high RF field during cooldown.

6.1.3. Model

The measured results are compared to the model developed by T. Kubo [64] but the model does not agree with the data. Therefore, a new phenomenological model is developed in cooperation with Prof. T. Kubo which explains the observed behaviour with help of a thermal force and a distribution function of the pinning strength. It is assumed that pinning centres only contribute to flux trapping when their pinning force is larger than the thermal force. Analysis of the data showed that there exists a term in the equation for the trapped flux magnitude which is quadratic in temperature gradient.

The newly developed model shows good agreement with data recorded with the large grain, single grain, and fine grain sample, and is able to predict trapped flux magnitude at different external magnetic flux densities.

The model also showed where there are still open questions that need to be answered: It is still not entirely understood how the de-pinning mechanism works and how the external magnetic field strength influences flux trapping on a microscopic level. Or why the large grain material reacts so differently to changes in the external field compared to the fine grain material. This must be topic of further research and work is ongoing with Prof. T. Kubo. However, this is an experimental thesis so the main focus lies on gathering new data which helps to understand flux trapping rather than developing new models.

Besides the new model, the dependence of trapped flux on cooldown rate was investigated and the flux line velocity estimated. The estimation showed agreement with the measurement data in the right order of magnitude as well as the trend for different temperature gradients.

6.2. Outlook

The capabilities of the new setup shows dependencies of trapped flux on various parameters in more detail than before which opened up new questions. To answer these questions by further theoretical analysis of the existing data as well as new measurements will be topic of further research. The theoretical description and explanation of the data will continue in collaboration with Prof. T. Kubo, and several steps can be taken on the experimental side to improve the underlying data:

One option to increase the quality of the data is to further improve the experimental setup. It is noted above that inconsistencies in temperature control and measurement are the largest source of error in the current setup. This could be reduced by enclosing the sample in a vacuum chamber so that the sample and the sensors are not directly cooled by helium gas. The sample temperature and temperature gradient would then only be influenced by copper blocks at the ends. A simpler approach that could also improve the temperature behaviour of the sample is to rotate the sample 90° so that in lies flat in the cryostat (long dimension along x- or y-direction). This decreases the natural temperature gradient on the sample caused by the temperature gradient in the surrounding helium gas. Additionally, the coils or their power supply could be upgraded so higher magnetic fields are achievable. This would enhance the parameter space and, therefore, could decrease uncertainties in fits.

Apart from enhancing the setup it could also be extended. This could be done with an array of thermal sensors like in T-mapping systems for cavities [98]. A prototype of such a setup is already built by A. Cierpka in the context of his bachelor thesis [97]. The benefit of a system like this is that inconsistencies in the phase front from left to right in the sample can be measured. This is already demonstrated in [97] where it is observed that the phase front is slightly tilted when it moves through the sample and is not perfectly horizontal. The resistors which are used as sensors in this setup could also be used to heat up the sample locally so that different phase front shapes can be generated. Additionally, a current could be forced through the sample horizontally to investigate if the Lorentz force created by the current can help de-pin flux lines.

But the setup can also be used in its current form to gather more data which might help to understand flux trapping. For this the existing samples can be treated in various ways, including surface treatments like BCP or electro polishing, temperature treatments at different temperatures, as well as other treatments like bending a sample back and forth to simulate some of the material strains during manufacturing. Of course other samples like nitrogen doped niobium, Nb_3Sn, multilayer structures ([25, 99]), or even other elements like lead can be tested to increase the available data. Combining the results gained from the different materials with other methods from material science like XRD can give insights on how for example grain structure influences trapped flux.

Complementary to measurements with this setup other methods like neutron tomography [95] can be used to investigate trapped flux, especially the phase front. In the course of this thesis an experiment using neutron tomography was carried out, but due to technical issues the critical temperature could not be reached. These issues are now resolved and the experiment can be repeated.

Using the gathered data methods to reduce trapped flux can hopefully be identified and pursued further.

A. Appendix

A.1. Supplementary Data: Active Field Compensation

Chapter 3.1.2 presents no detailed description of the small Helmholtz coil as it is similar to the large Helmholtz-coil. Therefore, a detailed description of the small Helmholtz-coil follows in the section below.

The small Helmholtz-coil pair is mounted perpendicular to the large Helmholtz-coil and creates magnetic field in y-direction (perpendicular to the largest sample surface). Figure A.1 and A.2 show the y-component of the magnetic flux density along the same lines as in chapter 3.1.2. Figure A.1 shows it along three vertical lines at $x = -3, 0, 3\,\mathrm{cm}$ and Figure A.2 along five horizontal lines in x-direction at $z = -5, -2.5, 0, 2.5, 5\,\mathrm{cm}$. The field profile along the y-direction is not depicted, since the sample is only $0.3\,\mathrm{cm}$ thick and no significant deviation of the design field is observed on such small scales.

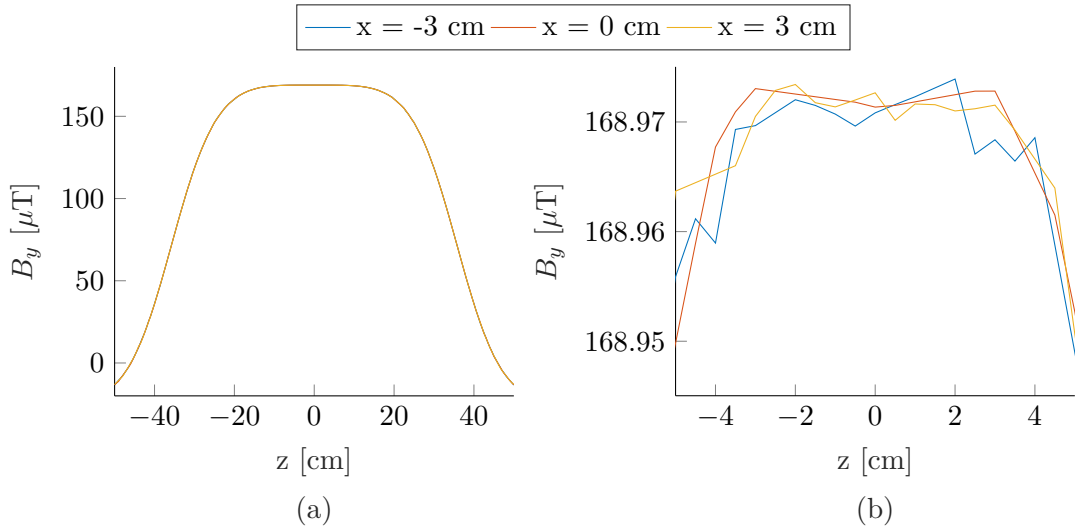

Figure A.1.: y-component of flux density created by the small Helmholtz-coil pair along three vertical lines at $x = -3, 0, 3\,\mathrm{cm}$. The coils are centred around $x = z = 0\,\mathrm{cm}$. The right plot shows a close up of the same data at the sample position from $z = -5\,\mathrm{cm}$ to $z = 5\,\mathrm{cm}$. The legend is identical for both plots. The field is nearly constant in the sample volume.

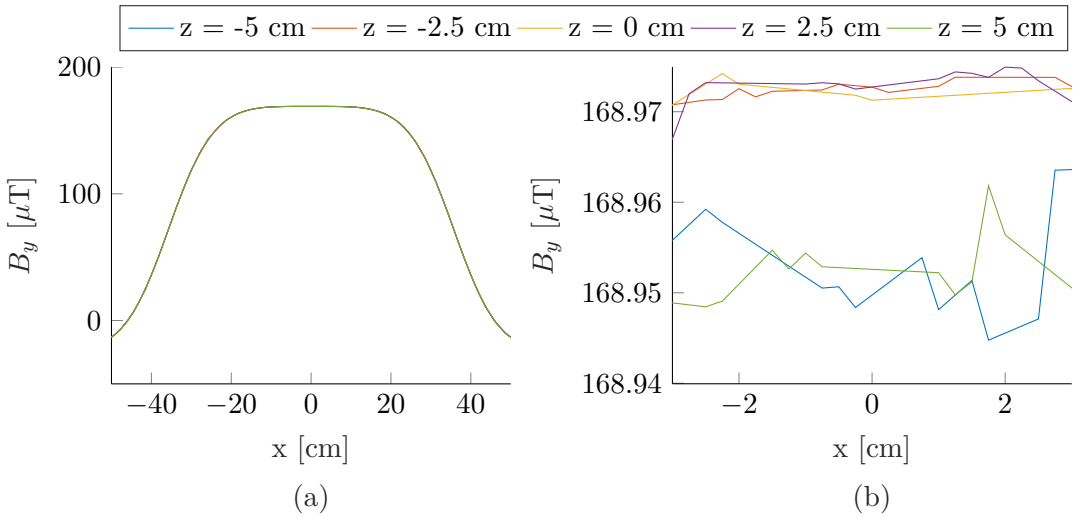

Figure A.2.: y-component of flux density created by the small Helmholtz-coil pair along five horizontal lines at $z = -5, -2.5, 0, 2.5, 5\,\text{cm}$. The coils are centred around $x = z = 0\,\text{cm}$. The right plot shows a close up of the same data at the sample position from $x = -3\,\text{cm}$ to $x = 3\,\text{cm}$. The colour legend is identical for both plots. The field is nearly constant in th sample volume.

The largest deviation of 0.02 µT is visible in Figure A.2 (b). This corresponds to a relative error smaller than 0.1%. If the sample is shifted an additional 2 cm up in the real experiment, the maximum deviation is only 0.05 µT. Therefore, a relative error of 1% in real experiments is again reasonable. The maximum generated magnetic flux density in y- and z-direction are both smaller than 0.1 µT and, therefore, negligible.

For a comparison between simulation and experiment, the coil current is ramped from -1.1 A to 1.1 A in 0.1 A steps. The span is smaller then for the solenoid, because the resistance of the Helmholtz-coils is higher and the employed power supply is limited to 70 V.

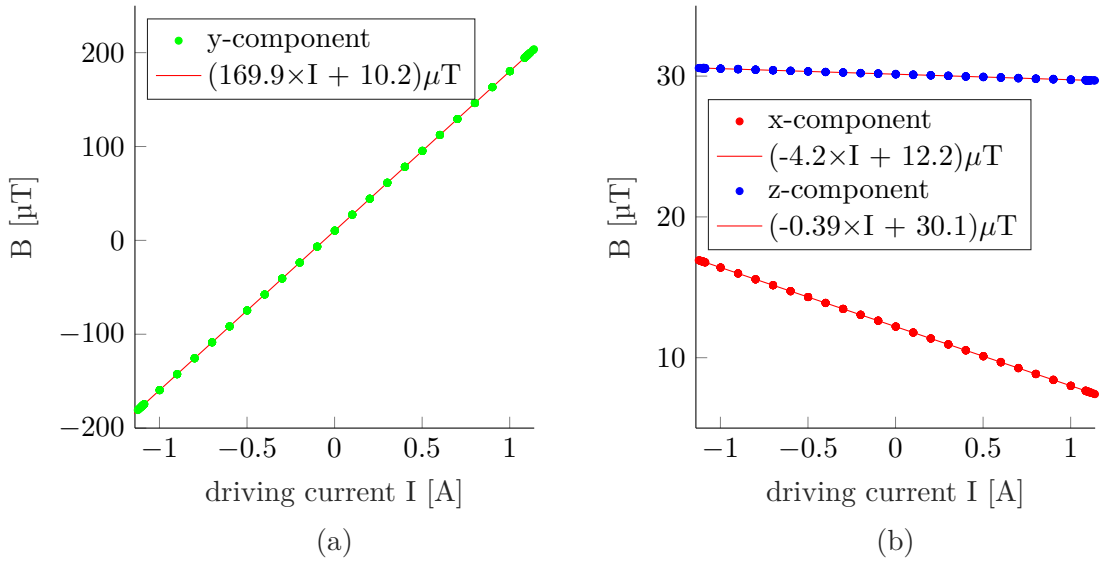

Figure A.3.: (a) measured y-component generated by the small Helmholtz-coil pair versus the excitation current with linear fit. (b) x- and z-component generated by the small Helmholtz-coil with linear fits. The slope in (a) fits well with the simulations. Due to a misalignment of sensors and coils the slopes in (b) are not zero.

The linear fit in Figure A.3 (a) shows a coil constant of 169.9 $\frac{\mu T}{A}$ while the simulation predicts 169.0 $\frac{\mu T}{A}$. The discrepancy between simulation and experiment is 0.5% and, therefore, the simulation agrees well with the real experiment.

The fits for x- and z-direction yield a non-zero slope. This is most likely caused by a misalignment of coils and sensors. A rotation of $\approx 1^\circ$ of the sensors compared to the coil is sufficient to result in the fitted slopes.

The offsets of the fits equal the earth's magnetic field and are same as in chapter 3.1.2.

Finally the parameters of all coils are summarized in table A.1 like in chapter 3.1.2. Additionally the field flatness and maximal field in a non-dominant direction are given in a $(10 \times 10 \times 10)\,\mathrm{cm}^3$ volume as well as a $(20 \times 20 \times 20)\,\mathrm{cm}^3$ volume. The volumes are assumed to be in the centre of each coil. Since the sample is shifted 5 cm up from the centre of the solenoid coil the field flatness is better in the $(10\,\mathrm{cm})^3$ cube than the sample volume. The field flatness in these volumes is not relevant for this thesis but since the coils might be used for different experiments it is given here for the sake of completeness.

Table A.1.: Summary of integrated coils. Field flatness and field in non-dominant region are calculated in the sample volume, a $(10\,\mathrm{cm})^3$ cube, and a $(20\,\mathrm{cm})^3$ cube. The field in non-dominant direction is given as a fraction of the field in dominant direction. The maximum flux density stated here is reached with a power supply limited at 70 V and 1.5 A.

	Solenoid	HHC Large	HHC small
Diameter / side-length [cm]	29	73.4	71.4
Length / coil distance [cm]	88	40	38.9
number windings	88	75	75
Coil constant (simulated) $[\frac{\mu T}{A}]$	117.9	164.2	169.0
Coil constant (experiment) $[\frac{\mu T}{A}]$	117.6	165.4	169.9
Max. flux density [µT]	180	190	180
Field flatness [%] sample	0.8	<0.1	<0.1
Field flatness [%]$(10\,\mathrm{cm})^3$ cube	0.4	0.2	0.2
Field flatness [%]$(20\,\mathrm{cm})^3$ cube	1.4	2.3	2.5
Max. stray field [%] sample	0.3	<0.1	<0.1
Max. stray field [%] $(10\,\mathrm{cm})^3$ cube	0.2	<0.1	<0.1
Max. stray field [%] $(20\,\mathrm{cm})^3$ cube	0.7	0.4	0.5

A.2. Supplementary Measurement Results

In this section measurement results are shown that are not presented in chapter 4 because no additional information is gained from them. But since they are part of the measurement data they are presented here. First, data from the fine grain sample with defect is shown. After that data from the fine grain sample with a 91 µm BCP is presented. Specifically trapped flux versus external field, and trapped flux versus cooldown rate data.

A.2.1. Fine Grain with Defect

Figure A.4 shows trapped flux magnitude versus the y-component of the external flux density. Since the field is applied in y-direction it equals the flux density magnitude.

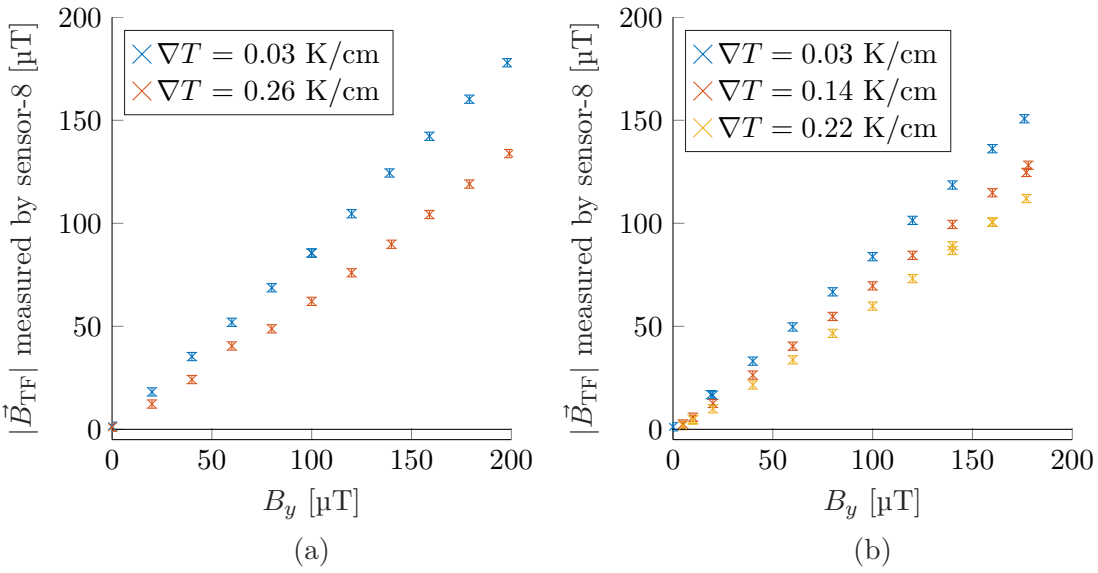

Figure A.4.: Trapped flux measured by the centre sensor group 8 versus B_y. (a) data of the fine grain sample with defect. (b) data of fine grain sample without defect for comparison. Both samples display a similar behaviour.

Figure A.4 shows that for $\nabla T = 0.03\,\frac{\mathrm{K}}{\mathrm{cm}}$ and $B_y = 160\,\mu\mathrm{T}$ the sample with defect trapped slightly more flux (142 µT) compared to the sample without defect (136) µT. But for smaller field amplitudes this difference becomes insignificant and no definite statement that the sample with defect traps more flux can be made from these results.

Next, $|\vec{B}_{\mathrm{TF}}|$ is plotted versus transition time in Figure A.5.

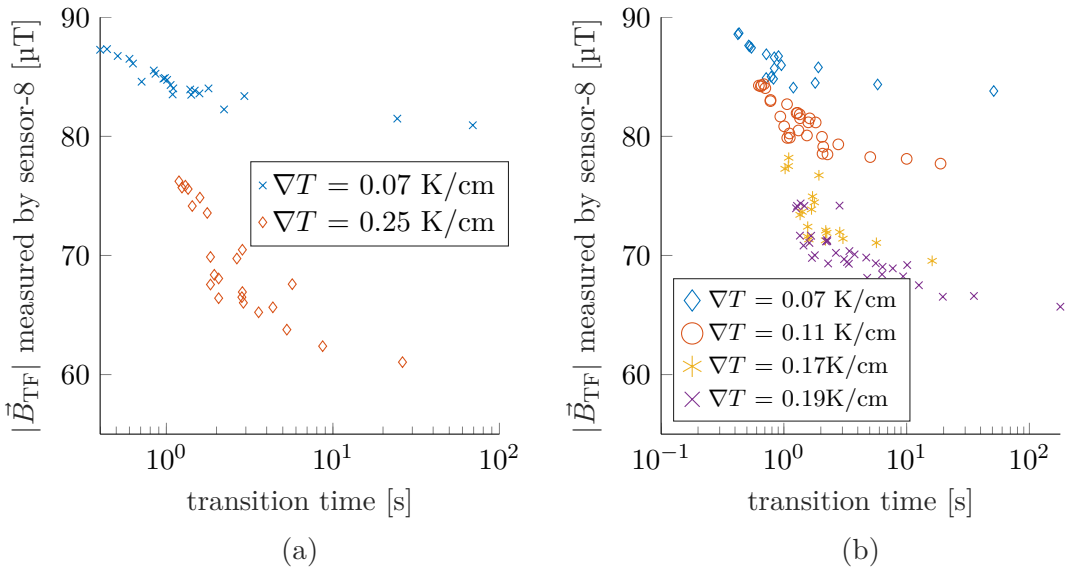

Figure A.5.: Trapped flux measured by the centre sensor group 8 versus B_y. (a) data of the fine grain sample with defect. (b) data of fine grain sample without defect for comparison. The same time constant is observed.

Here a sharp increase in trapped flux is again observed for transition times below one second.

A.2.2. Fine Grain 91 µm BCP

The following two figures show trapped flux versus external field and transition time for the fine grain sample after is was treated with BCP. Figure A.6 shows how trapped flux is influenced by the external flux density magnitude.

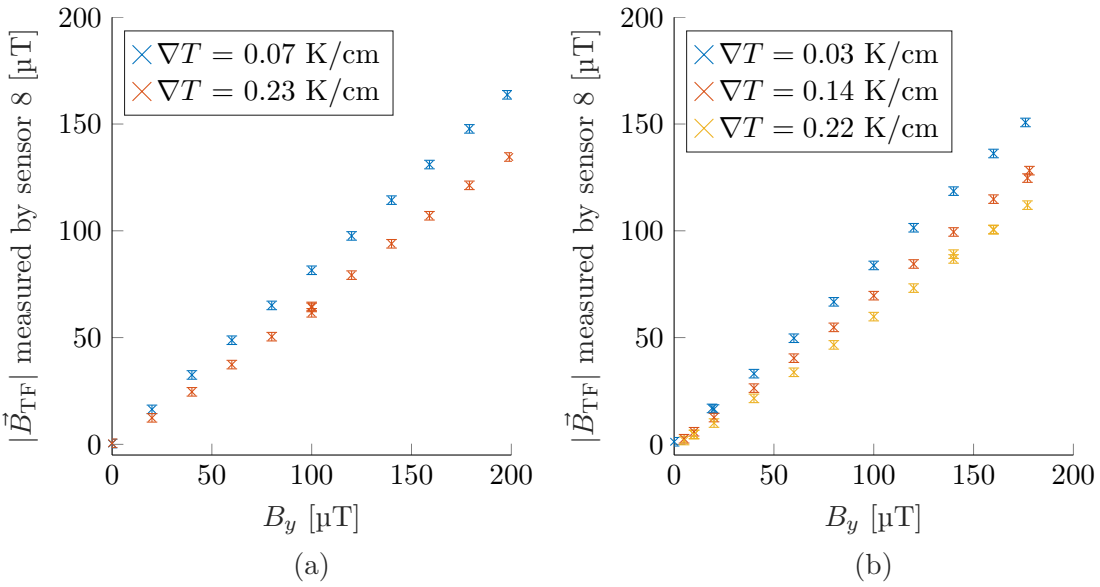

Figure A.6.: Trapped flux measured by the centre sensor group 8 versus B_y. (a) data of the etched fine grain sample. (b) data of fine grain sample before etching for comparison. No clear difference after BCP can be measured.

Taking an exemplary point at $B_y = 160\,\mu\mathrm{T}$ at the highest gradient the data suggests that the sample after the BCP traps more flux (107 µT) than the untreated sample (100 µT). But at smaller external fields this difference again becomes insignificant and no definite statement can be made from this data.

Lastly, trapped flux is plotted against the transition time in Figure A.7. It shows again a sharp increase of trapped flux for transition times shorter than one second. Additionally, trapped flux seems to decrease even for transition times longer than 10 s. But considering the error on this data it is insignificant.

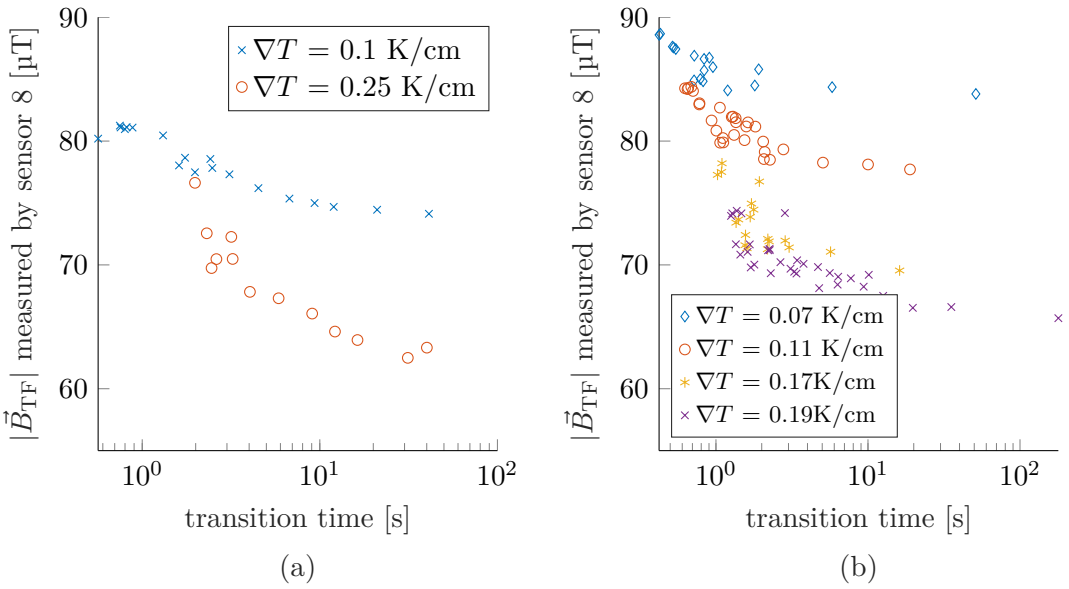

Figure A.7.: Trapped flux measured by the centre sensor group 8 versus B_y. (a) data of the etched fine grain. (b) data of fine grain sample without defect for comparison.

A.3. Technical Drawing of Copper Blocks

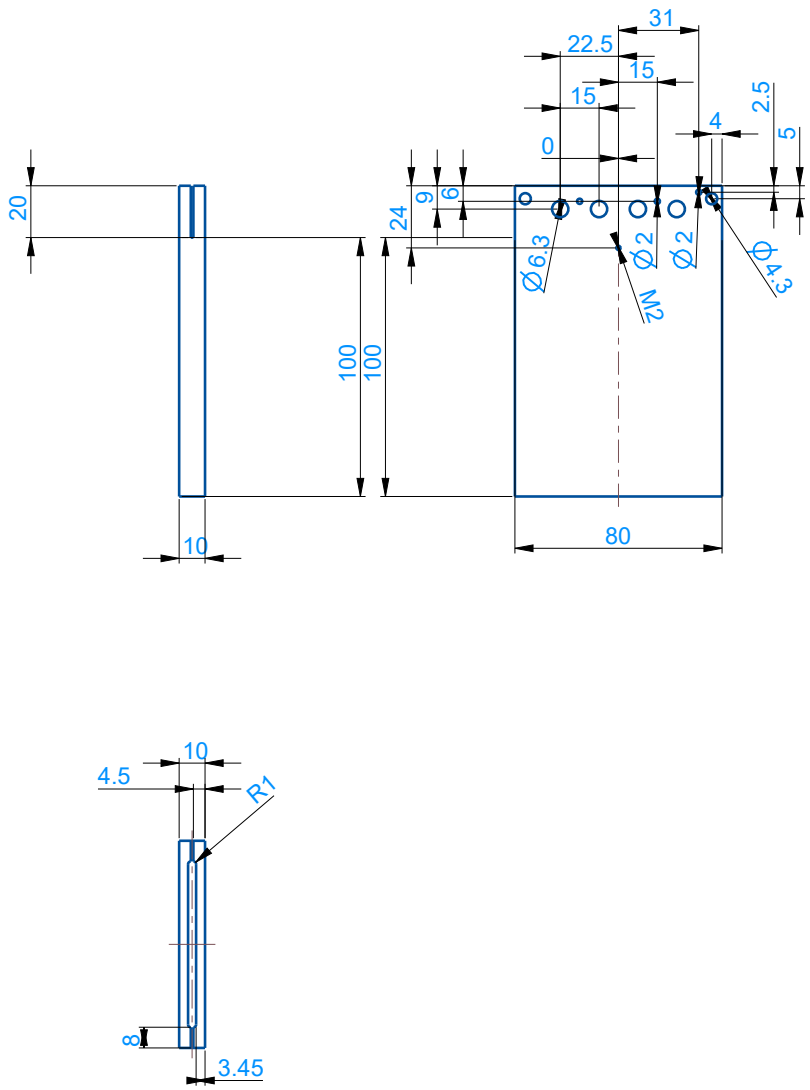

Figure A.8.: Technical drawing of copper blocks.

Bibliography

[1] "LHC Design Report Vol.1: The LHC Main Ring". In: (June 2004). Ed. by O. S. Bruning et al. DOI: 10.5170/CERN-2004-003-V-1.

[2] "CEBAF (Continuous Electron Beam Accelerator Facility) design report". In: (May 1986). DOI: 10.2172/6961172.

[3] H. Hahn et al. "The RHIC design overview". In: *Nucl. Instrum. Meth. A* 499 (2003), pp. 245–263. DOI: 10.1016/S0168-9002(02)01938-1.

[4] Ashley P. Black et al. "Synchrotron radiation based operando characterization of battery materials". In: *Chem. Sci.* 14 (7 2023), pp. 1641–1665. DOI: 10.1039/D2SC04397A.

[5] J. B. Pelka. "Synchrotron Radiation in Biology and Medicine". In: *Acta Physica Polonica Series A (Online)* 114.2 (2008), pp. 309–329. ISSN: 1898-794X.

[6] P. Staron et al., eds. *Neutrons and synchrotron radiation in engineering materials science: From fundamentals to applications*. Second edition. Wiley Online Library. Weinheim: Wiley-VCH, 2017. ISBN: 3527684514. DOI: 10.1002/9783527684489.

[7] M. Richter and G. Ulm. "Metrology with Synchrotron Radiation". In: *Synchrotron Light Sources and Free-Electron Lasers*. Springer, Cham, 2019, pp. 1–35. DOI: 10.1007/978-3-319-04507-8_63-1.

[8] C.M.B. Henderson, G. Cressey, and S.A.T. Redfern. "Geological applications of synchrotron radiation". In: *Radiation Physics and Chemistry* 45.3 (1995). Applications of synchrotron X-radiation, pp. 459–481. ISSN: 0969-806X. DOI: https://doi.org/10.1016/0969-806X(95)92799-5.

[9] P. Suortti and W. Thomlinson. "Medical applications of synchrotron radiation". In: *Physics in medicine and biology* 48.13 (2003), R1–35. ISSN: 0031-9155. DOI: 10.1088/0031-9155/48/13/201.

[10] H. Wiedemann. *Particle Accelerator Physics*. Springer International Publishing, 2019. ISBN: 9783319183176. DOI: 10.1007/978-3-319-18317-6.

[11] Helmholtz-Zentrum Berlin für Materialien und Energie. *BESSY II Light Source*. 10.03.2023. URL: https://www.helmholtz-berlin.de/forschung/quellen/bessy/index_en.html.

[12] M. Altarelli, ed. *The European X-Ray Free-Electron Laser: Technical design report*. Vol. 06-097. DESY. Hamburg: DESY XFEL Project Group, European XFEL Project Team, Deutsches Elektronen-Synchrotron (DESY) in der Helmholtz-Gemeinschaft, 2006. ISBN: 9783935702171.

[13] *WELCOME TO ALBA — en*. 10.03.2023. URL: https://www.cells.es/en/about/welcome.

[14] A. Denker et al. “Ion accelerator applications in medicine and cultural heritage”. In: *Nuclear Instruments and Methods in Physics Research Section A: Accelerators, Spectrometers, Detectors and Associated Equipment* 580.1 (2007), pp. 457–461. ISSN: 0168-9002. DOI: 10.1016/j.nima.2007.05.320.

[15] *Accelerator Facilities | NIDC: National Isotope Development Center*. 10.03.2023. URL: https://www.isotopes.gov/accelerator-facilities.

[16] U. Amaldi. “The importance of particle accelerators”. In: *Europhysics News* 31.6 (2000), pp. 5–9. ISSN: 1432-1092. DOI: 10.1051/epn:2000601.

[17] “The International Linear Collider Technical Design Report - Volume 3.II: Accelerator Baseline Design”. In: (June 2013). Ed. by C. Adolphsen et al. arXiv: 1306.6328 [physics.acc-ph].

[18] A. Abada et al. “FCC-hh: The Hadron Collider”. In: *The European Physical Journal Special Topics* 228.4 (2019), pp. 755–1107. ISSN: 1951-6401. DOI: 10.1140/epjst/e2019-900087-0.

[19] H. Padamsee, J. Knobloch, and T. Hays. *RF Superconductivity for Accelerators*. Wiley Series in Beam Physics and Accelerator Technology. Wiley, 1998. ISBN: 9780471154327.

[20] J. Bardeen, L. N. Cooper, and J. R. Schrieffer. “Theory of Superconductivity”. In: *Phys. Rev.* 108 (5 Dec. 1957), pp. 1175–1204. DOI: 10.1103/PhysRev.108.1175.

[21] P. Dhakal. “Nitrogen doping and infusion in SRF cavities: A review”. In: *Physics Open* 5 (2020), p. 100034. ISSN: 2666-0326. DOI: 10.1016/j.physo.2020.100034.

[22] A. Grassellino et al. “Unprecedented quality factors at accelerating gradients up to 45 MVm −1 in niobium superconducting resonators via low temperature nitrogen infusion”. In: *Superconductor Science and Technology* 30.9 (2017), p. 094004. ISSN: 0953-2048. DOI: 10.1088/1361-6668/aa7afe.

[23] H. Ito et al. “Influence of furnace baking on Q–E behavior of superconducting accelerating cavities”. In: *Progress of Theoretical and Experimental Physics* 2021.7 (2021). DOI: 10.1093/ptep/ptab056.

[24] M. Wenskat et al. “Vacancy-Hydrogen Dynamics and Magnetic Impurities During Mid-T Bake”. In: *Proc. SRF’21* (East Lansing, MI, USA). International Conference on RF Superconductivity 20. JACoW Publishing, Geneva, Switzerland, Oct. 2022, TUOFDV03, pp. 342–348. ISBN: 978-3-95450-233-2. DOI: 10.18429/JACoW-SRF2021-TUOFDV03.

[25] S. Keckert. “Characterization of Nb3Sn and Multilayer Thin Films for SRF Applications”. Dissertation. Siegen: Universität Siegen, 2019.

[26] S. Posen et al. “Advances in Nb 3 Sn superconducting radiofrequency cavities towards first practical accelerator applications”. In: *Superconductor Science and Technology* 34.2 (2021), p. 025007. ISSN: 0953-2048. DOI: 10.1088/1361-6668/abc7f7.

[27] R. C. Dhuley et al. “Thermal Link Design for Conduction Cooling of SRF Cavities Using Cryocoolers”. In: *IEEE Transactions on Applied Superconductivity* 29.5 (2019), pp. 1–5. DOI: 10.1109/TASC.2019.2901252.

[28] G. Ciovati et al. “Multi-metallic conduction cooled superconducting radio-frequency cavity with high thermal stability”. In: *Superconductor Science and Technology* 33.7 (May 2020), 07LT01. DOI: 10.1088/1361-6668/ab8d98.

[29] M. Martinello et al. “Effect of interstitial impurities on the field dependent microwave surface resistance of niobium”. In: *Applied Physics Letters* 109.6 (2016), p. 062601. ISSN: 0003-6951. DOI: 10.1063/1.4960801.

[30] P. Dhakal, G. Ciovati, and A. Gurevich. “Flux expulsion in niobium superconducting radio-frequency cavities of different purity and essential contributions to the flux sensitivity”. In: *Physical Review Accelerators and Beams* 23.2 (2020), p. 023102. DOI: 10.1103/PhysRevAccelBeams.23.023102.

[31] K. H. Bennemann and J. B. Ketterson, eds. *Superconductivity: Conventional and Unconventional Superconductors*. Berlin, Heidelberg: Springer Berlin Heidelberg and Springer e-books, 2008. ISBN: 9783540732532.

[32] S. Posen et al. “Efficient expulsion of magnetic flux in superconducting radiofrequency cavities for high Q0 applications”. In: *Journal of Applied Physics* 119.21 (2016), p. 213903. ISSN: 0021-8979. DOI: 10.1063/1.4953087.

[33] A. A. Abrikosov. “The magnetic properties of superconducting alloys”. In: *Journal of Physics and Chemistry of Solids* 2.3 (1957), pp. 199–208. ISSN: 0022-3697. DOI: 10.1016/0022-3697(57)90083-5.

[34] R. P. Huebener. *Magnetic Flux Structures in Superconductors: Extended Reprint of a Classic Text*. Second edition. Vol. 6. Springer series in solid-state sciences. Berlin, Heidelberg: Springer Berlin Heidelberg, 2001. ISBN: 978-3-642-08753-0.

[35] D. Dew-Hughes. “Flux pinning mechanisms in type II superconductors”. In: *Philosophical Magazine* 30.2 (1974), pp. 293–305. ISSN: 0031-8086. DOI: 10.1080/14786439808206556.

[36] A. Gurevich and G. Ciovati. “Effect of vortex hotspots on the radio-frequency surface resistance of superconductors”. In: *Physical Review B* 87.5 (2013). ISSN: 1098-0121. DOI: 10.1103/PhysRevB.87.054502.

[37] J.-M. Vogt, O. Kugeler, and J. Knobloch. “High- Q operation of superconducting rf cavities: Potential impact of thermocurrents on the rf surface resistance”. In: *Physical Review Special Topics - Accelerators and Beams* 18.4 (2015), p. 042001. DOI: 10.1103/PhysRevSTAB.18.042001.

[38] J.-M. Köszegi and J. Knobloch. “Advanced study of the thermoelectrically generated magnetic field in a nine-cell cavity during the superconducting phase transition”. In: *Physical Review Accelerators and Beams* 22.5 (2019), p. 052001. DOI: 10.1103/PhysRevAccelBeams.22.052001.

[39] T. Okada et al. “Observation of quenching-induced magnetic flux trapping using a magnetic field and temperature mapping system”. In: *Phys. Rev. Accel. Beams* 25 (8 Aug. 2022), p. 082002. DOI: 10.1103/PhysRevAccelBeams.25.082002.

[40] S. Posen et al. “Efficient expulsion of magnetic flux in superconducting radiofrequency cavities for high Q0 applications”. In: *Journal of Applied Physics* 119.21 (2016), p. 213903. ISSN: 0021-8979. DOI: 10.1063/1.4953087.

[41] S. Balachandran et al. “Direct evidence of microstructure dependence of magnetic flux trapping in niobium”. In: *Scientific reports* 11.1 (2021), p. 5364. DOI: 10.1038/s41598-021-84498-x.

[42] S. Ooi et al. “Observation of intermediate mixed state in high-purity cavity-grade Nb by magneto-optical imaging”. In: *Physical Review B* 104.6 (2021), p. 064504. ISSN: 1098-0121. DOI: 10.1103/PhysRevB.104.064504.

[43] S. Huang, T. Kubo, and R. L. Geng. “Dependence of trapped-flux-induced surface resistance of a large-grain Nb superconducting radio-frequency cavity on spatial temperature gradient during cooldown through Tc”. In: *Physical Review Accelerators and Beams* 19.8 (2016), p. 082001. DOI: 10.1103/PhysRevAccelBeams.19.082001.

[44] A. Romanenko et al. “Dependence of the residual surface resistance of superconducting radio frequency cavities on the cooling dynamics around Tc”. In: *Journal of Applied Physics* 115.18 (2014), p. 184903. ISSN: 0021-8979. DOI: 10.1063/1.4875655.

[45] A. Romanenko et al. “Ultra-high quality factors in superconducting niobium cavities in ambient magnetic fields up to 190 mG: Applied Physics Letters, 105(23), 234103”. In: *Applied Physics Letters* 105.23 (2014), p. 234103. ISSN: 0003-6951. DOI: 10.1063/1.4903808.

[46] F. Kramer et al. “Impact of geometry on flux trapping and the related surface resistance in a superconducting cavity”. In: *Physical Review Accelerators and Beams* 23.12 (2020), p. 123101. DOI: 10.1103/PhysRevAccelBeams.23.123101.

[47] D. Longuevergne and A. Miyazaki. “Impact of geometry on the magnetic flux trapping of superconducting accelerating cavities”. In: *Physical Review Accelerators and Beams* 24.8 (2021), p. 083101. DOI: 10.1103/PhysRevAccelBeams.24.083101.

[48] M. Martinello et al. “Magnetic flux studies in horizontally cooled elliptical superconducting cavities”. In: *Journal of Applied Physics* 118.4 (2015), p. 044505. ISSN: 0021-8979. DOI: 10.1063/1.4927519.

[49] M. Wenskat and J. Schaffran. “Analysis of the cool down related cavity performance of the European X-Ray Free Electron Laser vertical acceptance tests”. In: *AIP Advances* 7.11 (2017), p. 115110. DOI: 10.1063/1.5004482.

[50] A. Ivanov, T. Koettig, and A. Macpherson. *Partial Meissner effect measurement by a superconducting magnetic flux lens*. 2021. DOI: 10.48550/ARXIV.2103.06697. URL: https://arxiv.org/abs/2103.06697.

[51] K. Wille. *The physics of particle accelerators: An introduction*. Oxford, New York, and Milton Keynes UK: Oxford University Press and Lightning Source UK, 2000. ISBN: 0-19-850549-3.

[52] B. Aune et al. “Superconducting TESLA cavities”. In: *Phys. Rev. ST Accel. Beams* 3 (9 Sept. 2000), p. 092001. DOI: 10.1103/PhysRevSTAB.3.092001.

[53] D. Reschke et al. “Performance in the vertical test of the 832 nine-cell 1.3 GHz cavities for the European X-ray Free Electron Laser”. In: *Phys. Rev. Accel. Beams* 20 (4 Apr. 2017), p. 042004. DOI: 10.1103/PhysRevAccelBeams.20.042004.

[54] S. Posen et al. “High gradient performance and quench behavior of a verification cryomodule for a high energy continuous wave linear accelerator”. In: *Phys. Rev. Accel. Beams* 25 (4 Apr. 2022), p. 042001. DOI: 10.1103/PhysRevAccelBeams.25.042001.

[55] C.H. Rode. “Temperature optimization for superconducting cavities”. In: *IEEE Transactions on Applied Superconductivity* 9.2 (1999), pp. 873–876. DOI: 10.1109/77.783435.

[56] H. Kamerlingh Onnes. “Further experiments with liquid helium. C. On the change of electric resistance of pure metals at very low temperatures etc. IV. The resistance of pure mercury at helium temperatures”. In: *Koninklijke Nederlandse Akademie van Wetenschappen Proceedings Series B Physical Sciences* 13 (Jan. 1910), pp. 1274–1276.

[57] W. Meissner and R. Ochsenfeld. “Ein neuer Effekt bei Eintritt der Supraleitfhigkeit”. In: *Naturwissenschaften* 21.44 (1933), pp. 787–788. ISSN: 1432-1904. DOI: 10.1007/BF01504252.

[58] F. London and H. London. “The electromagnetic equations of the supraconductor”. In: *Proceedings of the Royal Society of London. Series A - Mathematical and Physical Sciences* 149.866 (1935), pp. 71–88. ISSN: 0080-4630. DOI: 10.1098/rspa.1935.0048.

[59] V. L. Ginzburg and L. D. Landau. “On the Theory of superconductivity”. In: *Zh. Eksp. Teor. Fiz.* 20 (1950). Ed. by D. ter Haar, pp. 1064–1082. DOI: 10.1016/B978-0-08-010586-4.50035-3.

[60] V. L. Ginzburg and L. D. Landau. “On the Theory of Superconductivity”. In: *On Superconductivity and Superfluidity: A Scientific Autobiography*. Berlin, Heidelberg: Springer Berlin Heidelberg, 2009, pp. 113–137. ISBN: 978-3-540-68008-6. DOI: 10.1007/978-3-540-68008-6_4.

[61] T. Matsushita. *Flux pinning in superconductors*. Third edition. Vol. 198. Springer series in solid-state sciences. Cham: Springer, 2022. ISBN: 9783030946395. DOI: 10.1007/978-3-030-94639-5.

[62] J. P. Turneaure, J. Halbritter, and H. A. Schwettman. “The surface impedance of superconductors and normal conductors: The Mattis-Bardeen theory”. In: *Journal of Superconductivity* 4.5 (1991), pp. 341–355. ISSN: 0896-1107. DOI: 10.1007/BF00618215.

[63] J.-M. Köszegi. “Surface resistance minimization in SRF cavities by reduction of thermocurrents and trapped flux”. Dissertation. Universität Siegen, 2016.

[64] T. Kubo. “Flux trapping in superconducting accelerating cavities during cooling down with a spatial temperature gradient”. In: *Progress of Theoretical and Experimental Physics* 2016.5 (2016), 053G01. DOI: 10.1093/ptep/ptw049.

[65] R. P. Huebener. "Superconductors in a temperature gradient". In: *Superconductor Science and Technology* 8.4 (1995), pp. 189–198. ISSN: 0953-2048. DOI: 10.1088/0953-2048/8/4/001.

[66] R. P. Huebener and A. Seher. "Nernst Effect and Flux Flow in Superconductors. I. Niobium". In: *Phys. Rev.* 181 (2 May 1969), pp. 701–709. DOI: 10.1103/PhysRev.181.701.

[67] N. B. Kopnin. "Thermodynamics of vortex motion in type II superconductors". In: *Journal of Low Temperature Physics* 93.1-2 (1993), pp. 117–130. ISSN: 0022-2291. DOI: 10.1007/BF00682284.

[68] P. R. Solomon and F. A. Otter. "Thermomagnetic Effects in Superconductors". In: *Physical Review* 164.2 (1967), pp. 608–618. ISSN: 0031-899X. DOI: 10.1103/PhysRev.164.608.

[69] C. P. Bean and J. D. Livingston. "Surface Barrier in Type-II Superconductors". In: *Physical Review Letters* 12.1 (1964), pp. 14–16. ISSN: 0031-9007. DOI: 10.1103/PhysRevLett.12.14.

[70] I. A. Campbell, A. Fert, and O. Jaoul. "The spontaneous resistivity anisotropy in Ni-based alloys". In: *Journal of Physics C: Solid State Physics* 3.1S (1970), S95–S101. ISSN: 0022-3719.

[71] H. Ebert, A. Vernes, and J. Banhart. "Anisotropic electrical resistivity of ferromagnetic Co-Pd and Co-Pt alloys". In: *Physical review. B, Condensed matter* 54.12 (1996), pp. 8479–8486. ISSN: 0163-1829. DOI: 10.1103/PhysRevB.54.8479.

[72] B. Schmitz. "Ortsauflösende Magnetometrie zur Untersuchung von eingefrorenem Magnetfluss in supraleitenden HF Kavitäten." Master Thesis. Siegen: Universität Siegen, 2017.

[73] *AFF755B MagnetoResistive Field Sensor*. Sensitec GmbH, 2018. URL: https://www.sensitec.com/fileadmin/sensitec/Service_and_Support/Downloads/Data_Sheets/AFF700_800/SENSITEC_AFF755B_DSE_06.pdf.

[74] F. Kramer. "Mapping Trapped Flux and the related Surface Resistance in Superconducting Cavities". Master Thesis. Siegen: Universität Siegen, 2019.

[75] COMSOL AB. *COMSOL Multiphysics v. 6.0*. Stockholm, Sweden, 2021. URL: www.comsol.com.

[76] A. R. Alvarez, E. Franco-Mejía, and C. R. Pinedo-Jaramillo. "Study and Analysis of Magnetic Field Homogeneity of Square and Circular Helmholtz Coil Pairs: A Taylor Series Approximation". In: *Proc. 2012 Andean Region International Conference* (2012).

[77] B. Schmitz et al. "Magnetometric mapping of superconducting RF cavities". In: *Review of Scientific Instruments* 89.5 (2018), p. 054706. ISSN: 0034-6748. DOI: 10.1063/1.5030509.

[78] NI. *LabVIEW version: 2016*. 11500 N. Mopac Expwy, Austin, TX 78759-3504 USA, 2016. URL: https://www.ni.com/de-de/shop/labview.html.

[79] LakeShore Cryotronics. *Cernox®*. Ed. by LakeShore Cryotronics. 13.03.2023. URL: https://www.lakeshore.com/products/categories/overview/temperature-products/cryogenic-temperature-sensors/cernox.

[80] *Model 218*. Lake Shore Cryotronics, Inc., 2017. URL: https://www.lakeshore.com/docs/default-source/product-downloads/manuals/218_manual.pdf?sfvrsn=6a03068_3.

[81] imc Test & Measurement GmbH. *imc SPARTAN*. 13.03.2023. URL: https://www.imc-tm.de/produkte/messtechnik-hardware/imc-spartan/ueberblick/.

[82] F. Primdahl. "The fluxgate magnetometer". In: *Journal of Physics E: Scientific Instruments* 12.4 (1979), pp. 241–253. ISSN: 0022-3735. DOI: 10.1088/0022-3735/12/4/001.

[83] *Mag-01H*. Bartington Instruments Ltd, 2023. URL: https://bartingtondownloads.com/wp-content/uploads/DS0003.pdf.

[84] The MathWorks Inc. *MATLAB version: 9.11.0.1809720 (R2021b)*. Natick, Massachusetts, United States, 2021. URL: https://www.mathworks.com.

[85] S. Posen et al. "Role of magnetic flux expulsion to reach Q0>3×1010 in superconducting rf cryomodules". In: *Physical Review Accelerators and Beams* 22.3 (2019), p. 032001. DOI: 10.1103/PhysRevAccelBeams.22.032001.

[86] O. Hryhorenko et al. "An Innovative Approach of Surface Polishing for SRF Cavity Applications". In: *Journal of Manufacturing and Materials Processing* 7.2 (2023), p. 62. ISSN: 2504-4494. DOI: 10.3390/jmmp7020062.

[87] S. Aull, O. Kugeler, and J. Knobloch. "Trapped magnetic flux in superconducting niobium samples". In: *Physical Review Special Topics - Accelerators and Beams* 15.6 (2012), p. 062001. DOI: 10.1103/PhysRevSTAB.15.062001.

[88] W. Singer et al. "Development of large grain cavities". In: *Physical Review Special Topics - Accelerators and Beams* 16.1 (2013), p. 012003. DOI: 10.1103/PhysRevSTAB.16.012003.

[89] P. Kneisel et al. "Review of ingot niobium as a material for superconducting radiofrequency accelerating cavities". In: *Nuclear Instruments and Methods in Physics Research Section A: Accelerators, Spectrometers, Detectors and Associated Equipment* 774 (2015), pp. 133–150. ISSN: 0168-9002. DOI: 10.1016/j.nima.2014.11.083.

[90] J.-M. Köszegi et al. "A magneto-optical study on magnetic flux expulsion and pinning in high-purity niobium". In: *Journal of Applied Physics* 122.17 (2017), p. 173901. ISSN: 0021-8979. DOI: 10.1063/1.4996113.

[91] W. Singer A. Brinkmann. "Nondestructive Testing of Niobium Sheets for SRF Cavities Using Eddy-current and SQUID Flaw Detection ". In: *Proc. 24th International Linear Accelerator Conference* (Vancouver, Canada). Linear Accelerator Conference. Sept. 2008, THP012, pp. 800–803.

[92] O.B. Malyshev et al. “Main Highlights of ARIES WP15 Collaboration”. In: *Proc. SRF'21* (East Lansing, MI, USA). International Conference on RF Superconductivity 20. JACoW Publishing, Geneva, Switzerland, Oct. 2022, WEPFDV007, pp. 571–575. ISBN: 978-3-95450-233-2. DOI: 10.18429/JACoW-SRF2021-WEPFDV007.

[93] O. S. Brüning et al. *LHC Design Report*. 2004. DOI: 10.5170/CERN-2004-003-V-1.

[94] S. Aull et al. “On the understanding of Q-slope of niobium thin films”. In: *Proc. 17th International Conference on RF Superconductivity (SRF'17)*. 2015, TUBA03. DOI: 10.18429/JACoW-SRF2015-TUBA03.

[95] A. Hilger et al. “Tensorial neutron tomography of three-dimensional magnetic vector fields in bulk materials”. In: *Nature communications* 9.1 (2018), p. 4023. DOI: 10.1038/s41467-018-06593-4.

[96] T. Junginger et al. “Field of first magnetic flux entry and pinning strength of superconductors for rf application measured with muon spin rotation”. In: *Physical Review Accelerators and Beams* 21.3 (2018), p. 032002. DOI: 10.1103/PhysRevAccelBeams.21.032002.

[97] A. Cierpka. “Investigation of Allen-Bradley resistors for use as sensors in a cryogenic temperature mapping system to study the superconducting transition in SRF materials”. Bachelor Thesis. Siegen: Universität Siegen, 2022.

[98] J. Knobloch. “Advanced Thermometry of Superconducting Radio Frequency Cavities”. Dissertation. Ithaca, New York, USA: Cornell University, 1997.

[99] A. Gurevich. “Enhancement of rf breakdown field of superconductors by multilayer coating”. In: *Applied Physics Letters* 88.1 (2006), p. 012511. ISSN: 0003-6951. DOI: 10.1063/1.2162264.

Acknowledgements

I would like to use this opportunity to thank all the people how made this work possible.

First I would like to thank my supervisor Jens Knobloch for giving me the opportunity to do this work in his institute, his support during the thesis, and the open discussions. I would also like to thank my second referee Wolfgang Hillert.

I am thankful to Takayuki Kubo for supporting me with the development of the phenomenological model and answering my questions.

A big thanks to my second supervisor Oliver Kugeler for always having an open door, and good advise. Thanks as well to Sebastian Keckert who not only was always open for discussions but also brought the glass cryostat in a state so I could start measurements right away. For the sample preparations I would like to thank Alena Prudnikava, and Yegor Tamashevich.

I extend my thanks to Alexander Cierpka and Vincent Strugalla who explored new sensor possibilities for the measurement setup and enhanced the capabilities of the setup in the course of their bachelor theses.

I would also like to thank Beñat Alberdi Esuain and Irma Schmidt for making the hours in the office more enjoyable.

Last but not least, I would like to thank my family especially my parents Thomas, and Elisabeth for always supporting me during my whole life and my girlfriend Vivien for not only helping me through the rough times but also for many discussions and support regarding the design of the setup, and gathered data as well as for asking the right critical questions.

Thank you!